Growth of InGaN nanowires for photovoltaic and piezoelectric energy harvesting

Martina Morassi

NNT : 2018SACLS249

Thèse de doctorat

Croissance de nanofils InGaN pour les dispositifs de récupération d'énergie photovoltaïques et piézoélectriques

Thèse de doctorat de l'Université Paris-Saclay
préparée à l'Université Paris Sud

École doctorale ELECTRICAL, OPTICAL, BIO-PHYSICS AND ENGINEERING (EOBE) n° 575
Spécialité de doctorat: Physique

Thèse présentée et soutenue à Orsay, le 18 septembre 2018, par

Martina Morassi

Composition du Jury :

Mathieu Kociak Directeur de Recherche, LPS-UPSud, CNRS (UMR8502)	Président
Eva Monroy Directeur de Recherche, CEA, Grenoble	Rapporteur
Lutz Geelhaar Directeur de Recherche, PDI, Berlin (Allemagne)	Rapporteur
Silvia Rubini Directeur de Recherche, IOM-CNR, Trieste (Italie)	Examinateur
Mathieu Kociak Directeur de Recherche, LPS-UPSud, CNRS (UMR8502)	Examinateur
Maria Tchernycheva Professeur, C2N-UPSud, CNRS (UMR9001)	Directeur de thèse
Noëlle Gogneau Chargé de Recherche, C2N-UPSud, CNRS (UMR9001)	Co-Encadrant de thèse

Université Paris-Saclay
Espace Technologique / Immeuble Discovery
Route de l'Orme aux Merisiers RD 128 / 91190 Saint-Aubin, France

"*È così bello fissare il cielo e accorgersi di come non sia altro che un vero e proprio immenso laboratorio di fisica che si srotola sulle nostre teste.*"

Margherita Hack

Firenze, 12 giugno 1922 – Trieste, 29 giugno 2013

Acknowledgements

With no doubts nor exaggeration, this Ph.D. thesis has been one of the most valuable, formative and important experience of my whole life. As I always repeat to my collegues (provoking a mix of laughing and disbelief), I would sign today a second PhD agreement, and start a new thesis next week. If even after three years of hard work, repetitive failures, experimental burnouts, dead-line runs and very strong adrenaline spikes I am still here saying that doing a Ph.D. is an incredibly valuable professional and personal experience, it is most of all thanks to my supervisors Noelle Gogneau and Maria Tchernycheva. You guided me all along this journey, always sharing with me all your knowledge about the different topics I addressed, and giving me wisdom directions when I was lost in my results. You gave me support when I was discouraged, energy when I was tired, trust when you sent me to many different conferences all around the world. You taught me how to be pragmatic in scientific research, yet rigorous. I deeply thank you for all this.

I would like to thank all the single members of the jury for accepting to be in my PhD defence and evaluating my work: Lutz Geelhaar, Eva Monroy, Silvia Rubini and Mathieu Kociak. I feel respect and admiration for the way you work, and it has been a great honor to have all of you in my jury.

This work would not have been possible without the scientific contributions of Ludovic Largeau, for all TEM, EDX and XRD measurements along with the teachings about the underlying theory behind these beautiful characterization techniques. Fabrice Oheler, for the nice CL maps on single NWs. Laurent travers, for its expert, essential and endless manutention work on our MBE machine (without you, we would be lost!!). Ali Madouri, for teaching me the graphene transfert process, the basics of Raman spectroscopy and for providing graphene flakes substrates. Christian Ulysse and Christophe Dupuis who teched me how to (properly!) use SEM, STEM and EDX in our Magellan SEM.

I want to thank two international collaborators, that defenetly enriched my thesis work with their scientific contributions: prof. Yong-Hoon Cho of the KAIST University of South Korea along with its Ph.D. students H-G. Song and Min-Ho Choi, and prof.

Vladimir Dubrovskii from ITMO of Saint Petersburg.

Also, I want to thank my colleagues Frank Glas and Jean-Christophe Harmand. Every time I needed your help or opinion, your doors and minds were always open, and every time I exit your offices, I felt enriched in knowledge and/or I had a much clearer vision on the further questions I had to ask myself. Every discussion has been interesting and fruitful. On few delicate points of my work, I think your contribution really made the difference.

I really want to thank Aristide Lemaitre. You know how important was for me to conclude successfully my Ph.D. and to write this manuscript as I wanted. Thank you for giving me the time to do it, and for the human and scientific support that you gave me in our coffee pauses. It has been really important for me, thank you.

Un pensiero importante va ai miei genitori, mia nonna Carolina e mia zia Sandra. Ci sono mille motivi per cui sono a voi grata, ma in questa occasione voglio ringraziarvi per un insegnamento particolare, per il quale, in diverse occasioni e ognuno a proprio modo, tutti voi avete contribuito. Voglio ringraziarvi per avermi insegnato ad andare fino in fondo alle cose, nel senso piu' lato ma anche piu' stretto del termine, e a mettere sempre amore, cura e dedizione nelle mie azioni perche' l'amore genera frutti e i frutti generano altri semi. Grazie a voi ho imparato che e' questo a fare la differenza fra un successo e un fallimento, a prescindere dal valore in se' del risultato che si ottiene.

During this Ph.D I knew many people. Some of them still work in this region, some of them flew far away. In sparse order: Valerio Piazza, Lu Lu, Nan Guan, Vladimir Neplokh, Lorenzo Mancini, Andrea Scaccabarozzi, Camille Barbier, Chalemchai "Buk" Imwas, Nuno "Nogno", Rebeca Diaz, Vishnu Kumaresan, Nicolas Jamond, Vivek Panappakam, Carlos Anton Solanas, Niccoló Somaschi, Jonathan Lee, Dimitris Kazazis, Konstantinos Pantzas, Amedeo Michaud, Vincent Brac, Hezhi Zhang, Quentin Gaimard, Carmen Gomez, Konstantinos Papatrifonos..and for sure I am forgetting some of you! With all of you I spent very nice moments, we laughed, we chatted and we had very deep discussions about science, politics, or even the meaning of life (of course, never conclusive). Thanks to all of you for being my friends all along this journey, this has been important for me, and I will always keep alive those nice memories.

Last but not least, a special thanks goes to my soulmate Giacomo. No words can describe how valuable and important is your presence in my life. And of course I am not only making reference to all the times you supported me (personally and professionally), you feeded me (since I was too busy during my work to even think about cooking) and you took care of everything which went beyond “my thesis writing”, i.e. my only obsession during these last, hard months. If I am here today, it’s most of all thanks to you and thanks to what we are.

Contents:

General introduction and thesis overview

Electrical energy is one of the most important outcomes of work that scientific research provided to the mankind, and its consumption steadily increases over the years. Among the large scenario of daily-life powered devices, nomad devices such as cell-phones and medical systems are mainly powered by external batteries. Despite the recent progress made in the development of new batteries, these sources are not fully autonomous, are usually voluminous in size and need to be regularly replaced due to their limited lifetime. In this context, the development of new lightweight nano-devices, able to convert environmental energies into usable electricity has become a priority. Solar energy and mechanical energies are two classes of renewable energies that could be efficiently harvested to bring energy independency to nomad devices.

This thesis aims is to study and contribute to the development of a new generation of light-weight solar cells and piezo-generators based on III-V heterostructured nanowires (NWs). The objective is to demonstrate an innovative concept of flexible devices, based on composite membranes: functional NWs are embedded into a polymeric matrix (detached from their epitaxial substrate), which could potentially be deposited on any type of carrying substrate, including plastic, metal or even tissues. A considerable part of the project focuses on NWs of III-Nitride materials, which are characterized by a strong piezoelectric response as well as by a photovoltaic conversion capacity in the blue and green parts of the solar spectrum.

A key element of this project relies on the synthesis of $In_xGa_{1-x}N/GaN$ heterostructured NWs and on the engineering of their functional properties, in relation to their internal structure and device design. Growing InGaN alloys in a NW form is moreover interesting, since strain can be accommodated elastically at their free lateral surfaces, offering the possibility to achieve high-quality In-rich InGaN heterostructures. In fact, the growth of In-rich InGaN layers on GaN substrates is a major challenge due to a complex interplay of strain (lattice mismatch between InN and GaN is as high as 11%) and kinetic factors, resulting in high threading dislocation densities and non-homogeneous alloy composition.

In this context, the ultimate purpose is to synthesize ordered arrays of InGaN/GaN NWs, with a high control over the composition (which determines the InGaN band-gap) and the crystal quality of the $In_xGa_{1-x}N$ heterostructures. For photovoltaic structures, an appropriate doping of the GaN segments is also required. This Ph.D. thesis constitutes a partial but still decisive fulfillment of all these objectives, with development along the following three fundamental axes:

- The rational and controlled growth of InGaN/GaN NW heterostructures by Plasma-Assisted Molecular Beam Epitaxy (PA-MBE) with tailoring of their morphology, band-gap and structural properties;
- The assessment of their optical properties, in accordance to their composition and strain-dependent band structure. This study is very interesting from a fundamental point of view, but is also crucial to identify the optimum InGaN/GaN NW photovoltaic structure;
- The identification of a viable selective-area growth strategy, to gather the best control over the III-N NWs morphology and positioning.

Results on all these topics are presented, constituting original improvements in the context of the actual scientific literature. Whenever possible, the experiments have been accompanied with a theoretical modeling, allowing a deeper comprehension of the physical phenomena in play and/or the identification of key parameters for further developments.

The manuscript is structured as follows:

Chapter 1 provides the most basic information, useful for the understanding of the manuscript. Here, I introduce the basic properties of III-N materials, the principles of epitaxial MBE growth, along with a concise literature review about nitride NWs growth and their properties. Also, the fundamental arguments for using InGaN/GaN NWs for photovoltaic and piezoelectric applications are described.

In Chapter 2, I describe a systematic investigation of the growth of InGaN heterostructures. Straightforward growth routes for the control-by-design of their basic and most relevant properties are traced based on detailed morphological, structural, and compositional characterizations. The results are then rationalized within a comprehensive flux-dependent growth diagram, where distinct morphological and In

incorporation regimes are identified. Based on the experimental evidences, the growth mode of the InGaN sections is then discussed through a theoretical model considering the interplay of strain and surface energies.

In Chapter 3, I address the optical properties of ensembles and single InGaN/GaN NWs. Their photoluminescence properties are discussed in relation to their structural and compositional properties. Then, I investigate the effect of the polarization field on the optical properties of thick In-rich InGaN sections, presenting a combined axial and core-shell structure. Specifically, their carrier dynamics and cathodoluminescence properties are analyzed in accordance to their simulated strain distribution, internal field and resulting band edge profile.

In Chapter 4, I demonstrate an alternative approach to achieve selective area growth (SAG) of nitride NWs by plasma-assisted MBE. CVD-grown graphene is transferred from its original copper substrates to amorphous layers of SiO_2, and used as seed substrate for the GaN NWs growth. The growth temperature allowing for a 100% SAG is identified, and the graphene properties after the growth process are analyzed. The temporal dynamics of GaN NWs nucleation and growth on patterned mono-layer graphene are investigated through a modeling of their length distribution. Finally, a strategy for further improvements of this SAG approach is discussed.

Finally, in Chapter 5, I provide some preliminary results concerning the growth of InGaN/GaN NWs on graphene substrates, the epitaxial growth and electron-beam induced current characterization of GaN NW p-n junctions and InGaN/GaN NW photovoltaic p-i-n junctions as well as some piezoelectric conversion measurements on InGaN/GaN heterostructured NWs. Perspectives concerning the future evolution of this work are provided.

Chapter 1

Basics of III-N materials and nanowires growth

This chapter provides an overview on the most basic and relevant properties of nitride materials, along with the motivations for using InGaN/GaN NW heterostructures for photovoltaic and piezoelectric devices. Some basic concepts of epitaxial PA-MBE growth are provided, as well as a review on the growth mechanism and basic structural properties of self-assembled GaN NWs by PA-MBE.

1.1 Brief history of III-N materials

III-nitrides are excellent wide band gap semiconductors, commonly used in modern devices such as light-emitting diodes (LEDs), lasers, ultraviolet detectors and high electron mobility transistors (HEMTs). However, before starting an active exploitation of their potential to create operational devices, it was necessary to understand their properties and solve several material problems.

From the first GaN single-crystal deposition by hydride vapour phase epitaxy in 1969[1], the exploitation of this material was for a long time impeded by the extremely high n-type background doping of the layers, attributed a large density of N vacancies. After more than two decades of efforts, a successful deposition of a good quality GaN was reported by Nakamura et al. by Metal-Organic Chemical Vapour Deposition (MOCVD) by growing a low-temperature GaN buffer layer to filter dislocations formed at the GaN/sapphire interface[2]. Using this strategy, Nakamura et al. were able to achieve a very high electron mobilities and low background electron doping.

In spite of improved quality, it was still difficult to obtain p-type conductivity in GaN samples. This fact was explained by the influence of hydrogen that forms acceptor-H complexes in p-doped GaN film causing hole compensation[3,4]. Post-growth thermal annealing of Mg-doped GaN samples under N_2 was applied to destroy these complexes, allowing to reach higher hole concentrations and mobilities[5]. On the base of these substantial material improvements, Amano et al. demonstrated the first LED based on p-n GaN junction[6]. Later, LED structure was further improved by insertion of InGaN layer between n- and p-GaN. LEDs based on a single InGaN quantum well and emitting different colors (blue and green) were demonstrated by Nakamura et al. in 1995[7]. The colors were adjusted by changing the In-composition from 20 to 70% in the alloy. Thanks to these exceptional results, in 2014 I. Akasaki, H. Amano and S. Nakamura were awarded with the Nobel Prize "for the invention of efficient blue light-emitting diodes which has enabled bright and energy-saving white light sources". Currently, InGaN is the usual material used in modern blue and green LEDs.

From this brief overview, it follows that the key achievements and developments in the field of III-N materials have been made by the MOCVD technique. In fact, in spite of many potential advantages of MBE growth, such as *in situ* monitoring techniques, MBE grown optoelectronic structures had a lower quantum efficiency at the beginning. This led many researchers to conclude that the only solution for MBE would be to bring the growth conditions as close as possible to the ones used in MOVPE, i.e. to apply high growth temperatures (~1050 °C for GaN) and high nitrogen precursor overpressures[8]. Indeed, ammonia MBE, which uses atomic beams for group III elements coupled with a large excess supply of NH_3 [8,9], has been successful in improving the optical quality of MBE nitride films and produced the first room temperature laser diode (LD) by Sharp Laboratories of Europe in 2004, and immediately after (same year) by C. Skierbiszewski[10]. However, the corrosive nature of ammonia compound and the undesirable high hydrogen background create additional technological challenges. In the more widely employed Plasma-Assisted MBE, purified nitrogen is activated using an RF-plasma and supplied to the growth surface, thus eliminating the problem of hydrogen background pressure. The breakthrough of this technique came with the finding that in metal-rich conditions, it is possible to grow high-quality and smooth layers at much lower growth temperatures compared to MOVPE (~750 °C for PA-MBE GaN)[11]. Sustained comprehension and refinement of the PA-MBE growth conditions on GaN/sapphire MOVPE templates[12–14] allowed the demonstration of promising LED devices[11], and now PA-MBE is a technique of choice for the growth of high-quality III-N compounds (and in particular, of In-rich InGaN alloys).

1.2 Basic properties of III-N

This chapter describes some basic properties of III-N materials, with an emphasis on the ones which are relevant for photovoltaic and piezoelectric applications.

1.2.1 Crystal structure

III-N materials crystalize either in a hexagonal or in a cubic-face-centered lattices, more usually referred as wurtzite (WZ, Fig. 1.1(a)) and zinc-blende (ZB, Fig. 1.1(c)). A common feature of these two structures is that they present a similar primitive plane

where the atoms are organized in a hexagonal pattern. Hence, both crystal structures can be described through a specific stacking of these primitive planes: the wurtzite structure has an ABABA… pattern along the [0001] direction, and the zinc-blende structure has an ABCABC… stacking along its [111] direction, shown in Figure 1.1(b,d).

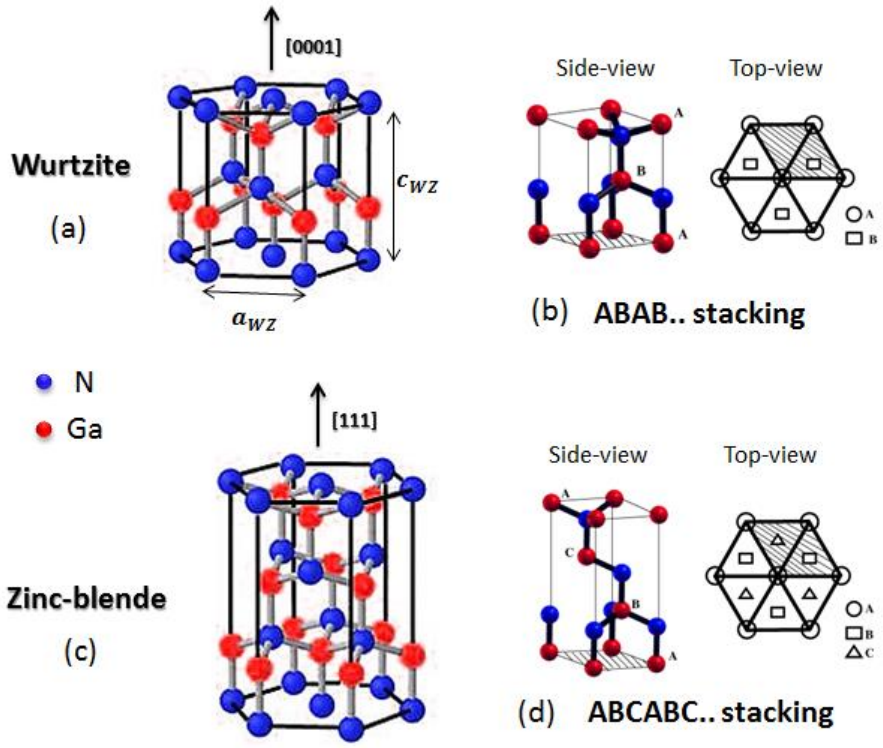

Figure 1.1 Schematic representations of the Wurtzite (a) and Zinc-blend (c) lattices, with their corresponding stacking sequences (b, d).

For nitrides, the WZ phase is thermodynamically much more stable than the ZB phase, and is the common crystal structure observed in epitaxial layers and NWs. However, the per atom energy difference between these two crystal phases is relatively small, with reported values of about 10 meV for both GaN and InN[15,16]. By consequence, the inclusion of small sections of ZB material, usually referred to as a stacking fault (SF), is a relatively common feature in III-nitride NWs. Specifically, stacking faults involving 2 to 9 MLs ZB inclusions have been reported for GaN NWs grown by plasma-assisted MBE[17,18].

The crystallographic directions of the WZ structure are defined by four indices (*h, k, i, l*), which obey to the constraint *h+k+i=0*. The most common are usually labeled by letters instead of the regular Miller indices. Hence, the [0001] direction is usually referred to as ***c***

or out-of-plane axis, while the ***a*** and ***m*** axes respectively, correspond to [1-100] and [11-20] directions. Similarly, the family of crystal planes perpendicular to these directions, are commonly referred to as ***c*** (0001), ***a*** (1-100) and ***m*** (11-20) planes. This notation will be often used in the manuscript. The wurtzite unit cell is univocally defined by its ***a*** and ***c*** lattice parameters, which are also used to compute in-plane and out-of-plane deformations and lattice mismatches in epitaxial heterostructures. These aspects are schematized in Figure 1.2, while the lattice parameters of III-N binaries are listed in table 1.1.

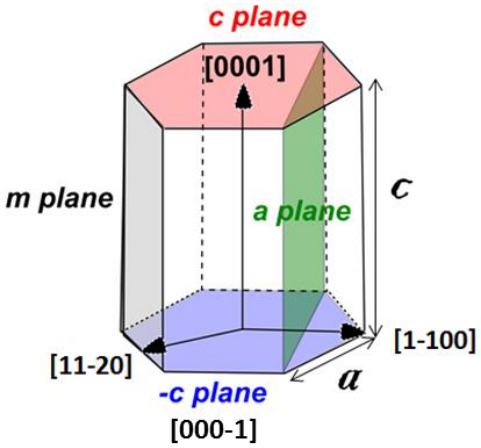

Figure 1.2 Principal families of crystal planes of WZ crystal structure and its lattice constants.

Table 1.1 Lattice constants of III-N binaries, measured at 300 K[15,16,19].

	InN	GaN	AlN
a (Å)	3.454	3.19	3.11
c (Å)	5.703	5.125	4.98

1.2.2 Crystal polarity

An important feature of the wurtzite crystal structure, is its lack of central symmetry. By consequence, the [0001] (c) and [000-1] (-c) directions are not equivalent, and the material can be defined as "polar". The polar orientation is commonly defined by considering the metal-to-nitrogen bonds directions parallel to the c axis: the +c vector (-c, respectively) corresponds to a metal-to-nitrogen (nitrogen-to-metal, respectively) orientation. Thus a metal-polar (M-polar) surface, results from a crystal where the lower (first) surface layer

is composed of nitrogen atoms (Figure 1.3, right), while for nitrogen-polar (N-polar) surfaces, the first atomic layer is metallic (Figure 1.3, left). It should be pointed out that due to the high reactivity of N dangling bonds, N-polar surfaces are often terminated by a mix of Ga and N atoms. As will be mentioned in different parts of the manuscript, in epitaxial growth, the surface polarity impacts the atoms adsorption-desorption processes, the surface diffusivity and the incorporation kinetics, and hence affects the morphology and composition of the epitaxial layers and NW heterostructuctures.

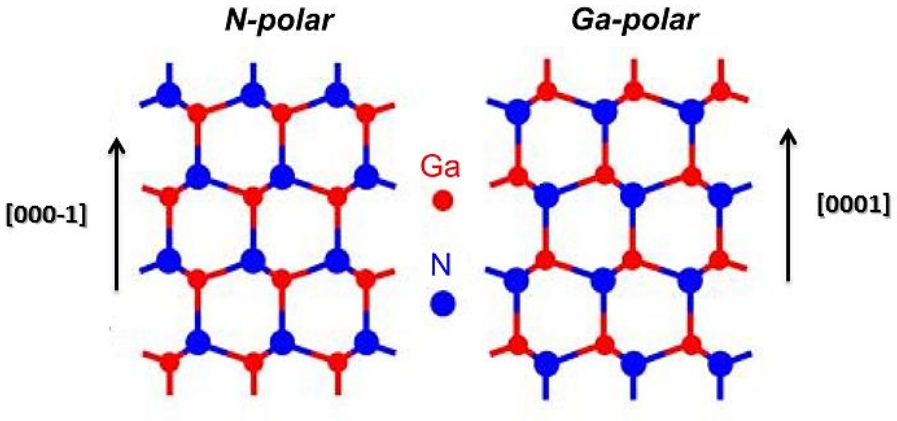

Figure 1.3 Drawing of a GaN structure with nitrogen (left) and metal (right) polarity.

1.2.3 Mechanical properties

Similarly to other semiconductors, the epitaxial growth of III-N materials results in a presence of strain. Depending on whether the relaxed lattice parameter of the epitaxial material (a_0) is greater or smaller than the one of the substrate (a_s), the growing crystal will experience a bi-axial in-plane strain which is either compressive or tensile. In 2D layers, due to the free top-surface, small amounts of in-plane strain can be accommodated by a small deformation of the lattice in the out-of-plane direction, as illustrated in Figure 1.4.

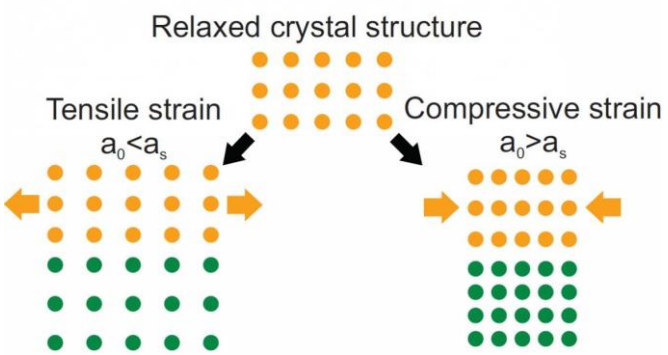

Figure 1.4 Visual representation of compressive and tensile strain in mismatched heteroepitaxial structures.

The basic principle of strained-layer epitaxy is that a certain amount of strain can be accommodated elastically by any material. However, this accommodation depends on both the layer thickness and on the percentage of the lattice mismatch. If one of the two parameters is fixed, there is a critical value of the second parameter above which the strained structure is unstable against plastic relaxation, which in most of the cases occurs through the formation of misfit dislocations. For $In_xGa_{1-x}N$ layers grown on GaN substrate along the c direction, due to the huge lattice mismatch between the two binaries (11 %) this critical thickness decreases rapidly with the In content. Specifically, it decreases from about 10 nm for x=0.10 to about 1 nm for x=0.40[20].

The mechanical deformations of an epitaxial layer can be described to a great degree of accuracy within the framework of elastic deformation theory. Specifically, the in-plane ($\varepsilon_{\parallel} = (\varepsilon_{xx} - \varepsilon_{yy})/2$) and the out-of-plane ($\varepsilon_{\perp} = \varepsilon_{zz}$) strains can be defined as:

$$\varepsilon_{\parallel} = \frac{a - a_0}{a_0} \qquad \text{(eq. 1.1)}$$

$$\varepsilon_{\perp} = \frac{c - c_0}{c} \qquad \text{(eq. 1.2)}$$

Where a and c are the observed lattice parameters of the epitaxial structure (and, as above, a_0 and c_0 are its strain-free lattice parameters). Thus, if the strain is compressive its value will be negative, and vice versa if the strain is tensile. These simple relations will be used in Chapter 2 to calculate the lattice deformation of InGaN NW heterostructures, by using the a and c parameters measured by X-Ray diffraction.

The mechanical deformations are related to the biaxial stress (σ_{ij}) imposed, for example, from the bulky underlying substrate, by the Hook's law:

$$\sigma_{ij} = \sum_{kl} C_{ij\,kl} \cdot \varepsilon_{kl} \qquad \text{(eq. 1.3)}$$

Where $C_{ij\,kl}$ is the tensor of the elastic module of the material. This tensor can be written in the form of a 6x6 matrix of elastic constants, where the crystal directions {xx, yy, zz, yz, zx, xy} are substituted by the numerical indexes {1, 2, 3, 4, 5, 6}. For a crystal having a hexagonal symmetry, the matrix has 6 elastic coefficients, among which 5 are independent ($C_{66} = C_{11}$-C_{12}). The InN and GaN elastic constants are summarized in Table 1.2, while in the case of InGaN, these are usually derived as linear interpolation of the binary's ones.

Table 1.2 Elastic constants of III-N binaries (in GPa)[21,22].

	C_{11}	C_{12}	C_{13}	C_{33}	C_{44}
InN	190	104	121	182	10
GaN	390	145	106	398	105
AlN	410	149	99	389	125

As far as the material's elastic constants are known, the lattice deformation can be calculated numerically for a specific heterostructure geometry. This is the basic principle used in the Comsol strain simulation presented in Chapter 3.

1.2.4 Spontaneous and piezoelectric polarization

Polarization is an important feature of WZ III-N materials, which sets them apart from other semiconductors, and drives their interest for the fabrication of novel III-N based piezogenerators[23]. The difference in electronegativity between N and metallic atoms displaces the bond's electron clouds towards N atoms and each atomic bond presents an electrical dipole. In turn, the lack of central symmetry of the WZ crystal structure does not allow a mutual annulation of the bond's electric dipoles, resulting in a macroscopic *spontaneous polarization* (P_{sp}), which is maximum along the c direction (oriented from the Ga to the N atoms). This is sketched in Figure 1.5.

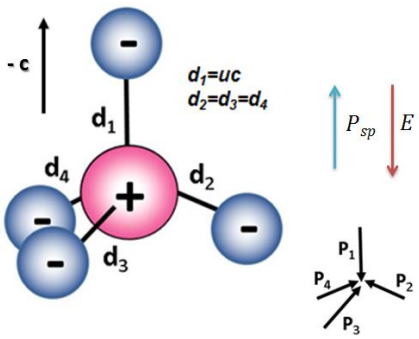

Figure 1.5 Scheme representing the spontaneous polarization (P_{sp}) and resulting electric field (E) for a [000-1] oriented III-N bonds tetrahedron.

Obviously, the spontaneous polarization changes for different materials depending on the III-N difference in electronegativity and on the bond's length (Table 1. 3).

Table 1.3 Spontaneous polarization and piezoelectric coefficients of III-N materials[24].

	InN	GaN	AlN
Spontaneous polarization (Cm^{-2})	-0.032	-0.029	-0.081
Piezoelectric coefficients (Cm^{-2}) :			
e_{15}	0.65	-0.3	-0.48
e_{31}	-0.055	-0.49	-0.6
e_{33}	1.07	0.73	1.46

The distance between negative and positive centroids is also influenced by strain, which leads to the so-called piezoelectric polarization (P_{pz}). Its components can be calculated from the piezoelectric 6x6 piezoelectric tensor:

$$\begin{bmatrix} P_x \\ P_y \\ P_z \end{bmatrix} = \begin{pmatrix} 0 & 0 & 0 & 0 & e_{15} & 0 \\ 0 & 0 & 0 & e_{15} & 0 & 0 \\ e_{13} & e_{13} & e_{33} & 0 & 0 & 0 \end{pmatrix} \begin{bmatrix} \varepsilon_{xx} \\ \varepsilon_{yy} \\ \varepsilon_{zz} \\ \varepsilon_{yz} \\ \varepsilon_{xz} \\ \varepsilon_{xy} \end{bmatrix} \qquad \text{(eq. 1.4)}$$

where the e_{ij} are the piezoelectric coefficients of the material, and ε_{ij} is the strain in the direction *ij*. Depending on whether the strain is compressive or tensile, the piezoelectric polarization can be parallel or antiparallel with respect to the spontaneous polarization. The effect of a compressive/tensile stress along the c axis on the piezoelectric polarization of a N-polar GaN NW is schematized in Figure 1.6.

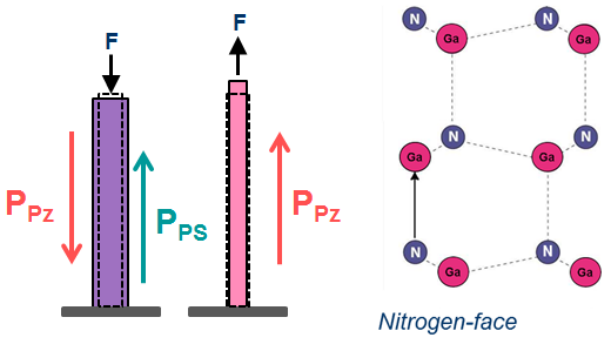

Figure 1.6 Spontaneous polarization in a N-polar GaN NW, and the corresponding piezoelectric polarization vectors for compressive and tensile out-of-plane stress.

Importantly, as concerns III-N ternary alloys, Bernardini and Fiorentini[24] showed that the appropriate method to compute the spontaneous and piezoelectric polarizations, consists in computing the polarization of the end-binaries first. However, differently from piezoelectric polarization, the spontaneous polarization has a strong non-linear component. This non-linearity can be modeled to a good degree by using a linear interpolation with a quadratic correction term analogous to the band-gap bowing:

$$P_{sp}^{ABN} = x\,P_{sp}^{AN} + (1-x)P_{sp}^{BN} + bx(1-x) \qquad \text{(eq. 1.5)}$$

where x is the alloy "AN" molar fraction, and b is a bowing parameter (an appropriate b for InGaN is 0.037 Cm^{-2} [25]). This expression has been used in the Nextnano simulations for the InGaN band edge profile described in Chapter 3, whereas for the piezoelectric polarization a linear interpolation was considered.

It is worth mentioning that the piezoelectric coefficients of InN are the highest among III-N (Table 1.3), an argument in favor of the integration of InGaN heterostructures for III-N NW-based piezo-generators.

1.2.5 Band properties

All III-N materials present a direct band gap covering wavelengths from the near-infrared (InN, λ=1800 nm, E_g=0.69 eV) to the far ultra-violet (AlN, λ=198 nm, E_g=6.23 eV) spectral regions. The band gap energies of the three binaries (E_g) are given in Table 1.4.

Table 1.4 III-N band gaps and Varshni parameters[26,27].

	InN	GaN	AlN
E_g at 0 K (eV)	0.69	3.51	6.23

σ (meV/K)	0.414	0.909	1.799
β (K)	454	830	1452

Here, are also reported the corresponding Varshni parameters. These describe the energy gap variation with the temperature, following the Varshni law (eq. 1.6), where α and β are empirical material constants.

$$E_g(T) = \frac{\sigma T^2}{\beta + T} \qquad \text{(eq. 1.6)}$$

If the precise values of GaN and AlN band gaps have been determined quite rapidly, the correct estimation of the one of InN involved almost 15 years of fierce controversies and debates on values which spanned from 0.60 eV up to 2.3 eV[28]. These huge discrepancies resulted from low crystalline quality of the epitaxial layers and, in particular, from a high residual n doping, which biased the absorption measurements. The 0.69 eV value (at 0 K) is the most widely accepted nowadays, and it has been confirmed also for dislocation-free InN in NWs[25].

The band gap energy of a ternary alloy $A_xB_{1-x}N$ is obtained by interpolating the energies of the binaries AN and BN using the following standard bowing equation (Thomson-Wooley formula):

$$E_g^{ABN} = xE_g^{AN} + (1-x)E_g^{BN} - x(1-x)b^{ABN} \qquad \text{(eq. 1.7)}$$

where b^{ABN} is the band gap bowing coefficient of the alloy. In the present work, we re-arranged this equation to estimate the In fraction of the InGaN NW heterostructures from the low-temperature energy gap measured by resonant photoluminescence. At this scope, a bowing parameter of 1.01 eV was used[25].

The graph in Figure 1.7 represents the evolution of the III-N bang gap energy with the a lattice parameter. The energy vs intensity of the solar irradiation is also included. This figure highlights the first argument in favor of InGaN alloys for solar cells applications: InGaN can, in principle, match the entire visible spectrum if its composition is adjusted accordingly.

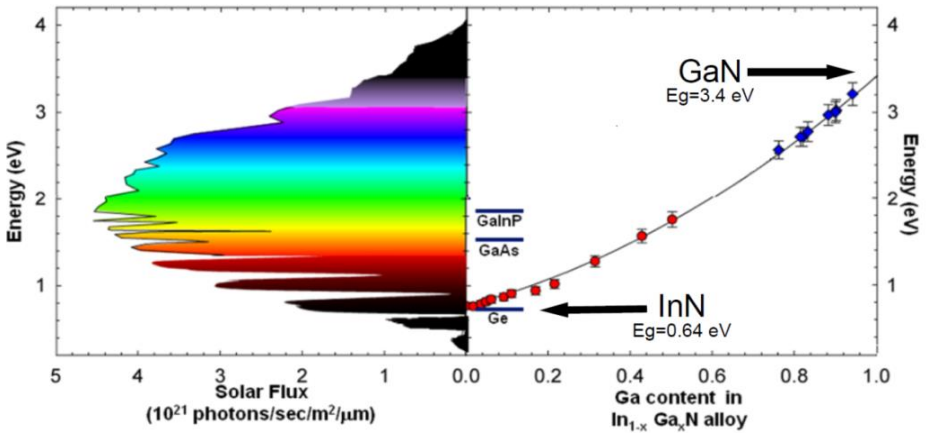

Figure 1.7 Solar spectrum versus InGaN band-gap energy as function of the alloy composition.

1.3 The interest of III-N NWs

In the last two decades, semiconductor NWs have received increasing attention for their potential applications in nano-electronics and nano-photonics. The main reason relies on the high crystal quality enabled by their NW geometry, even if grown on highly mismatched substrates. Noticeably, this stems from their ability to bend dislocations towards the side facets[29], and to release the strain through elastic surface deformations[30]. For GaN NWs, this statement is supported by their photo-luminescence, which usually emphasizes the absence of deep states in the gap and might feature band-edge excitonic recombination with energy line-widths comparable to the state of the art bulk GaN[31].
In the specific case of InGaN/GaN heterostructured NWs, green-yellow light-emitting diodes have been demonstrated[32,33] and today these systems are also considered as promising candidates for the realization of solar cells and piezo-generators.

<u>InGaN/GaN NWs for photovoltaics</u>

PV cells convert light energy directly into electricity. This happens through the photo-excitation of electron-hole pairs in a semiconductor material, which are subsequently separated to external electrodes, providing a voltage and photocurrent available for producing useful work. Fundamentally, this requires two main processes to occur: absorption of a large portion of the electromagnetic radiation from the sun to generate excited charge carriers, and separation of these excited charge carriers before

recombination losses occur. In conventional solar cells, this process requires the use of a p-n semiconductor junction, as sketched in Figure 1.8.

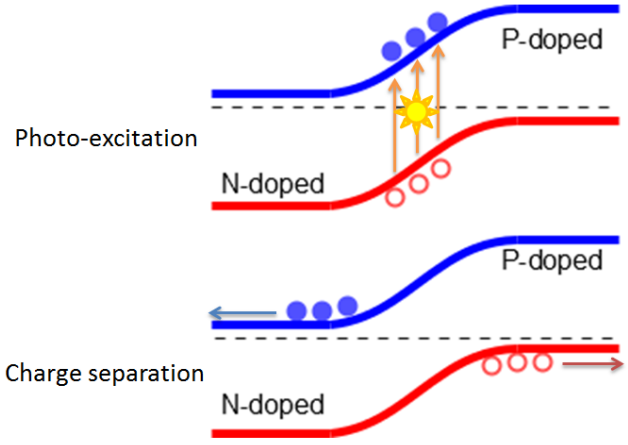

Figure 1.8 Sketch of the photovoltaic energy harvesting principle for a classical p-n junction.

The use of InGaN NW heterostructures as the active region for the photo-generation, combines their reduced defect density compared to 2D counterparts, to the advantages of InGaN alloy band-gap engineering and high absorption coefficients. In fact, for InGaN/GaN quantum-well (QW) based solar cells, although high external quantum efficiency has been realized at short wavelengths (blue photons with λ<450 nm)[34], the rapid trade-off between the epilayers quality and their In content, causes a dramatic efficiency decrease at lower band gap energies[35]. Importantly, this efficient light absorption can be further enhanced by their columnar micro arrangement. In fact, if on one side this results in an increased surface to volume ratio, on the other side it could allow to a better coupling with the incident light, which reduces reflection and enhances light scattering and trapping[36]. All these aspects allow for efficient light absorption, and the reduction of the active material volume in comparison to a planar architecture.

Last but not least, the growth of axial InGaN/GaN heterostructures along the c direction can benefit carrier extraction. In fact, in presence of a polarization field, electrons and holes will tend to drift in opposite directions, slowing down their radiative recombination. This aspect has a negative impact on the luminescence strength of polar InGaN/GaN LEDs, but could be beneficial for solar cells applications if the material architecture (usually a p-i-n junction, where InGaN is the intrinsic absorbing layer) is optimized according to the sign of the polarization field. These aspects underline the importance of a correct estimation of the NW polarity (which determines the sign of the spontaneous

polarization) and strain within InGaN NW heterostructures (which induces the piezoelectric field), and their coupled effect on the InGaN/GaN NW band structure.

InGaN/GaN NWs for piezo-electrics

Piezoelectric harvesters convert mechanical deformations into electricity. Specifically, when a piezoelectric material is subject to a stress, a microscopic polarization of the material is generated. As a result, the density of uncompensated charges at its surfaces increases, leading to a macroscopic piezoelectric field, whose sign is in accordance to the one of the build-in piezoelectric field. If the piezoelectric material is then connected to an external load, charged carriers drift in accordance to the piezoelectric field and power can be generated. Thus, the efficiency of the device depends critically on the piezoelectric capacity of the material and its mechanical properties.

The piezoelectric generators based on ZnO[37,38] and more recently nitride nanowires[23,39–42] (NWs) have emerged as excellent candidates to fabricate novel ultra-compact and efficient power sources. Their attractiveness stems from the fact that NWs present: a large degree of elastic deformation without mechanical deterioration[43]; a high sensitivity to deformations (they can be deformed under nano-Newton applied forces)[44]; exalted piezoelectric coefficients[45,46] (up to 6 times higher for GaN in a NW form than for GaN 2D-film or bulk form[47]).

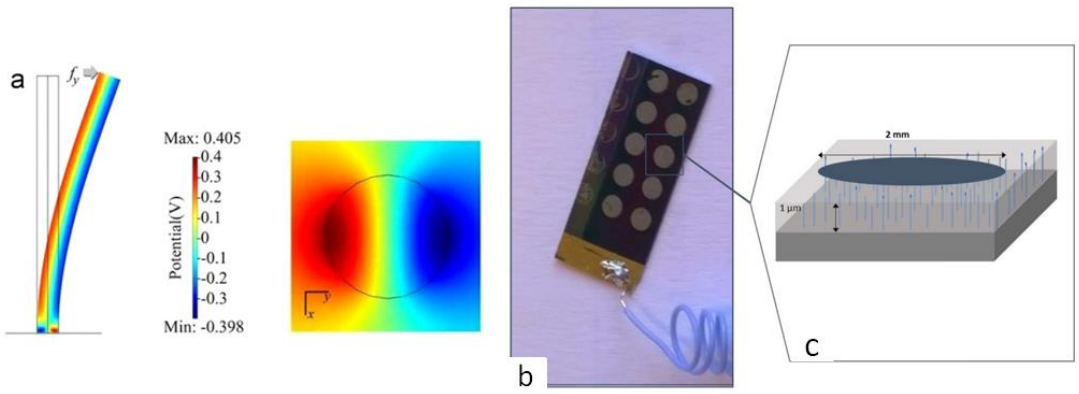

Figure 1.9 (a) Electric field potential within a bended NW[48]. Photo (b) and schematization (c) of a working piezo-generator based on GaN NWs[40].

While these energy sources can generate power densities in the µW-mW/cm^3 range, their use as micro-system power supplies is rather limited, especially due to their poor energy conversion. Indeed, to reach useful generation capacities, devices of several square

centimetres in size, and/or the application of pressures of the order of several MPa are required, not allowing their use as viable integrated energy sources. To consider the NW-based energy harvesting systems for supplying micro-devices, the improvement of the conversion capacity and efficiency of the piezoelectric active layer is a pre-requisite to the extension of the generator performances.
At present, the best mechanical-electrical conversion in terms of the output voltage has been demonstrated for III-N NWs. Hence, a maximum output voltage of about -440 mV and 1 V per NW have been generated for n-doped GaN[23] and InN[42] NWs, respectively. This latter value reflects the large piezoelectric coefficients of InN, which are the highest among all III-N materials. Thus, the integration of axial InGaN heterostructures in GaN NWs is an interesting possibility for improving the conversion capacity of III-N NWs.

1.4 Principles of epitaxial growth by PA-MBE

The term *epitaxy* comes from the Greek roots *epi* (ἐπί), meaning "above", and *taxis* (τάξις), meaning "an ordered manner". It can be translated as "arranging upon". The interest of this technique, stems from the fact that for most technological applications, it is desired that the deposited material form a crystalline overlayer that has one well-defined orientation with respect to the substrate crystal structure (single-domain epitaxy). In this context, homo-epitaxy refers to the growth of an overlayer on a substrate made of the same material, while all other cases are referred to as hetero-epitaxy.

High quality epitaxial thin films can be synthesized via chemical deposition (Chemical Vapor Deposition, CVD) or physical deposition (Molecular Beam Epitaxy, MBE). In this latter case, the epitaxial growth occurs in ultra-high vacuum (UHV) and involves the exposure of the heated substrate surface to ballistic[i] atomic fluxes. Indeed, the substrate temperature is a crucial parameter of epitaxial growth, since it activates different physical

[i] The atoms mean free path is much larger than the distance between the effusion cell from which they are evaporated, and the substrate surface. By consequence, before reaching the surface they do not collide between each other or with other impurities.

phenomena which occur to the atoms at the surface (adsorption/desorption, diffusion, nucleation, incorporation… as sketched in Fig. 1.10).

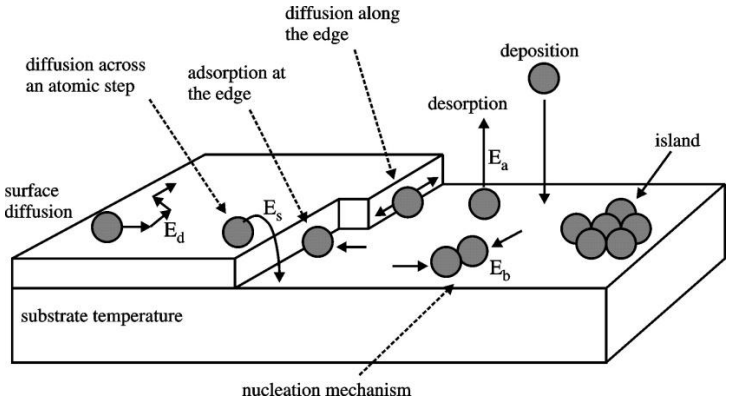

Figure 1.10 Illustration showing the physical processes that can occur on the substrate surface: adsorption, desorption, diffusion in different sites, as well as nucleation and incorporation on the crystal lattice[49].

MBE presents several advantages:

· Relatively low growth temperature. Substrates are heated at a temperature high enough to grow ordered films, but low enough to minimize unwanted thermally-activated processes.

· Slow and precisely controlled growth rate. The typical MBE growth rate is about 0.5-1 ML/s, which corresponds to approximately 0.5-1 μm/h. This ensures surface migration, hence improving surface smoothness, and precise (sub-monolayer) thickness control.

· Growing compounds or alloys is possible as far as a suitable vapour source is available. Even alloys that are barely miscible under thermodynamic equilibrium can be kinetically stabilized by MBE (for instance, In-rich InGaN).

· Ultra-High Vacuum conditions (UHV), necessary to avoid beam scattering and to reduce impurity incorporation. These conditions allow the grower to use in situ characterization techniques, for example reflection high energy electron diffraction (RHEED), X-ray photoemission spectroscopy, mass spectrometry, etc.

1.4.1 Epitaxial growth modes

In heteroepitaxial growth, various growth modes can be observed, schematized in Figure 1.11. These depend essentially on the lattice mismatch between the materials and the energy of the new surfaces that are created.

- Layer-by-layer growth mode, also called Frank Van der Merwe (FVM) growth[50], is a two-dimensional (2D) growth process. The formation of tilted facets is energetically unfavorable compared to the growth of a 2D layer. Thus, when the atomic fluxes reach the surface, atoms tend to incorporate at the step kinks leading to the lateral expansion of the growing film (step-flow growth), and the process is sustained ML after ML. In presence of lattice mismatch, after a critical thickness strain is released via the introduction of dislocations.
- Three-dimensional (3D) growth mode, called Volmer-Weber (VW) growth mode[51] is characterized by the nucleation and growth of small islands directly on the heterointerface. Generally, the formation of 3D islands is favored by their more efficient strain relaxation compared to 2D films.
- Stranski-Krastanov growth is an intermediate growth mode: the growth starts following the layer-by-layer mode with the formation of few monolayers. Once the critical thickness is reached, this 2D growth becomes energetically unfavorable and the growth continues with the formation of islands. This growth mode transition is favored by the strain relaxation.

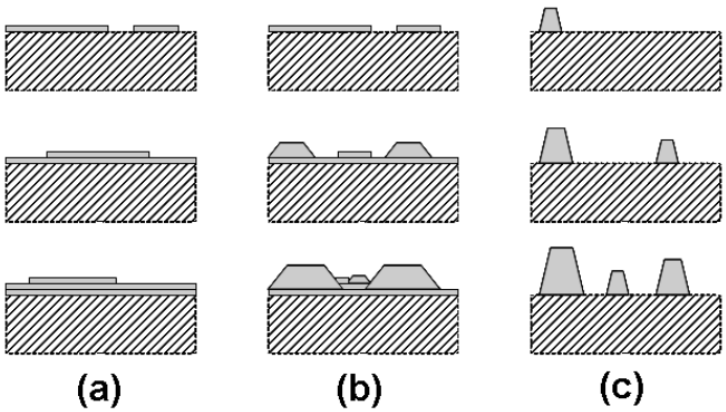

Figure 1.11 Scheme of the three heteroepitaxial growth modes. (a) FVM growth mode. (b) SK growth mode. (c) VW growth mode.

In PA-MBE, we note that for a given material system, the use of surfactant or anti-surfactant species allows to switch from one growth mode to another. In fact, surfactants modify the surface energies and hence affect the growth thermodynamics[13].

1.4.2 Our Plasma-Assisted MBE

Plasma-Assisted MBE is a category of MBE dedicated to the epitaxial growth of III-N materials. As the name suggests, in this technique, the active N species are provided by a radio-frequency (RF) plasma source. In this source, gaseous N_2 molecules are injected in a PBN cavity and are resonantly excited and dissociated by a 13.56 MHz RF electromagnetic wave. The flux of active N species can be adjusted by varying the N_2 flux and the RF power.

Previous spectroscopic studies have provided evidence that plasma discharges produce both atomic and molecular nitrogen in their ground (N and N_2) and electrically excited (N* and N_2*) states as well as molecular nitrogen ions N_2^+ [52]. At present, whether or not one of these species plays a dominant role it the growth of III-N is still under debate[53–55].

In this work, I made use of a Riber C12 Plasma-Assisted MBE. As shown in Figure 1.12, this is a compact MBE machine suitable for scientific research.

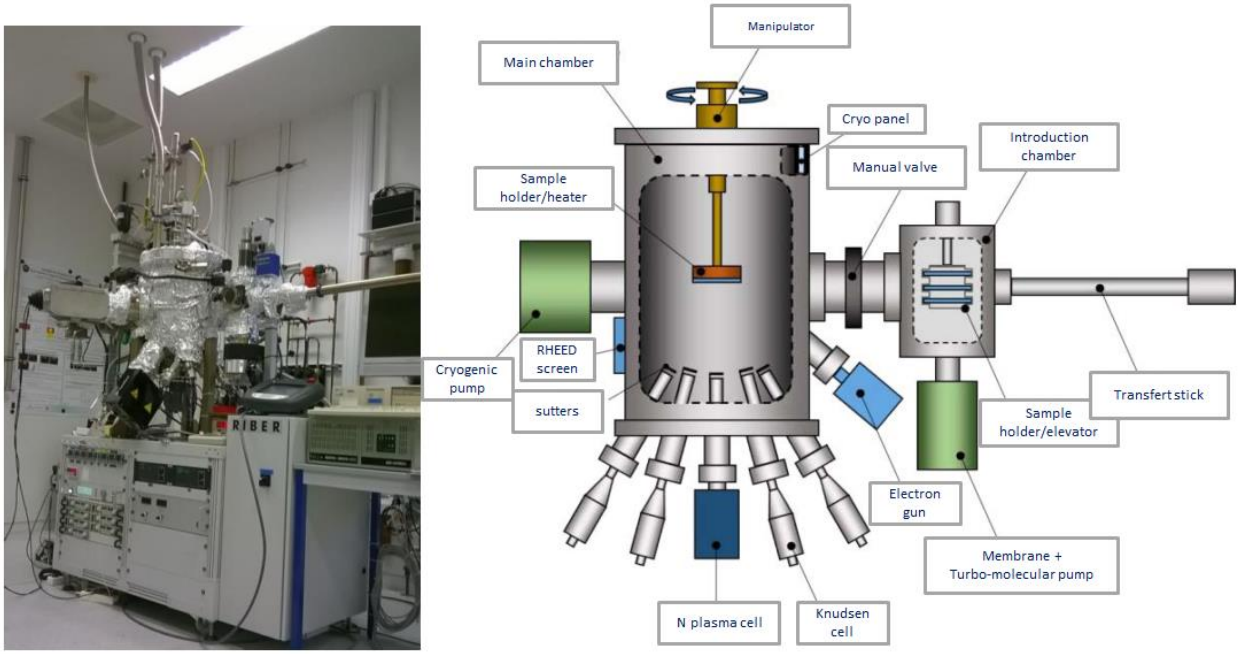

Figure 1.12 Photo of our Riber Compact 12 MBE chamber (left) and its schematic representation (right).

The chamber is equipped with:

- Three quasi-Knudsen effusion cells for metallic species: Ga, In and Al
- Two effusion cells for the dopant species: Mg and Si
- One Riber radio frenquency (RF) plasma source, equipped with a 149 holes PBN cavity (operative range is 0.2-1 sccm N_2 flux and 200-600 W RF power)
- One substrate heater allowing for reaching 800-850 °C substrate temperatures, suitable for the growth of III-N NWs.
- One reflective high-energy electron diffraction (RHEED) apparatus, interfaced through a camera with a prototype software for the time-resolved monitoring and analysis of diffraction patterns.

1.4.3 Temperature and fluxes calibration

The epitaxial growth process depends essentially on the substrate temperature (T_s) and the impinging atomic fluxes (Φ_a). As previously mentioned, the substrate temperature is the key parameter which activates the different phenomena occurring at the growing surface. The fluxes, in their absolute value and relative ratios, control the growth rate of the epitaxial structure, its composition and its morphology. Both of them need accurate and continual calibration to ensure a long-lasting reproducibility of results, as well as a reasonable consistency of epitaxial growth recipes between different MBE machines. The calibration strategies used in the present work are described in the following.

<u>**Temperature calibration: (7x7) Si(111) surface reconstruction**</u>

The control of the substrate temperature is one of the most delicate points of the MBE growth. This is usually performed by adjusting the substrate heating power in accordance to the feedback of an optical pyrometer and/or a thermocouple placed in the vicinity of the sample/sample holder. Both of them depend on the MBE chamber geometry: respectively, from the substrate angle with respect to the optical axis of the pyrometer, and from the specific position of the thermocouple. Furthermore, even by considering a fixed measurement geometry, both of them present sources of bias:

- the pyrometer output depends on the emissivity of the substrate/substrate holder as well as on the transparency of the window through which the thermal radiation is probed.

Thus, a progressive coating of the pyrometer window and/or of the substrate holder can cause a progressive drift of the measured temperature.

- a progressive coating of the sample holder could change its emissivity and affect the thermocouple measurement.

To tackle these limitations, temperature-dependent phenomena such as metal desorption from the substrate surface or the follow-up of surface de-oxidation processes by RHEED, are conventionally used for calibration of the substrate temperature.

In our MBE machine, the thermocouple is too far from the sample and is not reliable. In present work, we made reference to the pyrometer measurement, which was calibrated by following the disappearance of the 7x7 Si(111) surface reconstruction by RHEED[56]. After a 15 minutes degassing at 850 °C, to remove the last traces of oxide on the surface, the Si(111) temperature was decreased between 810 and 820 °C, to induce the formation of the 7x7 reconstruction, visible on the RHEED screen (Fig. 1.13(a)). Its "pearl necklace" appearance, reflects a 7 times lower periodicity compared to the usual 1x1 Si(111) surface (Fig. 1.13(b)). Then, the substrate temperature was increased by small steps, until observing its disappearance, which happens at the physical temperature of 830 °C[56]. It is worth mentioning, that this temperature is very near the one used for GaN NWs growth by MBE (around 800 °C), making this calibration reliable on the long period.

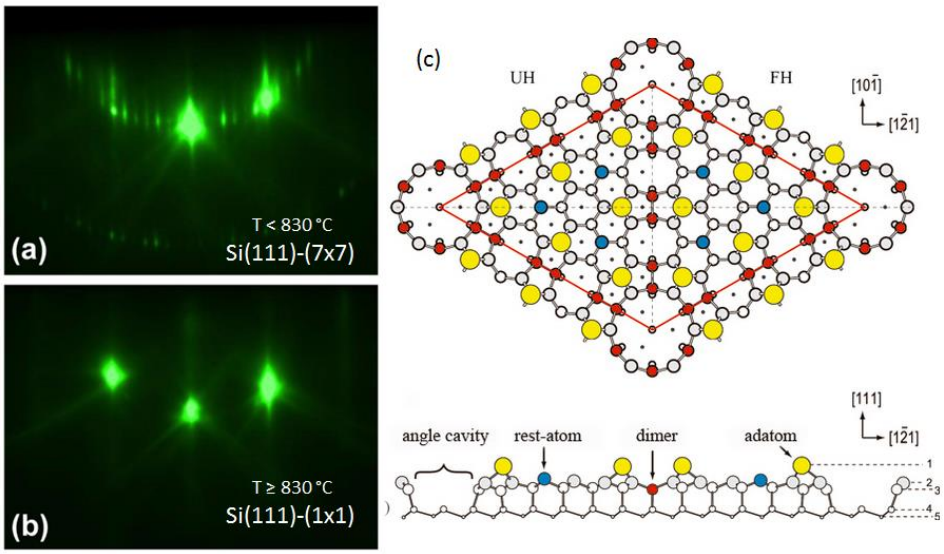

Figure 1.13 Si(111) surface RHEED pattern showing the (7x7) (a) and (1x1) (b) reconstructions[57]. (c) Schematical representation of the 7x7 surface reconstruction[58].

Fluxes calibration: RHEED oscillations

The fluxes of the atomic species are measured by an ion gauge, placed at the position of the substrate (in front of the cells) and retracted from this position during the growth. Although the ion gauge is designed to measure a pressure (or better, a number density which is converted into pressure of a reference gas), a proportionality between pressure and flux is established in the steady state. The pressure reading obtained this way is commonly referred to as beam equivalent pressure (BEP).
Clearly, the same BEP for two different materials corresponds to different effective fluxes (Φ, in ML/s or atoms per surface unit), because, even by neglecting geometrical effects, the ion gauge current depends on the ionization cross section of the element. Also, the progressive coating of the filament during its lifetime, can cause a drift of the measured BEP compared to the real flux. Thus the fluxes need to be calibrated for a correct estimation of the materials growth rate, as well as for its long-lasting reproducibility.

This can be done with the method of RHEED oscillations. The principle is based on the monitoring of the specular RHEED spot intensity during the layer-by-layer growth of a 2D film (Fig. 1.14(a)). When a ML is completed, the roughness of the surface is reaching a minimum, implying its larger reflectance. Hence, the specular RHEED spot intensity reaches a local maximum. Instead, when a ML is half completed, the several islands constituting the uncompleted layer increase the surface roughness, implying a more pronounced scattering of the impinging electrons. This results in a minimum of the specular spot intensity. Therefore, during one complete RHEED oscillation, one ML has been grown. Thus, by counting the number of oscillations in the unit of time, the effective 2D growth rate can be determined. An example of RHEED oscillations measured during the present work is given in figure 1.14(b).

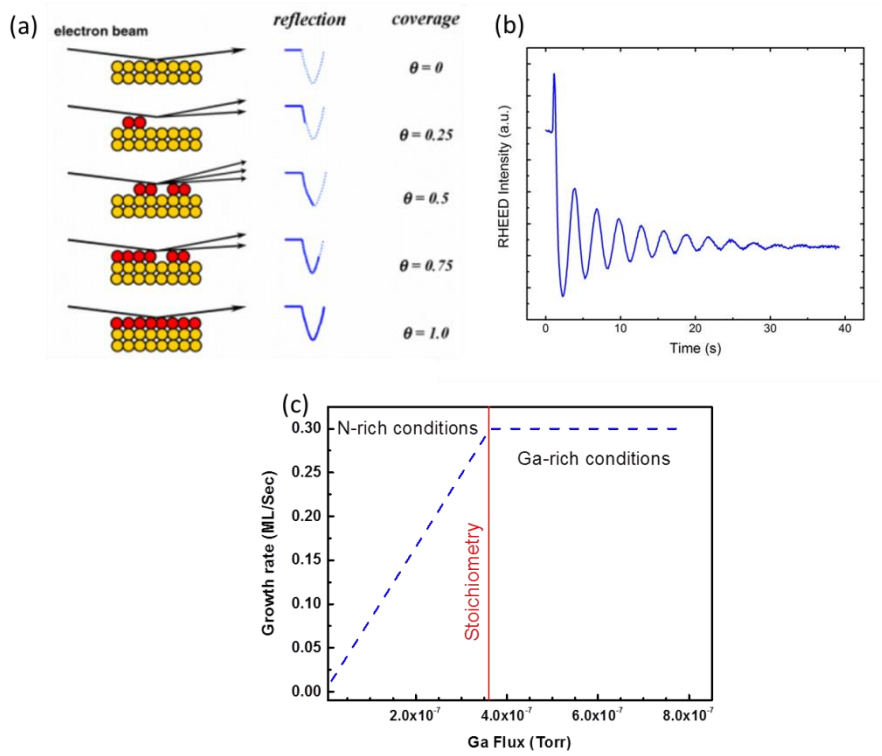

Figure 1.14 (a) Schematization of the RHEED oscillation principle; (b) GaN RHEED oscillations performed during this Ph.D. work; (c) Growth rate evolution for increasing Ga fluxes.

This procedure has been used for recurrent calibration of the Ga and N fluxes. The temperature of a GaN template was set to 730 °C, which corresponds to a regime of slow GaN decomposition. RHEED oscillations have been performed by fixing the N plasma cell parameters (N_2 flux and RF power), and by increasing in steps the Ga cell temperature. Then, the stoichiometry flux condition ($\Phi_{Ga} = \Phi_N$) was identified by the stabilization of the GaN growth rate (in ML/s) at a critical Ga cell temperature. In fact, this condition corresponds to the shift from a Ga-limited (N-rich) to a N-limited (Ga-rich) regime. The Ga BEP measured at this critical temperature, corresponded to the stoichiometry flux (in ML/s).

As concerns the In flux, this was not calibrated, and for its control we referred only to its BEP. The main reason for this, is the lack of commercial InN substrates for its homo-epitaxial deposition, which substantially complicates the measurement of RHEED oscillations. In fact, even if in principle the growth of good quality InN is possible on GaN templates[59,60], under N-rich conditions a rapid Stranki-Krastanov transition is observed[61]. Nevertheless, we will see that for the specific growth regime that we employed for the

growth of InGaN, the precise calibration of the In flux is less important compared to the one of Ga.

1.5 Epitaxial growth of GaN NWs by PA-MBE

In this section, we review some basic aspects of the catalyst-free Vapour-Solid growth of GaN NWs by PA-MBE. Specifically, some details concerning their substrates, nucleation process, crystal orientation and growth mechanism, as well as a concise description of their growth conditions is provided.

1.5.1 Substrates and orientation

NWs came as a side product of systematic studies aiming at optimizing the growth of GaN thin films on sapphire. In 1997 and 1998, two competing research groups, respectively led by K. Kishino[62] in Japan, and E. Calleja[63] in Spain, have reported the self-assembled growth of GaN nano-columns on c-oriented sapphire by PA-MBE. Later on, successful growth of these nanostructures was obtained on a variety of alternative substrates including Si(111) and Si(100)[64–66], SiC[67], Ti flexible foils[68], diamond[69] and recently also on transferred graphene[70]. Nevertheless, most of the studies involved Si(111) substrates. In fact, their low cost, together with their conductive character have been important elements for both their optoelectronic characterization and their integration in working devices[23,71].

Independently from the substrate, the NWs grow spontaneously along the c direction, and present a hexagonal cross section limited by m-planes. On a Si(111), they grow on a thin amorphous SiN_x layer or on an AlN buffer. In the case of growth on SiN_x, this layer forms spontaneously at the beginning of the NWs growth, due to the efficient nitridation of the surface by the N-plasma. Yet, the NWs grow perpendicularly on the substrate with a small in-plane twist and out-of-plane tilt and preserving their crystal orientation[72].

Concerning the growth with AlN buffer layers, this underlayer (typically 2-3 nm thick) improves the epitaxial relationship between the NWs and the underlying substrate, allowing a substantial reduction of both the NW twist and tilt[65,66]. Furthermore, if AlN nanocrystals are grown instead of a continuous AlN layer[73], these act as seeds for the NWs

nucleation, and a substantial reduction of their density is observed. This is a further advantage, since the typically high GaN NW surface density spurs their lateral coalescence and the formation of defects[18].
In this work, this latter strategy has been used, with the procedure published by Largeau et al.[73] (Figure 1.15).

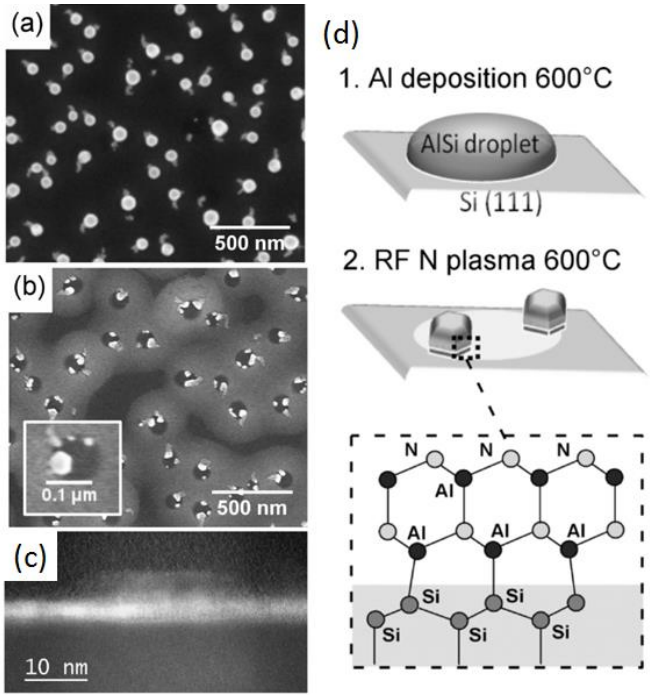

Figure 1.15 (a) Top view SEM images of a Si(111) surface after 40 s Al deposition (a) and after 60 seconds of nitridation (b); (c) High-angle annular dark field STEM cross-section image of an emerging AlN pedestal (d) Scenario of the AlN buffer growth, w

Specifically, the epitaxial growth of the AlN buffer involved the two following consecutive steps:

- The exposure of the oxide-free Si(111) surface to Al flux for a fixed amount of time, inducing the Ostwald ripening of Al/Si(111) alloyed droplets (Fig. 1.15(d1));
- The subsequent nitridation of the surface, inducing their crystallization in the form of ~50 nm large and ~2.5 nm thick AlN pedestals (Fig.1.15(d2)).

1.5.2 Growth diagram

The spontaneous growth of GaN NWs happens if the growth conditions allow for:

- The nucleation of individual GaN seeds
- An anisotropic adatom incorporation, resulting in a higher growth rate along the c axis

Systematic studies, demonstrated that these criteria are gathered for high substrate temperatures (T_s>750 °C), i.e. in a regime where the desorption and decomposition of GaN become significant, and under N-rich conditions. Figure 1.16 shows the reference GaN NW growth diagram for our MBE machine, where the window for the NW growth is evidenced.

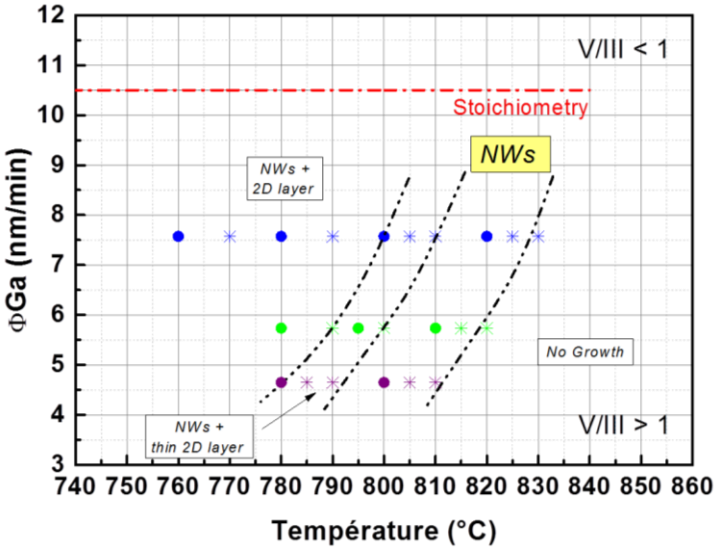

Figure 1.16 Growth diagram of GaN NWs on AlN/Si(111) substrates.

It can be seen that both a temperature decrease and/or a Ga flux ratio increase (V/III decrease), favor the formation of a compact polycrystalline 2D GaN on the surface (2D layer in Fig.1.16). By contrast, if the growth temperature is increased too much, no growth is observed. The frontier between the NW growth and no growth can be displaced towards higher temperatures, if a higher flux compensates the higher Ga desorption.

The NWs density and diameter can be adjusted as function of the growth temperature, the N/Ga flux ratio and the absolute growth rate. Generally, lower V/III ratios and lower temperatures (albeit within the NW growth window) lead to an increase of the NW diameter. The GaN NWs crystalize in the WZ crystal structure (Fig. 1.17(b)) and grow along the <0001> direction (Fig. 1.17(c)). They present a hexagonal cross section limited by m-planes (Fig. 17.(a)) and, in the present study the show diameters of 50∓20 nm. Their length can be controlled by adjusting the growth time.

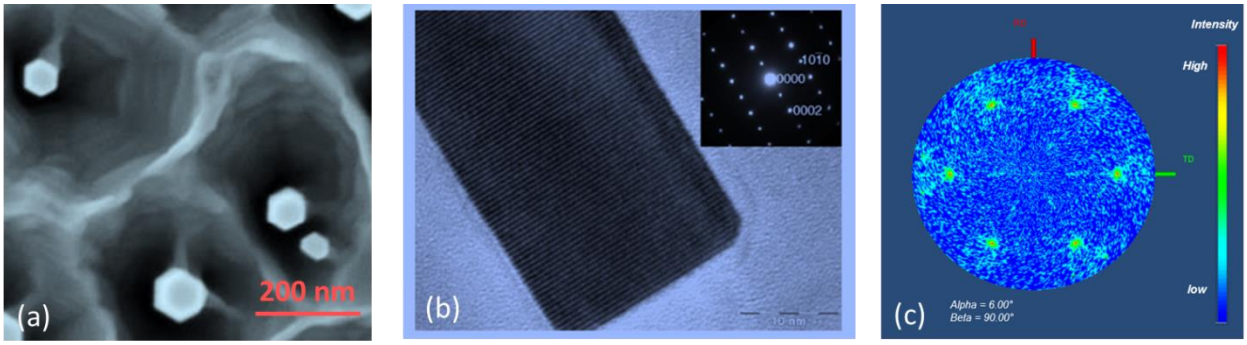

Figure 1.17 (a) Top-view SEM image of NWs, showing their hexagonal cross-section. (b) High-resolution TEM image of the NW tip ([1-210] zone axis)[74]. Inset corresponds to its WZ electron diffraction pattern. (c) X-ray 2D ($10^{-}11$) pole figure of GaN NWs grown on AlN/Si(111): the sharp peaks located at ϕ =62° indicate that the NWs are well oriented with their c-axis normal to the substrate surface[72].

1.5.3 Growth mechanism of GaN NWs.

The growth mechanism of GaN NWs involves two main steps: their nucleation and their elongation (this latter presents two regimes where the axial growth rate firstly accelerates and then stabilizes). At the present stage, the phenomena which regulate the NW nucleation are the less understood. For instance, during the in-situ RHEED monitoring, a delay between the shutters opening and the observation of the NW "spotty" RHEED pattern (shown in Figure 1.18) is systematically observed. This is the NW "incubation time" and for growth on Si, it can vary from about 30 seconds to about 30 minutes, depending on the specific growth conditions. It has been shown that during this time, after a certain delay in which the atomic species enrich the surface[64], these form stable GaN nuclei (Fig. 1.18(c)) which expand in the form of faceted domes (Fig. 1.18(d)); then, a shape transition from faceted domes to NWs (Fig. 1.18(e)) initiates the growth of the structures[75]. The driving force of this shape transition is at present unclear. In fact, although plastic relaxation though misfit dislocations has been idenfied as a key step for growth on AlN/Si substrates[75], GaN NW growth has been demonstrated also on homoepitaxial GaN templates[76] or amorphous substrates[77,78], where strain can be safely neglected.

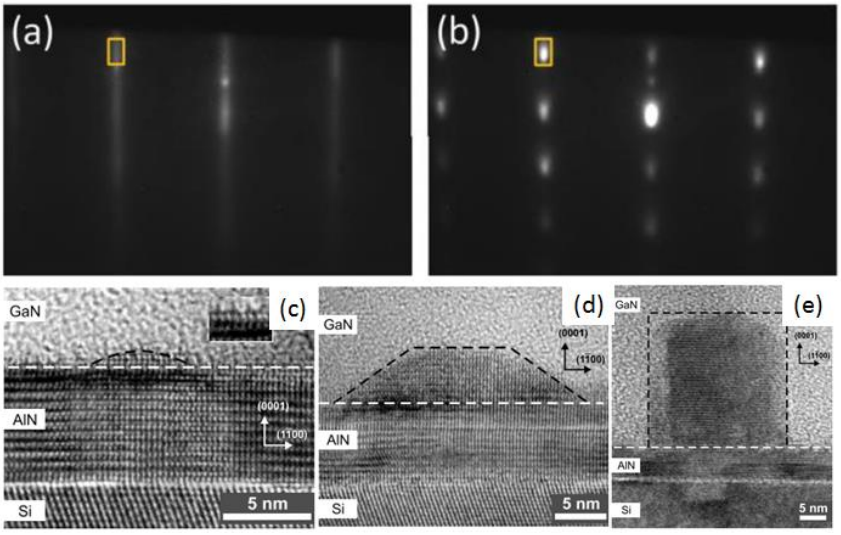

Figure 1.18 RHEED pattern before (a) and after (b) NWs nucleation on Si(111)/AlN. (c,d,e) HRTEM images of the different stages of GaN NWs nucleation[75].

Once the NWs have nucleated, the development of their high aspect ratio can be rationalized in terms of different kinetic barriers for the species incorporation associated to the different crystalline facets which appear. Then, the NW elongation rate and morphology is governed by both the atomic species which directly impinge the NW top facet (where the kinetic barrier should be lower), and the Ga adatoms which diffuse on the NW sidewalls (and also on the substrate in the first stages of growth) and reach the NW tip[79] (Fig. 1.19(a)). In fact, whereas Ga adatoms are highly mobile, N adatoms are unstable against the formation and desorption of N_2 molecules.

The important consequence of this different behavior of Ga and N, is that the amount of Ga reaching the NW tip can exceed the amount of active N available for the growth, even for impinging III/V flux ratios which are lower than 1. Under such conditions, the excess Ga which accumulates at the NW tip, induces radial growth of the NWs. This phenomenon has been evidenced by Fernandez-Garrido and co-workers[79], and explains the experimental observation of a NW enlargement when the Ga flux is abruptly increased (albeit maintaining N-rich conditions) during the GaN NW growth. However, this process self-regulates, since the III/V ratio at the NW tip decreases with an increasing NW radius. This leads to a recovery of vertical sidewalls, when quasi stoichiometric local conditions are re-established, as shown in Figure 1.19(b). The important consequence of these considerations is that the growth rate of GaN NWs is not limited by the Ga flux, as their nominally N-rich conditions would suggest, but it rather is quasi-stoichiometric.

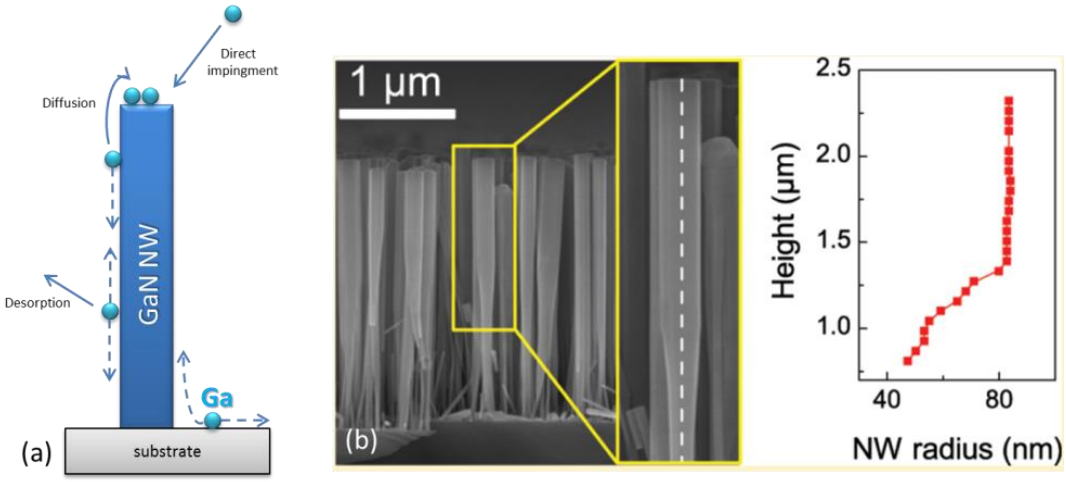

Figure 1.19 (a) Schematization of the diffusion-induced growth of GaN NWs by PA-MBE. (b) SEM image evidencing the diameter increase and subsequent stabilization following an abrupt increase of the Ga flux during GaN NW growth[79].

1.5.4 Polarity

Given their growth along the c direction, the assessment of the GaN NW polarity is of crucial importance. In fact, as introduced in section 1.2.2, the layer orientation determines the sign of the spontaneous and piezoelectric fields, which in turn impact their piezo-generation, as well as their optical and transport properties.

Among different techniques reported in the literature for the assessment of the GaN NW polarity, such as Convergent beam electron diffraction (CBED)[73] or Kelvin Probe Force Microscopy[80], KOH selective etching[81] is nowadays one of the most widely used method to probe a large number of NWs in short times. The etching is based on the following reaction[82]:

$$2GaN + 3H_2O \xrightarrow{KOH} Ga_2O_3 + 2NH_3$$

where OH^- ions act as chemical catalysts. The key point of selective etching is that these ions attack the Ga atoms, but are strongly repelled by the repulsive coulomb force with the negatively charged N dangling bonds. Thus, the morphology of Ga-polar surfaces is preserved during their etching, while the -c surfaces become faceted, developing (10-1-1) planes.

This technique has been used in the present work to investigate the polarity of GaN NWs and InGaN/GaN NWs grown on AlN/Si(111) and SiN_x/Si substrates. Specifically, the etching was performed for 5 minutes in a 0,5 M KOH solution heated at 40°C. In all cases, all the NWs exhibit faceted tips, indicating a prominent N-polarity. Figure 1.20 are shows the SEM images acquired for InGaN/GaN NWs before and after etching.

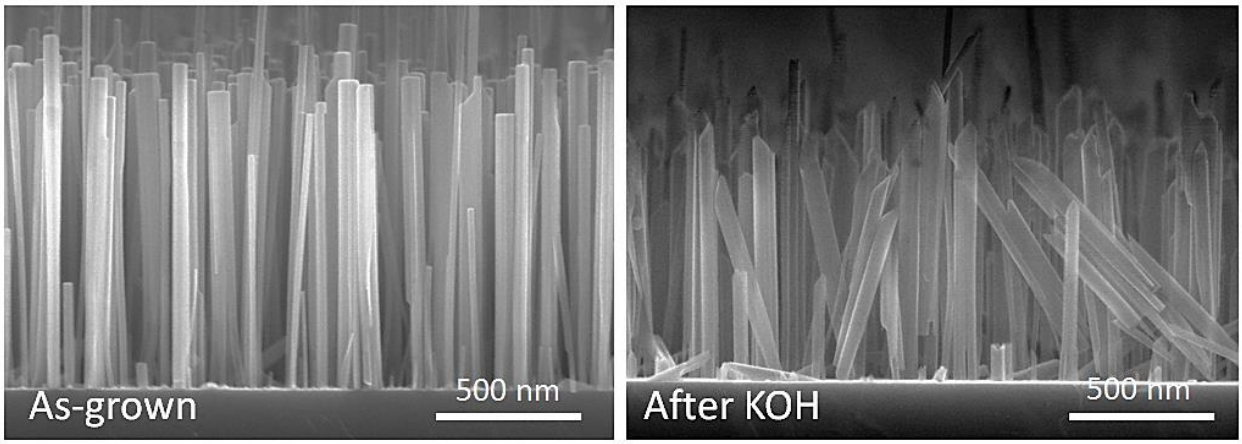

Figure 1.20 SEM cross-sectional images showing the InGaN/GaN NWs array morphology before and after the KOH etching.

Conclusions

In summary, in this chapter I have presented the basic properties of nitride semiconductors. This allowed me to introduce the motivations for the use of InGaN/GaN heterostructures for photovoltaics and piezoelectrics. I provided some general information

concerning the elaboration methods of III-N materials, with a special emphasis on the PA-MBE technique, which has been used in this work. I presented the general characteristics and growth conditions of the GaN NW structures by PA-MBE, as well as some details concerning the most recent literature on their formation mechanism.

Chapter 2

Tailoring the growth of InGaN axial nanowire heterostructures

One of the objectives of the present study is to reproducibly grow In-rich axial $In_xGa_{1-x}N$/GaN NW heterostructures, aiming to serve as active regions for light emission, photo-conversion and piezo-conversion. The synthesis of such type of heterostructures has been object of a certain number of studies so far which, however, offer a rather broad panorama of possible morphologies and alloy compositions. Tapered insertions presenting an island-like shape and relatively low In concentrations ($0.15<x_{In}<0.25$) have been observed by different groups[7-9], while higher In concentrations ($0.30<x_{In}<0.60$) have been associated with untapered disk-like morphologies[7,10,11]. Radially overgrown shapes in the form of nano-bells and nano-umbrellas, as well as irregular and defective InGaN deposits have also been observed, this time within a rather broad range of compositions ($0.10<x_{In}<0.60$)[12-15]. As a matter of fact, the lack of a unifying picture correlating the variety of results to specific growth parameters points to a low reproducibility, and contributes to the still limited understanding of their formation mechanism. The work described in this chapter, aims to fill these gaps by systematically investigating the growth parameters space for the fabrication of single axial InGaN insertions in GaN NWs.

2.1 Growth procedure

In this section we describe the growth route for the fabrication of the samples studied in this chapter: self-assembled GaN NWs presenting a several tens of nanometers thick $In_xGa_{1-x}N$ axial heterostructure at their top. The growths have been carried out following the temperature-time path schematized in Figure 2.1, which depicts each growth step.

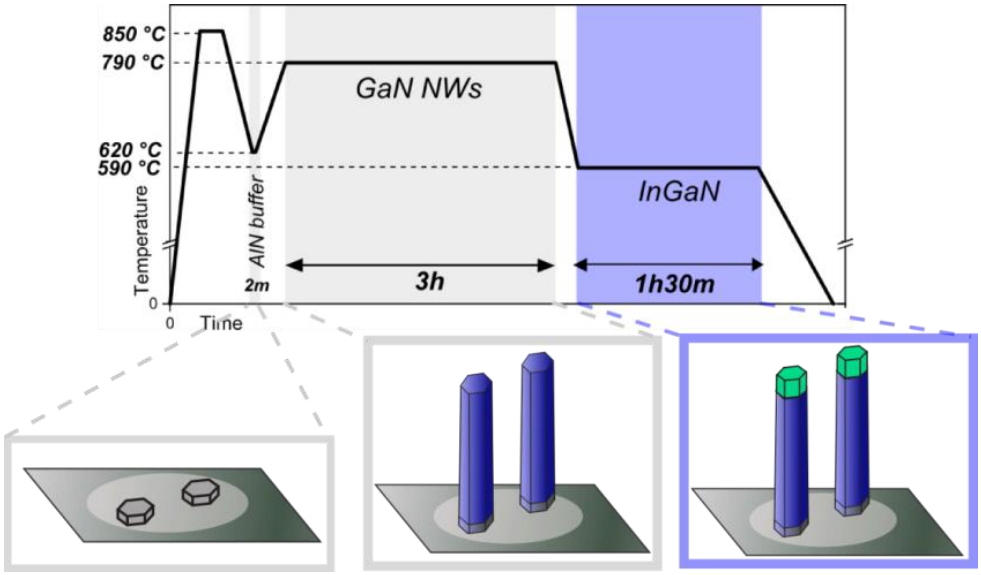

Figure 2.1 Temperature vs. time path for the epitaxial growth of axial InGaN/GaN NW heterostructures. The blue panel evidences the growth step under scrutiny.

Substrate. Polished ¼ 2 inch n-type Si(111) wafers were chemically cleaned for the removal of organic pollutants and native oxide before introduction in the MBE chamber. The substrate temperature was monitored using an optical pyrometer, calibrated before each growth by following the disappearance of the RHEED Si(111)-(7x7) reconstruction at 830 °C[56]. RHEED was used also to monitor each growth step.

AlN buffer. After a 15 minutes in-situ degassing at ~850 °C, the growth was initiated by depositing 2.5 nm of AlN ($Al_{BEP} = 8.0 \cdot 10^{-8}$ Torr, Φ_N=10 nm/min[i]) at 620 °C. The procedure is the one described in section 1.5.1, leading to the formation of 2-3 nm

[i] In the whole manuscript, the labelling "Φ" is used only for the calibrated Ga and N fluxes. Otherwise, the fluxes are expressed in equivalent beam pressure (in Torr).

thick AlN pedestals, serving as seeds for the nucleation of in-plane oriented GaN NWs of prevalent N-polarity.

GaN NWs. After a growth interruption, the substrate temperature was adjusted to 790 °C. Then, self-assembled GaN NWs were grown for 3 hours under nominally N-rich conditions (V/III=1.36) without the use of any catalyst. This set of growth parameters results in NW arrays with no interstitial polycrystalline GaN layer. The NW density was about $1.5 \cdot 10^{10}$ NW/cm^2, while the diameters (50 ± 10 nm) and lengths (1 ± 0.1 µm) were well approximated by single Gaussian distributions. Representative SEM images of the as-grown GaN NWs, with their diameter and length distributions are shown in Figure 2.2.

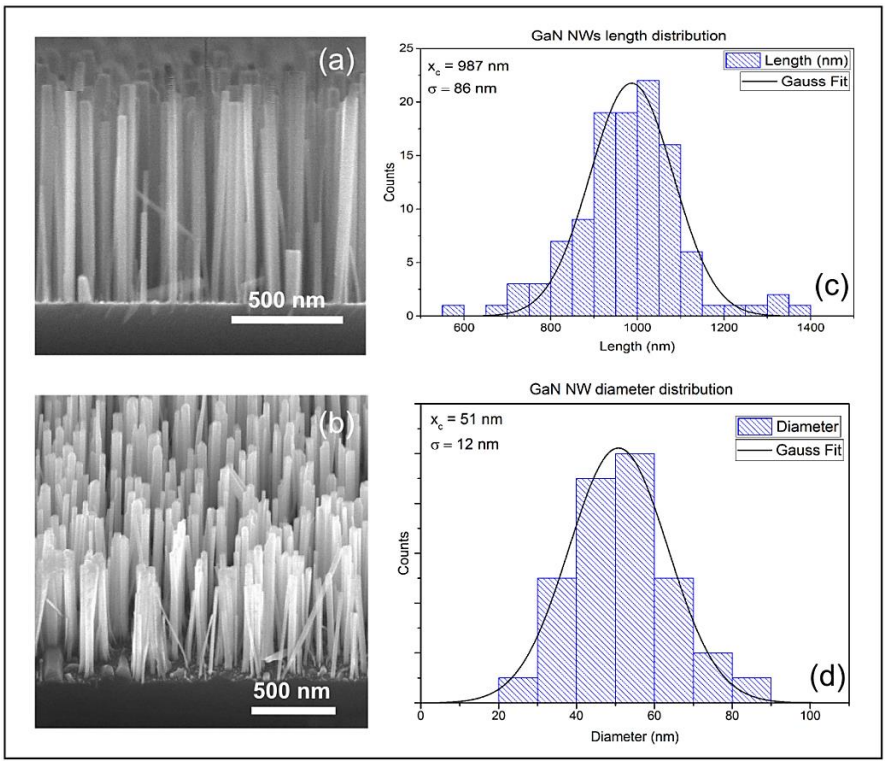

Figure 2.2 (a) Cross-section and (b) 45° tilted view of a representative ensemble of GaN NWs grown on AlN/Si(111) substrate. (c) Length and (d) diameter histograms representing the morphological dispersion of the GaN NWs.

InGaN. At the end of the GaN NWs growth, the substrate temperature was rapidly decreased to 590 °C. This temperature was chosen to reach sufficiently high In concentrations, despite the In losses caused by In-N decomposition and In desorption during InGaN growth[83–85]. The GaN NWs, which played the role of pseudo-substrates,

were then exposed to In, Ga and N fluxes simultaneously for a total growth time of 1 hour and 30 minutes. For the growth of planar InGaN layers, at a given temperature, the In fraction depends on both the In/Ga and the Ga/N flux ratios [86,87]. Thus, to study the growth of InGaN NW heterostructures, we fixed the N supply (Φ_N=3.7 nm/min), and we varied systematically the Ga and In fluxes through three series of samples.

- Series Ga#1: Φ_{Ga} was kept constant at 0.30 nm/min ($4.0 \cdot 10^{-8}$ Torr BEP), resulting in a Φ_N/Φ_{Ga} ratio equal to 12.5; the In BEP was varied to obtain In/Ga BEP ratios In/Ga_{BEP} ranging between 0.5 and 6.
- Series Ga#½: Φ_{Ga} was halved compared to series Ga#1 (0.15 nm/min, $2.0 \cdot 10^{-8}$ Torr BEP), resulting in a Φ_N/Φ_{Ga} ratio equal to 25; the In BEP was varied to obtain In/Ga BEP ratios In/Ga_{BEP} ranging between 0.5 and 6, as in series Ga#1.
- Series In/Ga#3: the Ga flux was varied to produce Φ_N/Φ_{Ga} flux ratios between 25 and 2.8, while the In BEP was adjusted to maintain a constant In/Ga_{BEP} ratio of 3.

For all these samples, we worked under N excess conditions (specifically, with a precursor V/III ratio going from a minimum of ~1.5 to a maximum of ~16).

2.2 Effect of the In/Ga flux ratio on the heterostructures morphology

The structures described in this section refer to the sample series Ga#1 and Ga#½, where the In flux is varied at constant Φ_N/Φ_{Ga}. As shown in the SEM micrographs of Figure 2.3, the InGaN deposits, located at the NW tips, exhibit markedly different morphologies depending on the In/Ga_{BEP}, whatever the initial Ga flux.

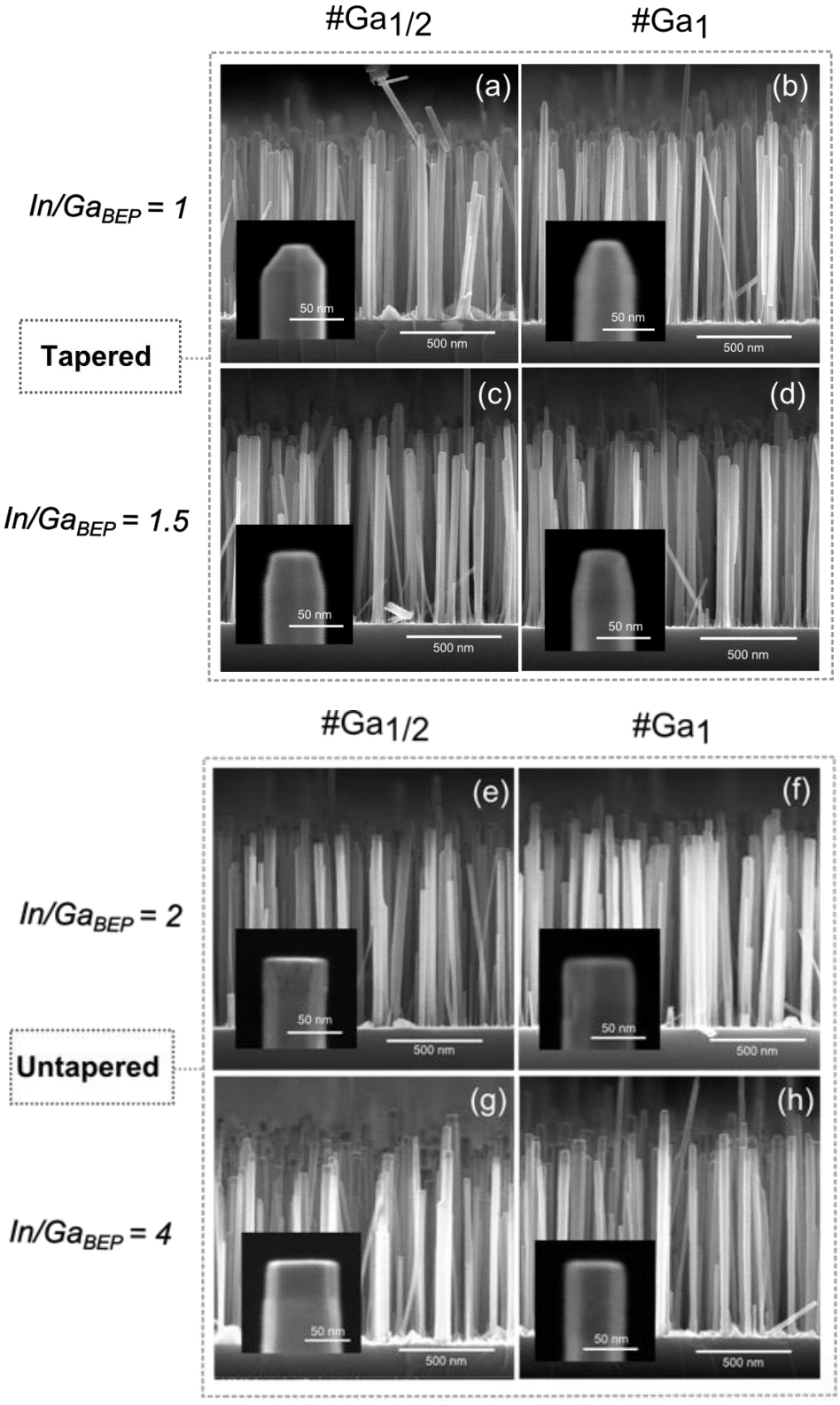
#Ga1/2
#Ga1
In/GaBEP = 1
Tapered
In/GaBEP = 1.5
(a)
(b)
(c)
(d)
50 nm
500 nm
#Ga1/2
#Ga1
In/GaBEP = 2
Untapered
In/GaBEP = 4
(e)
(f)
(g)
(h)
50 nm
500 nm

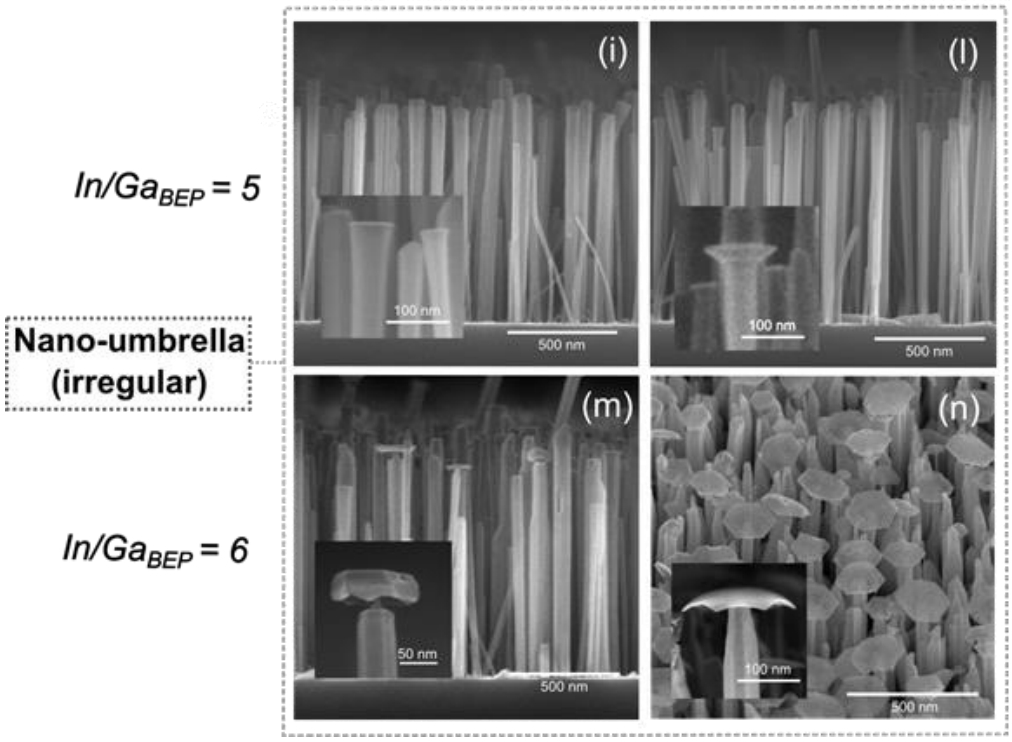

Figure 2.3 Cross section (a-m) and tilted (n) SEM images of the as-grown InGaN/GaN NWs grown at different Φ_{In}/Φ_{Ga} ratios: 1 (a,b), 1.5 (c,d), 3 (e,f), 4 (g,h), 5 (i,l) and 6 (m,n). The high-magnification insets highlight the shape of the InGaN heterostructures located at the NW tips.

Specifically, we identify three types of InGaN morphologies depending on the In/Ga_{BEP} conditions. Their average In composition measured by EDX statistics is also provided:

- Pyramidal or tapered sections (In/Ga_{BEP}<2, Fig. 2.3 (a-d)); In fraction x evolving from ~0.05 to ~0.30 for increasing In/Ga_{BEP}.
- Untapered morphologies (<2 In/Ga_{BEP}<4, Fig. 2.3(c-f)); constant In fraction of about ~0.40 and ~0.35 for Ga#1 and Ga#½ respectively;
- Radially overgrown and/or irregular InGaN deposits (In/Ga_{BEP}>4, Fig. 2.3(i-l)); In fraction x decreasing from ~0.40 (~0.35) to ~0.10 for increasing In/Ga_{BEP}.

Details concerning the EDX measurement and the InGaN compositional evolution with the growth parameters, will be provided in section 2.5. The main structural characteristics of these three types of sections, together with a concise literature review, are described in the following.

Tapered island-like InGaN sections

For $In/Ga_{BEP} < 2$, the InGaN sections exhibit a truncated pyramidal shape. As shown in Figure 2.4(a), HAADF-STEM observations in the [11-20] zone axis reveal a spontaneous core-shell In distribution, characterized by a narrow In-rich core of uniform diameter, surrounded by a thick (10-15 nm) Ga-rich shell. The tapered outer morphology results then, from the sharpening of the shell at the NW top. No misfit dislocations or other strain relieving defects were observed along the different InGaN/GaN interfaces in this type of sections (Fig.2.4(b,d)), while one or more stacking faults terminating on the free NW sidewalls can be occasionally present (Fig.2.4(c)).

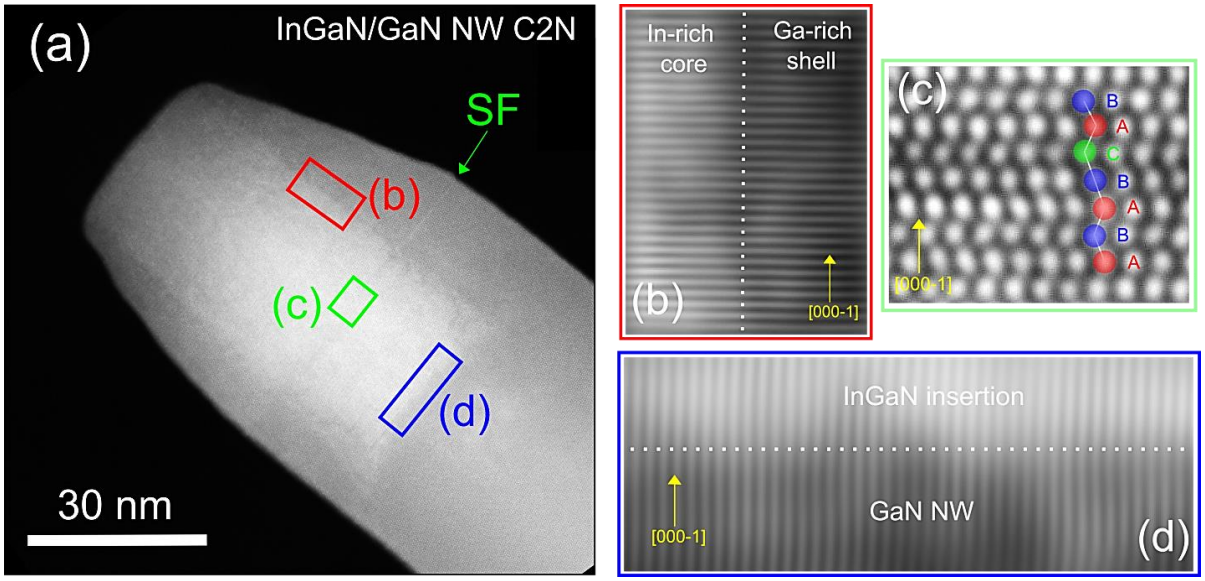

Figure 2.4 (a) STEM-HAADF image in the [11-20] zone axis of a tapered InGaN section (series Ga#1, In/GaBEP=1); Fast Fourier Transform (FFT) of the planes perpendicular (b) and parallel (d) to the substrate surface at the axial and core-shell interfaces,

Different authors reported InGaN/GaN axial NW heterostructures with similar core-shell geometries[32,88–90](Figure 2.5(a-c)). Their formation resulted from nominally low In/Ga ratios, N-rich flux conditions and quite different growth temperatures (500 to 650 °C). For shorter growth times, the InGaN sections were found to exhibit a truncated island geometry[32,88] (Fig. 2.5(a)) similar to the one of SK InGaN quantum dots grown on planar GaN substrates[91]. By contrast, Turbot et al.[90] reported that longer growth times result in higher aspect ratios and more uniform core diameters (Figure 2.5(b)), as observed in our case. As will be discussed further in the

manuscript, these morphologies are most likely to result from a strain-induced islanding process.

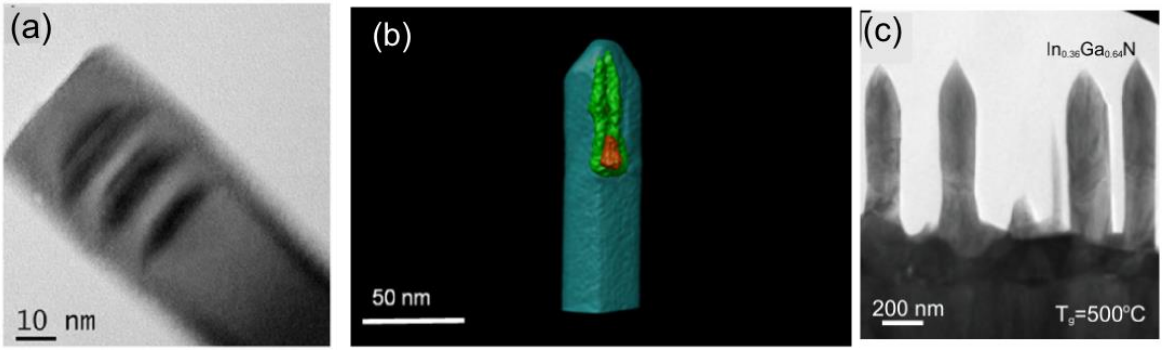

Figure 2.5 Tapered InGaN NW heterostructures reported by: Tourbot et al. (a)[88] and (b)[90] , and by Kong et al. (c)[89].

Untapered disk-like morphologies

For $2 < In/Ga_{BEP} < 4$, most of the InGaN sections present a straight (untapered) morphology, while a small NW fraction still exhibits faceted tips. This coexistence of morphologies is more evident at the tapered-untapered boundary conditions (In/Ga=2, Fig. 2.3 (e,f)), and can be in part assigned to beam shadowing effects and diameter variations, both influencing the effective In and Ga fluxes reaching the NW top-plane.

Figure 2.6 (a) shows the HAADF-STEM micrograph of a representative untapered InGaN section. Figures 2.6(b-c) depict similar InGaN morphologies reported in the literature, whose growth involved In/Ga flux ratios higher than one, and growth temperatures between 500 and 590 °C[90,92,93]. Differently from tapered morphologies, these sections are constituted by a wide In-rich core, surrounded by a thin and uniform (2-3 nm) Ga-rich shell (Fig. 2.6(a,b)). For thick sections, the out of plane tensile strain experienced by the shell can, in some cases, lead to the formation of sidewall cracks (arrows in Fig. 2.6(a,c). Indeed, these morphologies have been previously associated different plastic relaxation mechanism (cracks or edge dislocations) due to their higher In concentrations (in the literature, x_{In} 0.30-0.60). This phenomenon could be also promoted by the different thermal expansion coefficients between InN and GaN. In our case, no dislocations were observed, consistently with the reports of Alert et al. (Fig. 2.6(d)). The formation mechanism of these "disk-like" sections, is at present unclear and largely unexplored.

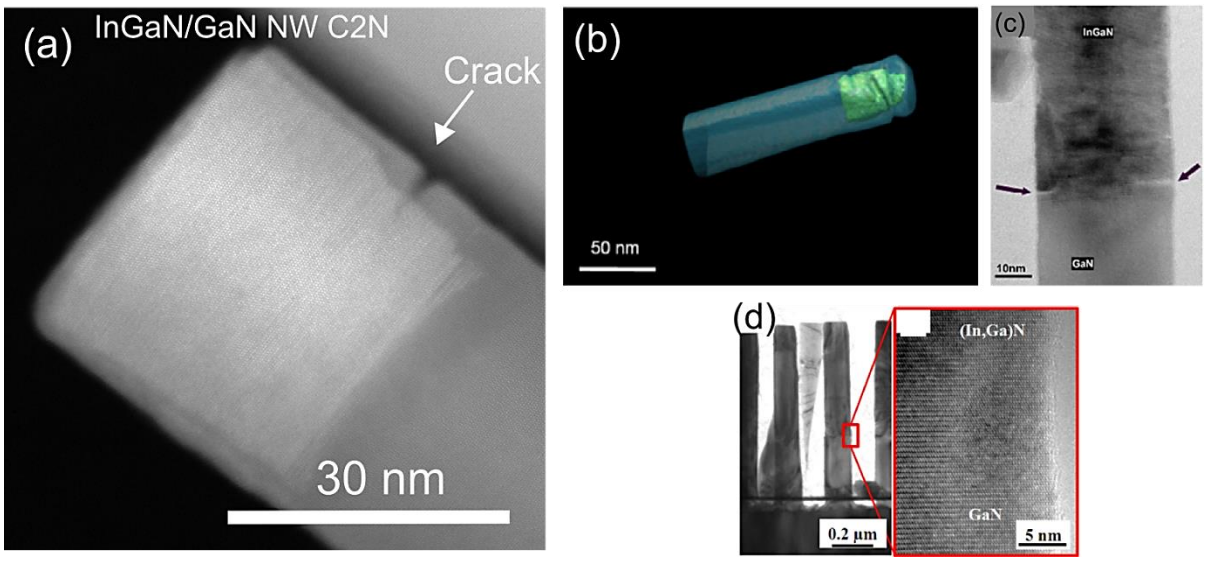

Figure 2.6 (a) STEM-HAADF micrograph of a disk-like section (series Ga#1, In/Ga_{BEP}=3); Similar InGaN morphologies reported in the literature: (b,c)[90] and (d)[92].

Radially overgrown/irregular morphologies

For In/Ga_{BEP}>4, the samples exhibit a significant dispersion of shapes, where NWs terminating with tapered, untapered, irregularly faceted or radially overgrown (so-called nano-umbrella) morphologies coexist. With reference to this latter population, we remark that the widening of the heterostructures is more pronounced for higher In fluxes (insets of Fig. 2.3(i-n)). Similarly to the case of GaN NWs grown under locally Ga-rich conditions[79], Zhang et al. associated this phenomenon to an accumulation of metal (In in this case) at the NW top facet[88,94]. Specifically, the authors speculated that this leads to a reduction in the N availability at the growth front: the growth could then proceed mostly at the boundaries of the metallic layer, resulting in a more pronounced lateral expansion of the structure [88,94]. Compared to other similar morphologies reported in the literature (Fig. 2.7(b,c)), our sections look quite defective, with irregular borders, holes and protrusions appearing in the bottom of the nano-umbrellas (Fig. 2.7(a)). This complex scenario indicates that at such high In/Ga_{BEP} conditions, growth is not sustainable within our experimental conditions. Nevertheless, in this work we payed less attention to these morphologies. In fact, island-like and especially disk-like sections, seem more adapt to the fabrication of more complex InGaN/GaN architectures, as the ones needed for photovoltaics and piezoelectrics.

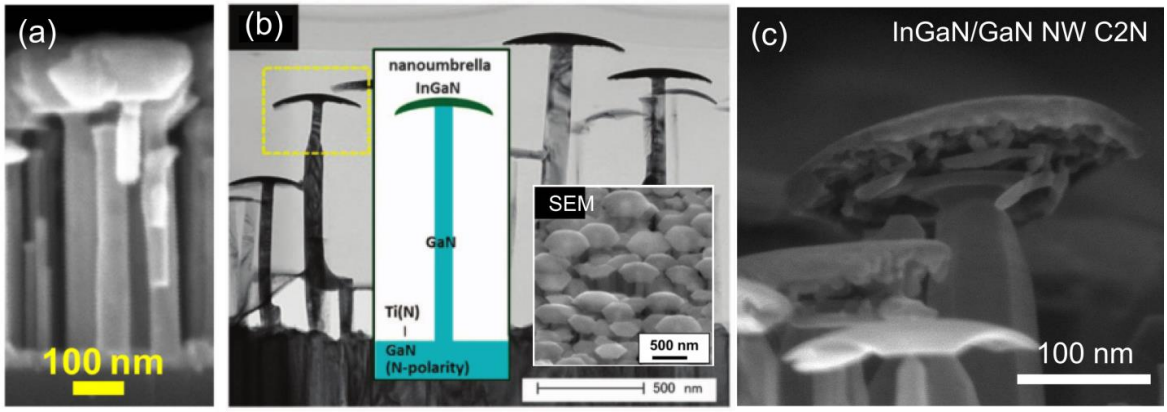

Figure 2.7 Nano-umbrella morphologies reported by Zhang et al.: (a)[95] (b)[96]; (c) cross-sectional SEM image of a nano-umbrella InGaN section (series Ga#1,In/Ga_{BEP}=6).

2.3 In incorporation in tapered and disk-like InGaN heterostructures

InGaN epilayers typically exhibit compositional fluctuations and inhomogeneities, whose entity and spatial extension depend on a complex interplay of thermodynamic and kinetic factors[97,98]. Specifically, their non-ideal mixing behavior, the markedly different In and Ga surface kinetics and the large difference in bonds length (strain) between GaN and InN, have been related to various phase separation, In clustering, and chemical ordering processes in both InGaN layers[99] and NW heterostructures[32,90,100]. Thus, before analyzing the dependency of the In incorporation on the flux conditions, it is important to investigate the alloy homogeneity at the nanometer scale. This has been done on tapered and untapered sections by combining the chemical accuracy of Energy Dispersive X-Ray Spectroscopy (EDX) with the spatial resolution of STEM.

2.3.1 Alloy homogeneity

As a first step, we evaluated the In and Ga spatial distribution within the heterostructure volume by acquiring EDX chemical mappings on both the NWs side-view and cross-sections. This technique has already been used to illustrate inhomogeneous In distributions in InGaN nanopillars[101], nanopyramids[102] and nanorods[103]. The results for the different morphologies are shown in Figure 2.8(a-n).

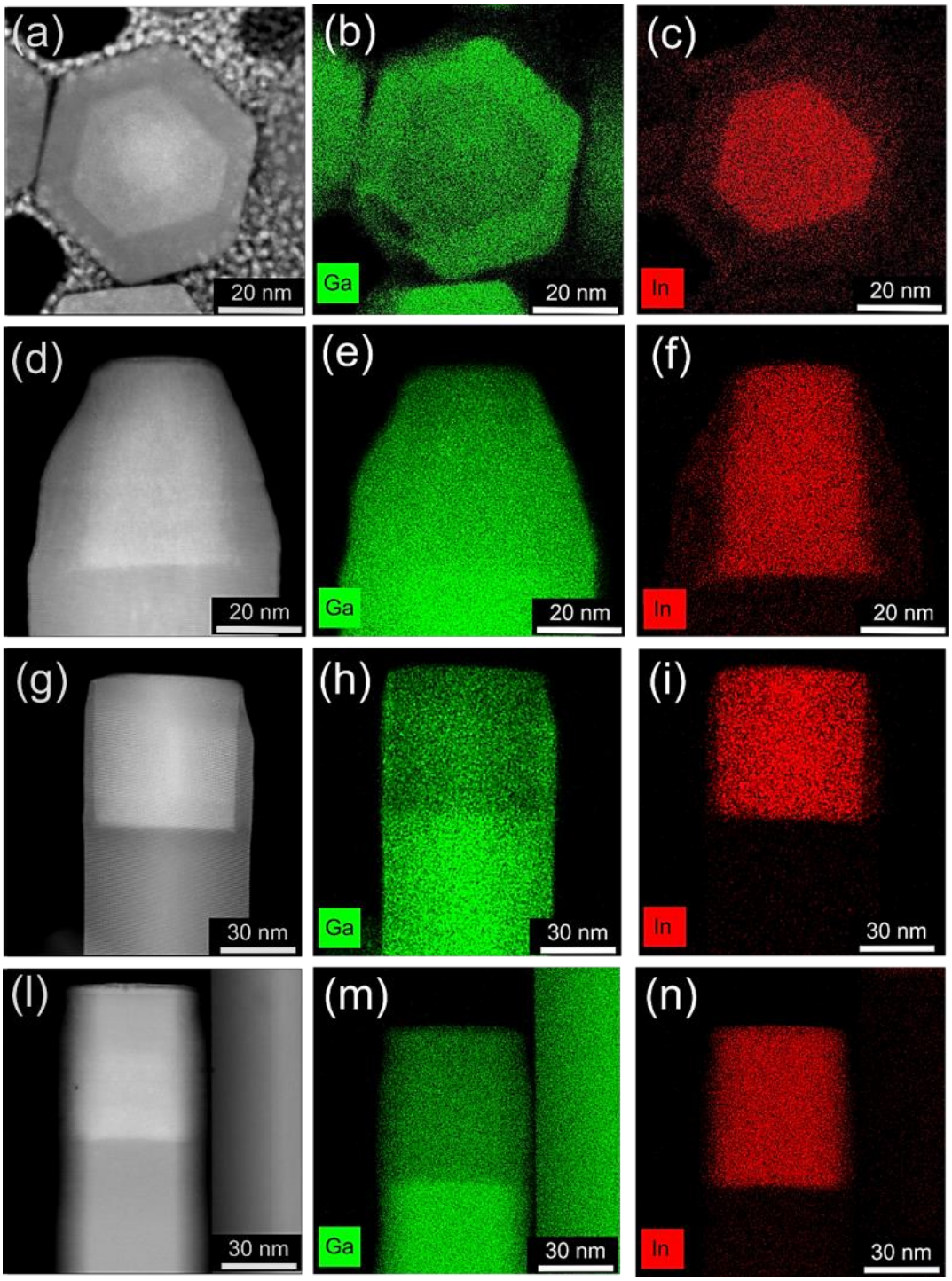

Figure 2.8 HAADF-STEM micrographs and the corresponding EDX mappings, illustrating the In and Ga compositional distribution within InGaN heterostructures grown with different In/Ga_{BEP} in series Ga#1: (a-c) cross-sectional NW, $In/Ga_{BEP} = 1.5$; (d-f) island section grown at $In/Ga_{BEP} = 1$, [11−20] zone axis; (g-i) $In/Ga_{BEP} = 1.5$, [11−20] zone axis; and (l-n) disk section grown at $In/Ga_{BEP} = 3$, [10−10] zone axis.

For side-view mappings, the measurements were acquired during a conventional STEM session. When possible, to better resolve the core-shell structure, the sample holder was tilted to obtain a [11-20] zone axis alignment (electron beam parallel to the NW m-facets). To extract radial mappings, the as-grown InGaN/GaN NWs were mechanically dispersed on a Si epi-ready substrate, and a TEM lamella embedding a large number of NW portions was prepared by means of a dual-beam FEI Scios focused ion beam (FIB) system (Fig. 2.9(a) in the next section). For all measurements the electron gun was operated at 200 kV, and to maximize the signal-to-noise ratio we made use of long acquisition times (20-30 minutes).

The results shown in Figure 2.8(a-c) clearly confirm the presence of a spontaneous phase separation between a Ga-rich shell and In-rich core of hexagonal cross-section. As also evidenced by the side-view mappings (Fig. 2.8(f,i,n)), both the core and the shell present rather uniform compositional distributions and abrupt interfaces. For instance, despite the high In fraction (from x~0.20 of island sections to x~0.40 of disk ones) the insertions do not show detectable In-rich clusters. Clusters can exhibit a much higher In concentration compared to the surrounding matrix and can extend over 5-10 nm[90,104]. This result suggests that clustering might take place, if at all, on shorter length scales (lateral spatial resolution is of about 2 nm), possibly in the form of In-N-In chains or InN clusters of a few In atoms[105].

2.3.2 Compositional profiles

Line-scans were used to study the elemental distribution across the radial and axial NW directions. At this scope, the net X-Ray counts were converted in relative In (x) and Ga (1-x) concentrations by using the Cliff-Lorimer method[ii], which employs empirical proportionality factors to relate the measured characteristic X-ray intensities to the composition of the specimen.

Fig. 2.9(b) shows a cross-sectional EDX line scan performed on a InGaN NW section grown with In/Ga ratio of 1.5 (series #Ga1). The alloy composition is remarkably constant in both the shell and the core parts, where the small nanometer scale compositional fluctuations ($x \mp 0.05$ at most) confirm a short range phase separation for

[ii] For thin samples, this method allows to decrease the measurement error (typically 1-2%) compared to other standard-less methods. A detailed description of its fundamentals can be found in refs.[243,244]

these InGaN heterostructures. A small asymmetry is observed in this profile as well as in the hexagonal shape and positioning of the InGaN core, which can be assigned to beam shadowing effects during the growth.

This measurement allows investigating relative compositional variations, but lacks quantitative valence. The main reason is that we don't have access to the exact positioning of the cross sectional lamella along the NW, which could potentially include a portion of GaN stem.

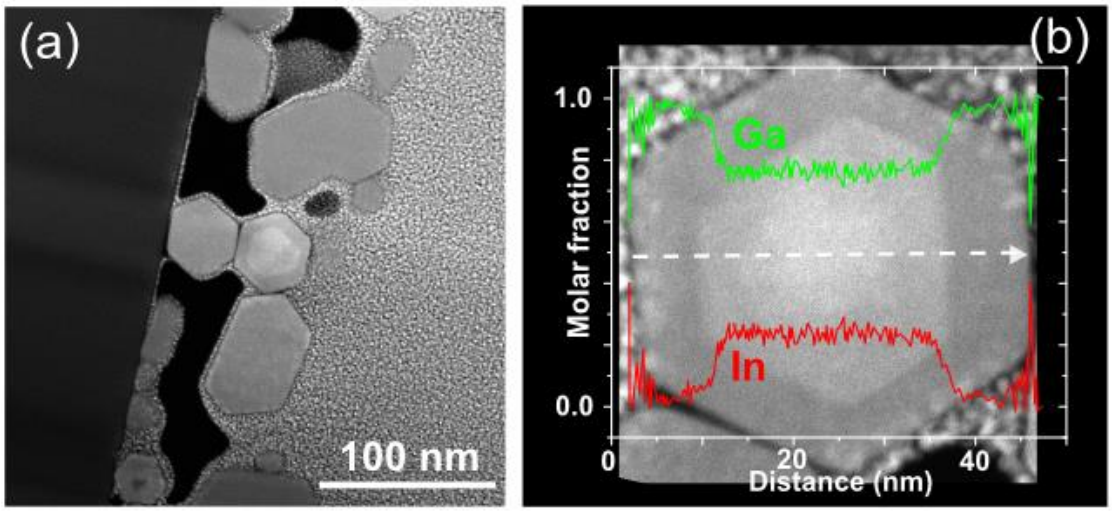

Figure 2.9 (a) Cross-section HAADF-STEM image of the FIB lamella embedding portions of different InGaN/GaN NWs; (b) Cross-sectional HAADF-STEM image and EDX line scan of a InGaN insertion grown with a In/Ga flux ratio of 1.5.

Similarly, in axial line scans, the chemical analysis integrates across the core-shell structure, leading inevitably to an underestimation of the In content within the In-rich core. Furthermore, unrealistic compositional gradients can be produced if the shell thickness is not uniform, as is case for tapered sections. It is thus crucial to subtract the shell contribution to estimate the In fraction within the In-rich cores. This can be done for [11-20] zone axis acquisitions, since the shell thickness can be precisely measured. The geometrical approach we adopted is depicted in Figure 2.10 and described in the following.

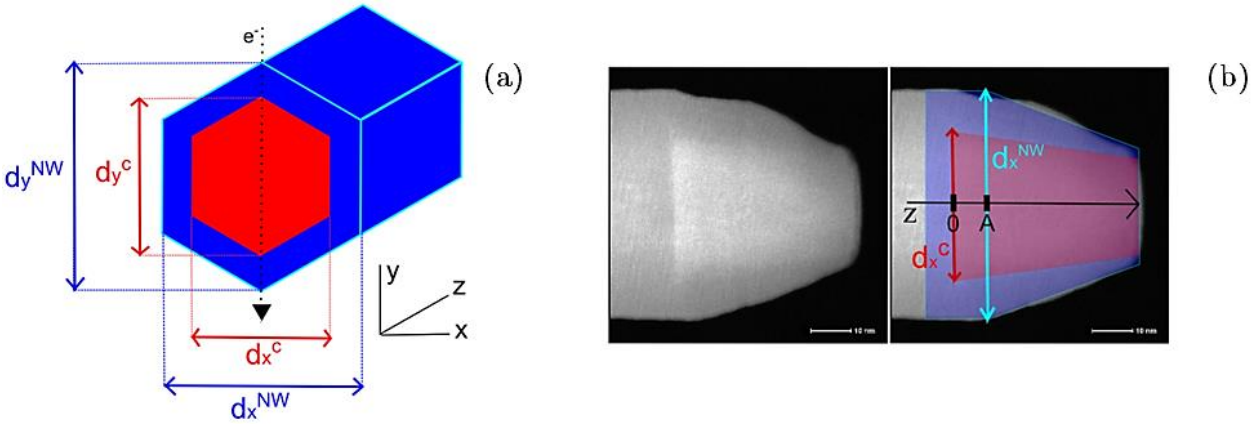

Figure 2.10 (a) Geometrical scheme of an EDX-STEM experiment on a core-shell hexagonal structure with the electron beam aligned in the [11-20] zone axis. (b) HAADF image (left) with its corresponding core-shell geometrical approximation (right).

For two regular and concentric hexagons, the following identity is valid:

$$\frac{d_y^{NW}}{d_y^c} \equiv \frac{d_x^{NW}}{d_x^c} \left(= \frac{d^{NW}}{d^c}\right) \qquad (eq.\,2.1)$$

where d^{NW} and d^c are the heterostructure (core+shell) and core diameters, and y and x two axis labels of the NW cross section (shown in Fig. 2.10(a)). By considering a shell of pure GaN, the In fraction measured at the position z along the NW axis (x_m^z) can be related to the corresponding core composition (x_c^z) by means of a correction factor equal to $\frac{d_z^{NW}}{d_z^c}$, where:

$$x_c^z = x_m^z \cdot \frac{d_z^{NW}}{d_z^c} \qquad (eq.\,2.2)$$

For EDX line scans, the correction factor must be substituted by a correction function $\frac{d^{NW}(z)}{d^c(z)}$, which takes into account the variation of the core and shell thicknesses along the growth axis. For each analyzed NW, this function has been built by considering linear variations of the shell and, eventually, core diameters in z, i.e. by approximating the core-shell geometry as shown in the example of Figure 2.10(b).

In Figures 2.11(a-d) are shown the measured (dashed line), and corrected (full line) In and Ga profiles along the heterostructures axes (white arrow). We see that the shell subtraction is essential for tapered heterostructures (Fig. 2.11(a-c)): if the non-corrected EDX profiles indicate a gradient of InGaN composition all along the growth

axis, the corrected profiles show that the gradient is more likely confined in the first ~20 nm from the c-plane GaN/InGaN interface. This gradient width is compatible with the one measured in disk sections (Fig. 2.11(d)). Note that in this latter case, the measured and corrected profiles since the effect of the correction is negligible and lies within the measurement error bar[iii]. The In fraction for the NWs of Figure 2.11 saturates at: x~0.30 and ~0.22 for (a,b) (grown with a In/Ga_{BEP}=1), ~0.40 for (c) (In/Ga_{BEP}=1.5) and ~0.50 for (c) (In/Ga_{BEP}=3).

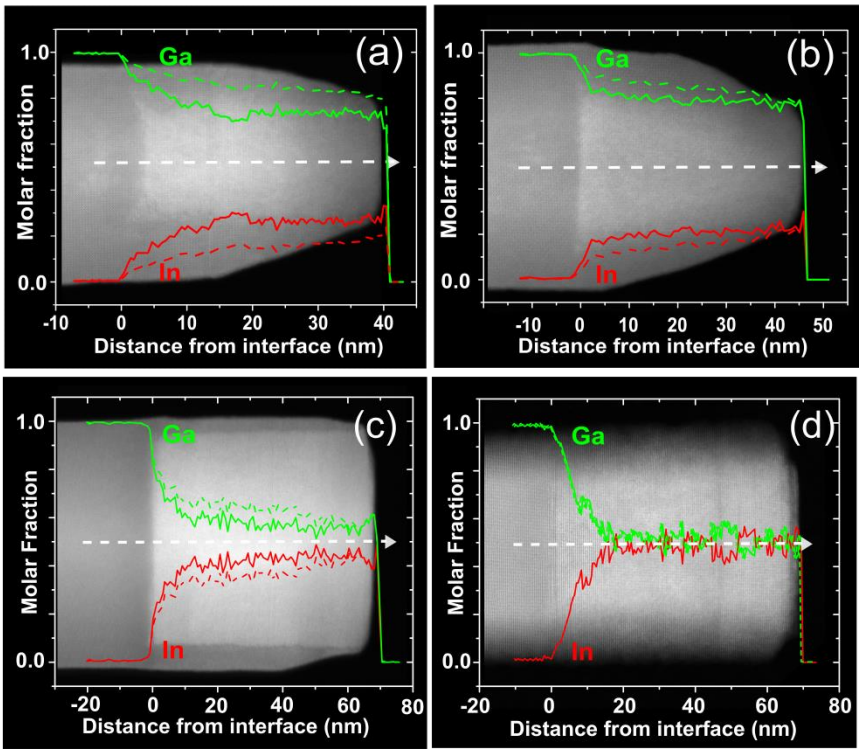

Figure 2.11 HAADF-STEM/EDX axial line-scans of InGaN/GaN NWs grown under different In/Ga_{BEP} conditions: (a,b) In/Ga_{BEP}=1; (c) In/Ga_{BEP}=1.5; (d) In/Ga_{BEP}=3

It is widely accepted that lattice mismatch can lead to significant compositional variations in the vicinity of InGaN/GaN planar heterointerfaces. This happens through the so-called "lattice pulling" effect[89,106–108], in which the in-plane misfit strain between the InGaN layer and the GaN substrate "pulls" the alloy composition towards lattice matching conditions by hindering the In incorporation. For instance, it has

[iii] This is true for representative NW diameters (~50 nm) with thin and uniform shell thicknesses (2 nm).

been shown that as the layers grow thicker and strain is progressively relaxed, this effect tends to vanish, resulting in a stabilization of the alloy composition[89,107].
In this view, our results may suggest that both types of structures are able to accommodate the large majority of the in-plane strain after approximately 20 nm of growth, independently from their average In fraction: this strain relaxation, might allow a stabilization of the In incorporation to the value expected by the given growth conditions. Note, however, that in NW axial heterostructures, the strain accommodation is expected to depend on the NW radius, as well as on the eventual presence of structural defects. Thus, generally speaking, this critical gradient width must vary to some extent, for different samples[30].

These results call for a more detailed structural investigation, to better understand how misfit strain is relaxed within the heterostructure volume. This has been done by combining Geometrical Phase Analysis (GPA) on STEM images for atomic scale resolution, with Grazing Incidence and High-resolution X-Ray Diffraction measurements, to gather statistical information on the a and c lattice parameters of the NW ensembles.

2.4 Strain state in tapered and disk-like heterostructures

Structural investigations have been carried out on samples grown with a In/Ga_{BEP} of 1 and 3, presenting respectively an island-like and disk-like morphology. Figure 2.12 presents the GPA catrographies reconstructed from the correspoding STEM images.

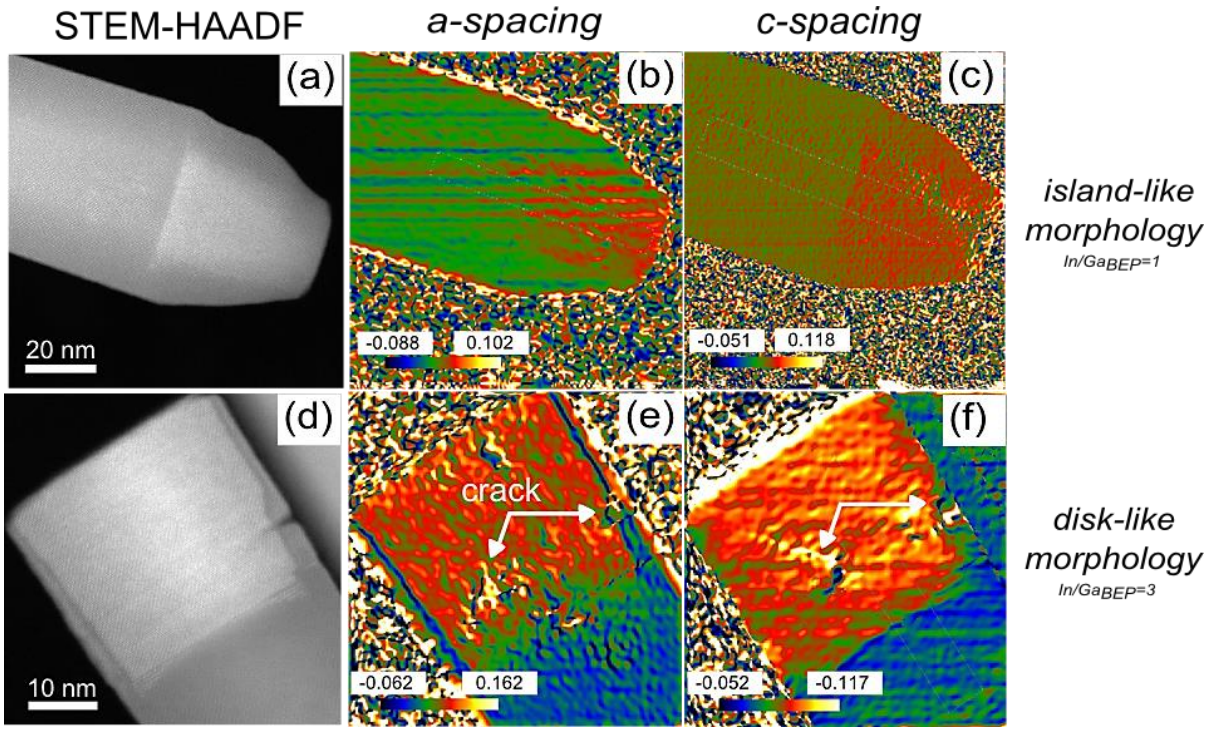

Figure 2.12 STEM-HAADF (a,d) and GPA cartographies of the in-plane (a,c) and out-of-plane (b,d) crystal deformations of a island-line (a-c) and disk-like (d-f) InGaN section.

In both cases, the a-spacing cartographies (Fig 2.12(b,e)) reflect the core-shell In distribution previously evidenced by EDX and HAADF-STEM analysis: the a lattice parameter of the shell resembles the one of the underlying GaN NW, while the one of the core is much higher. By contrast, the GPA analysis reveals rather uniform lattice deformations in the out-of-plane direction (Fig. 2.12(c,f)), where the In-rich core and the Ga-rich shell seem to adopt a common c lattice parameter. In disk-like geometry,

the plastic relaxation of strain through sidewall cracking leads to localized lattice distortions, evidenced by the arrows.

These results correlate well with the X-ray diffraction scans around the (11-20) and the (000-2) spectral spots, shown in Figure 2.13. In each of these spectra (black lines) we can distinguish at least two diffraction peaks: one corresponding to the relaxed GaN NW base, and one to the InGaN heterostructures. While the (11-20) reflections can be described only by considering distinguished shell and a core contribution (see fitted curves in Fig. 2.13(a,c)), this is generally not true for the (0002) reflections. In this latter case, only one broad peak is observed in addition to the GaN diffraction peak, more clearly separated for the disk-like sections, and in the form of a small shoulder for the tapered ones (Fig. 2.13(b,d)).

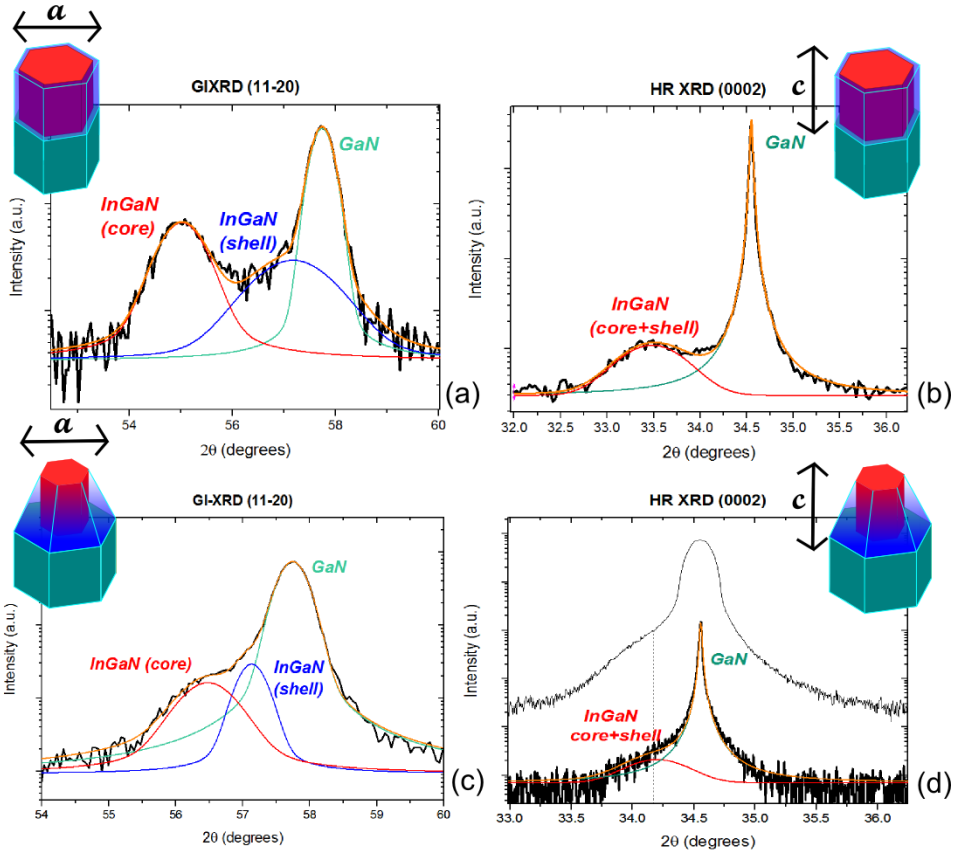

Figure 2.13 $2\theta/\omega$ GIXRD (a,c) and HRXRD scans (b,d) of the InGaN/GaN NW arrays with disk-like (a,b) and island-like (c,d) InGaN sections. In HRXRD scans, the triple-axis scan is shown. Pseudo-Voigt functions were used for the fits.

The fitted curves allow to extract the a and c lattice parameters corresponding to each of the diffraction peaks. These are summarized in Table 2.1. For comparison, we

also reported the lattice parameters computed in the limits of Vegard's law (strain free approximation), by considering the average core compositions measured by EDX statistics[iv] and the binary lattice parameters reported in Section 1.2.1.

Table 2.1 Lattice parameters calculated from the Bragg's diffraction angles (Experiment) and calculated in the limits of Vegard's law (Strain-free).

	x_{In} (EDX)	a_{core}	a_{shell}	c_{core}	c_{shell}
Island-like	0.20 core 0.10 shell	**Experiment (XRD)**			
		3.256	3.221	5.24	5.24
		Strain-free (Vegard's law)			
		3.268	3.225	5.290	5.213
Disk-like	0.40 core 0.10 shell	**Experiment (XRD)**			
		3.335	3.219	5.348	5.340
		Strain-free (Vegard's law)			
		3.332	3.225	5.393	5.213

As concerns the a lattice parameters, the measured and strain-free values show small differences, indicating low ($|\varepsilon_{\parallel}|$<0.4%) residual in-plane strain in both the shell and core parts. This result is consistent with the ε_{xx} profile depicted in Figure 2.14(a) (disk section): this shows a gradual increase of the a lattice parameter in the first 18 nm of insertion, which then stabilizes to its strain-free value (plateau composition x_c=0.55, corresponding to a $\Delta a/a$=0.06). In Figure 2.14(b) reports the ε_{xx} profile of the tapered. Due to its more complex core-shell geometry, the profile doesn't allow a straightforward access to the core strain state. Nevertheless, in agreement with the rapid accommodation of the lattice mismatch in axial NW heterostructures, typically well below the point where the heterostructure reaches an aspect ratio of 1[30], these results suggest that we can consider most of the heterostructure volume as largely in-plane relaxed. This statement further supports the idea that the In fraction

[iv] Note that for sample C016, the core composition has been calculated by subtracting the shell contribution, as described in the previous section.

compositional gradient at the heterointerface vicinity arises from a lattice-pulling effect. In fact, for disk-like sections, the critical section thickness for the stabilization of the a lattice parameter to its strain-free value (~18 nm), is absolutely compatible with the compositional gradient width measured by EDX (~20 nm).

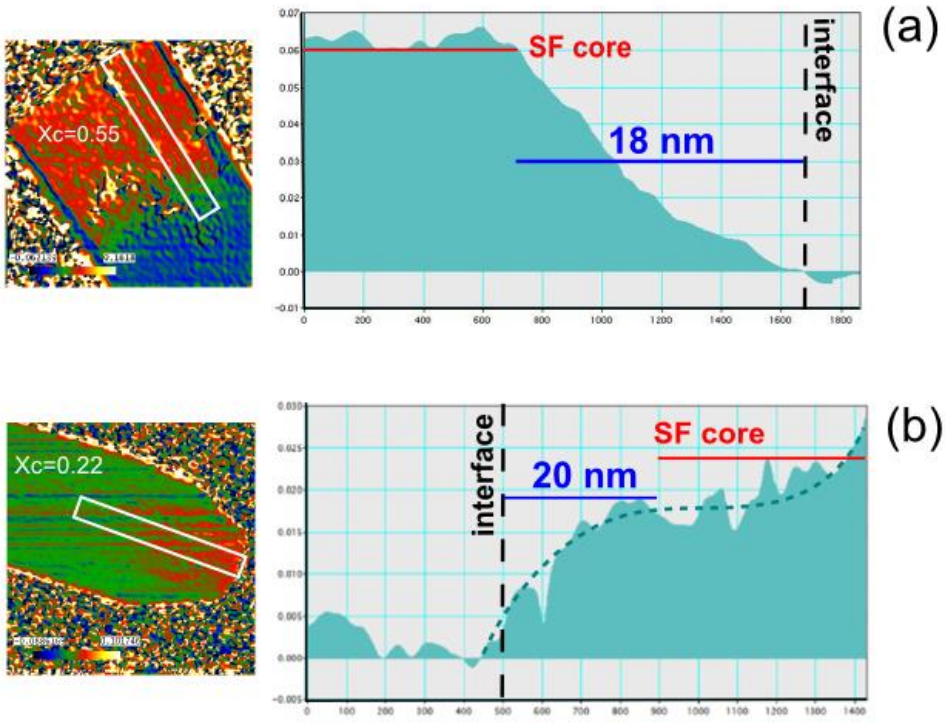

Figure 2.14 GPA profiles of the disk-like (a) and island-like (b) InGaN sections, traced by averaging over the width of the white rectangles.

The situation is quite different in the out-of-plane direction. Here, the difference between the measured and strain-free c lattice parameters indicates a non-negligible axial strain, which is compressive in the core and tensile in the shell. However, the strain partitioning between the core and the shell is different for tapered and disk-like sections. For tapered sections, the average lattice deformation is higher in the core (-1%) than in the shell (+0.5%). By contrast, for disk-like sections the situation is reversed and most of the deformation is stored in the shell (+2% tensile strain in the shell and -1% compressive strain in the core). In this latter case, the high tensile strain in the shell could explain the appearance of sidewall cracks in this specific type of structures.

This anisotropic strain partitioning can be understood by considering the case of a nominally infinite core-shell NW[30,109]. Specifically, if R is the core radius, and H is the shell thickess, for a given lattice mismatch, two extreme cases can be drawn: if H>>R, the axial strain localizes in the core, whether if H <<R, the situation resembles the 2D case, with most of the core playing the role of a thick substrate. Owing to the different core-shell geometries of tapered and untapered structures, the different strain partitioning in tapered and disk-like sections, seems to reflect two intermediate cases: in tapered sections H is comparable to R, and most of the strain is stored in the core; by contrast, in disk-like sections, H<R and the shell deformation is more pronounced.

In conclusion, the experimental results described in this part, establish that the strain distribution within the InGaN NW heterostructures is rather anisotropic and reflects their combined axial and core-shell nature. In the in-plane direction, both tapered and untapered structures relax the majority of the strain imposed by the underlying GaN NW. For one disk-like section it is shown that this happens after a critical thickness of approximately 18 nm. Importantly, this thickness matches quite accurately the extension of the In fraction gradient measured by EDX line scans (section 2.3.2), further supporting its assignment to the lattice pulling effect. In the out-of plane direction, strain is largely dominated by their core-shell geometry, where the core *shares* the axial strain (ε_{zz}) with the outer shell, while maintaining a weak coupling with its in-plane components (ε_{xx} and ε_{yy}) [30,109]. An obvious reason for this non intuitive strain distribution is that the core, being entirely surrounded by the shell, has little space to expand laterally for compensating its out-of-plane deformation, and maintains at best its strain-free lattice parameter.

2.5 InGaN heterostructures growth diagram

To build the InGaN NW heterostructure's growth diagram, the main properties of the InGaN sections must be correlated with their specific growth conditions. Thus, after analyzing In incorporation and strain distribution in single heterostructures, we present here the variation of the In fraction as function of the In/Ga flux conditions (series Ga#½ and #Ga1), for the different morphologies. The composition was measured by point-type SEM-EDX measurements on ~30 NWs per sample. Specifically, the core composition was probed by focusing the electron beam on the top most of the InGaN sections (the lowest section thicknesses are of about 35 nm, so the measurement is performed far from the heterointerface compositional gradient). For tapered sections, the In fraction has been multiplied by d_{NW}/d_{tip}[v]. For radially overgrown morphologies the measurements were taken in random positions of the InGaN nano-umbrellas. The results are summarized in the growth diagram of Figure 2.15.

Despite the presence of compositional fluctuations from wire to wire, which can be related to our self-assembled growth approach, the evolution of the InGaN section morphology described in section 2.2, is clearly accompanied by a non-monotonic variation of the average In fraction. In the specific, we identify three distinct growth regimes as function of the In/Ga_{BEP} parameter:

Regime I. For $In/Ga_{BEP} < 2$, the island-like InGaN sections are associated to an increasing behavior of the In fraction with Φ_{In} ; this increases from x~0.05 up to x~0.40 (respectively, to ~0.30) for #Ga1 (respectively, #Ga½).

Regime II. For $2 < In/Ga_{BEP} < 4$, disk-like shapes are associated to a stable In fraction of x~0.40 (respectively, 0.30) for #Ga1 (respectively, #Ga½).

---

[v] Due to the low shell thickness at the heterostructure tip and to the quasi-vertical core sidewalls, the tip diameter (d_{tip}) is a good approximation of the core diameter (d_c). Thus, provided that a 10 kV acceleration voltage is used for the measurements, so that the electron beam passes through the NW, the core composition can be estimated by multiplying the measured In fraction by d_{NW}/d_{tip}.

Regime III. For In/Ga_{BEP}>4, the increasing tendency towards radial overgrowth and/or morphological degradation is accompanied by a steep decrease of the In fraction from ~0.40 for #Ga1 (respectively, ~0.30 for #Ga2) to ~0.10 (for both the sample series).

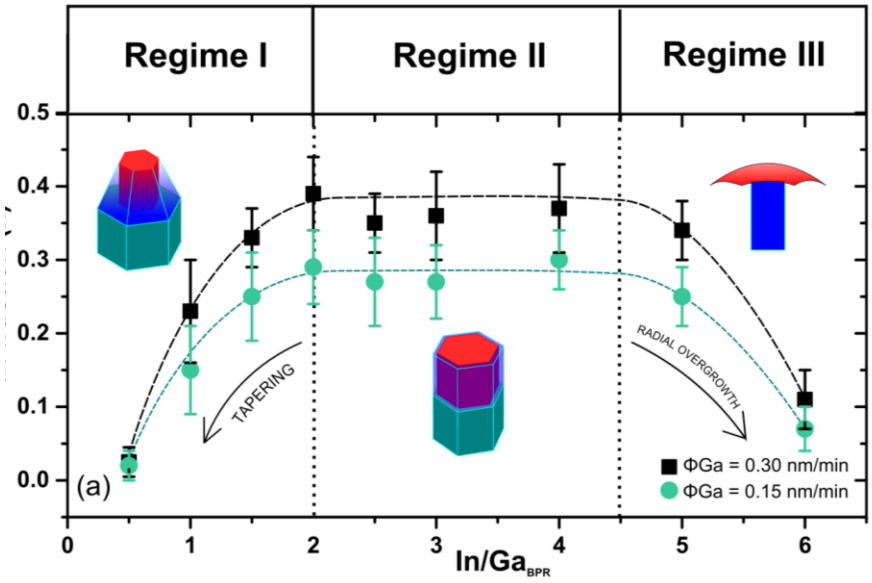

Figure 2.15 In fraction (x) measured by EDX as a function of the In/Ga_{BEP} conditions for series #Ga$_1$ (ϕ_{Ga} = 0.30 *nm*/min) and #Ga$_{½}$ (ϕ_{Ga} = 0.15 *nm*/min). The three growth regimes and the corresponding InGaN morphologies are evidenced.

2.5.1 Effect of the In/Ga ratio on the local V/III conditions

The experimental growth diagram shown in Figure 2.15 provides useful guidelines to tailor the spontaneous formation of InGaN NW heterostructures within a relatively broad range of compositions (x_{In} 0.05-0.4). Still, it raises a fundamental question on the nature of the three observed growth regimes, and the role played by the In/Ga_{BEP} parameter in setting their boundaries. In this context, if the formation of InGaN nano-umbrellas has been previously associated to In-accumulation growth regimes, the origin of island and disk-like heterostructures, as well as the mechanism responsible for the transition between the two morphologies, are at present unclear and largely unexplored.

It is well established that the morphology of III-N materials and their alloys grown by PA-MBE is extremely sensitive to the relative abundance of metal at the growth

surface. In the growth of 2D III-N layers, three growth regimes are usually observed as function of the V/III ratio parameter:

- N-rich conditions: the epitaxial growth happens in the form of rough surfaces of 3D islands, which may follow the Stranski-Krastanow (SK) growth mode in presence of strain, mostly depending on the nature of the deposited material and underlying substrate[60,110–112].
- M-rich conditions: the 3D growth is inhibited [113,114], resulting in a sustainable layer-by-layer (Frank–Van der Merwe, FM) growth mode and smooth surface morphologies. This behavior refers to the peculiar property of III-N surfaces to thermodynamically stabilize metallic (1-2 ML) adsorbed layers at the growth front, which play the role of surfactants or self-surfactants [14,98,113].
- *highly* M-rich conditions: droplets accumulation on the top of the adsorbed metallic layer leads to a marked deterioration of the surface morphology and eventually to a growth stop[60,86,115]. The main reason for this, is that the metallic droplets locally perturb the growth by preventing the N species to reach the underlying growth front.

These three growth regimes have been observed for GaN[14,113,115], AlN[14] and InN[60,84,116117] layers of both polarities, and are also observed for InGaN layers deposited on Ga-polar GaN substrates [86,108]. Specifically, in this case In is the excess metal which segregates at the growth front due to its weak bonding energy compared to Ga.
We suggest a parallel between the three growth regimes observed for 2D InGaN and the ones observed for InGaN NW heterostructures (Fig. 2.15). Specifically, we propose that the island-like, disk-like and nanoumbrella/irregular morphologies of regimes I, II and III result respectively from the establishment of locally N-rich, In-adlayer and In-accumulation conditions at the NW growth front. Indeed, in the specific case of nano-umbrella morphologies, other authors associated their formation and their decreased In incorporation to the accumulation of metallic In at the growth front[94,95].

Note that these statements could hold even by considering that our V/III *precursor* ratio is highly N-rich and differs of a factor of 2 between the two #Ga series. On one side, due to the peculiar collection geometry of the atomic fluxes, which involve both the direct impingement on the NW top and atoms diffusing from the m-facets, the local V/III conditions at the NW tip can significantly differ from the nominal (2D)

ones[79]. On the other side, in InGaN growth, it should be possible to accumulate In on the surface, *even by working under high N excess*. From a qualitative point of view, this could happen because the maximum In fraction that can be incorporated is limited by the In-N bonds decomposition, which depends mostly on growth temperature and polarity[83]. In other words, for fixed substrate polarity and growth temperature, even if the metal (Ga+In) fluxes are decreased to produce V/III precursor ratios far below the stoichiometry (so that Ga and In do not compete for a limited amount of N), the high amount of In supplied at high In/Ga flux ratios cannot incorporate, but could, in principle, segregate at the growth front.

Growth rate measurements

To verify our hypothesis on the local V/III conditions, we studied the evolution of the average growth rate (v_{InGaN}) of InGaN sections with the In/Ga_{BEP} conditions in regimes I and II. In fact, for a fixed N-supply, the growth rate should increase with the metal flux under N-rich conditions, and should stabilize when the stoichiometry is reached. To take into account the various heterostructures shapes, v_{InGaN} was estimated in terms of equivalent axial growth rate as

$$v_{InGaN} = \frac{V}{\pi r^2 \cdot \Delta t} \qquad (eq.\,2.3)$$

where V is the heterostructure (core+shell) volume, r is the GaN NW radius and Δt is the growth time, which was identical for all samples. V was obtained by approximating the heterostructure by a cylinder, a truncated cone or the sum of the two, the geometrical parameters of which were measured on ~30 STEM micrographs per sample. Three examples are given in Figure 2.16, while the results of growth rates are plotted as function of the In/Ga_{BEP} in Figure 2.17.

In agreement with our hypothesis, the growth rate follows the behavior expected at the N-rich/In-rich local stoichiometry boundary: a linear increase in In-limited (N-rich and Ga-limited) conditions (Regime I), and a plateau at ~0.30 nm/min (~0.65 nm/min) for Φ_{Ga} = 0.15 nm/min (Φ_{Ga} = 0.30 nm/min) in In-rich (still N-rich and Ga-limited) conditions (Regime II). In fact, in In-rich conditions, the growth rate is independent on the In supply and is essentially driven by the Ga flux, following[10,86]

$$v^{th} = \frac{\Phi \mathrm{Ga}}{(1-\mathrm{x})} \qquad (\mathrm{eq.}\,2.4)$$

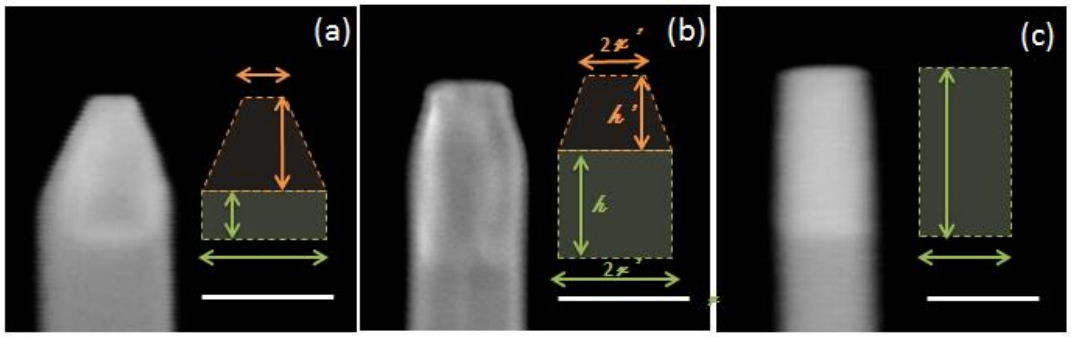

Figure 2.16 HAADF-STEM micrographs of representative InGaN sections acquired in a SEM set-up (25 kV acceleration voltage), with sketch showing their approximated geometry: In/Ga_{BEP} of 1 (a), 1.5 (b) and 2 (c).

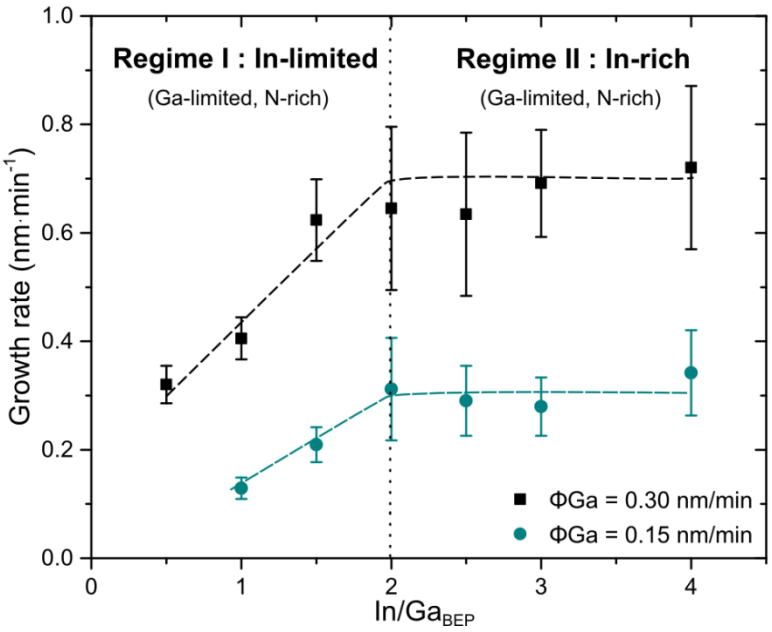

Figure 2.17 Average growth rate of InGaN heterostructures as a function of the In/GaBEP. The growth rate increases in Regime I, while it is approximately constant in Regime II, indicating respectively In-limited and In-rich growth conditions at the NW growth front.

These results tend thus to confirm that within our experimental conditions, In/Ga_{BEP}=2 corresponds to the N-rich/In-rich stoichiometry boundary for InGaN NW heterostructures growth.

Since at 590 °C Ga desorption can be safely neglected, eq. 2.4 can be applied by considering the average alloy composition measured by EDX statistics and the Ga fluxes directly impinging on the NW top plane (calibrated by RHEED oscillations).

The equation returns v^{th} values of 0.54 nm/min (Φ_{Ga} = 0.30 nm/min) and 0.23 nm/min (Φ_{Ga} = 0.15 nm/min), which underestimate only slightly our experimental measurements (0.60 and 0.35 nm/min, respectively). This suggest a low flux contribution from Ga adatoms diffusing on the NW sidewalls and reaching the NW tip which, from our estimations, should roughly correspond to 1/5 of the total Ga flux contributing to the heterostructure growth.

In stability on the GaN NW (000-1) planes

In the literature, different groups investigated the In stability on Ga- or N-polar GaN surfaces, where the In adorption/desorption kinetics was studied by RHEED[108,118], line-of-sight quadrupole mass spectrometry[84] or spectroscopic ellipsometry[119]. For N-terminated surfaces, the most stable In coverage is defined by the (1×1) In adlayer structure, which consists of 1 ML of In strongly interacting with the N dangling bonds and making overall surface metallic[98]. Stemming from ab-initio calculations, the N-polarity offers a considerably wider temperature range, i.e. ~200K higher temperatures, for the In adlayer stabilization as compared to Ga-polar surfaces[97] (Fig. 2.18(a,b)).

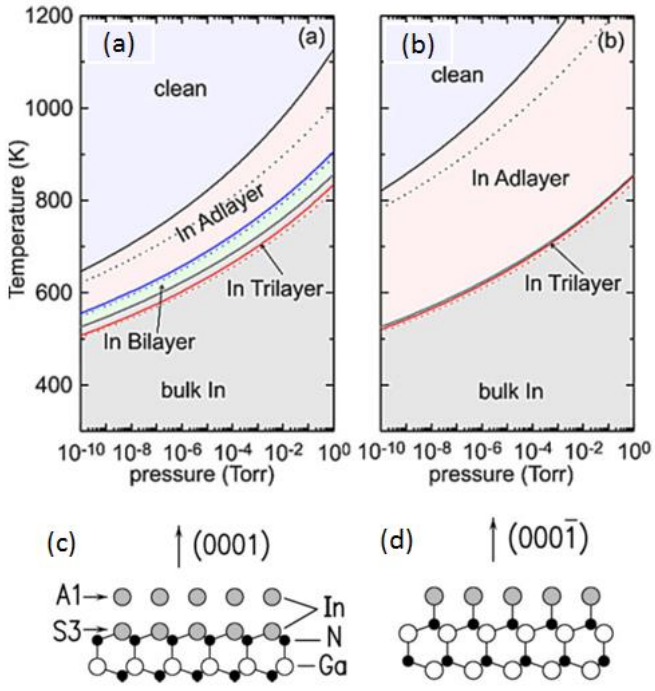

Figure 2.18 In adlayer stability diagram (ab initio calculation) and corresponding adlayer most stable structures for a Ga-polar (a,c) and N-polar (b,d) GaN surface[97].

To support the argument that Regime II corresponds to an In-adlayer mediated growth regime, we analyzed *in situ* by RHEED the In stability on the (000-1) NW top surface at the temperature used for InGaN growth (590°C). This was done by exposing the NWs to the In flux during a given time and by recording the oscillatory transient of the RHEED intensity during subsequent In desorption under vacuum. This procedure has already been used to study the stability of In on (0001) and (11−22) oriented GaN planar surfaces[87,120].

GaN NWs grown of Si/SiNx[vi] substrate were exposed for different times (from 2 to 40 seconds) to an In BEP of 1.8x10^{-8} Torr. This value corresponds to the In excess flux (non-incorporated) at the InGaN stoichiometry boundary (In/Ga_{BEP} =2) for the $\boldsymbol{\Phi_{Ga}}$ = 0.15 nm/min series. After shuttering the In cell, the desorption time was determined from the second inflection point of the RHEED intensity transient. This was recorded by integrating on the vertical stripe in the proximity of the specular spot (yellow rectangle in Fig. 2.19(a), which corresponds to the first order diffraction of the (000-1) GaN surfaces. Note that to prevent any parasitic effect, the radio-frequency plasma cell was off during these experiments, and a sufficiently long amount of time was allowed between each measurement.

Figure 2.19(b) shows the recorded absorption and desorption RHEED transients, observed respectively after opening and closing the In cell shutter. These are roughly symmetric, and depend on the exposure time. In the specific, for exposure times higher than 10 seconds, while the adsorption transient reaches a constant minimum, the desorption time becomes constant. This is more clearly shown in Figure 2.19(c), where the time corresponding to the second inflection point of the RHEED intensity recovery under vacuum is plotted as function of the exposure time. Since the desorption time depends on the surface coverage [121], its plateau reveals the establishment of a self-regulated In adlayer, such that the In impinging flux exactly compensates the In desorbing flux. These results confirm that the adsorbed In atoms can form a stable

[vi] The choice to use GaN NWs grown on Si/SiN_x instead of Si/AlN substrates, stems from their higher average diameters (70∓15 nm instead of 50∓10 nm under our experimental conditions) and better length homogeneity. This leads to a higher intensity for the (000-1) top-planes diffractions (vertical stripes in Fig. 2.18(a)). Note that the N-polarity of the NWs was verified by the appearance of the characteristic pencil-like tips after KOH etching.

wetting layer on the [000−1] GaN NW top-plane, and that Regime II might correspond to an In-adlayer mediated growth regime.

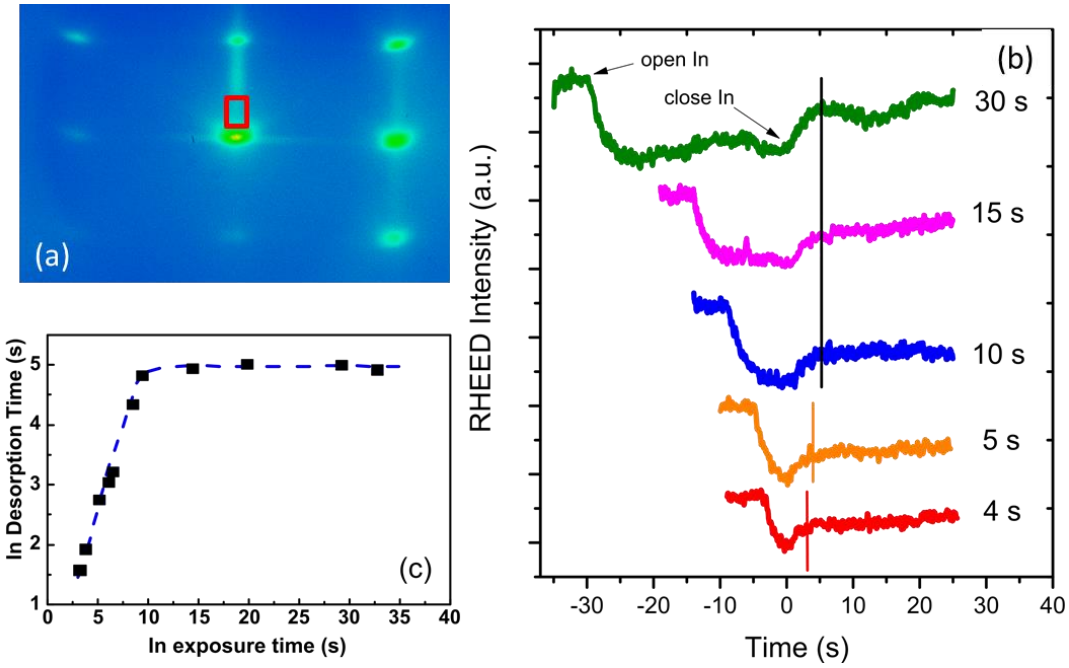

Figure 2.19 (a) GaN NWs RHEED pattern. The intensity is integrated over the area delimited by the red line. (b) Recorded RHEED intensity profile for different exposure times. The black line highlights the stable regime of the In desorption transient duration. (c) Evolution of the In desorption from the GaN (000−1) NW surfaces as a function of the In exposure time.

2.5.2 Effect of the Ga flux on the In incorporation and heterostructure growth rate

In the previous section, we observed that the Ga flux essentially drives the heterostructure growth rate: in Figure 2.17 we showed that when the Ga flux is halved (series #Ga1/2), the heterostructure growth rate decreases accordingly. In addition, we remark that Φ_{Ga} also impacts the alloy composition, since as previously shown in the growth diagram (Fig. 2.15), the In content seems systematically lower when the Φ_N/Φ_{Ga} ratio is increased of a factor of 2. To further investigate this effect, we grew a third set of samples (In/Ga#3) where the Φ_{Ga} was varied to produce Φ_N/Φ_{Ga} ratios between 25 and 2.8, while the In flux was adjusted to maintain a constant Φ_{In}/Φ_{Ga} ratio of 3 (In-adlayer conditions). As done for the two # Ga series, we evaluated the heterostructures' morphology, the average In fraction (far from the interface) and the

average axial growth rate (v_{InGaN}). In addition, to gather some information about the Ga and In incorporation rates, we estimated the GaN (v_{GaN}^{eq}) and InN (v_{InN}^{eq}) equivalent growth rates by multiplying v_{InGaN} to the corresponding In and Ga fractions measured by EDX statistics.

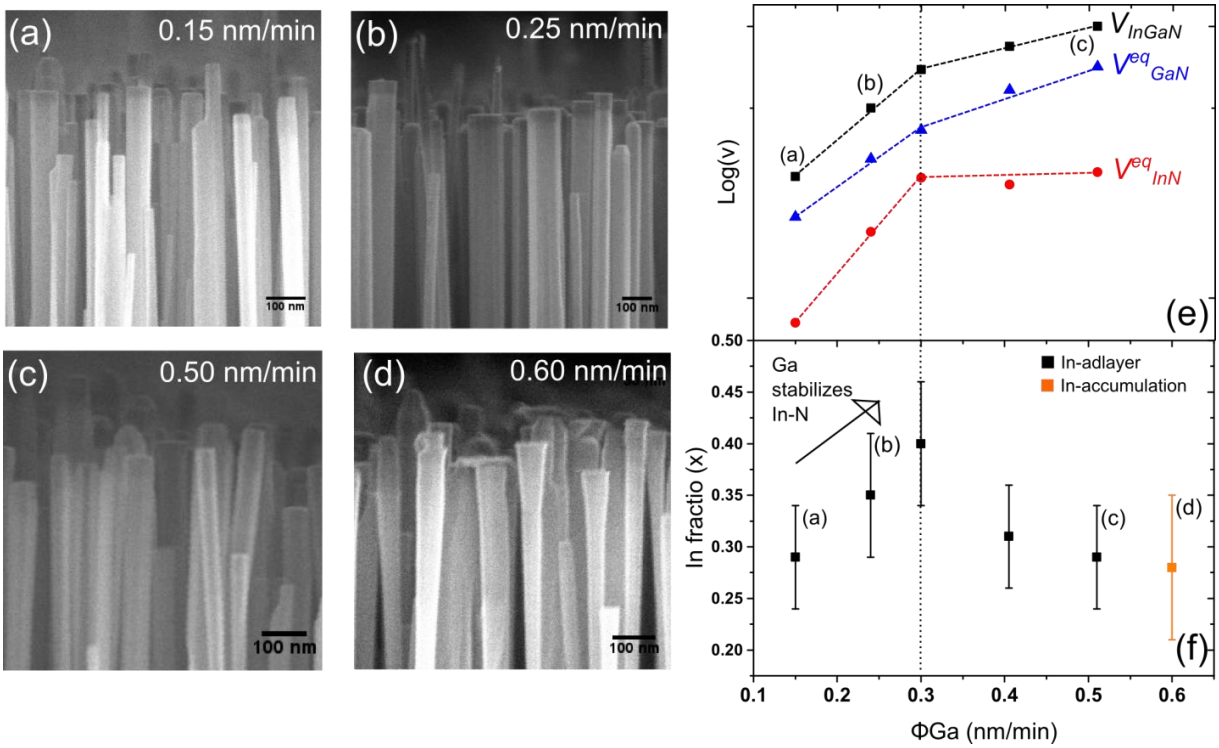

Figure 2.20 (a-d) cross-section SEM images of the as grown InGaN/GaN NWs grown with a Φ_N/Φ_{Ga} ratio of 25, 15, 7 and 6 respectively. (e) InGaN, InN, and GaN equivalent growth rates and (f) In fraction as a function of Φ_{Ga} under In-adlayer growth conditions. The last point shown in (f) (orange) corresponds to InGaN morphologies characteristic of In-accumulation local conditions (lateral overgrowth), and thus has not been considered for the growth rate calculations.

As shown in figure 2.20(a-c), a disk-like morphology resulting from In-adlayer conditions is observed for all samples except for the highest Ga flux considered, where slightly enlarged InGaN sections start to appear (Fig. 2.20(d)). The growth rate measurements are shown in Figure 2.20(e). As a result of the N-rich flux conditions, v_{InGaN} and v_{GaN}^{eq} show the same increasing behavior since there is still N available in the environment. By contrast, a different trend is observed for v_{InN}^{eq} : when Φ_{Ga} is increased from 0.15 to 0.30 nm/min (corresponding to the two reference #Ga fluxes), v_{InN}^{eq} increases faster than v_{GaN}^{eq} , while for Φ_{Ga}> 0.30 nm/min, it stabilizes to a constant value. This results in a non-monotonic dependency of the In content on the

Ga flux: x increases firstly from ~0.30 to ~0.40, and then decreases from ~0.40 to ~0.27 for Φ_{Ga}>0.30 nm/min (Fig. 2.20(f)).

As previously mentioned, due to the much lower bonding energy of In-N compared to Ga-N, Ga completely displaces In in competing for incorporation. This behavior is consistent with the decreasing In content when $\frac{\Phi_{Ga}}{\Phi_N}$ ratios increases towards fluxes stoichiometry [83,122] ($\Phi_{Ga} + \Phi_{In} \sim \Phi_N$), and can explain the In content decrease observed for Φ_{Ga}>0.30 nm/min. For the upper Φ_{Ga} value considered (Φ_{Ga}=0.60 nm/min), the In incorporation rate is too low compared to the In arrival rate. Hence, In accumulation starts to take place, as inferred from the inverse tapering of some InGaN morphologies (Fig. 2.20(d)). By contrast, for Φ_{Ga}<0.30 nm/min, the opposite dependency is observed. The In incorporation rate and the In content *increase* with the Ga flux, suggesting a stabilizing effect of Ga on In-N bonds formation.

A similar phenomenon has been reported by Turski et al. for planar M-polar InGaN layers [123]. The authors theoretically demonstrated that, in the limit of really low Ga fluxes ($\Phi_{Ga} < 1\ nm/min$), the Ga adatoms have a certain ability to hinder the In-N bonds decomposition at InGaN atomic step kinks. As depicted in Figure 2.21, such kinetic effect increases with the attachment rate of Ga but is somewhat self-limiting, resulting in a maximum of In content (similarly to our case) before disclosure of its usual decreasing behavior.

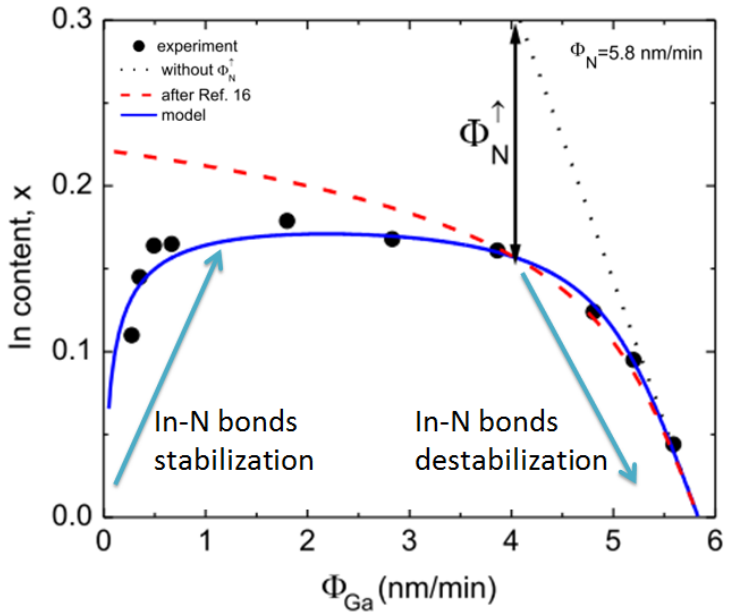

Figure 2.21 In content as function of Ga flux (In-adlayer conditions) for planar Ga-polar InGaN growth by PA-MBE; adapted from Turski et al.[123].

Given the fact that the NW top surfaces are N-polar, we cannot speculate if this atomic-scale mechanism may apply to our case as well. However, the results depicted in Figure 2.21 clearly show that the impact of the Ga flux on the heterostructure composition and morphology should be thoroughly considered in the aim of a good control of InGaN heterostructures growth rate and composition. For instance, it also indicates that as far as In-excess (adlayer) conditions are concerned, a precise calibration of the Ga (an N) fluxes with RHEED oscillations is sufficient to assure reproducibility.

2.6 Growth mechanism of InGaN NW heterostructures

As observed in the previous sections, the morphology and core shell structuration of the InGaN insertions is essentially controlled by the *relative abundance* of In at the NW growth front. Hence, locally N-rich and In-adlayer conditions lead respectively to the formation of island-like and disk-like sections. We also saw that whatever the morphology, a spontaneous phase separation between an In-rich core and Ga-rich shell is systematically observed. This spontaneous core-shell feature seems common to all III-N alloys grown in NW form, since it has been reported for InGaN[90,124,125], AlGaN[126] and AlInN[127] NWs. The outer phase substantially richer in the element of lower surface diffusivity (Ga for InGaN and Al for AlGaN and AlInN respectively). Thus, the formation of the shell is often assigned to a the radial growth of the structure, where the Ga adatoms which are not able to reach the top-plane growth front, incorporate radially. However, if this simple mechanism could account for a natural InGaN/GaN core–shell structures in disk-like sections, it is doesn't seem sufficient to explain the much thicker shell observed for tapered geometries, whose volume is ~3 times higher for an identical growth time and Ga flux. In fact, here, the formation of an In-rich core much narrow than the underlying NW, rather suggests the presence of a driving force for the segregation of the alloy during the heterostructure growth. In this section, we discuss the origin of this segregation, and the underlying mechanism governing the island-like to disk-like morphological transition.

2.6.1 Island-like sections

Recent studies demonstrated that the In radial distribution in InGaN NW axial heterostructures can be significantly affected by the presence of compressive strain [88,125,128]. In fact, single InGaN quantum dots (QDs) spanning the whole GaN NW diameter are rarely reported in the literature, while a progressive widening of these thin insertions accompanied by a decrease of their thickness and/or In-enrichment, can be observed when these are subsequently stacked between thin GaN barriers[88,125,129]. Bartolome et al[125] have shown that for InGaN heterostructures, this phenomenon can be univocally explained by the vertical strain interaction between QDs. Each QD reaches an equilibrium shape that minimizes the overall energy of the system, given by the sum of the surface and elastic energies of the QD itself and the barrier below. This gives rise to a cumulative process, which leads to a QD aspect ratio smaller in comparison with the one grown just before. Compatible results were obtained also for similar AlGaN/GaN NW architectures[130], as well as for vertically correlated stacks of GaN/AlN QDs on planar GaN substrates[131].

According to atomistic-strain-model Monte Carlo simulations of layer-by-layer epitaxial growth of InGaN islands on the whole NW top facet [132], the most efficient strain relaxation should occurring by concentrating the element of higher lattice parameter at the borders of the structure. However, this is opposite of what is observed experimentally, where the element of highest atomic number concentrates in the core. Thus, it is usually suggested that island-like core-shell morphologies result from two parallel processes: a strain-driven growth of a narrow InGaN island at the center of the NW top-plane, and a parallel radial capping in the subsequent stages of growth, by the "filling" of the remaining lateral free space at the island periphery.

The core-shell compositional distribution could then result from a preferential strain-driven incorporation of In on the top of the island, where lattice parameter is maximum[90]. Also, it could be explained by the typically inefficient In incorporation on high index planes, which would rapidly develop at the island sides to constitute its lateral facets. Concerning this last point, it has been established that the strong anisotropy of the GaN crystal facets' surface energy per unit area (γ) favors the In incorporation on polar over semipolar and nonpolar crystal directions[120,133].

A compatible growth scenario for axial heterostructures grown with a vapour-solid approach, has been proposed originally by Glas and Daudin[128]. Specifically, the authors investigated the propensity of a coherent heterostructure to adopt either the shape of a disk as wide as the NW, or of a narrower island at the center of the NW top plane. The purely thermodynamic model described the competition between strain relaxation (which favors islanding) and deposit sidewall energy (which favors disk morphologies), as function of lattice mismatch, NW radius and deposit volume. The main result predicts that, in a wide range of lattice mismatches and NW radii, the island morphology provides a substantial reduction of the total energy of the system (up to 55%) compared to a disk of the same volume. This is shown in Figure 2.22, where the colored surfaces depict the total energy ratio between the optimal InGaN island and a disk of the same volume.

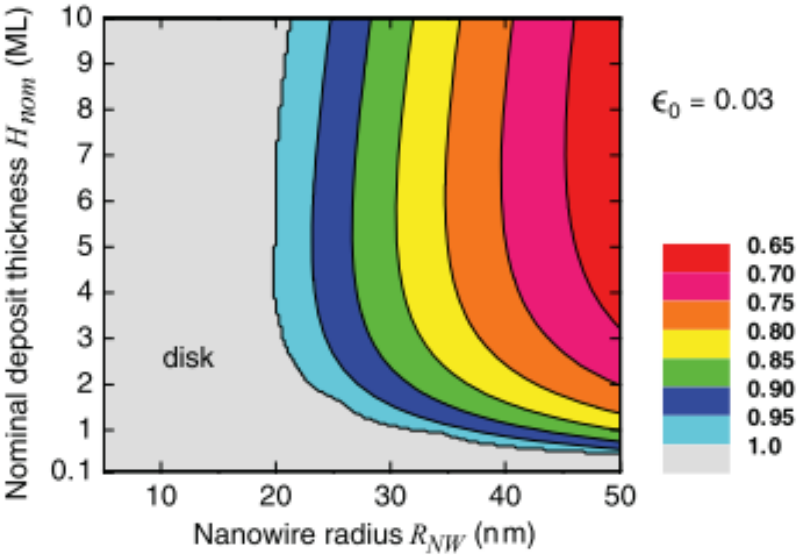

Figure 2.22 Ratio (color line) of the minimum energy of the system (with its optimal island radius) to its energy in the disk configuration, as a function of NW radius and nominal deposit thickness (in monolayers of 0.27 nm). The lattice mismatch between the misfitted deposit and the underlying NW is 3%[128].

The model designates that for a given deposit thickness and lattice mismatch, the optimal shape of the deposit depends on the NW radius. In particular, it states the existence of a critical NW radius, under which a disk morphology should be always favored, and above which the island should become increasingly narrow. This behavior is depicted in Figure 2.23(a), where the ratio between the deposit radius r_c and the

NW radius r_{NW} is plotted as function of r_{NW} for a lattice mismatch of 3% and different deposit thicknesses.

We thus compared the experimental r_c/r_{NW} values, with the ones predicted by the model. Being the shell thickness negligible at the island top (1-2 nm), and the In-rich core sidewalls quasi-vertical, the r_c/r_{NW} parameter has been derived by measuring ratio between the NW tip and GaN NW diameter. This was done on SEM images of ~50 dispersed NWs. The results are plotted in Figure 2.23(b) as function of the GaN NW radius.

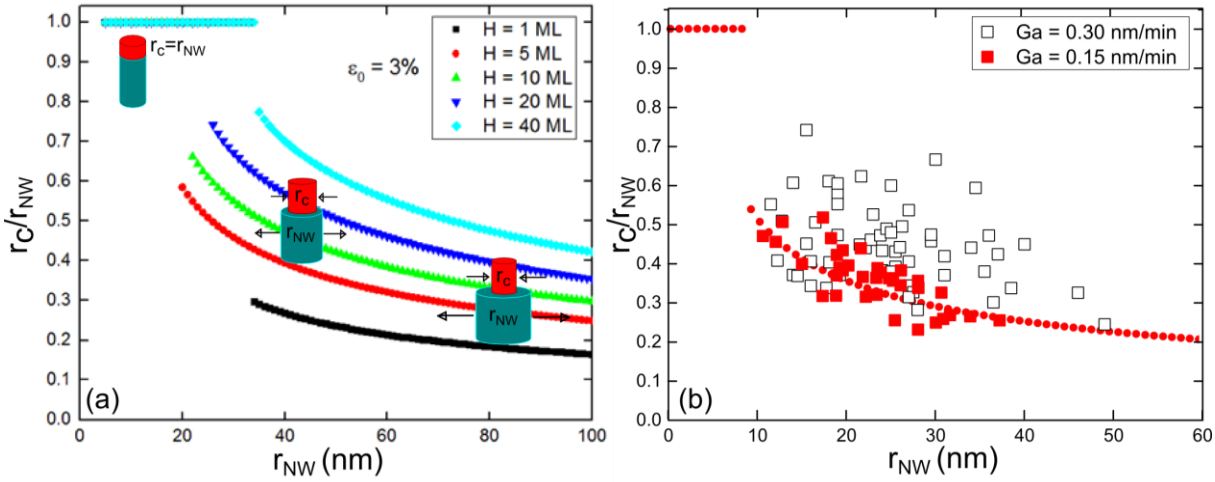

Figure 2.23 (a) Evolution of the optimal (calculated) r_c/r_{NW} ratio as function of r_{NW} for a heterostructure deposited on a nominally infinite NW with 3% lattice mismatch. The calculations have been performed for different deposit volumes, expressed in 0.27 nm thick ML units. (b) Evolution of the measured r_c/r_{NW} ratio as function of r_{NW} for island-like heterostructures grown under locally N-rich conditions, with a In/Ga ratio of 1 and different absolute Ga (and In) fluxes. Dotted line corresponds to best fit with the model.

The data corresponding to thicker InGaN sections (Φ_{Ga}=0.30 nm/min, empty black squares in the figure) are quite scattered, while for the shorter insertions (Φ_{Ga}=0.15 nm/min, red squares) they are more consistent. The experimental points of both samples show a similar decreasing behavior of r_c/r_{NW} with r_{NW}. By contrast, no critical radius is observed experimentally. By considering a lattice mismatch compatible with their average In content (2.5%), the experimental red points are better fitted by considering a sidewall surface energy equal to 0.65 Jm^{-2}. It must be pointed out, however, that the model described here is quite simple to allow a quantitative comparison. This is mostly because it considers the same Young's modulus and Poisson's ratio for the NW base and the deposit, while InN presents

quite different elastic constants compared to GaN (as seen in section 1.2.3). Nevertheless, the substantial reduction of the total energy of the system predicted for islanding (up to 55%) and the qualitative agreement in the dependency of the island width on the NW radius, strongly supports the idea that the narrow InGaN cores observed in tapered structures results from a strain-induced 3D growth mode.

2.6.2 Island-to-disk transition

With only the two abovementioned ingredients (strain and sidewall energy), the model of Frank and Daudin[128] predicts that, at fixed NW radius, larger deposit misfits would *increase* the tendency to form a coherent narrow island. However, experimentally, we clearly observe the opposite: the widening of the InGaN core as the In content increases in locally N-rich conditions, and the systematic observation of disk-like InGaN sections in In-adlayer conditions, where the In content has reached its maximum.

In the SK growth of InGaN and InN QDs on planar GaN substrates, the decrease of the height/diameter aspect ratio for increasing metal-to-nitrogen ratios and/or deposited volumes is usually attributed to a gradual transition to a uncoherent SK growth mode, where residual strain is relaxed by the formation of dislocations[61,134]. However, in our case, the island-to-disk transition observed from N-rich to In-adlayer conditions, can be hardly justified by a more efficient strain relaxation, since no dislocations were observed in the two types of structures. This indicates that other factors must be taken into account to explain the observed morphology transition.

As briefly mentioned before, metallic adsorbed layers modify the heterostructure growth mode by playing the role of surfactants. In 2D layers growth, two main mechanisms are usually reported. The first is kinetic, and related to the surface diffusivity of N adatoms. Neugebauer and co-workers[98] theoretically predicted that on a bare GaN (0001) surface, the barrier for nitrogen diffusion is of 1.3 eV, while the barrier along a path passing *underneath* an In adatom is reduced to 0.5 eV. This allowed concluding that the rough-to-smooth morphology transition observed among stabilization of metallic adlayers on the growth surface, results from an adlayer enhanced lateral diffusion (AELD) of N adatoms. The second mechanism is related to the energetics of 2D/3D transitions. Gogneau et al.[113,135] demonstrated that as soon as

a Ga layer is self-regulated at the surface (bi-layer for GaN(0001) and mono-layer for bare GaN(000-1)[135]), the SK transition of GaN on AlN substrate is inhibited, even after a N flux interruption. For instance, only when the Ga flux is interrupted and the Ga layer is completely desorbed, a rapid transition from streaky to spotty RHEED pattern is observed[113]. This experimental fact was explained by the reduced surface energy in presence of the Ga layer[97,136].

Based on these considerations, we suggest that, similarly to what is observed for the growth of mismatched III-N layers on planar substrate, the In-adlayer acts as auto-surfactant, by inhibiting strain driven islanding and by allowing a layer-by-layer growth of disk-shaped insertions. In particular, due to the ineffective AELD on N-polar surfaces[98], we argue that the adlayer may favor a disk morphology by decreasing the (000-1) plane surface energy.

Therefore, to understand the shift between a relatively narrow core (Regime I) and a wide one (Regime II), we consider the complex interplay of strain and surface energy, both depending on the In flux: the former via the deposit composition, the latter via the In adlayer. To this end, we use the previously mentioned model of Glas and Daudin [128] where, in addition to strain and sidewall energy, we also consider that the top surface energy of the InGaN deposit is reduced from that of the GaN stem by a certain amount $\Delta\gamma$. At this stage, we ignore the precise value of this quantity (which probably depends on growth conditions). A further complication arises from the variation of the In content in the first 20 nm of InGaN and the strain field modification that ensues. At the moment, our model assumes a fixed deposit misfit, ignoring this effect.

To test our explanation, we thus computed the ranges of favored islanding (in terms of nominal amount of full InGaN MLs deposited) as a function of $\Delta\gamma$, for several values of misfit. The materials were taken as elastically isotropic with a Poisson ratio of 0.33 and a Young's modulus of 324 GPa [128]. The results are summarized in Figure 2.24 for a NW stem radius of 25 nm, representative of our experimental conditions.

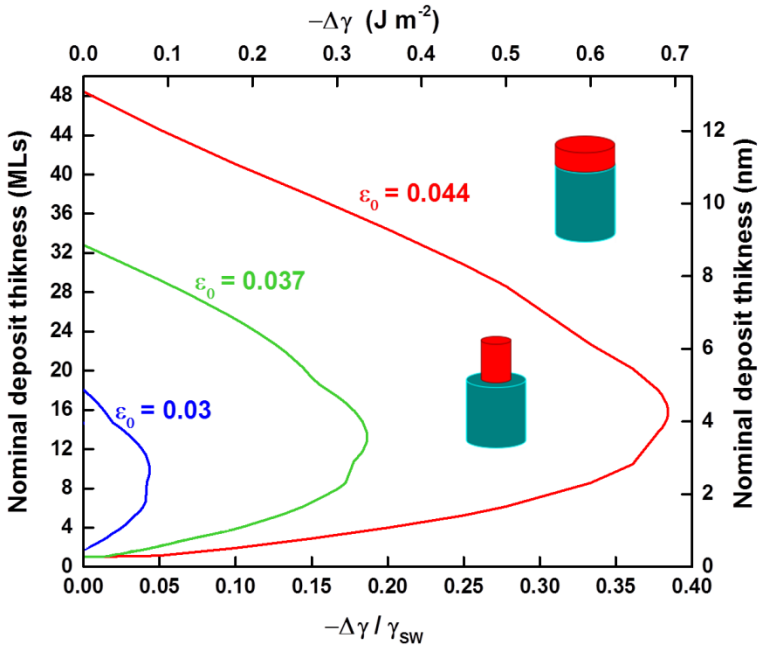

Figure 2.24 Calculation of the range of nominal thickness of an InGaN deposit (expected to form an island narrower than the GaN nanowire stem) as a function of the difference $\Delta\gamma < 0$ of surface energy between the top of the deposit and that of GaN. Nominal deposit thickness is expressed in terms of disk thickness in MLs. Each line curve (relative to the deposit misfit indicated) separates the domain of preference for disk (outside) and island (inside), as schematized for $\varepsilon_0 = 0.044$. The top scale gives the absolute value of $-\Delta\gamma$, the bottom one gives its value as a fraction of the sidewall energy of the deposit (here, 1.8 Jm−2).

For each of the three misfits considered, the island morphology has only a limited domain of existence (we recall that, among all the possible island configurations for a given deposit volume, we find the one with lowest energy[128]). For a given relative misfit ε_0, the range for islanding narrows when $|\Delta\gamma|$ increases and finally vanishes. However, this range is very sensitive to misfit. For the higher misfit considered (ε_0 = 4.4%, corresponding to one of the stabilized InGaN compositions in Regime II), the range for islanding is still broad whatever $|\Delta\gamma|$, whereas for $\varepsilon_0 \sim 3\%$ it vanishes even for low positive values of $\Delta\gamma$. Anyway, the highest misfits considered here might never be reached in practice. In fact, what matters is the misfit of the new InGaN MLs relative to the stem on which they are deposited, which for the upper InGaN MLs (~40% In stabilized composition) is not GaN anymore but a partially or totally relaxed InGaN. Furthermore, by considering that due to the lattice pulling effect, the In composition is substantially lower in the vicinity of the heterointerface, i.e. where misfit strain should be higher, and that the In-adlayer surfactant effect must be active

from the first stages of growth, a small decrease of the top-surface energy might be indeed sufficient to inhibit islanding.

2.6.3 InGaN NW growth diagram explained

The ensemble of our experimental results and theoretical predictions brings support to our explanation, which may be summarized as follows.

In Regime I, the growth occurs under locally N-rich conditions. Since there is no complete In-adlayer formed at the NW top-facet, the surface energy of the deposit is not reduced and InGaN islands tend to form even at relatively low misfit. This view is in agreement with the model developed by Glas and Daudin [128]. The In-poor shell may form subsequently by a preferential incorporation of Ga at the periphery/sidewalls of the growing island, possibly related to strain or to the low incorporation of Indium on high index facets [137]. Due to the In-limited growth conditions, both the In content and the average heterostructure growth rate increase with the In flux, if the Ga supply is kept constant (Figs. 2.15 and 2.17).

By contrast in Regime II, the growth occurs under locally In-rich conditions, with the formation of a complete In adlayer at the NW growth front. The surface energy of the top of the deposit is thus reduced, inhibiting 3D growth and favoring a disk morphology, even at higher misfits. Again, the very thin In-poor shell may be formed via a preferential sidewall incorporation of Ga. Since the In surface coverage is self-regulated, the growth conditions are limited mostly by the Ga supply, and both the In incorporation (Fig. 2.15) and average growth rate (Fig. 2.17) do not change within a significant range of In fluxes.

Finally, in Regime III, the In impinging flux is sufficiently high to overcome the energetic barrier for In accumulation at the NW growth front, a condition which can be defined as *highly* In-rich. As proposed by Zhang et al. [95], this excess of metallic In may enhance N adatom diffusivity, causing a reduction in the N availability at the NW top facet. Therefore, the growth could in proceed through N incorporation at the boundaries of the metallic layer, resulting in the lateral expansion of the NW structure with little addition on the vertical direction. This explanation correlates well with the reduced In incorporation and vertical growth observed under large In/Ga_{BEP} [95].

Conclusions

In the present chapter, I have systematically investigated the growth of InGaN NW axial heterostructures by PA-MBE. Detailed compositional and structural investigations have been carried out, and a comprehensive flux-dependent diagram allowing rationalizing the different InGaN NW morphologies reported in the literature has been built. In the specific, I have experimentally and theoretically demonstrated that the InGaN deposited on top of GaN NWs may follow distinct growth modes and thus adopt markedly different morphologies depending on the relative abundance of In at the NW growth front. In summary, low In/Ga flux ratios establishing locally N-rich conditions, lead to strain-driven InGaN islanding at the center of the NW top plane. The parallel growth of a Ga-rich non-uniform shell around the narrow InGaN core results in a tapered outer morphology. On the contrary, intermediate In/Ga flux ratios allowing the formation of a stable In adsorbed layer at the NW growth front (locally In-rich conditions), promote the growth of untapered sections. In this case, a disk-like insertion fitting almost the entire NW diameter is surrounded by a thin uniform shell. In agreement with theoretical predictions, the island-to-disk transition is assigned to the surfactant effect of the In adsorbed layer, which inhibits strain-driven islanding even at high lattice mismatches by lowering the surface energy of the InGaN deposit. Finally, I have shown that high In/Ga flux ratios trigger a pronounced radial overgrowth or morphological deterioration of the InGaN sections (highly metal-rich conditions). The effects of metal fluxes and strain pulling on the In incorporation are discussed. All these results allowed me to identify the best growth conditions to fabricate In-rich (x_{In}~0.40), highly homogeneous InGaN sections presenting abrupt interfaces and a disk-like morphology.

As in the growth of planar InGaN layers, the three observed growth regimes are expected to exist also at different growth temperatures, offering the possibility to select the specific heterostructure morphology even for different alloy compositions, and thus to be relevant in view of a full control-by-design of their basic properties.

Credits

All the Scanning transmission electron microscopy (STEM) images and the X-ray Diffraction spectra shown in this chapter have been acquired by Ludovic Largeau from C2N. The thermodynamic model and related simulations have been developed and performed by Frank Glas (C2N).

Chapter 3

Optical characterization of InGaN/GaN NWs

In chapter 2, I evidenced the existence of non-negligible compositional variations from NW to NW, as well as within single NWs (gradient). Also, depending on their In content, the strain relaxation was observed to occur elastically or plastically. This aspect stems from the fact that these heterostructures are highly lattice mismatched, but it is also related to their combined axial and core-shell geometry. All these aspects must influence the optical properties of the InGaN sections, and their study can provide further insights on their structural, compositional and electronic properties. In this chapter I made use of different optical characterization techniques to investigate the luminescence properties of InGaN/GaN NWs, from the macro-scale of as-grown NW arrays to nanoscale of single heterostructures.

3.1 Samples and methods

In this section I describe the samples studied in this chapter. I also provide a brief introduction on the optical characterization techniques that have been used, as well as some details on the simulation of the InGaN NW heterostructures band profile.

Samples

The samples analyzed in the present chapter are the following:

- ~1 um long GaN NWs presenting a single InGaN insertion at their top and described in the previous chapter (synthesized on Si/AlN substrates). Specifically, the InGaN sections were grown with the same nominal Ga flux (0.30 ML/s) and with In/Ga flux ratios equal to 1 (island-like, #C016), 1.5 (island-like, #C028), 2 (disk-like, #C017) and 3 (disk-like, #C041) (Fig. 3.1). This resulted in an average In core composition ranging from about 20% to about 40%, and in an average insertion thickness ranging from ~30 to ~60 nm. Their emission wavelength and room temperature PL efficiency is discussed in section 3.2, in relation with their structural and compositional properties.

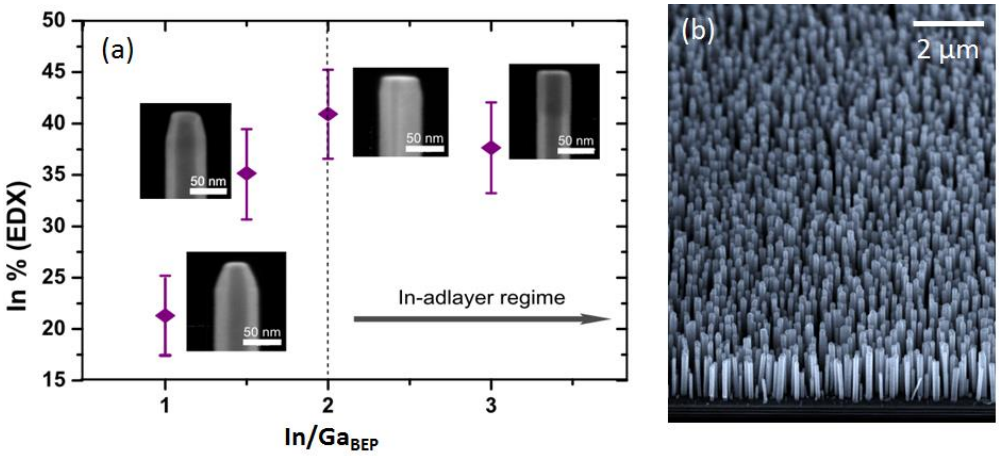

Figure 3.1 (a) Average InGaN core composition as a function of the In/Ga flux conditions. The SEM insets evidence the morphology of the InGaN section. (b) 45° tilted view of the InGaN/GaN NW sample grown under In-adlayer conditions (In/Ga_{BEP}=3).

- One sample of "capped" InGaN/GaN NWs on Si/AlN substrate (#H004). The growth conditions of this sample were from all points of view identical to the

In-rich uncapped samples grown under In-adlayer conditions (In/Ga ratio of 3). Thus, they presented ~60 nm thick disk-like insertions with a nominal In fraction of about 0.40. Additionally, a 20 nm GaN capping layer was grown for 20 minutes at 650 °C (N/Ga ratio of 25). This low growth temperature was chosen to preserve abrupt InGaN/GaN interfaces. Figure 3.2 shows a cross-sectional SEM image of this sample, together with its STEM-HAADF and EDX mapping characterization.

This sample was characterized by temperature-dependent and power-dependent macro-PL, time-resolved u-PL on NW ensembles and cathodoluminescence on single NWs (section 3.3).

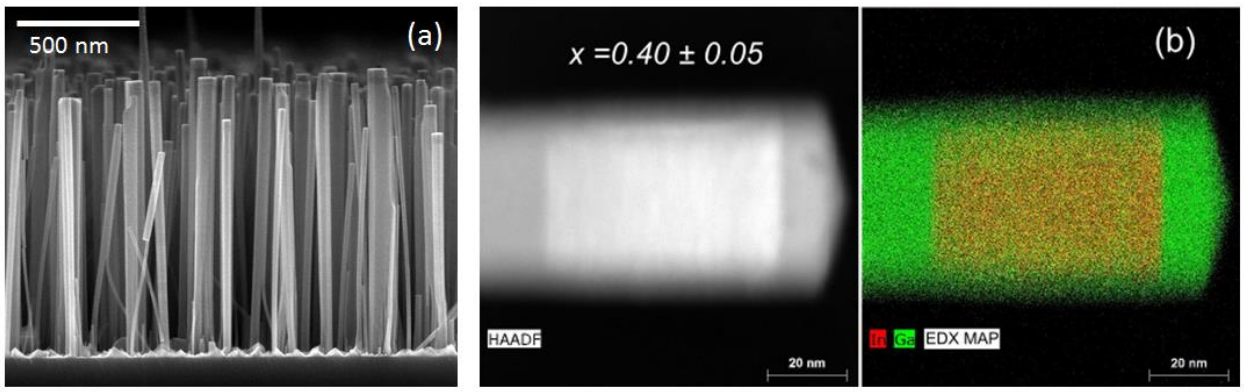

Figure 3.2 (a) Cross-section SEM view of the InGaN/GaN "capped" NW array. (b) STEM-HAADF (left) and related In and Ga EDX mappings (right) of a representative InGaN/GaN capped NW.

Steady-state photoluminescence

Time-integrated photoluminescence is a relatively simple and widely used technique which allows to probe the lower states of the electronic potential landscape of a material. The technique consists in generating electron-hole (e-h) pairs through a laser excitation and to measure their radiative desexcitation. Different parameters can be varied (sample temperature, excitation wavelength, laser power…) to give different and complementary information. In this work, the optical properties of InGaN/GaN NWs have been characterized by micro-photoluminescence (µ-PL, laser focused on 1 µm diameter spot), and macro-photoluminescence (macro-PL , ~100 µm spot diameter).

The systems were analyzed at 300 K and lower temperatures (down to 5 K) in a continuous He flux cryostat. The excitation was provided by a continuous Ar_2^{++} laser source at different wavelengths: 244 nm (µ-PL), 405 or 375 nm (macro-PL). Generally,

a nominal incident power density of 1 W/cm^2 was used for both µ- and macro-PL experiments. This value was the lowest excitation power allowing to measure some signal from the InGaN sections at 300 K, and is much lower than the one needed to induce significant band-filling effects and related spectral shifts in InGaN alloys (several hundreds of W/cm^2)[138]. The generated PL signal was dispersed by a 600 grooves/mm (500 nm peak efficiency) grating, for optimal acquisition of the InGaN PL signal. The luminescence was collected by a LN2-cooled silicon charge-coupled device (CCD).

Time-resolved PL

In this technique, the e-h pairs are generated by a short laser pulse. The spectral *and* temporal evolution of the emission is recorded by an ultra-high-speed detector, which captures light emission phenomena occurring in extremely short time periods (streak camera detector). Thus, the measurement of the optical spectrum as a function of time provides a means to measure the transition energies *and* their lifetimes, giving insight into the material's recombination dynamics.

A frequency-doubled Ti-sapphire laser (375 nm, FWHM = 2 nm, repetition rate = 4 MHz) provided the optical excitation through a macro lens with a long working distance (200 mm, resulting in a spot size of about 100 µm diameter). A closed-cycle cryostat (Montana instruments, Cryostation) allowed for controlling the sample temperature within the 20-300 K range. The emitted signal was dispersed on a spectrometer grating with 600 grooves/mm. A streak camera (Hamamatsu, C7700-01) with temporal resolution of around 8 ps was used for studying the dynamics of the PL emission.

Cathodoluminescence

The basic principle of Cathodoluminescence (CL) is somehow analogous to the one of PL, with the main difference that the high energy e-h are generated by means of an electron beam in a SEM set-up. Thanks to the SEM beam focusing, CL has the supplementary ability to probe the optical activity of the specimen with a good spatial resolution and construct a luminescence map when the electron beam is scanned the sample surface. Furthermore, CL allows a much higher excitation efficiency compared

to PL, since one single electron generates in average 100 e-h pairs along with its multiple inelastic scattering processes in the material.

In this chapter we made use of CL to investigate the optical response of single (capped) InGaN/GaN NWs dispersed on a Si/SiO_2 substrate. The experiments were carried out between 5 and 300 K sample temperature, with a continuum electron beam excitation of 6 kV acceleration voltage and a beam current of 2 nA. The CL signals were dispersed by a 600 grooves/mm and 1800 grooves/mm gratings for optimal acquisition of the InGaN and GaN signals respectively. These were collected by a LN2-cooled silicon charge-coupled device (CCD).

To estimate the expected resolution for our experimental conditions, Fig 3.3(a) displays Monte-Carlo simulations of the electrons paths in a simplified structure consisting of a 2D GaN layer having a thickness equal to the NW diameter (50 nm) on a Si substrate. It is seen from the calculated trajectories, that the CL resolution can be compromised by a parasite e-h excitation by electrons which are back-scattered from the underlying Si substrate (red lines in Fig. 3.3(a)). Therefore, we conclude that for non-suspended nanostructures a further increase of the acceleration voltage would degrade the spatial resolution. For the chosen conditions, 70% of the CL signal is generated within a ±10 nm region from the beam position (Fig. 3.3(b)), so one can expect from the beam-matter interaction calculations a resolution close to 20 nm[i].

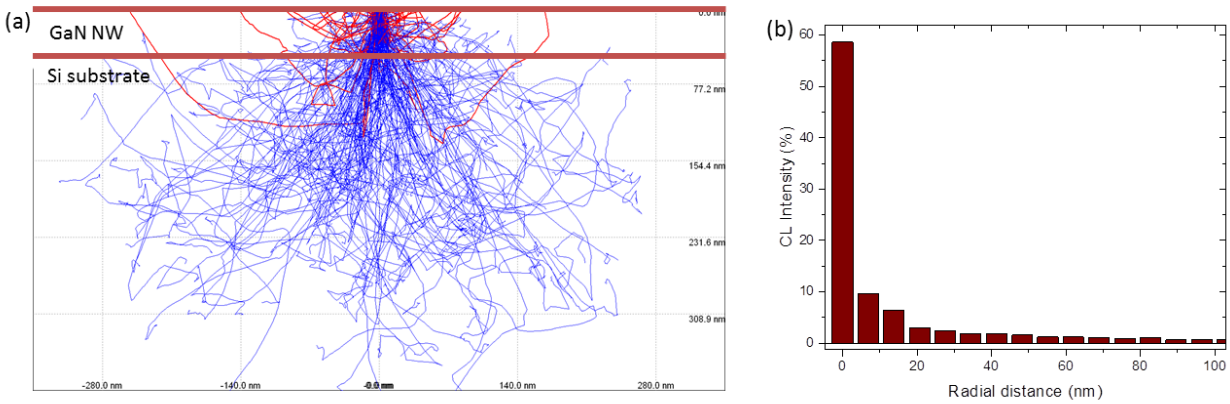

Figure 3.3 (a) Electron path within a 2D structure constituted of 50 nm of GaN on a bulk Si substrate; blue lines correspond to electrons that are "lost" in the material, red lines to back-scattered electrons. (b) Histogram showing the CL radial intensity (electron beam corresponds to a zero position).

[i] We note that the effective resolution can be worse since in these considerations we only consider the interaction volume and we neglect the carrier diffusion before radiative recombination.

Simulation of the InGaN/GaN NW band edge profile

To interpret the optical properties of the NWs, we need to know the potential landscape inside the InGaN insertion. The band edge profile along the axis of a capped InGaN/GaN NW heterostructure has been calculated in 2 steps using the following procedure. Firstly, the strain state of an InGaN/GaN NW (sketched in Fig. 3.4) has been assessed using experimentally-measured composition values as an input parameter. The heterostructure was taken as 60 nm thick, embedded in a 25 nm radius GaN NW (of hexagonal cross section) and radially encapsulated by a 2 nm thick GaN shell. To be consistent with the results of our EDX-STEM analysis, the InGaN composition was taken as radially homogeneous, while the axial compositional gradient was considered by means of a fit function of the experimental profile (black line in Figure 3.4). Note that in this way, local In fluctuations were neglected.

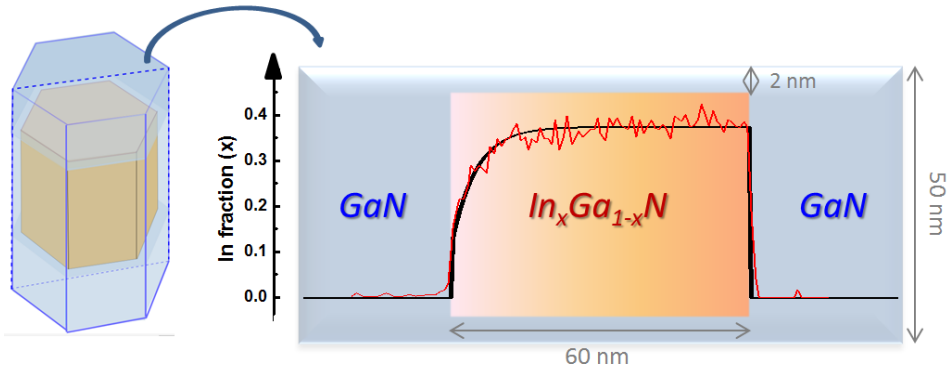

Figure 3.4 Slice of the simulated InGaN/GaN NW. Its geometrical parameters and compositional profile are shown (red line is the experimental *core* composition, black line is the smoothed profile considered in the simulation).

The numerical simulation was performed in the framework of the continuum elasticity theory, by minimizing the elastic energy of the system within a finite element approach (Comsol Multiphysics software). In each point of the InGaN insertion, the elastic constants have been calculated as a linear interpolation of binary's ones, by considering the local In fraction.

Then, the calculated strain tensors along the InGaN/GaN NW rotational axis have been used as input parameters to compute the gamma point conduction and valence band profiles along the [000-1] crystallographic direction (1D simulation). This has been done with the commercial Nextnano software, which solved self-consistently the

Poisson and Schrödinger equations within the effective mass approximation. Except from the strain-free InGaN band-gap and the spontaneous polarization, which were derived through the corresponding bowing equations (see section 1.2.5), all the InGaN parameters used for the calculations (such as band discontinuities and piezoelectric potential) have been derived from linear interpolation of the InN and GaN ones[15,16], by considering the fitted compositional profile.

3.2 General aspects of InGaN/GaN NWs PL

3.2.1 Micro-PL from single NWs and NW arrays

As a first step, the optical properties of the InGaN/GaN NWs have been investigated by means of non-resonant (244 nm) μ-PL. This was done on both as-grown arrays and on 10 single InGaN/GaN NWs. In this latter case, the NWs were cut by sonication in iso-propanol and dispersed with a very low density on a lithographically marked Si/SiO_2 substrate; during the measurements, the NWs were identified on the camera image by their bright luminescence when irradiated by the laser (Figure 3.5(c)).
Figure 3.5 shows a μ-PL spectra acquired at 5 K on a NW array (a,b) and on one single NW (d,e) from a representative InGaN/GaN NWs ensemble (capped sample #H004). In the following, the GaN and InGaN luminescence will be discussed.

GaN near band edge luminescence

The near band edge (NBE) PL generated by the GaN bases was in general much more intense than the InGaN-related signal. As evidenced in Figures 3.5 (b) and (d), the NBE was dominated by the Si and/or O bound excitons recombination (D_0,X_A) peaked at ~3.47 eV, together with a broader emission peak at 3.45 eV, which is systematically present in our samples. This PL signature has been associated for a long time to the two-electron-satellite effect, but the recent in-depth analyses from T. Auzelle et al.[139] and Pfüller et al.[140] have unambiguously associated it to the excitons bound to inversion domain boundaries (IDBs).

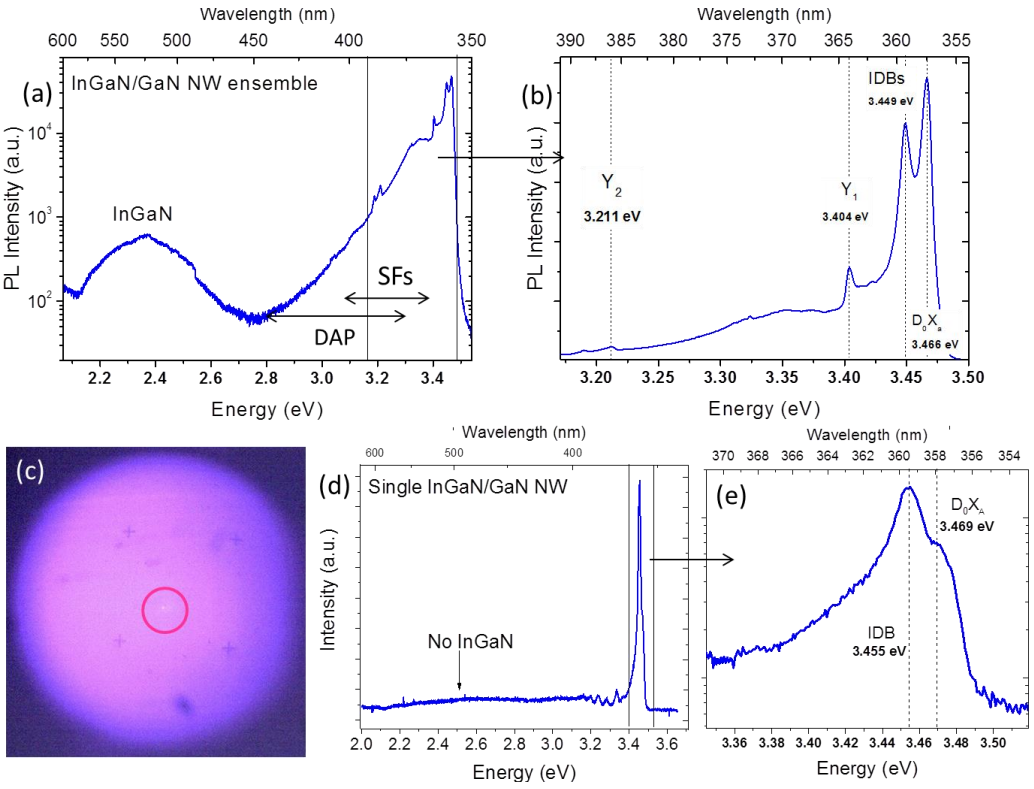

Figure 3.5 μ-PL spectra of the capped InGaN/GaN NW array (a) and of a single NW (d) with their respective GaN BE PL insets (b and e respectively). (c) Camera view of a bright InGaN/GaN NW.

The IDBs are interfaces between two GaN domains of opposite polarities which form spontaneously in GaN NWs grown on Si[139,141], and present a core-shell geometry which extends all over their length. Consistently, our STEM analysis (Fig. 3.6(a)) showed that some NWs presented the characteristic pipe-like contrast, which indicates the presence of a core of inverted (Ga-) polarity[139] embedded inside the N-polar NW body (sketched in Fig. 3.6(b)). In the limits of our statistical analysis, from one sample to another 10 to 30% of the NWs showed this characteristic, while other authors reported values as high as 50%[139]. In fact, the formation of such type of defects is at present far from being controlled or understood and may be related with the NW nucleation kinetics.

The PL on NW arrays evidenced other defect-related features. For instance, a broad band extending from the GaN NBE up to ~2.8 eV is observed (Fig. 3.5(a)). This spectral region corresponds to the one of stacking-fault-related emissions (3.15-3.42 eVs)[17], and partially overlaps with the region of donor-acceptor-pair transitions (DAP, 2.8-3.3 eV)[18]. More clearly separated emission lines appear at 3.403 eV (Y_1) and 3.211

eV (Y_2) (Fig. 3.5(b)). The first could be assigned to stacking faults of ~2ML thickness[17], while the second has been tentatively associated to excitons bound to NW basal defects (stacking-faults/dislocations) which form at the coalescence joints of the NWs[142].

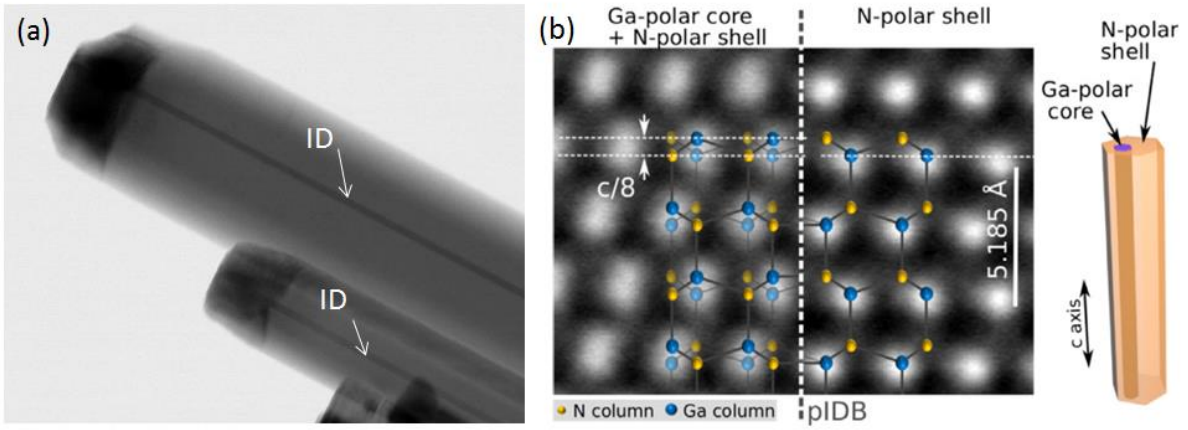

Figure 3.6 (a) Dark-field STEM image of two island-like InGaN insertion in GaN NWs hosting an inversion domain. (b) HR-HAADF-STEM images with ball-and-stick representation of an inversion domain boundary and sketch of its typical geometry in the NW (adapted from Auzelle et al.[139]).

InGaN luminescence

A general feature of all the InGaN/GaN systems analyzed in the presence work, is a rather weak InGaN emission. In fact, the PL signal had a rather low intensity for NW arrays (Fig. 3.5(a)). Also, despite many attempts on a large number of single wires, set-up optimization and the use of long integration times, we were not able to measure any InGaN PL from single NWs (Fig. 3.5(d)). This indicates that the PL signal generated by these thick In-rich insertions was too low to be detected by our experimental set-up, an aspect for which we do not have a straightforward interpretation. Possibly, the use of a 244 nm excitation is not well suited to study InGaN, since we have a strong absorption in the GaN stem and low In-content shell, and for some unclear reason the carriers from the barriers cannot be efficiently transferred to the insertion. However, another possible reason could be related to a strong polarization field within the structure, which separetes e-h pairs and decreases the recombination efficiency. The possible origins of this low PL intensity will be discussed later in the chapter. For the further analysis, we investigated the InGaN PL with resonant excitation wavelength, i.e. by using a laser below the GaN band-gap.

3.2.2 Effect of the In/Ga flux ratio on the PL peak position and efficiency

Macro-photoluminescence measurements were carried out on the uncapped InGaN/GaN NWs ensembles by using an excitation wavelength of 405 nm. This wavelength has been chosen to selectively excite the InGaN insertions without exciting the GaN stems and Ga-rich shells. Indeed, the energy of its photons corresponds to a band gap of 3.06 eV (equivalent composition of $In_xGa_{1-x}N$ is x~0.10). Figure 3.7(a) shows the spectra acquired at a cryogenic temperature for samples grown with increasing In/Ga ratio. Generally, the signals were very broad (few hundreds of meV FWHM) and usually exhibited bi-modal shapes. These aspects will be discussed in the next section.

Since the PL experiments with a ~100 μm spot size reflect the optical properties of a large number of nanowires, the PL maximum represents, in practice, the *average* band-gap of the InGaN heterostructures ensemble (E_g^{InGaN}). This can be used to estimate the alloy composition by rearranging the standard bowing equation for InGaN alloys (see section 1.2.5). The In fraction estimated by the PL peak positions is shown in Figure 3.7(c) together with the one measured by EDX statistics at the top of the insertion (before and after shell deconvolution). The two experimental techniques show a fairly good agreement. Especially, for tapered heterostructures (In/Ga<2) they confirm the reasonable accuracy of the shell subtraction procedure, since only if this is applied, the In fraction estimation from the PL peak positions falls within the EDX error bars.

It is generally assumed (although this can be wrong in highly defective samples) that at a cryogenic temperature non-radiative recombination processes can be neglected, while the thermal activation of non-radiative recombination channels causes a quenching of the radiative processes at room temperature. This phenomenon depends mainly on the crystalline quality of the material, i.e. on the density of structural defects and/or impurities.

As shown in Figure 3.7(b) all samples present a measurable signal at room temperature. However, the ratio between the integrated PL intensity at 300 and 10 K (which will be referred to as the "PL IQE") decreases sharply when the In fraction is increased above ~20%. For instance, it decreases from about 17% for tapered sections

grown at In/Ga=1, to about 5% for the tapered/untapered insertions of higher In content (Fig. 3.7(d)). As seen in Chapter 2, the strain relaxation is elastic for tapered sections and plastic for untapered ones, with the formation of cracks which extend within the InGaN volume. However, this phenomenon doesn't seem sufficient to explain the observed decrease in the PL IQE, since it starts dropping before the critical In/Ga flux condition delimiting the sidewall cracking regime (Fig. 3.7(d)).

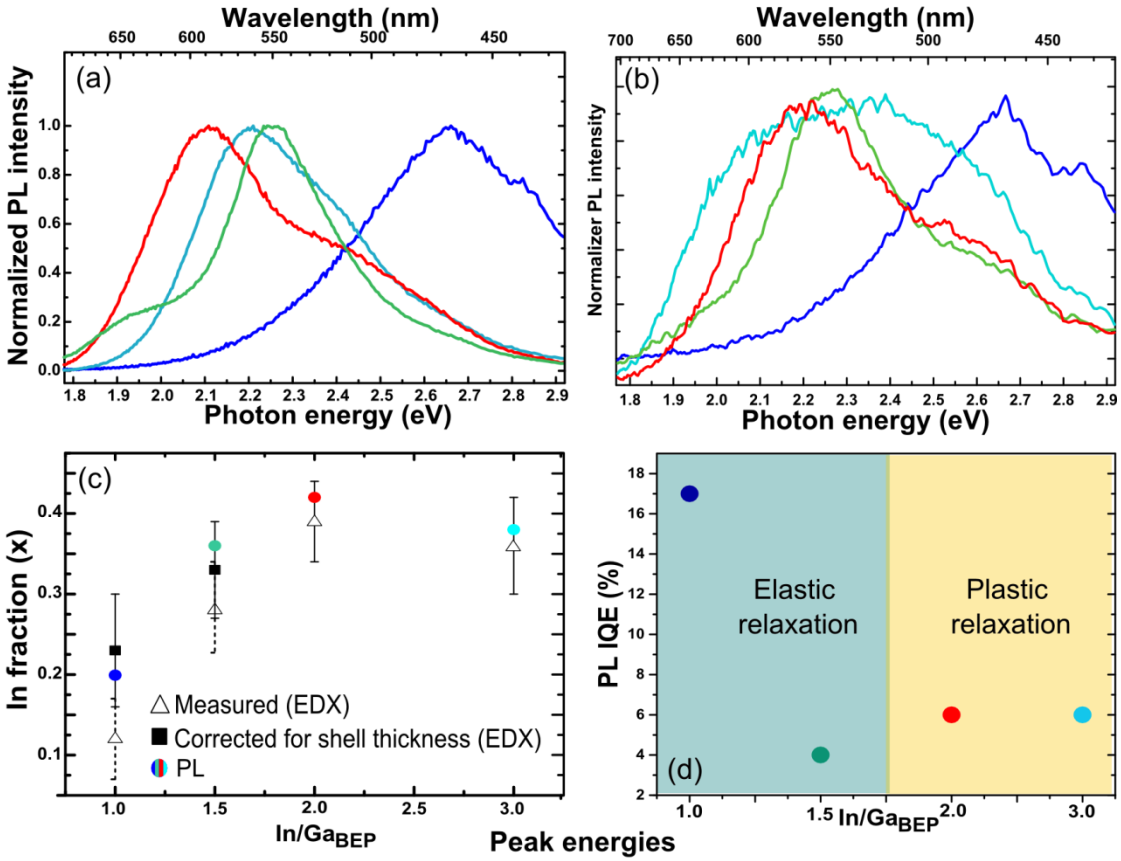

Peak energies

In/Ga	Sample name	4 K (eV)	300 K (eV)
1	#C016	2.65	2.7
1.5	#C028	2.25	2.3
2	#C017	2.2	2.2
3	#C041	2.1	2.3

Figure 3.7 Macro-PL on InGaN/GaN NWs ensembles with different In fractions at 10 K (a) and 300 K (b). (c) In fraction estimated from the PL peak energies and measured by EDX before and after shell subtraction. (d) PL IQE for samples #C016, #C028, #C017, #C041.

It is generally assumed (although this can be wrong in highly defective samples) that at a cryogenic temperature non-radiative recombination processes can be neglected,

while the thermal activation of non-radiative recombination channels causes a quenching of the radiative processes at room temperature. This phenomenon depends mainly on the crystalline quality of the material, i.e. on the density of structural defects and/or impurities.

As shown in Figure 3.7(b), all samples present a measurable signal at room temperature. However, the ratio between the integrated PL intensity at 300 and 10 K (which will be referred to as the "PL IQE") decreases sharply when the In fraction is increased above ~20%. For instance, it decreases from about 17% for tapered sections grown at In/Ga=1, to about 5% for the tapered/untapered insertions of higher In content (Fig. 3.7(d)). As seen in Chapter 2, the strain relaxation is elastic for tapered sections and plastic for untapered ones, with the formation of cracks which extend within the InGaN volume. However, this phenomenon doesn't seem sufficient to explain the observed decrease in the PL IQE, since it starts dropping before the critical In/Ga flux condition delimiting the sidewall cracking regime (Fig. 3.7(d)).

At present stage, it is not simple to give a straightforward interpretation of this phenomenon. One possible explanation could be related to the high surface-to-volume ratio of the NW systems, which results in non-radiative surface recombination[143]. Specifically, it is plausible that surface recombination could become more important as the Ga rich shell becomes thinner (from ~15 nm at the NW base in tapered sections, to ~2 nm for untapered ones). To limit this effect, the overgrowth of a thicker intentional GaN or AlGaN shell could be done to passivate the heterostructure surface states. Indeed, surface recombination in InGaN/GaN nanowires was identified in the literature as one of the main sources of losses and the growth of a protective AlGaN shell around the active InGaN/GaN region was shown to improve the luminescence yield[144,145].

As mentioned previously, another possibility could be related to the polar nature of these heterostructures. Specifically, the presence of strong electric fields within the InGaN core volume, could induce a spatial separation of the e-h pairs, which is more pronounced as the temperature is increased (i.e. when e-h pairs delocalize from the potential minima associated to In fluctuations). This point will be discussed in more detail in Section 3.3.

3.2.3 Possible causes of the PL broadening and bimodal shape

Figure 3.8(a) presents the low-temperature PL spectrum of sample the capped InGaN/GaN NWs ensemble analyzed in the previous section (#H004). The broad PL signal originating from the InGaN insertions is well approximated by the convolution of two Gaussian contributions: one at lower energy (peaked at about 2.15 eV), and one at higher energy (at about 2.40 eV). The InGaN/GaN NW samples analyzed during this Ph.D. often presented similar bi-component PL spectra, and this feature did not show any correlation to the specific sample composition, insertion shape or thickness.
The much higher luminescence broadening of InGaN/GaN NWs self-assembled systems[90] compared to InGaN/GaN single QWs[87] (several hundreds vs several tens of meV), essentially results from a superposition of different emission colors/intensities of individual NWs with different alloy composition[146,147]. This statement is consistent with the results showed in figure 3.8(b), where we plotted the histogram of the emission energies of single NWs measured on the insertion top by low-temperature CL (the measurements are described further in the chapter): despite the low (10) number of NWs analyzed, the histogram reproduces quite accurately the bi-component macro-PL. This result supports the idea that the two PL peaks result from a double population of NWs, characterized by a higher (x~0.40 for 2.15 eV) and lower (x~30 for 2.40 eV) average In fraction respectively. The question turns on the possible origin of this double population.

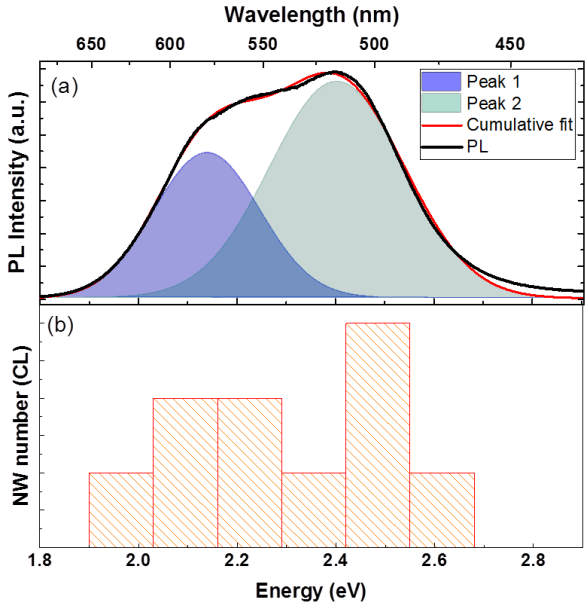

Figure 3.8 (a) Macro-PL spectrum of the InGaN/GaN NW array. (b) Histogram representing the number of NWs producing cathodoluminescence at different energies as a function of energy.

Sekiguchi et al.[147] demonstrated that the different diffusion lengths of In and Ga adatoms on the NW sidewalls, lead to diameter-dependent emission colors in ordered InGaN/GaN NW arrays. Thus, the broad PL of self-assembled systems is often associated with the NW diameter dispersion and shadowing effects, both altering the effective In and Ga fluxes reaching the NW tip[90,146]. However, in section 2.1 we observed that both the NWs lengths and diameters show statistical distributions which are well approximated by a single Gaussian function. Thus, if all these phenomena could in principle justify the general broadening of the signal, they don't seem sufficient to explain the presence of a double population of NWs with different average In composition.

One possible explanation could relate to the presence of a population of NWs presenting inversion domains. In fact, our STEM analysis on samples grown under In-adlayer conditions, revealed that the InGaN sections hosting an inversion domain showed systematically a 3D island-like shape and a lower In composition (typically, 10-15% lower than the disk-like sections of the same sample). This is shown in figure 3.9. The reason of this might be a perturbation of the In incorporation kinetics and/or heterostructure growth mode, enabled by the double polarity of the GaN base. In fact, the model of Frank and Daudin[128] described in section 2.6, emphasizes the critical effect of surface and interface energies in determining the InGaN heterostructure growth mode. Thus, an abrupt change of growth mode could be expected if the NW polarity is partially switched. This could be the case, if the nucleation of the InGaN insertion happens in proximity of the IDB (i.e. near the center of the NW top surface). We speculate that the lower In composition in these sections could be somehow related to the substantially reduced In incorporation (of about 20%) on Ga-polar substrates compared to N-polar ones reported in the literature [83,85]. We suppose that although the surface of the domain of inverted polarity is small compared to the NW cross-section, it still can have a significant impact on the growth mode of the InGaN section. Further investigations are needed to confirm this hypothesis. We have attempted to do a CL statistics on single NWs analysing both the InGaN insertion emission and the GaN NBE emission with the objective to correlate the appearance of the IDBs 3.45 eV signal with the In variation. Unfortunately, the CL broadening of the GaN NBE was too large to allow for an unambiguous identification of the IDB peak, which was

masked by the NBE broadening. Further experiments implementing μ-PL and CL correlated statistics are planned in the future.

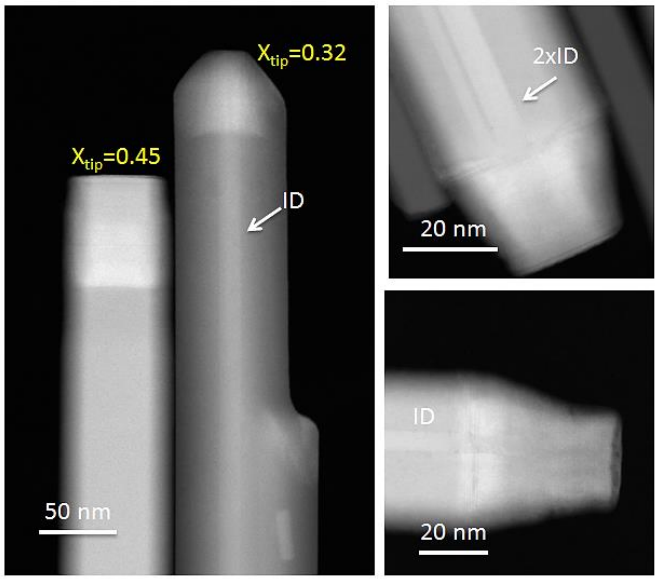

Figure 3.9 HAADF-STEM images of uncapped InGaN NWs grown under In-adlayer conditions (sample #C041). The In fraction measured by EDX at the heterostructure tip (x_{tip}) is reported.

3.3 Influence of strain and electric field anisotropy on different emission colors and recombination dynamics from thick In-rich InGaN disks

In conventional c-plane InGaN QWs, the existence of strain-induced piezoelectric fields leads to spatial separation between the electrons and holes wave-functions. The charge separation becomes more severe for InGaN QWs with emission wavelengths in the green and longer wavelenghts[148], resulting in a marked slowdown of the inter-band and excitonic optical transitions and in a weak luminescence power.

Recently, InGaN/GaN heterostructures formed by GaN NWs with 2-3 nm thick InGaN disks have been proposed to tackle this problem. Indeed, the radiative recombination dynamics of these heterostructures is found to be much faster, which is

often attributed to the strain accommodation and reduced (or even suppressed) quantum confined Stark effect (QCSE)[149–152]. However, in section 2.4 we showed that thick InGaN NW heterostructures can only marginally relax the strain due to their combined axial and core-shell geometry. This peculiar strain distribution is expected to result in anisotropic electric field distributions within the heterostructure's In-rich cores which, in principle, could impact the heterostructure's recombination dynamics and their overall radiative power.

The purpose of this section is to investigate the luminescence properties and the temporal PL dynamics of In-rich thick InGaN/GaN NW heterostructures and to correlate them with their simulated band structure. In particular, the capped sample #H004 has been analyzed by means of temperature- and power-dependent macro PL, temperature-dependent time-resolved PL, and CL on single NWs.

3.3.1 Temperature-dependent PL

Figure 3.10(a) presents the (normalized) temperature-dependent PL spectra of the InGaN/GaN NW array. We see that the low energy contribution (P_{LE} peaked at ~2.15 eV), is totally quenched at about 200 K, while the higher energy one (P_{HE} peaked at ~2.4 eV) dominates the PL up to room temperature.

As evidenced in Figure 3.10(b), despite the low laser power density employed (1 W/cm^2)[ii], the temperature evolution of the high energy peak position does not show a clear "S-shape" behavior. The S-shape is the optical signature of the temperature-induced redistribution of carriers in deep and shallow localized states, intrinsic of InGaN alloys[90,153]. Only for the low energy contribution, a blue-shift is observed between 30 and 100 K, which could denote a carrier delocalization from deep states[22]. It is possible that the broad PL signal arising from the wire-to-wire fluctuations could in part mask this effect, which otherwise is expected also for the high-energy contribution. In fact, the temperature-depend peak positions deviates significantly from the standard Varshni law (dashed line for P_{HE}), an aspect which is typically explained by the presence of compositional fluctuations[154].

[ii] An increase of the excitation power leads to a disappearance of the 'S- shaped' variation due to a saturation the local potential minima[90].

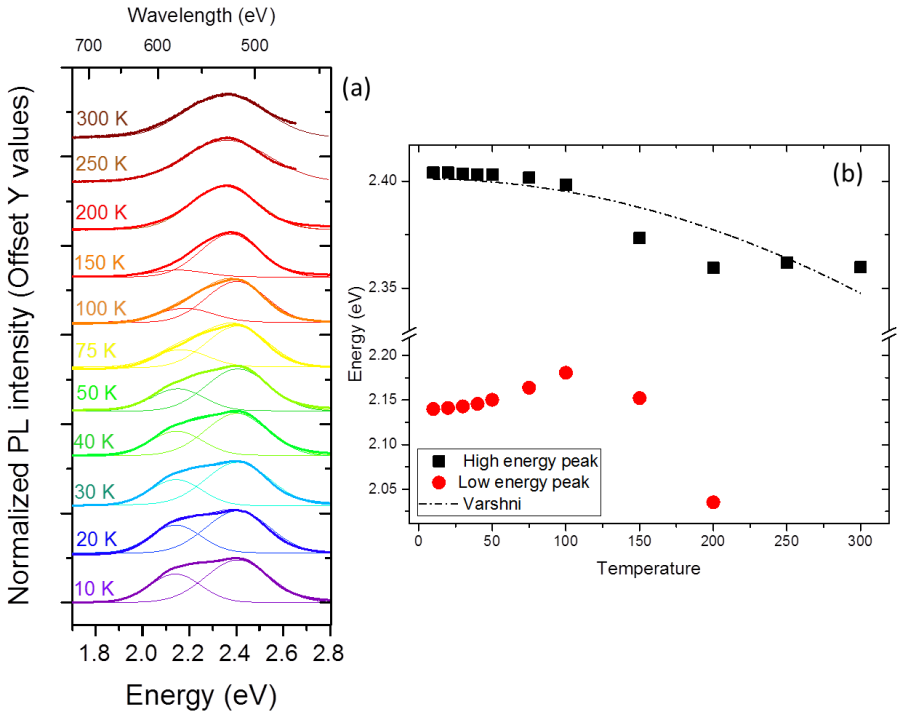

Figure 3.10(a) Temperature-dependent PL spectra of the InGaN/GaN NW arrays. Gaussian fits are also shown. (b) Temperature dependent peaks positions, Varshni dependency is shown with a dashed line.

The evolution of the PL intensity with the temperature is generally described by the thermal escape of the carriers out of a confining potential and capture by non-radiative recombination centers. The activation energy of this process is correlated with the depth of the confining potential. As shown in Figure 3.11, the temperature-dependent intensity variation of the two PL contributions is well fitted by the following Arrhenius function:

$$I(T) = \frac{I_0}{1+a_{01}\exp(-E_{a1}/k_BT)+a_{02}\exp(-E_{a2}/k_BT)} \qquad \text{(eq. 4.1)}$$

where E_{a1} and E_{a2} are the activation energies of two different mechanisms of PL quenching, a_{01} and a_{02} are their respective weighting factors, I_0 is the integrated intensity at 10 K and k_B is the Boltzmann constant. In InGaN alloys, the two activation energies describe the escape of the photo-generated carriers out from shallow (E_{a2}) and deep (E_{a1}) potential fluctuations, arising from local compositional inhomogeneities[153,155].

The activation energies extracted from the fits were quite similar for the two peaks, and compatible with other values reported in the literature[153,155,156]: 9 meV (E_{a2}) and 62

meV (E_{a1}) for the high energy component, 9 and 54 meV for the low-energy one, respectively. The earlier quenching of the low-energy PL component is rather reflected by its a_{01} pre-exponential factor, which is one order of magnitude higher than for P_{LE}. This might indicate a higher density of non-radiative defects in the NW population with higher In fraction.

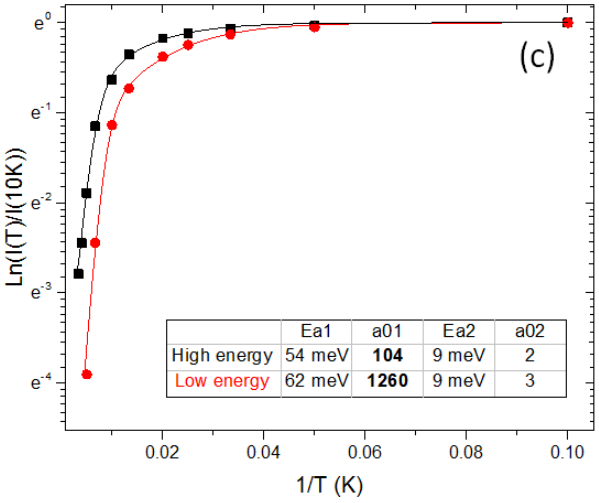

Figure 3.11 Arrhenius plot of the integrated PL intensity of the low and high energy PL contributions: I(T) corresponded to the integrated area of the Gaussian component at the temperature T.

3.3.2 Power-dependent PL

Power-dependent PL is a widely used technique to investigate the mechanism of light emission in semiconductors. In general, the collected PL intensity is proportional to the excitation power P with a power index for a fixed spot size of the pumping laser. Therefore, the PL intensity can be expressed as $= P^F$, where I is integrated PL intensity, P is excitation power, and F is a fitting parameter. The value of the parameter F can give an insight on the recombination processes in the sample. Specifically, it is predicted that for free-exciton recombination $F \approx 1$ and for band gap recombination, i.e., free-carrier electron-hole bimolecular recombination, $F \approx 2$[157].

Figure 3.12(a) shows the PL spectra acquired at a cryogenic temperature (10 K) for increasing excitation power, while the PL intensity dependency for the two components is plotted in Figure 3.12(b). The linear fits returned F values of 0.97 and 0.86 for the high and low energy components, respectively. These values indicate that the PL is dominated by the radiative recombination of free excitons[158]. Note that the low energy component presents the lowest F value. As a result, for increasing

excitation powers its intensity increases less rapidly, leading to a decrease of the overall PL broadening (Figure 3.12(a)).

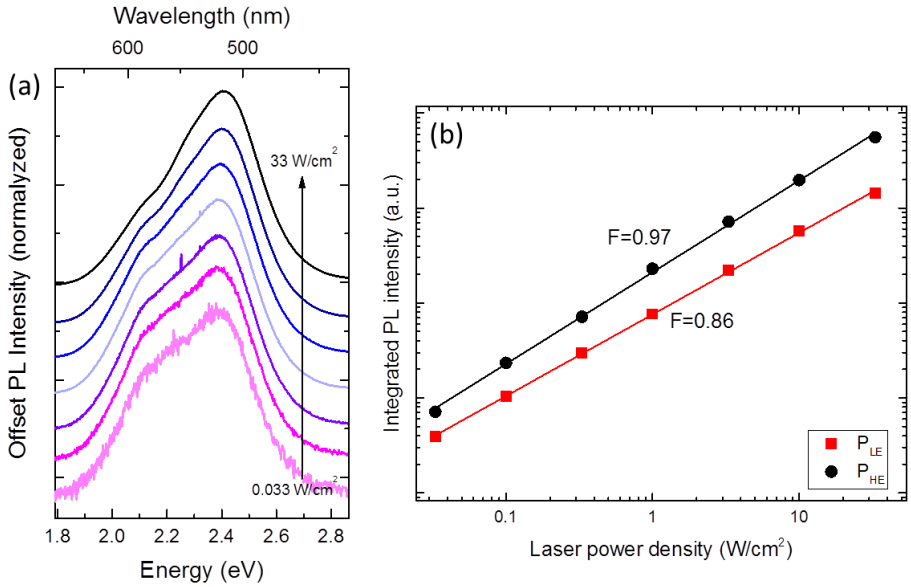

Figure 3.12 (a) Power-dependent PL spectra at 10K (spectra are vertically shifted for clarity). (b) Power-dependent PL intensity.

It is worth mentioning that, consistently with other literature results on similar systems[149,159,160], the PL peak positions did not change appreciably with excitation power. Since the screening of piezoelectric fields is expected to result in a displacement of the signal towards higher energies (10-45 meV shift in InGaN QWs[161,162]), this result suggests that QCSE doesn't play a significant role in the excitons recombination processes. As will be shown in the next section, these results are consistent with the relatively fast carrier dynamics measured by TRPL.

3.3.3 Carrier dynamics

The temporal dynamics of the InGaN/GaN NW PL has been investigated by resonant TR-PL for temperatures between 20 and 300 K. Figure 3.13 shows the streak camera images acquired at 20 K, 100 K, 200 K and 300 K. It can be seen that the low energy PL component shows a much faster decay compared to the high energy one (lifetime of ~500 ps at 20 K at 580 nm) and that, consistently with steady-state measurements, its intensity goes to zero above 200 K. We focused the analysis on the high energy contribution (P_{HE}), which is present in the entire temperature range.

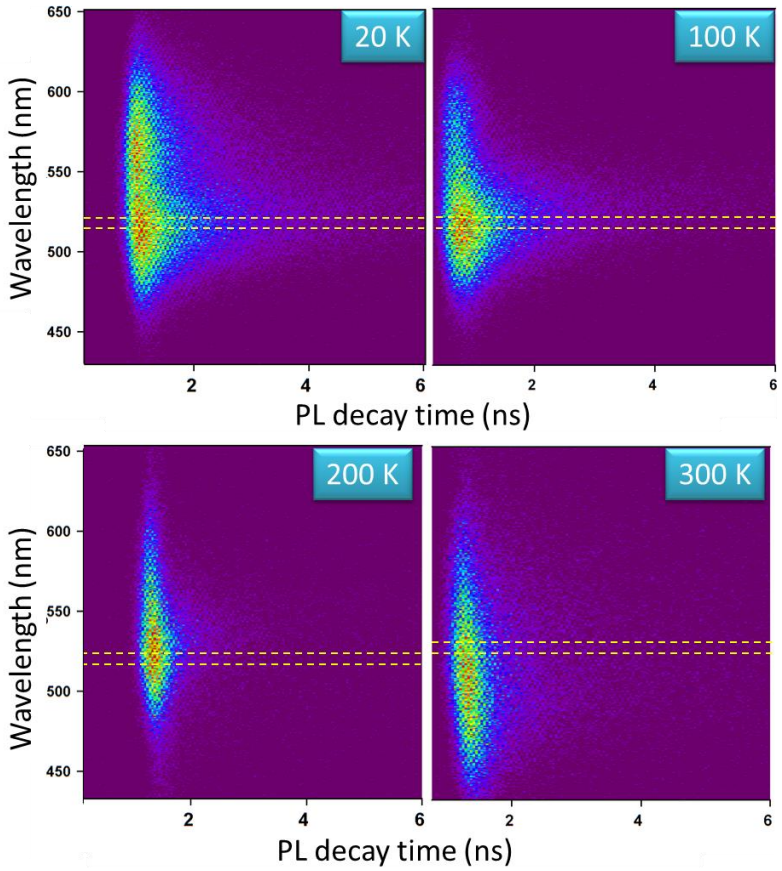

Figure 3.13 Streak camera images recorded at 20, 100, 200 and 300 K on sample #H004.

The decay traces shown in figure 3.14 were extracted by averaging over a 10 nm wavelength region around the PL peak position, by taking into account its variation with temperature (dashed lines in Figure 3.13). As for different InGaN QW[163], QD[164] and NW[149,150,156,163] systems, the curves were non-exponential, and could be fitted only by bi-exponential functions of the form:

$$I(t) = a_{slow}\, exp\left(-\frac{t}{\tau_{slow}}\right) + a_{fast}\, exp\left(-\frac{t}{\tau_{fast}}\right) \qquad (eq.3.2)$$

where τ_{fast} (~0.47 ns at 20 K) and τ_{slow} (~1.7 ns) are its fast and slow lifetime components. This bi-exponential dependency was observed also for decay traces extracted at other spectral positions.

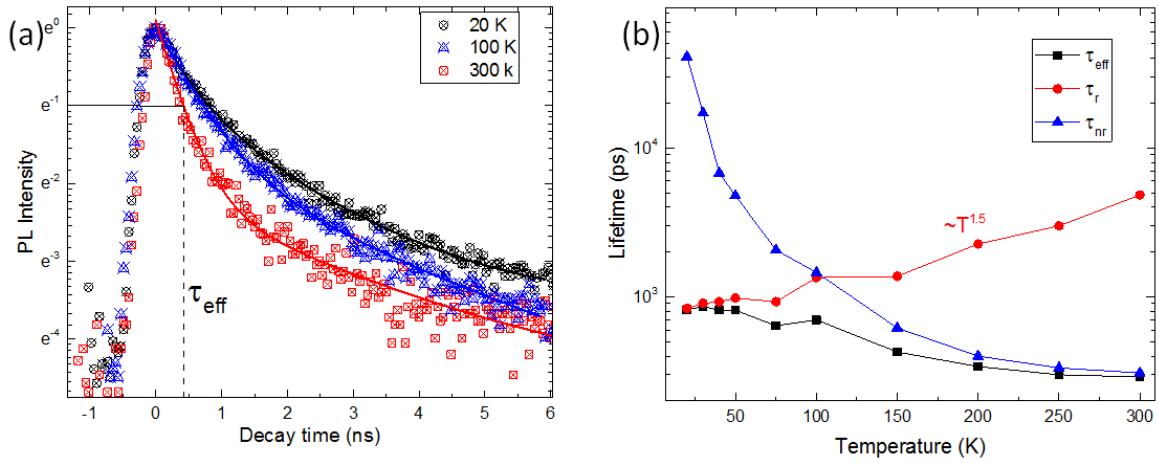

Figure 3.14 (a) Decay traces extracted at the peak energy of the high-energy PL component. (b) Temperature evolution of the effective, radiative and non-radiative lifetimes.

Recent studies comparing TRPL measurements on single InGaN/GaN NWs and on NW arrays, showed that the fast lifetime component (~400 ps in their case) had roughly the same value in single NWs, where the traces exhibited single-exponential decays[150]. We note that in c-plane QWs the excitonic raditive recombination is much longer[148,149,165]. The authors have explained the observed short excitonic recombination time by carrier localization in InGaN allow fluctuations and by a reduced QCST in NWs[150]. However, the physical origin of the slow decay constant is still debated. Different interpretations have been proposed in the literature, including non-exitonic recombination of spatially separated electrons and holes[150], dynamical de-screening of built-in polarization fields[151] and different decay rates for excitons confined in deep and shallow localization centers[163]. An alternative explanation could be related to size, shape, and compositional dispersion of InGaN heterostructures, where the NWs with similar transition energies have different In composition and insertion size, and thus exhibit different electron-hole wave-function overlap.

Due to the lack of a straightforward interpretation of these bi-exponential dependencies, to analyze the temporal dynamics of PL decay as a function of temperature, we considered the *effective* lifetime (τ_{eff})[156,166], i.e. the time at which the PL intensity was decreased by a factor e^{-1} (shown in Fig. 3.14(a)). Then, radiative (τ_r) and non-radiative (τ_{nr}) lifetimes have been derived by combining the equations of PL efficiency (η_{PL}) and effective lifetime (τ_{eff})[156]:

$$\eta_{PL} = \frac{1}{1+\tau_r/\tau_{nr}} \qquad \text{(eq. 3.3)}$$

$$\frac{1}{\tau_{eff}} = \frac{1}{\tau_r} + \frac{1}{\tau_{nr}} \qquad \text{(eq. 3.3)}$$

where η_{PL} is a ratio between the PL intensity at a given temperature and the one measured at 10 K (see Fig. 3.11 for the Arrhenius plot of the P_{HE} component). The results are shown in Figure 3.14(b). We see that the evolution of τ_{eff} (τ_r) is small up to 100 K, and is followed by a rapid decrease (increase, respectively) for higher temperatures. This change of slope indicates that the excitons start to delocalize and be trapped by non-radiative recombination centers. This phenomenon is also reflected by a $\propto T^{1.5}$ dependency of τ_r which is the usual dependency observed for excitons which get delocalized in a bulk material (i.e. where no spatial confinement is provided)[167]. Then, the rapid decrease τ_{nr} above 100 K, reflects the thermally activated diffusion and consecutive capture of excitons by non-radiative defect states, leading to the rapid quenching of the PL intensity seen in section 3.2.2.

If we make the hypothesis that non-radiative recombination is quenched at 10 K, we estimate that at 20 K τ_r is ~800 ps. This value is more than one order of magnitude lower than the typical radiative lifetimes of violet to green polar InGaN/GaN QWs (from few ns up to 20 ns) with large overlap designs[148,149,165], and comparable to the typical values (few hundreds of ps) reported for m-plane InGaN/GaN QWs[165,168]. This could indicate that QCSE is negligible in the excitons recombination dynamics of InGaN NW insertions, in agreement with the results of Bardoux et al.[169] and Tsai et al.[150]. However, it could also indicate that non-radiative recombination channels (for instance, recombination on surface states) are active also at low temperature. At the present stage of our study we cannot discriminate between these two possibilities. In any case, both interpretations don't seem sufficient to explain the extremely weak InGaN μ-PL of single NWs mentioned in section 3.2.1. In fact, if surface recombination could reduce the InGaN PL intensity also at low temperature, we would expect a similar effect on the GaN NBE luminescence, which however is rather intense. Therefore, other type of defects than surface states should be blamed for the non-radiative recombination in InGaN at low temperature. On the other hand, if a pure radiative recombination is supposed at low temperature, the short carrier lifetimes measured by TRPL indicate that the recombination process is very efficient. This aspect should result in an intense InGaN signal (at least at low temperature). To gather more insight on this aspect, we investigated the luminescence properties of

single NWs by CL. In this technique, the excitation is stronger and position-selective. The results of this investigation will be presented in the next sections.

3.3.4 Room-temperature CL

Figure 3.15(b) shows a RT panchromatic image, filtered for the energies of the corresponding InGaN and GaN emissions, which are depicted in the adjacent spectrum (Fig. 3.15(c)).

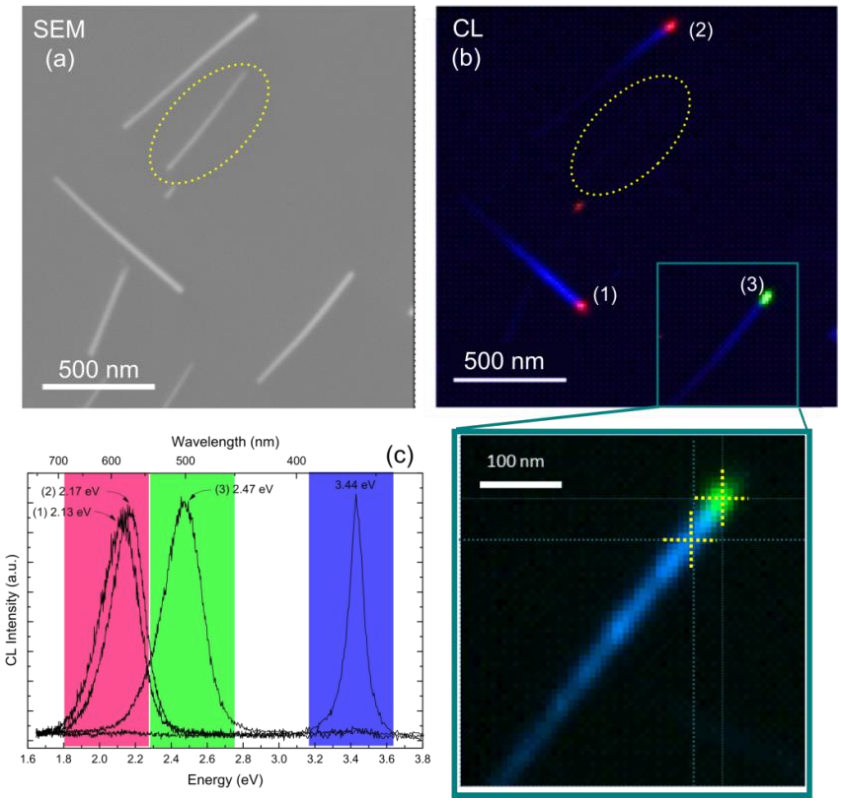

Figure 3.15 (a) SEM image and (b) RT CL map of dispersed InGaN/GaN NWs spectrally filtered for three spectral ranges marked with the corresponding colors in panel c. Inset shows a close-up of the CL map of one nanowire. (c) CL spectra for different NWs a

As evidenced by the yellow circle, few NWs did not emit either in their InGaN or GaN parts (or had emission intensity below the detection limit of the CL setup). This feature has been observed on similar InGaN/GaN NWs by other autors[170] and could be assigned to some damage occurred during their mechanical dispersion. In fact, it seems unlikely that electron beam damage could cause this discrepancy, since nanowires in this experiment were all irradiated with the same minimal beam exposure before data collection.

For the sufficiently bright NWs shown in Figure 3.15, a strong and relatively broad (~300 meV FWHM) InGaN CL was detected at the NW tip, whose wavelength dispersion reflects the In compositional variations from wire to wire (Fig. 3.15(c)). The GaN NBE emission is also shown at 3.44 eV. This had a comparable intensity with respect to the InGaN signal at the insertion vicinity, and decreased monotonically towards the NW bottom, with no detectable spectral shift. Owing to the non-negligible degree of coalescence in the nanowire base part, which characterizes our samples and, more generally, PA-MBE GaN NWs on Si substrates[171–173], the injected carriers could be captured by the multiple dislocations which form at the coalescence joints to accommodate the small in-plane mis-orientation of the thin basal nanowires[18,174]. This may explain the reduction of the NBE GaN CL intensity toward the NW base.

3.3.5 Cryogenic temperature CL

The InGaN/GaN NW CL was analyzed also at low temperature (5K). In this case, the non-negligible drift that was present at cryogenic temperatures limited the acquisition time and therein imposed a lower spatial resolution (pixels of about 10x10 nm or 50x50 nm in the maps described afterwards). Nevertheless, the benefit of performing CL experiments at low temperatures is that spectral peaks are not broadened by the carrier-phonon interaction and are better defined.

Figure 3.16 shows a panchromatic image acquired at the top of an InGaN/GaN NW (NW1). The RGB channels correspond to the following spectral regions: blue (300 - 400 nm), green (450 - 510 nm) and red (510 - 550 nm). The CL spectra measured in different positions of the NW (pixels labelled from 1 to 9 in the CL spectra) are shown in the adjacent plot. The GaN BE emission (positions 1 to 3) was found 20-30 meV blue-shifted with respect to its usual peak energy (3.47 eV) of PL experiments, with a FWHM of ~80 meV, significantly larger than our spectral resolution (∓ 10 meV). This characteristic appeared in all the analyzed NWs and independently from the probed position, and can be assigned to band filling effects associated with a high carrier density generated by the electron beam excitation. Defect-related features such as emissions coming from basal stacking faults[17,18] (3.40-3.42 eV, not shown) and excitons bound to shallow impurity states[175,176] (3.39 eV, shown for NW3 in Figure 3.17) have also been observed. Unfortunately, due to the large peak broadening, the IDB transition expected at 3.45 eV was masked by the main peak and could not be analyzed.

As concerns the InGaN section CL, the signals are still broad despite the low temperature, covering a ~200 meV spectral region independently from the position where CL is probed. We primarily relate this feature to the short range potential

fluctuations arising from the local compositional inhomogeneities[177]. In addition to this broadening, most of the analyzed NWs unambiguously showed two distinct CL contributions. The first, labelled as E_1 in the figure, was peaked at higher energies (2.20 eV for NW1) and had a higher intensity in proximity of the bottom InGaN/GaN interface (positions 1 to 4 in the figure). The second (E_2), was peaked at lower energies (2.05 eV in this case) and dominated the InGaN CL in the upper portion of the InGaN section (positions 5-7). Both of them exhibited an asymmetric broadening with a tail extending towards lower energies. For the E1 transition, the low-energy tail could result from the sizable interaction volume of the electron beam, which may excite the sections not only at their base but also in their upper portion (albeit with a much lower intensity). Regarding the E2 transition, its origin will be discussed further.

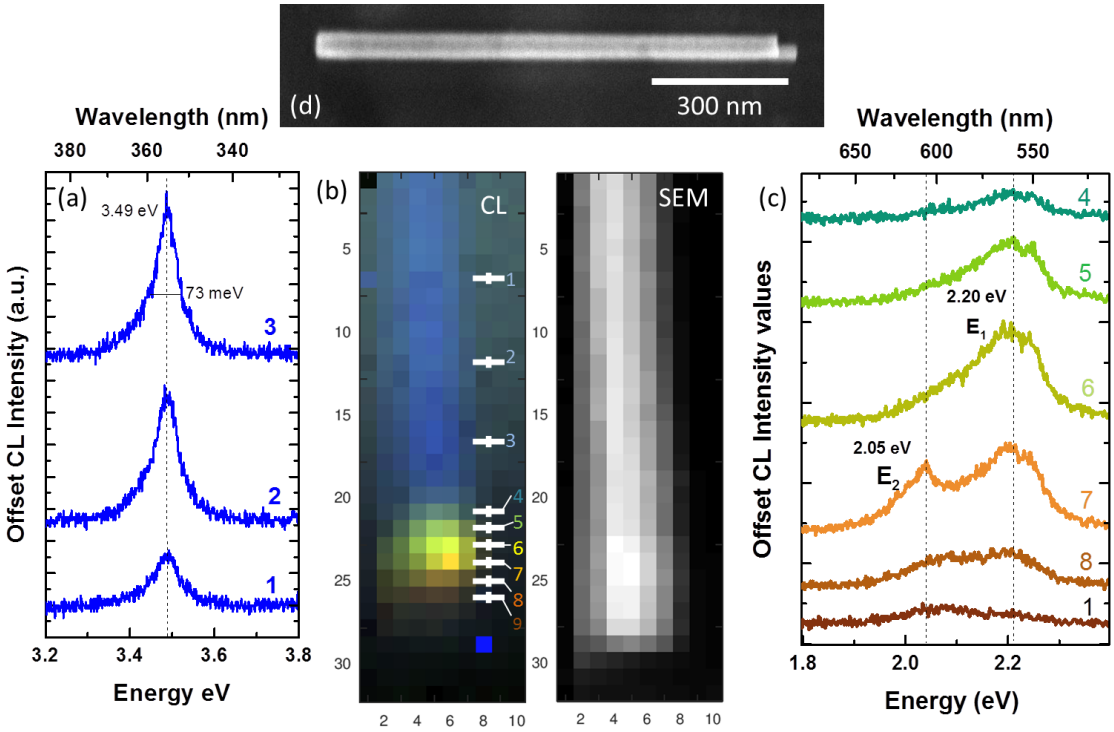

Figure 3.16 CL spectra acquired in different positions of a capped InGaN/GaN NW: (b) spectrally-filtered CL map and the corresponding SEM image acquired simultaneously with CL with the same spatial step; (a) GaN NW base emission (positions 1 to 3 in (b), acquired with a 1800 grooves/mm grating); (c) InGaN section emission (positions 1 to 6 in (b), acquired with a 600 grooves/mm grating); (d) SEM image of the wire in normal resolution.

For different NWs, the E_1 contribution could have comparable intensity to E_2, lower intensity compared to E_2 (NW2 in Fig. 3.17) or, in few cases, it could be absent (NW3 in Fig. 3.17). As a result of the different alloy composition, the spectral position of the two peaks changed between different NWs, however in most of the cases the energy shift between the two contributions (E1-E2) was between 100 and 150 meV. The

complete list of peak positions and spectral shifts is given in Table 3.1. As shown for NW3 (positions 4 to 1), in some cases the E2 peak was found ~50 meV blue-shifted when its intensity was higher, an aspect that could be related to the saturation of its deep localized states induced by the high injection current.

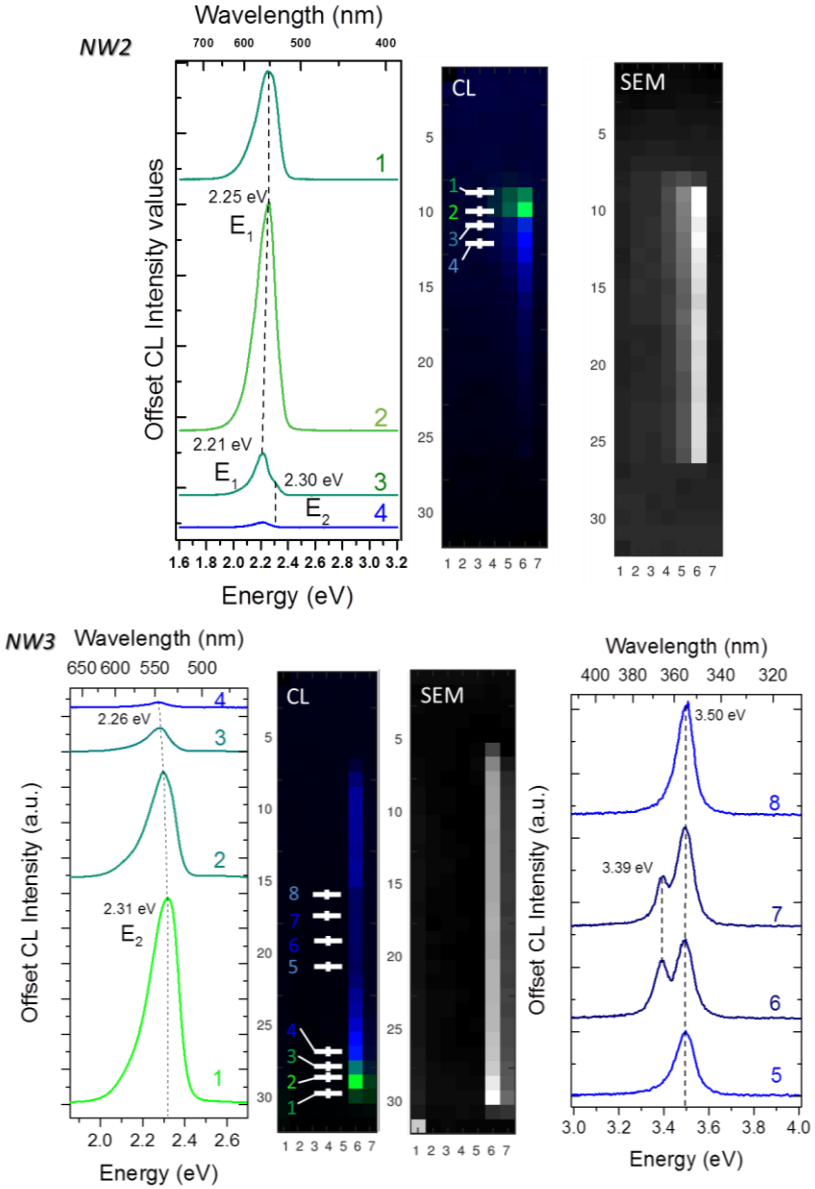

Figure 3.17 CL maps (SEM at the side) and CL spectra acquired in labeled positions of two InGaN/GaN NWs (NW2 above, NW3 below).

As shown in Chapter 2, due to the lattice pulling effect, the InGaN sections present an increasing In composition over a 20 nm thick region before reaching a "plateau" of maximal In content. This region represents about 1/3 of the insertion thickness. If this compositional gradient is taken into account, a red-shift of the InGaN CL emission could be expected when the electron beam is moved from the lower to the upper

portion of the insertion. This should be especially the case for low temperature CL experiments, since the absence of thermal excitation tends to localize the e-h pairs on local potential minima preventing them from diffusing to the global potential minimum located in the upper part of the insertion[178]. However, the appearance of the two position-dependent CL peaks points to a presence of a more efficient carrier recombination in two distinct sites of the insertion. We will now try to understand the origin of this phenomenon.

Table 3.1 E_1 and E_2 peak energies and their difference (in eV) measured by CL for different NWs.

NW	E_1	E_2	E_1-E_2
1	2.20	2.05	0.15
2	2.30	2.20	0.10
3	--	2.26	
4	2.25	2.11	0.15
5	2.62	2.46	0.16
6	2.81	2.49	0.32
7	2.57	2.44	0.13
8	--	2.28	--
9	2.13	2.08	0.05
10	--	2.55	--
11	2.4	1.98	0.42

The intrinsic tendency of InGaN to phase separate is generally invoked when it comes to carrier localization in InGaN alloys. Specifically, In-rich clusters create deep localized states within the conduction and valence bands which can "trap" the carriers and promote a radiative recombination at these potential minima. Our STEM-EDX analysis did not evidence sizable In-rich clusters, indicating that if they are present (which is inevitable since statistical alloy fluctuations take place in any ternary alloy), they should have comparable or smaller size compared to the exciton Bohr radius (~3 nm in GaN). Sharp emission lines due to 0D confinement in In-rich regions were indeed observed on other InGaN insertions by micro-PL[179,180]. However, this explanation of small scale random alloy fluctuations doesn't seem to apply to our case, since both the E_2 and E_1 transitions can be quite broad (FWHM of about 200 meV as in NW1) and, more importantly, present emission energies which do not deviate appreciably neither between each other, nor from the expected InGaN band gap.
Another important feature affecting the luminescence properties of polar InGaN/GaN heterostructures is the strong anisotropy in polarization fields near and far from the

heterointerfaces. This can significantly affect the electron-hole (e-h) spatial distribution within the structure. In fact, the rather complex strain distribution within the InGaN/GaN heterostructure, arising from its combined axial, core-shell and NW nature, is expected to result in a band edge profile which deviates from the one of the most classical InGaN/GaN polar heterostructures. To further investigate this point, and to help the interpretation of the CL results, the InGaN/GaN band edge profile along the NW axis has been simulated following the procedure described in methods section, by taking into account its peculiar strain distribution.

3.3.6 Assessment of the InGaN/GaN band edge profile

In a first step, we simulated the strain distribution of a 25 nm radius GaN NW embedding a 60 nm thick axial InGaN heterostructure with a 2 nm thick surrounding GaN shell. As described in the methods section, the interface compositional gradient (x from 0.20 to 0.40 along ~20 nm thickness) was taken into account in the simulation. In Figure 3.18 are shown the side-view projections of the out-of-plane (a), in-plane (b) strain fields simulated by Comsol. The corresponding hydrostatic strain is shown in Figure 3.18(c). The strain in the InGaN disk is found to be compressive and increasing in proximity of the c-plane heterointerfaces. It is less important in the "bulk" of the structure (~1.5% deformation in the out-of-plane direction), due to the NW core-shell geometry. Note that these results are in good agreement with our strain estimations by XRD analysis, which indicated a ~1% out-of-plane compressive strain within the In rich core (Section 2.4).

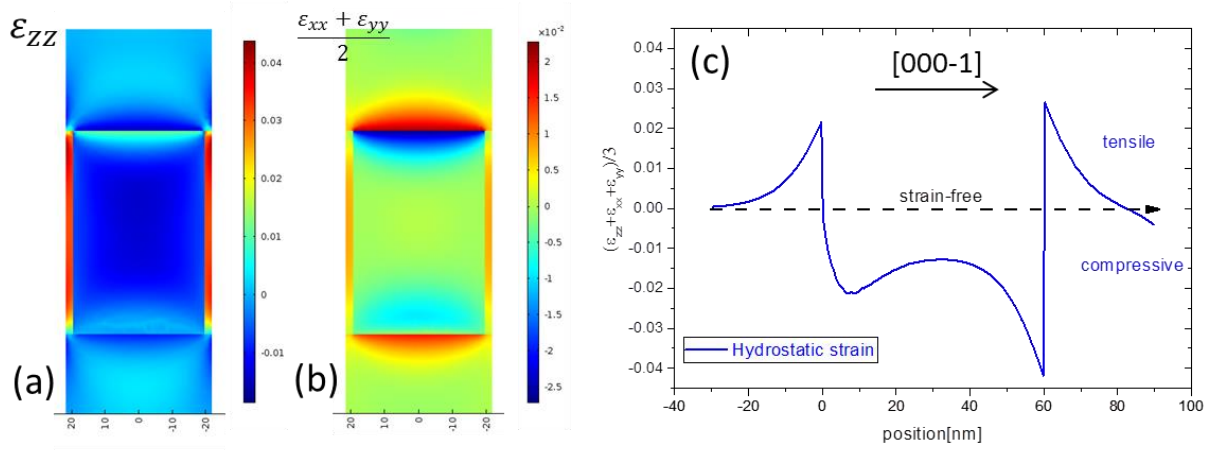

Figure 3.18 (a) Out-of-plane and (b) in-plane *local* strain projections (11-20 zone axis) of a GaN NW embedding a 60 nm thick disk-like heterostructure with a graded In fraction at the bottom interface. (c) Corresponding hydrostatic strain along the NW axis (dashed line in (a) and (b), corresponds to zero strain).

In a second step, the calculated strain tensors along the NW rotational axis have been used as input parameters to compute the band structure (1D approximation) with the same compositional and geometrical properties (Nextnano). In figure 3.19(a) we plotted the net (axial) electric field within the structure and the resulting InGaN/GaN band edge profile. The anisotropic strain distribution leads to a strong and positive electric field close to the nanodisk polar interfaces and to a weaker (but still not zero) negative electric field in the bulk of the structure. Also, due to the shared deformation between the InGaN heterostructure and the GaN NW and the high density of uncompensated polarization charges, the electric field at the interfaces presents marked discontinuities.

The band-edge profile along the heterostructure's core axis is shown in Figure 3.19(b). The spontaneous and piezoelectric fields generate a strong and anisotropic conduction/valence band bending the edges (at the top and bottom heterointerfaces) and within the "bulk" of the polar InGaN section. As a result, the e-h generated over the entire polar InGaN volume, may get rapidly separated by the internal field according to the sign of their charge: electrons drift toward the conduction band absolute minimum (CB_{Am} in the figure), while the holes drift toward the valence band maxima (VB_{AM}). Therefore, both electrons and holes may eventually accumulate in the potential wells created by the strong electric field. This is shown in Figure 3.19(b), where the electron and hole wavefunctions quadratic moduli for the lowest energy derived by solving the Schrödinger equations (T= 5K) are shown.

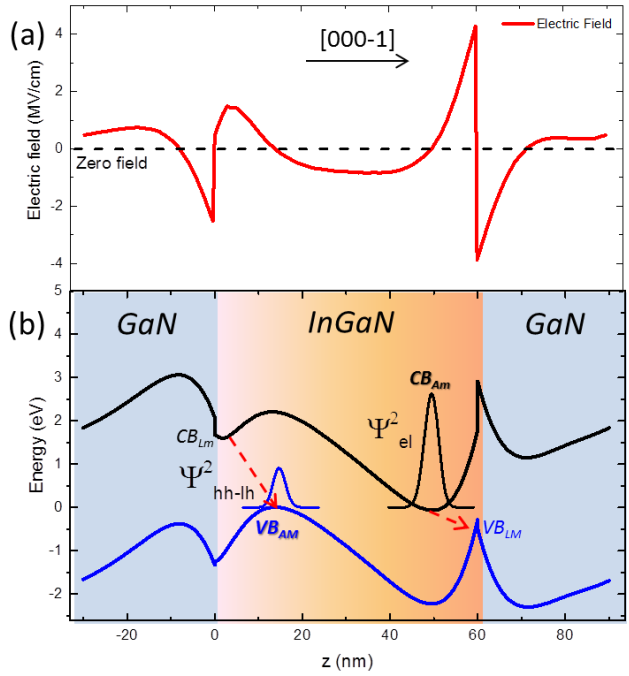

Figure 3.19 Net electric field (a) and the resulting band edge profile (b) along the InGaN/GaN NW axis.

Obviously, due to the huge e-h spatial separation (~30 nm) and the resulting zero wavefunction overlap, the recombination of the electrons and holes confined in these absolute bands minima (maxima) cannot be observed experimentally. Furthermore, at low temperature, the carrier trapping at local potential minima prevents them from reaching the global minimum : carrier motion can happen only on a short length scale[178]. The hypothesis of radiative recombination between the bands absolute minimum (maximum) can therefore be rebutted.
The band edge profile in Figure 3.19(b), shows that the band offsets and polarization-related discontinuities at the interfaces generate one local minimum in the CB (CB_{Lm}) and one local maximum in the VB (VB_{LM}). Thus, possible optical transitions could involve the two main reservoirs of holes and electrons, and the holes and electrons which get localized in CB_{LM} and VB_{LM} (red dashed arrows in Fig. 3.19). This could be reasonable for excitations happening in their proximity, since the carriers should cover a shorter distance to relax in the two couples of potential wells. This statement could also explain the observation of two distinct position-dependent CL peaks. However, due to the still high e-h spatial separation (about 10 and 15 nm) these transitions would yield a very slow recombination, which sharply contradicts the low radiative lifetimes measured by TRPL, and doesn't correlate well with the absence of spectral shifts in power-dependent PL. Furthermore, this hypothesis predicts an energy difference between the two optical transitions which is much larger (ΔE~1 eV) than the one observed experimentally (from a minimum of ~50 meV to a maximum of ~400 meV). For these reasons, we rule out also the hypothesis of radiative recombination between the local CB (VB) and global VB (CB) minima (maxima).

3.3.7 Identification of the dominant optical transitions

Power-dependent PL measurements revealed a power law dependency of the integrated PL intensity which is typical of excitonic recombination. This means that the optical transitions must involve excitons (i.e. electrons and holes which are effectively bound by Coulomb forces). In fact, this attraction provides a binding energy of about 45 meV in InGaN QWs[181]. The excitons thus can be dissociated only by electric fields above 150 kV[181]. For AlGaN/GaN NW heterostructures, a similar value of 80 kV has been reported[182].
If this aspect is taken into account, the two optical transitions observed by CL could then result from the recombination of electrons and holes confined in their absolute potential minima, and the holes and electrons which are distributed in their proximity (black arrows in Figure 3.20(b)). In fact, the local internal electric field in these positions is close to zero, so that the separation of excitons is not expected (Figure

3.20(a)). In other regions electric filed should dissociate excitons. In this view, the corresponding "vertical" transitions (plane black arrows), denote the excitonic recombination around the zeros of the internal field that we believe is observed in CL experiments. These transitions predict a E_1-E_2 energy difference of about 50 meV, which is in reasonable agreement with the one measured experimentally (~120 meV). Also, being them spatially direct, they must imply a high oscillatory strength, in agreement with the low radiative lifetimes measured in TRPL and with the absence of electric-field screening/de-screening effects in power-dependent PL. Then, the asymmetric broadening of the two signals on the low energy side could be explained by the distribution of electrons (holes, respectively) to lower energy states (going "downhill" for electrons or "uphill" for holes). This is energetically favourable, but results in spatially indirect transitions, leading to a decrease of the emission intensity (due to a decreased e-h wave functions overlap) as the e-h get more spatially separated.

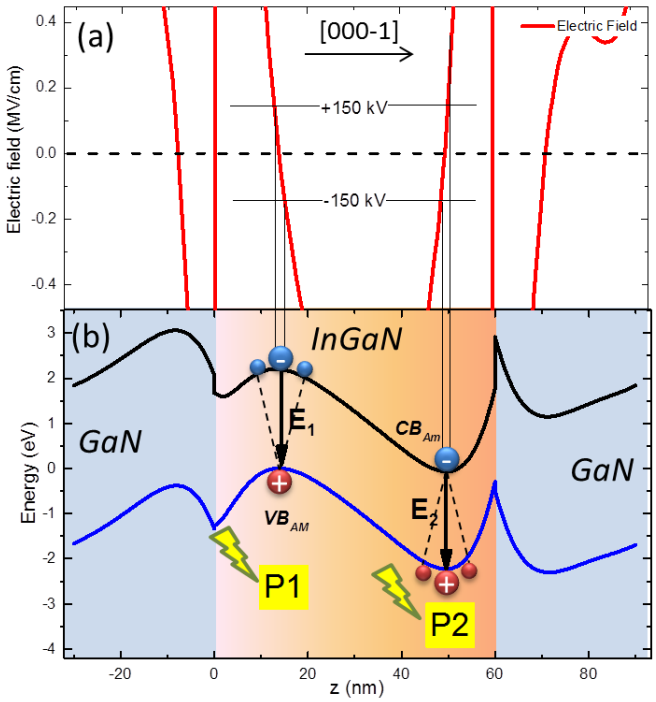

Figure 3.20 (a) Electric field and (b) band edge profile along the NW growth axis, showing the possible optical transitions within the InGaN/GaN NW heterostructure.

Unlike the internal electric field, which draws electrons and holes in opposite directions, the increasing In content toward the disk top draws both types of carriers upwards. In this process, the electrons are getting additionally accelerated towards the NW top (CB absolute minima), while the holes are getting decelerated in their drift towards the bottom VB minimum. Thus, in principle, the transitions far from the NW

bottom (i.e. in the In-rich portion of the InGaN sectio) should be more favorable. This could be especially true for high temperature measurements, since e-h have a sufficient thermal energy to escape from local potential fluctuations and diffuse to their absolute minima. This statement correlates well with the temperature dependency of the E1 and E2 relative intensities, shown in Figure 3.21: as the temperature is increased from 5 to 150 K, both the E1 and E2 transitions become weaker and broader, while at 300 K only the low-energy E2 emission, located at the NW top, can be distinguished. Similar results have been observed in InGaN QDs in GaN NWs using a STEM-CL setup, where the authors reported a peaked CL intensity when the electron beam excited the upper (In-rich) region of each insertion[88].

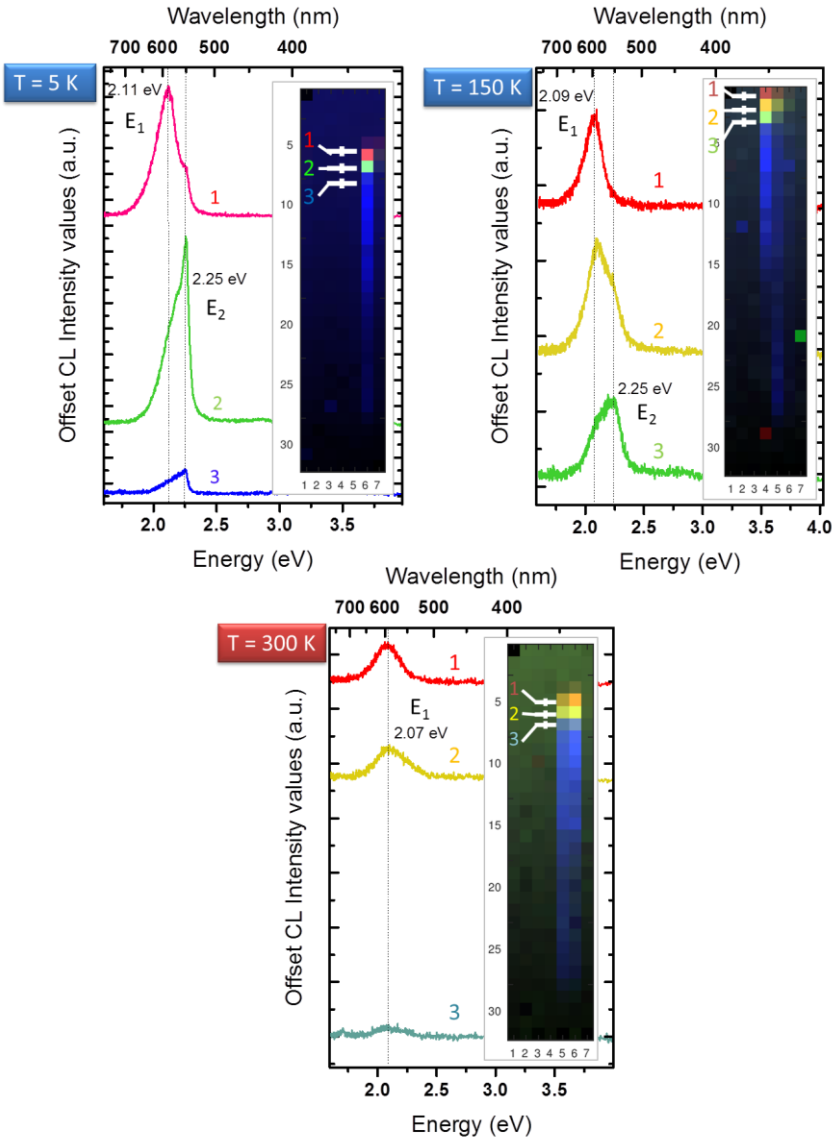

Figure 3.21 CL spectra measured on NW4 at 5 K, 100 K and 300 K.

In this analysis, we considered only the axial profile. In fact, since the strain relaxation is inhomogeneous in both the axial and radial directions, a comprehensive study of the InGaN heterostructure band profile would require to solve a 3D problem. It has been theoretically demonstrated that the strain relaxation at the NW sidewalls and Fermi level pinning at the NW surfaces results in a radial e-h separation[182–184]. However, for thick In-rich heterostructures the influence of the surface potential on the band profile is weak compared to the polarization field, and might be also mitigated by the presence of the Ga-rich shell[183]. We also note that for N-polar GaN QDiscs in AlGaN NWs with a surrounding AlGaN shell, a parabolic radial potential has been theoretically predicted, whose intensity is minimum at the NW center[182]. The structure considered by Jacopin et al.[182] is similar to our case (if the GaN insertion is replaced by InGaN and the AlGaN shell is replaced by a Ga-rich shell). Thus, we could reasonably expect that exciton recombination is favored in the center of the nanowire, whereas the nanowire periphery could be almost optically inactive.

Based on these considerations and as a general conclusion, if only the electric field along the NW axis is considered, e-h pairs created in all other positions far from P1 and P2 might experience, at low temperature, the competition of two effects: the confining potential arising from In fluctuations which keeps them together, and the strong electric field which tends to take them apart. Therefore, a weak CL emission could be expected in all other positions where the internal field is high enough to dissociate excitons, leading to a pronounced reduction of the overall luminescence power of the InGaN section. This aspect could in part explain the generally weak InGaN emission evidenced in this study, and specifically, the fact that we have not been able to measure any InGaN μ-PL signal from single NWs, even at low-temperature. On the contrary, we note that the observed potential profile tending to separate carriers can be advantageous in photovoltaic devices, where the photo-generated carriers need to be separated and extracted to produce the useful current.

Conclusions

In the first part of the chapter I investigated the μ-PL of InGaN/GaN NW ensembles and single InGaN/GaN NWs. General features involved weak (NW ensemble) or absent (single NWs) InGaN PL at room and low temperature under non-resonant optical excitation. By contrast, the GaN BE PL was intense on both NW ensemble and single NWs, allowing the identification of the 3.45 eV signature associated to IDBs.

Under non-resonant excitation, the NW arrays exhibit broad (FWHM of few hundreds of meV) and often bi-component PL spectra, in spectral regions which well fit their average core composition. The broad PL emission has been primarily associated to the dispersion of In contents between different NWs which characterizes our self-assembled growth approach. In parallel, the presence of bi-component PL signals, has been tentatively assigned to a second population of NWs presenting IDBs and a decreased In incorporation.

Generally, temperature-dependent PL measurement showed that In-rich sections (x>0.35) presented a lower PL IQE (about 5%) compared to In-poor structures (x~0.20, about 17%), even when our STEM investigations did not reveal structural defects. I proposed that this could be in part explained by the high surface-to-volume ratio of the NWs presenting a thin Ga-rich shell, which could increase the non-radiative surface recombination, but could also arise from the polar nature of the heterostructure and its anisotropic strain distribution.

To better investigate this point, in the second part of the chapter I studied more in detail the band-edge profile and optical properties of ~70 nm thick In-rich disk-like sections. Consistently with our XRD and GPA analysis of Chapter 2, our theoretical simulations showed that strain can only marginally be relaxed, resulting in an anisotropic polarization field and non-intuitive band edge profile along the heterostructure axis. Specifically, this simulated profile indicated that in most of the heterostructure volume, the e-h hole pairs might be taken apart by the strong electric field, and hence generate a very weak emission. Indeed, the absence of spectral shifts in power-dependent PL, the fast radiative lifetimes (~800 ps at 20 K) measured by time-resolved PL, and the presence of two distinct position-dependent Cathodoluminescence contributions in many single InGaN NW heterostructures,

strongly suggested that the low-temperature emission process is dominated by two excitonic recombination processes, confined in small areas at the base and at the top of the InGaN section.

Credits

The macro-PL experiments presented in this chapter were carried out by L. Mancini and me at C2N for 244 nm excitation and by H.G. Song in the KAIST University in South Korea for resonat excitation. As concerns cathodoluminescence measurements, these were performed by my colleague, Fabrice Oehler at C2N. Strain field and band edge simulations were performed by my colleagues Frank Glas and Lorenzo Mancini at C2N.

Chapter 4

SAG growth of GaN NWs on transferred graphene

Currently, a tremendous amount of activity is being directed towards the study of graphene and its implementation in a variety of applications. This interest stems from, but is not limited to, its exceptionally large electrical and thermal conductivity, high mechanical strength and flexibility, and high optical transparency. In parallel, thanks to its and sp^2 crystalline structure, graphene could be potentially used as a compliant epitaxial substrate for the growth of III-V semiconductors, and since very recently also of GaN NWs by PA-MBE. Especially, a high degree of selectivity can be obtained if graphene is transferred on an amorphous carrying substrate such as SiO_2. In fact, this is one of the most recent hot topics in the field of NWs growth, since it opens, at least in principle, the possibility of using graphene as both epitaxial seed layer for the selective-area growth (SAG) of GaN NWs and in-situ ohmic bottom-contact. However, the growth of GaN NWs on graphene is still at the level of "proof of concept", and there are many open questions concerning the nucleation mechanism of NWs on these substrate, the possible damage to the graphene properties by the N-plasma, and the control of the growth itself. In this chapter, we will mainly focus on the study of SAG growth of GaN NWs on transferred graphene (mainly mono-layered), as well as the possible modifications to the graphene crystalline and electrical properties due to the growth process. Finally, optical characterization of the GaN NWs is provided.

4.1 State of the art of III-N NWs growth and epitaxy on graphene.

In the previous chapters, we have shown that GaN NWs can be efficiently and controllably grown on AlN/Si(111) substrates by a self-assembled growth method. With this approach, however, the height and diameter of NWs have relatively broad distributions. This leads not only to a poor control of the size of the fabricated nano-devices, but also to difficulties in establishing contacts to the NWs. Also, for heterostructured nanowires, and in the specific case of InGaN/GaN NWs, both the length and diameter dispersion influences the effective atomic fluxes reaching the NW tips, lending ultimately to a broad dispersion of In content, heterostructures growth rates and InGaN section morphologies. A high control on all these aspects is needed for device applications. It is therefore necessary to go for selective area growth approach (SAG) where the NW nucleation spots are controlled resulting in a homogenous predetermined NW density.

Traditionally, the main requirements for SAG of GaN NWs are that the substrate should (i) be monocrystalline helping NWs to grow vertically, in order to avoid coalescence and to provide contacts to NWs, (ii) induce nucleation of NWs faster than on the mask layer, in order to confine the NW growth spots and (iii) have lattice parameters close to the one of GaN, in order to avoid defects at the base of NWs. With these requirements, there have been several attempts to grow GaN nanowires selectively by PA-MBE (Fig.4.1). Specifically, the leader of this domain in terms of both pioneerism and actual research progress, is the group of Prof. K. Kishino, which employs Si(111) substrates with Ti masks[185–187]. SAG of GaN NWs has also been demonstrated on Si(111)[188–191], diamond[192] and sapphire[76,193,194] substrates, with either TiN_x[180,193,194], SiN_x[190,191] or SiOx[188,189] masks. In most of these cases, the GaN NW growth requires an intermediate layer or template of either AlN[185,188,191,195] or GaN[76,187,191,193], to promote NW nucleation in the mask holes and help to reduce the defects arising from the lattice mismatch with the Si or Sapphire substrate. The growth of this intermediate layer adds one epitaxial step to the preparation of the patterned substrates. Also, the success of the SAG relies much on the flatness of the mask. These

are the main factors acting as constraints for the robustness and the scalability of the technique.

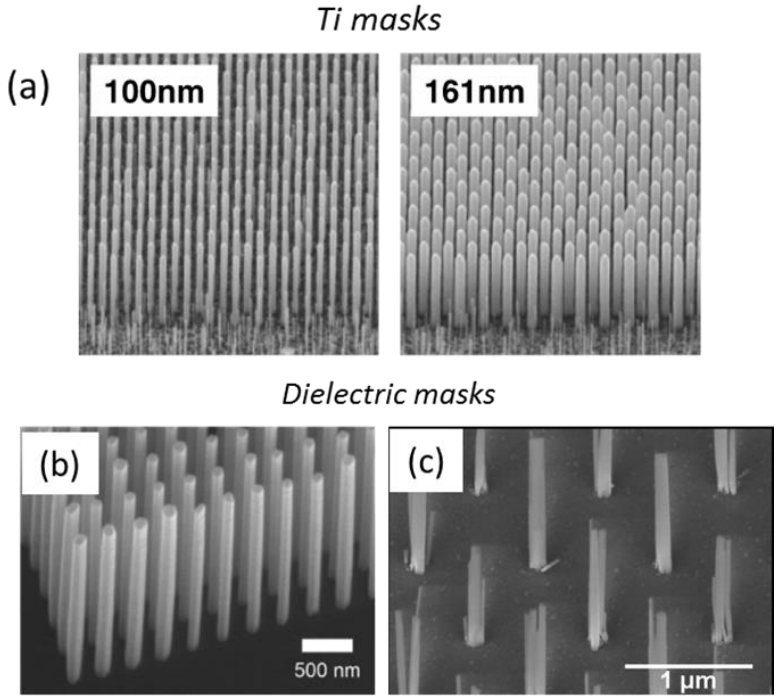

Figure 4.1 SEM images of SAG GaN NW grown by MBE on (a) GaN template with Ti mask[187], (b) on Si(111)/SiN_x[190] (b) and AlN/SiO_2[188] (c).

Recently, the PA-MBE epitaxial growth of GaN NWs on graphene has emerged as a promising strategy to overcome these limitations[70,196,197]. On one hand, due to the dangling-bond-free two-dimensional (2D) structure of graphene, the direct growth of III−V compounds on graphene is in principle expected to be mediated by van der Waals forces. Van der Waals epitaxy relaxes the strict requirements of conventional heteroepitaxy (i.e. there are, at least in principle, no constraints on either the surface symmetry or the lattice parameter of the overgrown material). On the other hand, a recent study of our group demonstrated that GaN NWs can be grown epitaxially and with a good selectively on graphene by PA-MBE, if the latter is transferred on an amorphous substrate[196].

The growth was carried out on large mono-layer graphene patches (Fig. 4.2(a)) and multi-layers "staggered" graphene domains (Fig. 4.2(b)), in both cases transferred on Si(100) with a 300 nm thick SiO_2 overlayer. Growth of vertically aligned GaN NWs (<0001> growth direction) was observed on the graphene, with no or limited growth

on the SiO_2 matrix. For multi-layer staggered graphene structures, it was shown that the NW density decreases, as the number of graphene layers increases from 1 to 5, possibly due to the different strain partitioning between GaN and graphene layer(s)[196] (Fig. 4.2(b)). However, it must be mentioned that these results are in sharp contrast with the ones obtained by Ramsteiner et al. on epitaxial graphene layers on SiC[70]: in this case, growth was obtained only on multi-layered graphene (especially at step-edges and defects, Fig. 4.2(c)), and no growth was observed on ML graphene, since this was totally etched by the N-plasma source. The contrast appearing between the two works results from the fact that the possible graphene modifications (incorporation of N and/or local deterioration of the graphene honeycomb structure) occurring during PA-MBE growth, and the possible role played by such defective sites on the NW nucleation remain unknown.

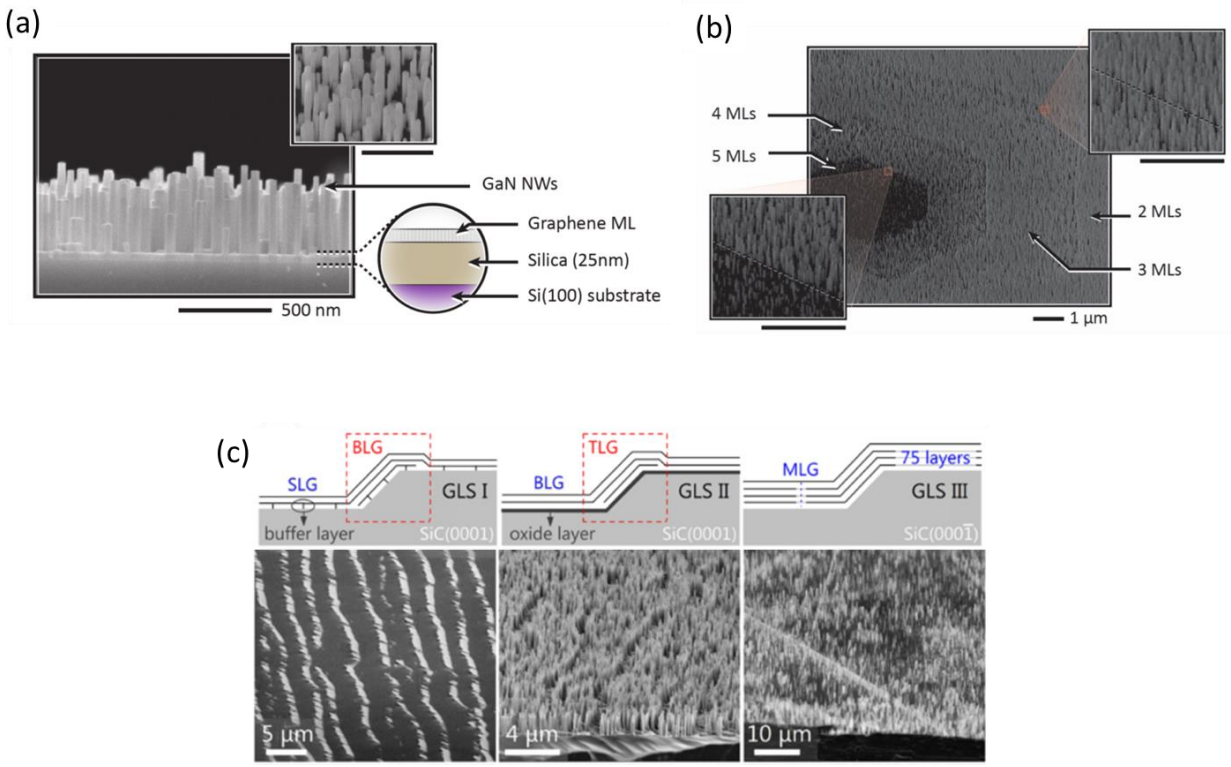

Figure 4.2 (a) Vertical GaN NWs grown by PA-MBE on a ML graphene patch (a) and a multi-layered staggered graphene domain (b), both transferred on SiO_2/Si(100) substrates[196]. (c) GaN NWs grown on epitaxial graphene on SiC, for different layer thicknesses[70].

Nevertheless, in both studies by Kumaresan[196] and Ramsteiner[70], a clear in-plane orientation of the NWs was observed. Specifically, Kumaresan et al. showed that in-plane oriented NWs grew on areas corresponding to the graphene monocrystalline grains (Fig. 4.3(a)). This clearly demonstrates the establishment of an epitaxial relationship between graphene and GaN, which was tentatively explained by a supercell alignment depicted in Figure 4.3(b) (where lattice mismatch should be 3.1%).

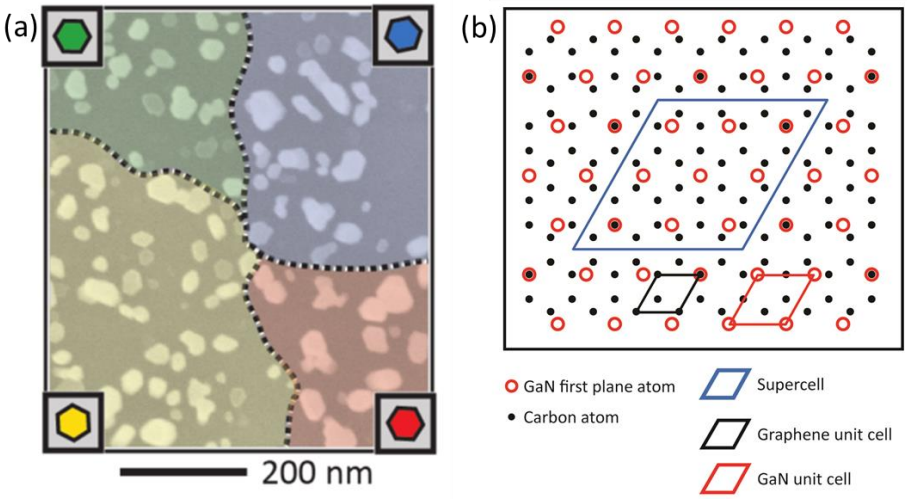

Figure 4.3 (a) Top view SEM image showing four domains (marked with different background colors) with different NW in-plane orientations. (b) Schematics of a possible epitaxial relationship between the graphene and the first atomic plane of GaN NWs. The blue diamond is the cell of coincidence of the two lattices, strained to accommodate a -3.1 % misfit[196].

These results are different compared to the ones obtained by MOVPE, where the NWs grow along several directions[198,199], unless a buffer layer is used[200] or unless graphene lies on a crystalline substrate[201], which, in turn, yields no clear evidence of epitaxial relationship between the GaN and the graphitic surface.

Despite the presence of several open questions, mainly related to the ability of graphene to withstand the GaN NW growth by PA-MBE, the preliminary results of Kumaresan et al. open a new and original prospective on the possible use of graphene to perform selective-area epitaxial growth of GaN NWs, with the ultimate objective of controlling their morphology and positioning. In this view, the aim of this chapter is to:

- Investigate the selective growth of GaN NWs on graphene domains of different sizes, transferred on a SiO_2/Si(100) surface;

- Investigate the possible modifications to the graphene crystalline and electrical properties during the growth process.

4.2 Substrate preparation and experimental methods

In this chapter, we investigate the growth of GaN NWs on three types of substrates:

Mono-layered 1 cm^2 graphene patches. Commercial mono-layered (MLG) and polycrystalline (grain size up to 20 µm) graphene patches were purchased from Graphene market. These were grown by chemical vapour deposition (CVD) on copper foils, which were also their carrying substrates for shipping.

Graphene domains with a size of about 1 µm. These were home-grown at our laboratory by A. Madouri, on Cu foils by pulsed-chemical vapour deposition (CVD) technique. The employed experimental conditions involved a gas pressure of 25 mbar, a growth temperature of 1000°C and the use of ten cycles of CH_4 (20 sccm, 5 s) and H_2 (960 sccm, 55 s). These conditions refer to the work of Z. Han et al.[202] and were applied to our commercial Aixtron BlackMagic system. To obtain separated hexagonal graphene domains, the growth was interrupted before their lateral coalescence.

Patterned mono-layered graphene patches. Graphenea MLG patches transferred on Si/SiO_2 substrates, were patterned by e-beam lithography.

The procedures used for the graphene transfer and e-beam patterning are described in the following.

4.2.1 Wet-transfer of graphene Si/SiO_2 substrates

Both MLG patches and graphene flakes domains were transferred on Si/SiO_2 substrates following the procedure described in ref. [203] and schematized in the work-flow of Figure 4.4(a). In a first step, the CVD graphene-on-copper foil was spin-coated with a ~50 nm-thick poly-methyl methacrylate (PMMA) layer. This step is essential to prevent the graphene from collapsing and thus to facilitate its handling during the transfer process. Then, the copper foil underneath the graphene was etched with a

$(NH_4)_2S_2O_8$ bath solution, leaving a floating graphene/PMMA layer on the liquid surface. This was rinsed into multiple deionized water baths, and eventually fished with a Si(100)/SiO_2 substrate, which was dried in atmosphere under the hood. Finally, the PMMA protective layer was removed by solvent cleaning (acetone, isopropyl alcohol), and the substrate was introduced in vacuum within few days from its preparation.

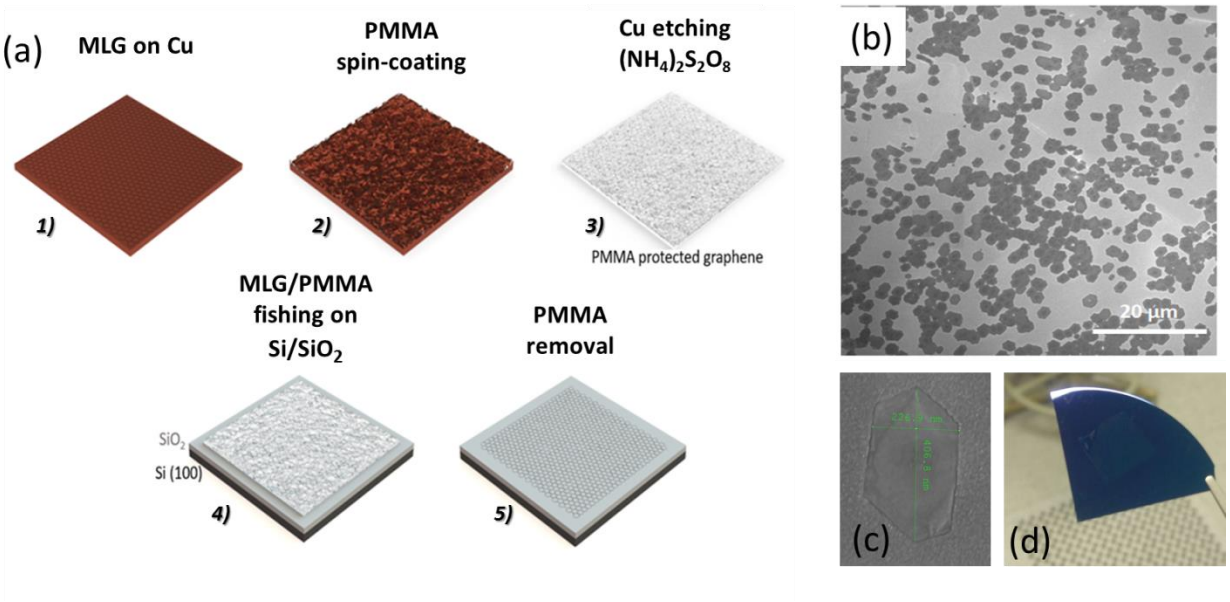

Figure 4.4 (a) Work-flow of PMMA-assisted wet transfert technique. (b) SEM image of graphene domains on Cu, synthetized in C2N laboratory. (c) Magnification of one 200 nm sized graphene flake. (d) Optical image of a as-transferred MLG patch on Si/SiO_2 substrate.

4.2.2 MLG patterning

The fabrication procedure of the patterned substrates consists of two parts: transfer of the graphene onto SiO_2/Si substrates (steps previously shown in Fig. 4.4(a)), and patterning of the graphene by e-beam lithography performed by Nan Guan. In this step (work-flow of Fig. 4.5(a)), the transferred graphene was spin-coated with a ma-N negative resist, exposed to the electron-beam, and undergone a O_2 plasma etching. Finally, the reticulated ma-N resist on the graphene dots was removed in acetone and isopropanol bath.

The mask used for e-beam lithography is shown in Figure 4.5(b). The design consists of 12 sections with dots of radii between R = 45 nm and R = 250 nm. In the same section, the dots were positioned in 5 different zones, characterized by a different pitch (0.25 µm, 1 µm, 1.5 µm, 2.5 µm and 5 µm[i]). Micrometer-size markers with a L-shape and the label of the reference dot radius were also lithographed in each section, to investigate the growth of the NWs on micro-scale graphene, and also to help to localize the NWs on the desired areas during the observations and characterizations.

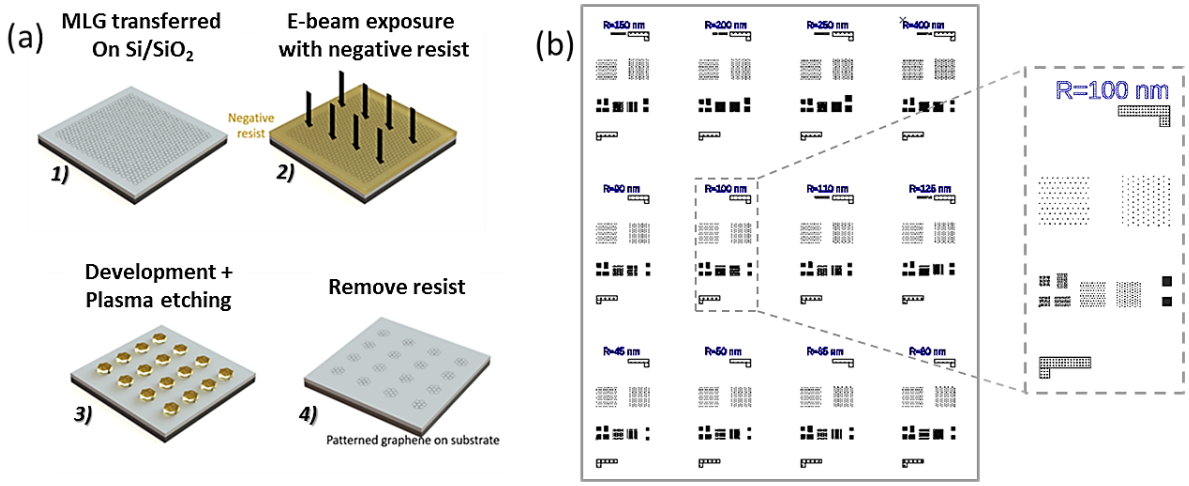

Figure 4.5 (a) Work-flow of the MLG on Si/SiO_2 patterning procedure. (b) Sketch of the mask used for e-beam lithography.

4.2.3 Raman spectroscopy for mono-layer and multi-layer graphene characterization

Raman spectroscopy is a technique that makes use of inelastic scattering of light with matter. When a laser beam is directed towards the sample, the energy of a small fraction of its photons changes after interacting with the atoms of the sample or molecules: these photons are said to be inelastically scattered, a phenomenon known as the Raman effect. This change in energy carries the information about vibrational, rotational and other low frequency modes of the material under analysis. The inelastic scattered radiation can correspond to either an excitation of the sample's phonons (the photon's energy has decreased in this case, and this part of scattered signal is called

[i] Distance between graphene dots borders.

Raman Stokes signal), or to their relaxation (the photon's energy has increased and the effect is called Anti-Stokes Raman scattering). The elastically scattered photons generate a so-called Rayleigh transition. This is sketched in Figure 4.6(a).

Graphene has very specific fingerprints in Raman spectroscopy, and can be therefore quite effectively identified by this method. In fact, Raman spectroscopy can be used to probe its structural properties, and to characterize its monolayer/multilayer nature. The most prominent features of its Raman spectra are two Stokes peaks called "G" and "2D", and a third band known as "D". These bands are sketched in Figure 4.6(b) for mono-layer, bi-layer and multi-layer graphene, and described in the following.

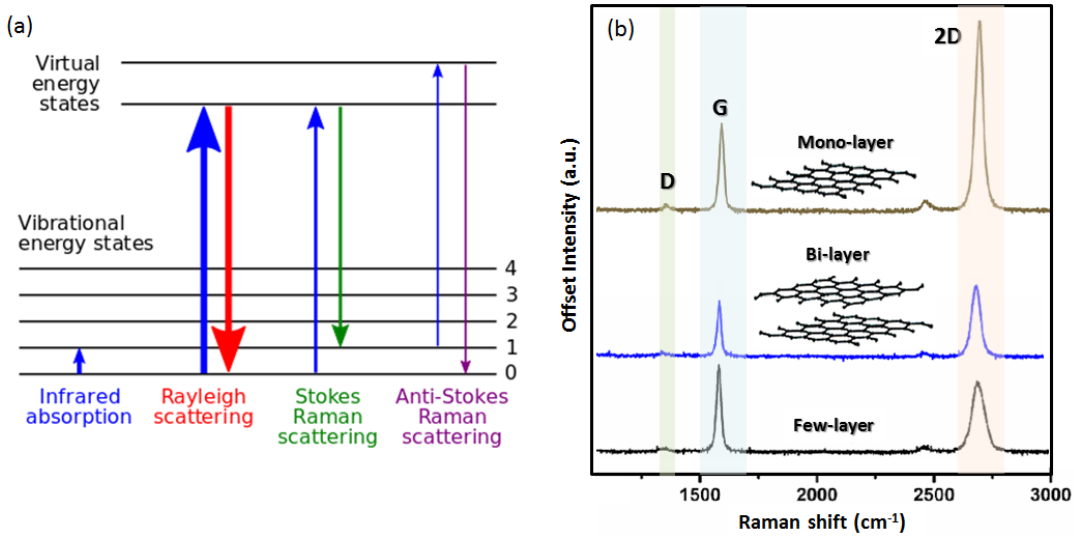

Figure 4.6 (a) Energy-level diagram, showing the states involved in a Raman spectroscopy experiment. (b) Examples of Raman spectra of a mono-layer, bi-layered and multi-layered graphene (adapted from[204]).

The G band is observed at about 1580 cm^{-1}. This corresponds to a first order (one-phonon) Raman transition originating from the zone-centre in-plane TO (transversal optical) and LO (longitudinal optical) vibrations. Its intensity is proportional to the number of graphene layers stacked, while its position can depend on many factors including graphene doping, strain and temperature. In the present chapter, we considered only the intensity of this peak.

The 2D band is observed at about 2700 cm^{-1}. It is a second order (two TO phonons) feature, with a double-resonant nature, associated to the symmetric stretching of the

graphene bonds, also known as ring "breathing" mode. For a single layer graphene, the 2D band is observed to be a single symmetric peak with a FWHM of ~30 cm^{-1}. As the number of graphene layers increases, because of added forces from the interactions between layers (in AB sequence), the 2D peak splits in an increasing number of modes, resulting in a wider, asymmetric and higher frequency peak. Thus, the number of layers can be derived from the ratio of peak intensities I_{2D}/I_G (of about 2-2.5 for MLG), as well as the position and shape of the 2D peak[205,206].

The D band peaks at about 1350 cm^{-1}. It involves the same two-phonon ring breathing mode of the 2D band, but it is activated only in presence of nearby defects such as edges, grain boundaries and substitutional dopants. The band is typically weak in monocrystalline graphene and, if significant, it indicates that there is a non-negligible density of defects in the material.

In the present work, Raman spectra were recorded with an inVia Micro Raman spectrometer system using a frequency-doubled NdYag laser operating at 532 nm. The spectrometer is a 1800 lines/mm grating allowing spectral resolution of 0.40 cm^{-1} for 10 s acquisition time. A confocal optical microscope with a ×100 objective lens was used, yielding a spot-size fixed by the diffraction limit of 300 nm. The sample sits on a piezoelectric stage which is scanned to take a Raman spectrum at specific points along the graphene sheet. The microscope's objective serves both to focus the incoming laser light onto the surface, and to gather the outcoming photons, which are then directed towards the monochromator and eventually collected by a photodiode.

4.3 Growth of GaN NWs on SiO_2/Si(100) transferred graphene

As mentioned in section 4.1, the studies of Kumaresan et al. demonstrated one very interesting advantage of the epitaxial growth of GaN NWs on graphene/SiO_2 substrates: with specific conditions GaN NWs nucleate preferentially, or even exclusively, on the graphene layer rather than on the SiO_2 surrounding matrix. This result opens new perspectives for obtaining selective area growth (SAG) of GaN NWs, i.e. for controlling their positioning in specific areas of the substrate, by modifying the dimensions of the graphene layers.

Traditionally, SAG is obtained on bulk crystalline substrates, covered by a dielectric mask in which openings are defined by lithography, and the selectivity conditions depend strongly on the epitaxy technique. For the growth techniques based on metalorganic compounds, such as metalorganic vapor phase epitaxy (MOVPE), the III-V material grows inside windows opened in the mask, since the mask does not catalyze the decomposition of the metalorganics. Therefore, the condition for SAG using metalorganic-based techniques relies mostly on the mask type and weakly on the growth conditions[207]. By contrast, in MBE (and PA-MBE makes no exception) due to the elemental sources, the realization of the SAG is not achievable in a wide range of growth conditions. In fact, in principle, the selectivity mechanism is strongly related to the difference in sticking and diffusion processes of group-III elements within the holes and on the mask. These processes are largely influenced by the growth temperature. Thus, to have more insight into the SAG growth of GaN NWs on graphene, we investigated the effect of the substrate temperature for GaN NW growth on large graphene patches.

4.3.1 Growth on graphene large patches: optimization of selectivity

The growth of GaN NWs was carried out under the same flux conditions used by Kumaresan et al., namely a V/III ratio of 1.1, with a Ga flux corresponding to a 0.62 ML/s equivalent GaN growth rate, and a total deposition time of 3 hours. The effect of the growth temperature on the NWs formation is illustrated in figure 4.7 for graphene patch substrates. At the lower substrate temperature in this series (805 °C, figure 4.7(a,b)), well-developed GaN NWs are grown in high density on both the SiO_2 matrix and the areas where graphene was transferred. Importantly, the NWs on graphene are highly vertical and show a clear in-plane orientation, while on SiO_2, their twist and tilt are more pronounced (insets of fig. 4.7(a)). The growth is quasi-selective at 810 °C, with few short NWs nucleated on SiO_2 and well-developed NWs on the MLG Fig. 4.7(c,d)). The perfect selectivity is attained at 815 °C, with no NWs on the SiO_2 mask and high-density vertical NWs on graphene (Fig. 4.7(e,f)). However, when the temperature is increased by only 5 degrees, the NW density decreases sharply (Fig. 4.7(h,g), and above 820 °C no growth is observed.

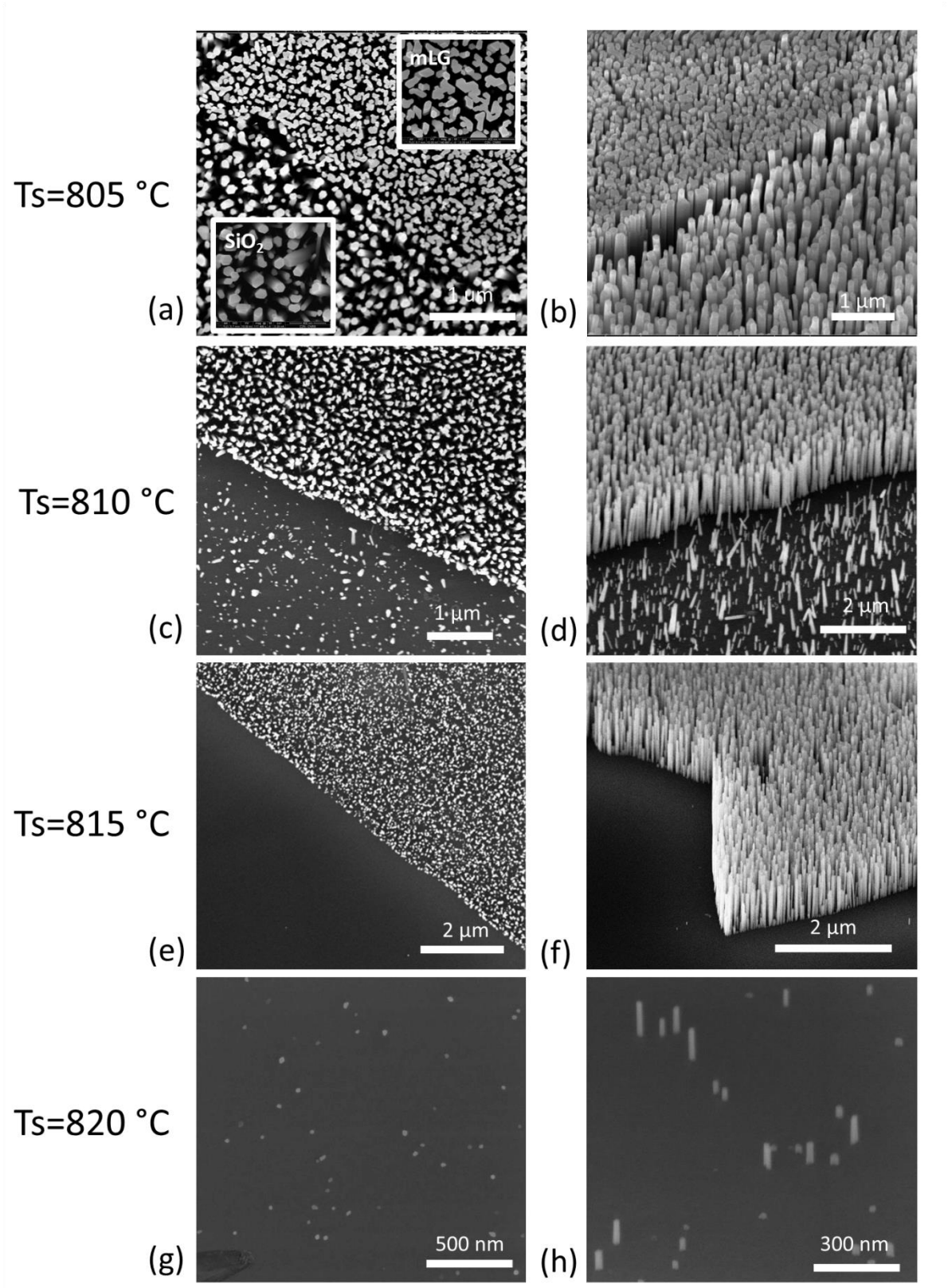

Figure 4.7 Top-view (left column) and 45° tilted view (right column) SEM images of GaN NWs grown on transferred MLG at different temperatures: (a,b) 805 °C, (c,d) 810 °C, (e,f) 815 °C, (e,f) 820 °C.

From these results, it is clear that the GaN NWs grow preferentially on SiO_2 in the 810-815 °C temperature range. However, for growths in these conditions, the first specular RHEED spot appears systematically after a deposition time of about 1 hour at 810 C°[ii] and 1 hour 20 minutes at 815 °C. The long incubation times indicate a very low nucleation probability (per area and time unit) on graphene, most probably associated to a very high desorption rate of Ga from the graphene surface. This statement is supported by the fact that at lower growth temperature, Ga desorption decreases, and the NW nucleation accelerates[208]. Therefore, since the NW incubation time is long and it increases exponentially with temperature[208], a small increase of temperature is sufficient to inhibit the growth also on the graphene, resulting in a sharp transition from selective growth to no growth at all.

This narrow temperature window for selectivity creates problems in obtaining selective growths on graphene with a good level of reproducibility. In fact, the lack of a physical temperature-dependent phenomena related to these substrates, as for instance the 7x7 reconstruction stability on oxide-free Si(111) surfaces, does not allow an easy and reliable in-situ calibration of the substrate temperature. As a result, from our experience, the use of Si substrates with different oxide thicknesses, the progressive coating of the pyrometer window or even the use of different sample holders, generate a bias in the pyrometer reading, which can be sufficient to loose selectivity. To tackle this problem, we opted for a practical approach: before all growth series on transferred graphene substrates where selectivity was required, we routinely performed 2-3 growths on these "reference" graphene patches. The correct pyrometer temperature for selectivity on a given molyblock was then identified, by adjusting the growth temperature to obtain a 100% selective growth of ~1 µm long GaN NWs (reference NW length for 4 hours of total deposition time in perfect selectivity, not shown). Then, the same sample holder was used for all subsequent growths.

[ii] At this temperature the NWs density and length is much higher on graphene than SiO_2, thus it is resonable to assume that the NW nucleation signature observed by RHEED corresponds to nucleation on graphene.

4.3.2 Growth on graphene domains

GaN NWs were grown under identical fluxes and temperature conditions on µm-size graphene transferred domains. These gave absolutely compatible results, namely a loss of selectivity for temperatures below 815 °C, and no growth for temperatures above 820 °C. For instance, Figures 4.8(a) depicts a growth carried out in selective conditions (815 °C), where no NWs are present on the SiO_2 matrix surrounds the hexagonal graphene domains.

The reader might notice that on the majority of the domains, the GaN NWs nucleate preferentially on the edges (so-called "hollow" domains), and their density and diameter decrease sharply when moving to their central region (Fig. 4.8(b)). In fact, only few graphene domains present a dense and homogeneous NW coverage (so-called "full" domains, Fig. 4.8(c)). In all cases, a clear in-plane orientation of the GaN NWs is always observed, with their m-planes aligned to the zig-zag edges of the graphene domains. This is consistent with the GaN to graphene epitaxial relationship proposed by Kumaresan et al., and is shown for a "full" graphene domain in Figure 4.8(d).

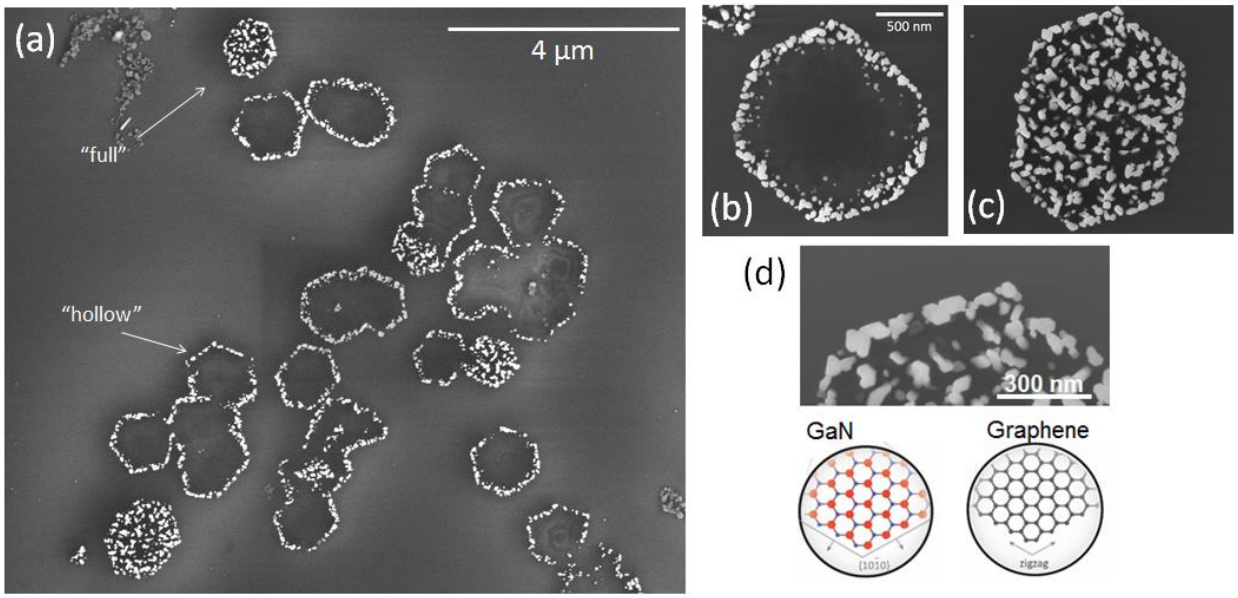

Figure 4.8 (a) Top-view SEM image of GaN NWs grown on Si/SiO_2 transferred graphene domains. (b,c) SEM views of one "hollow" and "full" graphene domain, respectively. (d) Top-view SEM image, zoomed at the edge of the domain showing the orientation of the NWs facets; the insets show the orientation of the GaN NWs m-planes and the graphene zigzag edges at the periphery of the hexagonal flake.

These samples are characterized by a mixture of mono-layered domains and multi-layered domains with an inverted-ladder geometry. This bi-modal population is believed to depend on whether or not the graphene layer forms on a Cu defective site (Fig 4.9(a)). Generally, after the catalytic decomposition of CH_4 precursors on the Cu surface, C atoms diffuse and eventually rearrange in a sp^2 hybridization (with no chemical bonding to the Cu surface). This process leads to the nucleation and lateral growth of graphene domains of strictly 1 ML (left side of Fig. 4.9(a))[209]. However, if the growth takes place in proximity of a defect, C atoms can diffuse within the Cu substrate, and when they re-emerge, they incur into subsequent nucleation and growth events. These processes lead eventually to the growth of a multi-layered graphene[210,211] with an inverted-ladder structure (right-side of Fig. 4.9(a)), i.e. with a number of layers which increases from the edge of the domain towards its center.

Kumaresan et al. demonstrated the existence of a relationship between the number of atomic layers composing the graphene substrate and the density of the GaN NW array growing on their top[196]. Specifically, it was shown that the NW nucleation is progressively delayed when the number of monolayers is increased, resulting in shorter, thinner and more sparse NWs. Such a behaviour was tentatively ascribed to the partitioning of the interfacial strain between the graphene and the GaN nucleus, where a higher number of graphene layers increases the elastic energy stored in the system and hence elevates the NW nucleation barrier. In this view, the growth of "hollow" GaN NW domains can be assigned to the inverted-ladder structure of the graphene domains underneath, and specifically to the fact that only on the domains' edges the graphene thickness equals one monolayer.

To verify this point, we performed Raman measurements on several graphene domains before the growth[iii] (blue line in Fig. 4.9(b)) and on several "hollow" domains after the growth (red line in figure 4.9(b)). The observed blue-shifted and asymmetric 2D peaks clearly indicate that the graphene domains are not mono-layered, giving support to our statement. In our Raman experiment, the spatial resolution was too low (300 nm

[iii] In our Raman experiment, the spacial resolution is to by the laser spot diameter (300 nm), thus for µm domains the output of one point-type measurement integrates on almost the whole domain area, not allowing to resolve its « pyramidal » stracking.

diameter, 532 nm wavelength) to resolve the inverted-ladder MLG structure. However, the secondary electron contrast of Figure 4.9(c), clearly shows that multiple stacks might be present. These results tend thus to support our hypothesis.

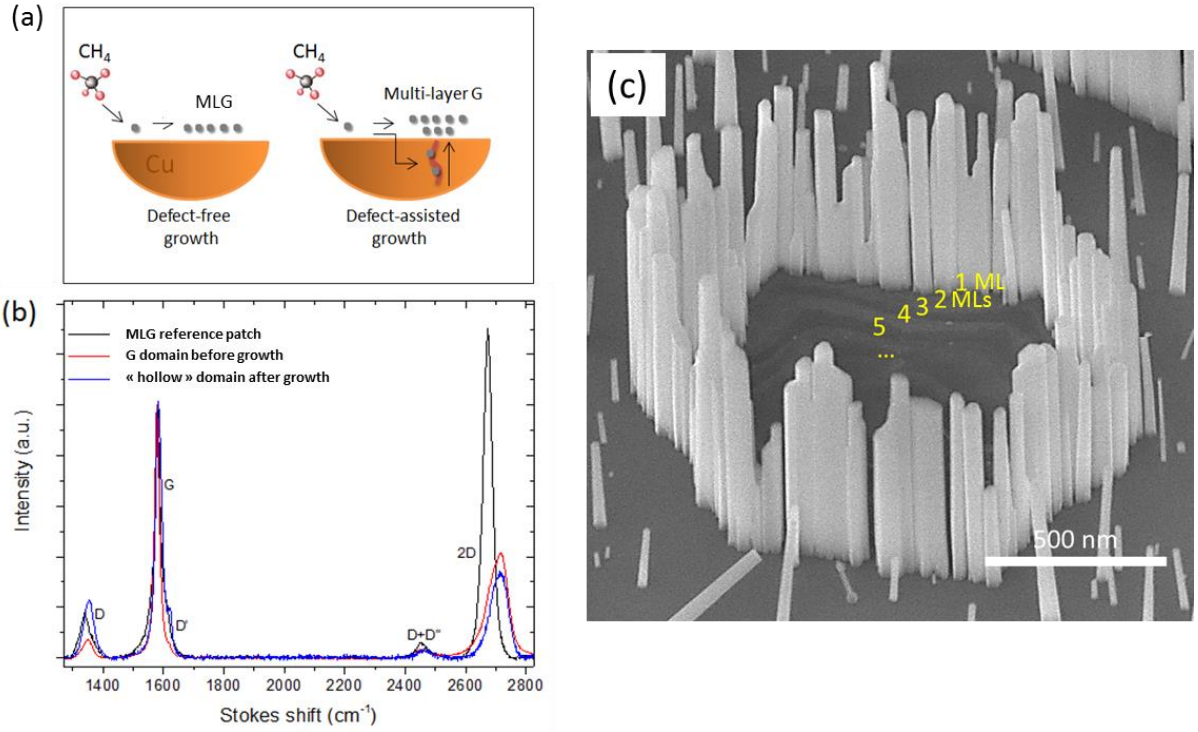

Figure 4.9 (a) Schematic showing the defect-free and defect-assisted growth of ML and multi-layered graphene domains by CVD. (b) Raman spectra of a reference MLG patch, of a graphene domain before the growth and a "hollow" GaN NWs/graphene domain after the growth. (c) Tilted-view SEM image showing a layered contrast within a hollow domain grown at 810 °C, possibly reflecting the multi-layered staggered structure of the graphene domain.

4.3.3 Effect of the NW growth and long incubation time on the MLG properties

The long NW incubation times do not only affect the reproducibility in terms of GaN NW growth, but also saws a doubt on possible modifications of the graphene by N-plasma exposure. As mentioned previously, Ramsteiner et al.[70] demonstrated that graphene directly grown on SiC substrates exhibits a weak stability under N-plasma exposure: in their case, growth of GaN NWs by PA-MBE could be observed only on multi-layer graphene, since MLG was totally etched by the N plasma as verified by

Raman spectroscopy. Furthermore, exposure to N-plasma is known to promote N incorporation/doping in the graphene layers, by breaking the carbon rings and forming N-C complexes with different bonding configurations[205,212]. This results in a loss of its semi-metallic properties and, in an increase of its defectivity[19]. Hence, we investigated the graphene properties after GaN NW growth, as well as after a N-plasma exposure whose duration is comparable with the NW incubation time.

<u>Graphene properties after growth</u>

Figure 4.10(a) depicts a top-view SEM picture of one sample grown at 810 °C (quasi-selective conditions). The area corresponds to a defective site of the sample, where the NWs are misoriented (Position 1, P1 in Fig. 4.10(b)) and in-plane oriented (Position 2, P2 in Fig. 4.10(c). In some positions at the periphery of this defective region, the SEM contrast denotes the presence of a "rolled" graphene sheet (Fig. 4.10(d), suggesting that such defective regions aroused from some mechanical damage of the graphene, possibly occurred during its transfer process. Nevertheless, in most of the peripheric positions, the graphene is clearly visible at the base of the NWs (Position 4, P4 in Fig. 4.10(e)).

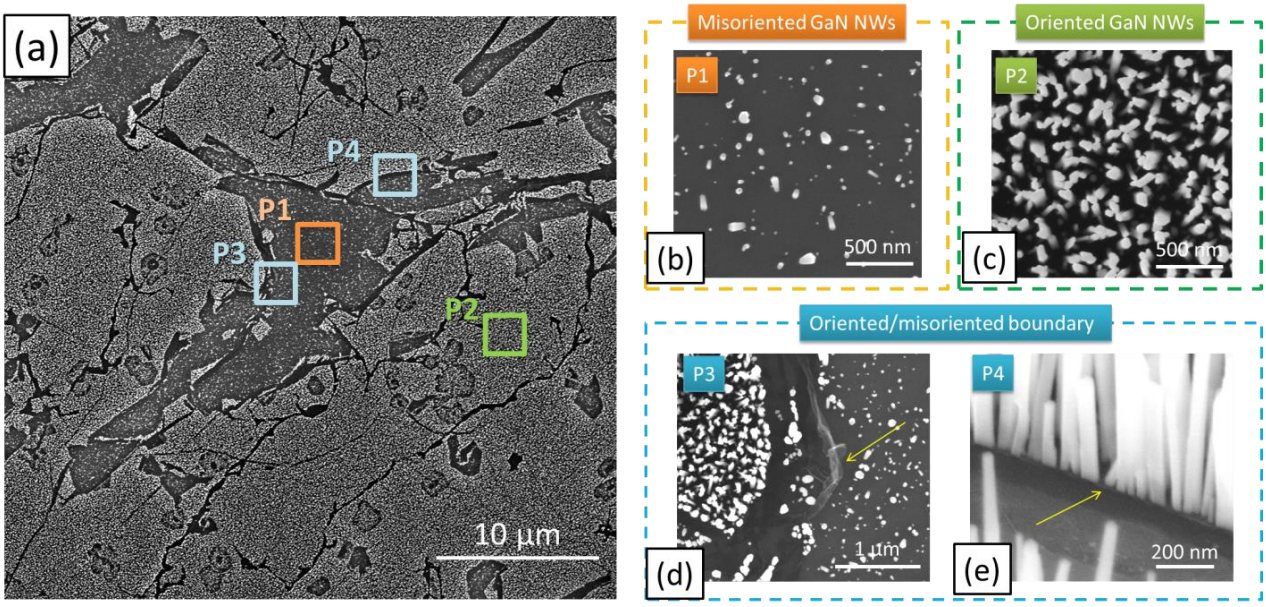

Figure 4.10 (a) Top-view SEM picture of a defective region of a graphene patch, where GaN NWs have been grown for three hours under quasi-selective conditions (810 °C). (b-d) top-view and (e) 45° tilted view of different regions of the sample (P1, P2, P3 and P4 in (a)).

Raman spectra were acquired in the same region of the samples, by focusing the spot in the different positions previously denoted by P1, P2 and P4 (the optical microscope picture is shown in Figure 4.11(a)). Consistently with the presence of short and misoriented NWs, in P1 none of the peaks characteristic of graphene was detected, and the Raman spectra were dominated by a weak signal peaked at about 1450 cm^{-1} (Fig 4.11(b)). This peak is systematically observed on samples presenting GaN NWs, and can be assigned to a second order overtone of the A_1 longitudinal optical mode of GaN[213,214]. When the spot is focused in the region where dense and oriented NWs are present (P2), the G and 2D peaks are generally not observed in normal acquisitions, and only by using a high excitation power, they slightly overcome the base-line noise (Fig. 4.11(c)). This suggests a strong scattering of the impinging laser and/or backscattered signal by the NW array. In fact, by focusing the laser on the boundaries of these areas (P3, Fig. 4.11(d)), both the G and 2D peaks present a much higher intensity due to the enhanced laser penetration and/or signal collection. This measurement was repeated in several peripheral positions similar to P3, giving compatible (if graphene was "rolled up") or identical results. Specifically, the systematic appearance of a strong and symmetric 2D peak confirmed the presence of a MLG underneath the NWs (FWHM ~ 33 cm^{-1}).

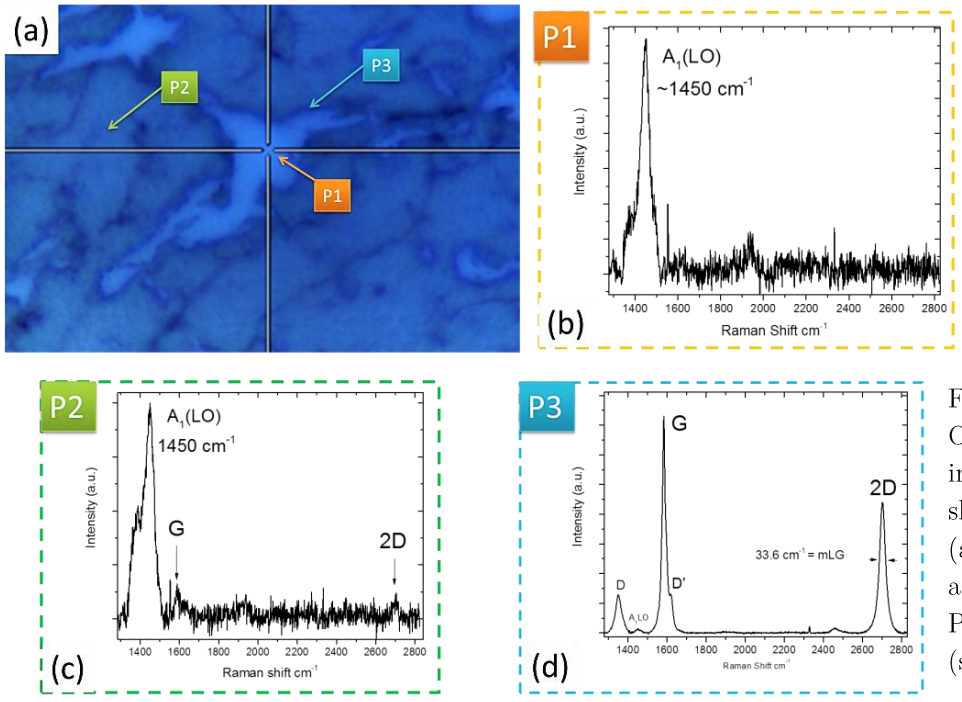

Figure 4.11 (a) Optical microscope image of the region shown in Fig. 4.10(a). (a-c) Raman spectra acquired in positions P1, P2 and P3 (shown in (a)).

Effect of the N-plasma exposure on the MLG electrical properties

To investigate the possible modifications of the graphene properties during the growth incubation time, we analyzed the Raman and I-V characteristics of two samples: one as-transferred MLG patch on Si/SiO_2 substrate (sample A), and one nominally identical sample, exposed to the N-plasma flux for 1 hour (350 W RF power, standard configuration used for GaN NW growth) at a substrate temperature of 800 °C (sample B).

Figure 4.12(a) shows the Raman spectra averaged across a 25 μm^2 region of the samples, while Figures 4.12(b,c) shows the corresponding I-V characteristics measured in a conventional 2-probe configuration[iv].

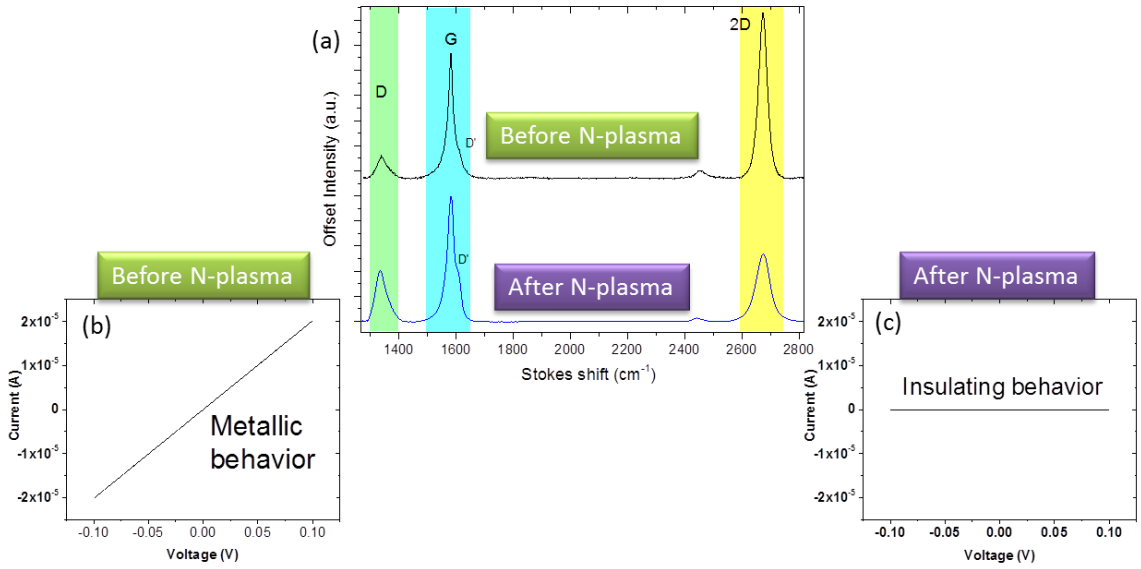

Figure 4.12 (a) Raman spectra acquired before and after 1 hour of N-plasma exposure in MBE environment (800 °C). (b,c) I-V characteristics of two nominally identical MLG transferred patches before and after plasma exposure, respectively.

For both samples, the Raman fingerprints of pristine graphene are present: the D band (~1350 cm^{-1}), G-band (~1570 cm^{-1}) and a symmetric 2D band (~2680 cm^{-1}). However, after N-plasma exposure, the intensity of the 2D peak appears reduced (I_{2D}/I_G from 1.84 to 1.0 after N-plasma), while the defect-related D band intensity is substantially increased (I_G/I_D from 3.2 to 1.7 after N-plasma), with no detectable spectral shifts. In parallel, while sample A exhibits ohmic I-V characteristic (albeit with a relatively high

[iv] With Ag contacts deposited at the corners of the cm-size graphene patch.

resistivity of ~1 kΩcm), sample B is characterized by a clear insulating behavior (current is below 10^{-11} A under 1 V applied bias). Since the 2D-band reflects the band structure of the graphene, and the D band is related to defects or non sp^2 bonding, this preliminary analysis suggests that during the growth incubation time, the N-plasma might generate a sufficiently high density of defective sites killing its long-range electrical conductivity. This could be related to the much higher RF powers employed in MBE (350 W in our case), compared to the mild conditions employed to obtain N-doped graphene (typically 50 to 100 W).

As a general conclusion, these findings suggest that ML transferred graphene might be not usable as a bottom-contact layer in III-N functional NWs grown by PA-MBE. However, despite its increased defectivity, our Raman investigations after both GaN NW growth and after N-plasma exposure indicate that the MLG sheets are able to withstand a standard growth process in our experimental conditions. This must imply that the graphene honeycomb crystal structure is sufficiently preserved to allow a good coincidence between the GaN and graphene lattice. Only this statement could justify the observation of in-plane oriented NWs on large areas of the patch[196], and is an argument in favor of its use as a seed layer for SAG epitaxial approach. However, it cannot be excluded at the present stage, that the presence of localized defects (edges and/or N substituted sites) could be helpful for the NW nucleation. Indeed, it is a general fact that NWs can easily nucleate in correspondence of morphological and/or chemical defective sites. Further investigations are currently carried out by our research group in the framework of a Ph.D. work to clarify this complex and intriguing scenario of possibilities.

4.3.4 Optical properties of III-N NWs on graphene

μ-PL measurements with excitation wavelength of 244 nm were carried out by L. Mancini on NW arrays and single dispersed NWs grown on: transferred graphene 1 cm^2 patch (sample C) and Graphene sub-micrometric domains (sample D). Both growths were carried out at 815°C for 3 hours under selective conditions.

GaN NWs on transferred graphene patches

Sample C was analysed at 5 K in a continuous He flux cryostat. Laser incident power of around 1 μW and 100 μW were used for NW arrays and single dispersed NWs,

respectively. The generated PL signal was dispersed with an 1800 grooves/mm grating in a 460 mm focal length spectrometer allowing for a spectral resolution of around 0.5 meV, and collected by a LN2-cooled silicon charge-coupled device (CCD).

Fig. 4.13 reports the SEM images and steady-state µPL spectra acquired for a NW array on MLG patch (a,b) and on standard Si(111)/AlN substrate (c,d). The systems exhibit a near band edge emission dominated by the donor bound exciton recombination process (D^0,X_A), peaked around 3.471 eV. Its spectral broadening (FWHM) is 1.1 meV for the AlN/Si(111) substrate and 2.6 meV for NWs on graphene/SiO_2/Si(100). Contributions from the free exciton recombination (F,X_A) at 3.478 eV and donor bound exciton recombination (D^0,X_B) (on graphene) are also observed. Importantly, the broad emission at 3.45 eV which, corresponds to excitons bound to IDBs is absent on graphene substrates. We note that indeed IDBs were never observed in grown-on-graphene NWs by structural analyses. In 2D GaN layers this type of defects is usually assigned to the GaN growth on ML stepped Si(111) surfaces with AlN buffer layers, as they are not observed for Si surfaces covered by amorphous SiN_x[215]. A similar mechanism could, in principle, apply also to GaN NWs grown on AlN/Si(111) substrates and hence justify their absence on graphene/SiO_2. Further investigations are needed to confirm this point.

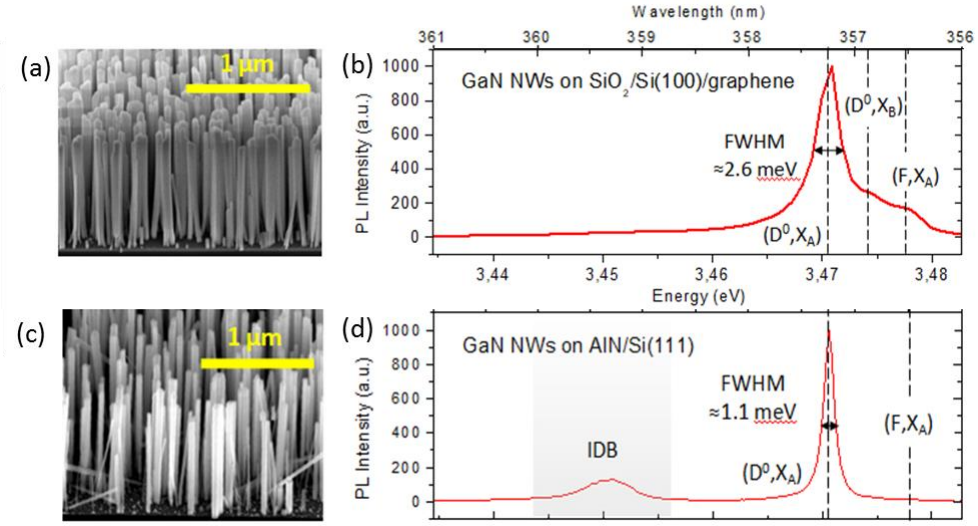

Figure 4.13 (a,b) Tilted view of GaN NWs grown on MLG patch transferred on SiO_2/Si (a) and on AlN/Si(111) substrate (b), with the corresponding µPL spectra (b,d respectively) measured on NW arrays.

The spectral signature of the grown-on-graphene NWs was further addressed by performing µPL analysis of single dispersed NWs. Figure 4.14 reports spectra acquired

from 3 individual NWs. Sharp D^0,X_A peaks with a spectral broadening as low as 1.3 meV (NW1) were observed. The broader emissions of NW2 and NW3 can be ascribed to the convolution of peaks corresponding to the Si and O donor bound recombination processes (Si_0,X_A) and (O_0,X_A). The spectral shift of NW3 can in turn be ascribed to the influence on the emission energy of the diameter of the NW[216].

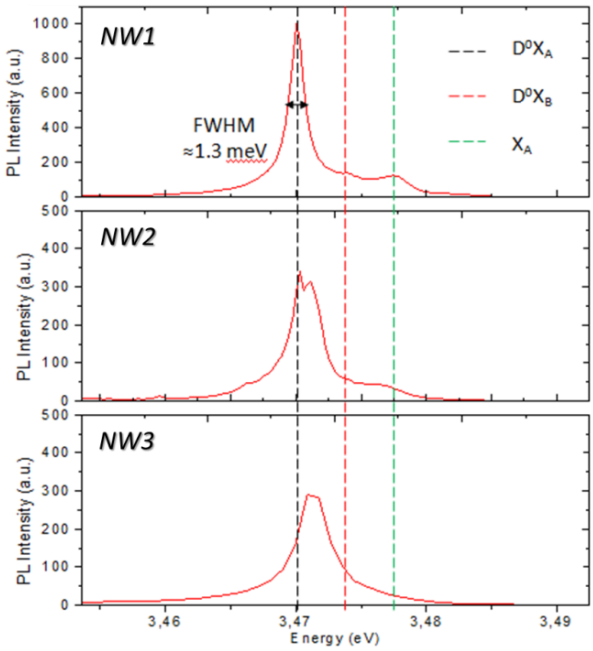

Figure 4.14 µPL spectra of three single GaN NWs grown on MLG patch transferred on SiO_2/Si substrate.

GaN NWs on graphene domains

GaN NWs grown on multi-layer graphene domains (Fig. 4.15(a,b)) were analysed at PDI by C. Sinito under continuous 324 nm laser excitation through a M Plan APO NUV HR 50x objective with NA=0.65, providing an excitation density going from 900 W/cm to 9 kW/cm. Samples were cooled down to 10 K and the emitted signal was dispersed by 2400 grooves/mm spectrometer grating allowing for a spectral resolution of 250 µeV within the considered spectral range. In Figures 4.15(c,d) are reported two steady-state µPL spectra acquired by focusing the laser on two different domains. Vertical dashed lines highlight the energy values corresponding to donor-bound (O_0,X_A), (Si_0,X_A), (O_0,X_B), acceptor-bound (A_0,X_A) and free (FXA) exciton recombination processes for bulk unstrained GaN[217–219].

The spectra consist of multiple narrow lines generated by a small number of NWs contained within a single graphene domain. The sharp peaks characterizing the spectra

could be unambiguously attributed to one of the main excitonic transitions by taking into account their relative energy differences: as previously observed for NW arrays, the emission is dominated by donor bound exciton, but in this case, the higher spectral resolution ensured by the experimental setup and the relatively small number of excited NWs allow for distinguishing the contributions from the oxygen and silicon donor-bound excitonic recombinations (O_0,X_A) and (Si_0,X_A), separated in energy by 0.8 meV.

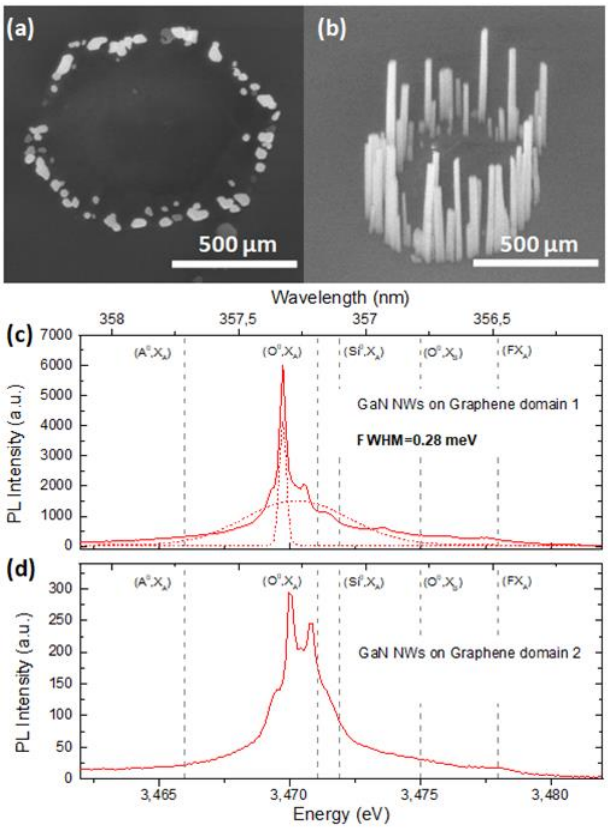

Figure 4.15 (a) Top-view and (b) tilted view SEM images of a hollow GaN/graphene domain. (c,d) µPL spectra acquired for two different domains.

Both spectra reported in Fig.4.15(c,d) show oxygen and silicon donor-bound excitonic transitions which are red-shifted of around 1 meV with respect to the energies of the corresponding transitions expected for unstrained GaN. The lowering in energy of these transitions can be ascribed to the micro-strain introduced by the coalescence of adjacent NWs [220–223]. In Figure 4.15(c) the Gaussian fit of the O^0,X_A transition peak is reported (red dashed line). The spectral broadening of the fitted peak is the smallest observed for the grown-on-graphene NWs, with a FWHM of only 0.28 meV (i.e. at the

limit of the spectral resolution, which was 0.25 meV). It is worth noting that, to the best of our knowledge, the state of the art in terms of broadening for GaN NWs grown on crystalline substrates is 0.4-0.5 meV[224]. It should also be pointed out that no emissions around 3.45 eV ascribable to IDB transitions were observed also for NWs grown on graphene domains.

From these results we can conclude that GaN NWs grown by PA-MBE on monolayer graphene on SiO_2/Si(100) and multi-layer graphene domains present state of the art optical properties and show no emission from excitons bound to IDBs.

4.4 SAG of GaN NWs on patterned graphene

The selective growth of GaN NWs was studied in a set of samples where 1 cm^2 MLG patches where transferred on SiO_2/Si substrates (300 nm thickness of thermal oxide) and subsequently patterned by e-beam lithography. The steps involved in obtaining micro-and nano- graphene patterns are described in section 4.2. The growth presented in the following, involved 3, 4 and 6 hours of a total exposure time ("short" - 3 hours - and "long" - 4 and 6 hours - growths, respectively), at a V/III ratio of 1.1 (Ga equivalent flux (in GaN planar growth rate) of 0.62 ML/s) and at 815°C. These growth rate and flux conditions are identical to the ones employed by Kumaresan et al[196].

4.4.1 "Short" growth

Figure 4.16 depicts the results obtained on micrometer-size markers. As can be seen, the growth is perfectly selective, with high-density vertical GaN NWs nucleated on the graphene markers, and no NWs on the SiO_2 matrix. Also, the morphology of the markers is well preserved, indicating that the MLG is well preserved after the whole process of e-beam lithography, and growth.

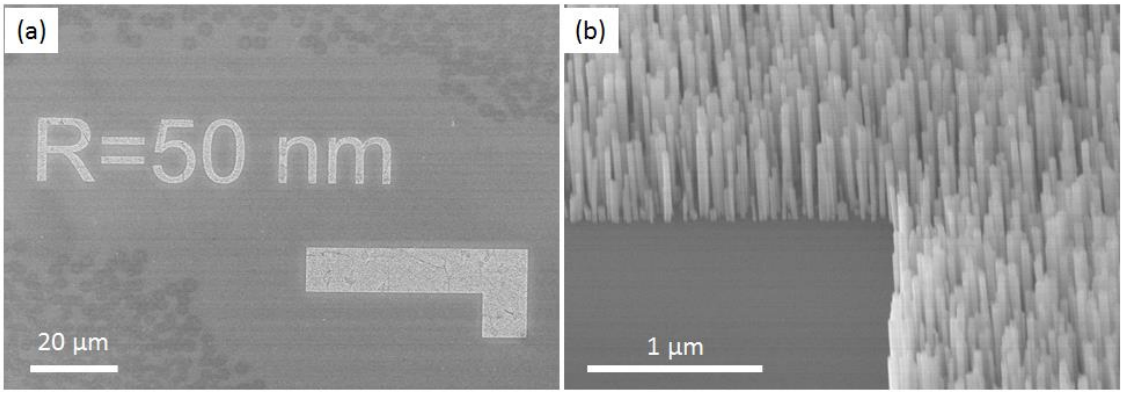

Figure 4.16 Top-view (a) and 45° tilted-view (b) of GaN NWs grown on micrometer-size patterned markers.

For the same sample, when looking to graphene dots of 100 nm radius (pitch 2 µm), their hexagonal pattern can be easily recognized (Figs. 4.17(a,d), since multiple NWs nucleated in most of the dots that compose the matrix. However, the main difference compared to big markers, is that the GaN NWs appear much shorter (their length is of about 300 nm on these graphene dots, while it is of about 600 nm on the markers), and they do not occupy the whole area supposedly covered by graphene (Fig. 4.17(b,c,e,f)). Also, their number varies a lot between different dots (from 1 NW up to 11 NWs).

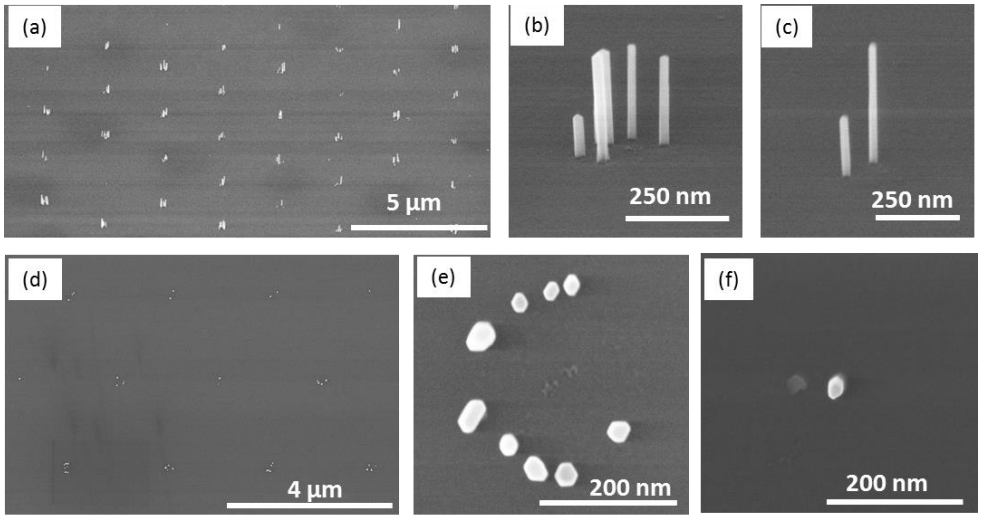

Figure 4.17 (a-c) Tilted-view and (d-f) top-view of GaN NWs grown in correspondence of patterned graphene dots of 200 nm diameter.

For dots presenting three or more NWs, it can be readily seen that these nucleate preferentially at the dot periphery (Fig. 4.17(e,f)). As will be further shown, this

phenomenon is observed also for longer growth times. Importantly, the clear in-plane orientation (Fig 4.17(e)) of the NWs indicates that they are epitaxial. Hence, they must nucleate on the graphene border, and not on SiO_2 at the step edge with graphene.

Recent simulations performed by molecular dynamics evidenced that the adsorption energy of Ga on graphene is enhanced by the presence of vacancy "core" defects or dopants, compared to pristine graphene[225]. Also, in some cases the presence of oxygen functionalities at the graphene surface provides reactive sites for the nucleation and growth of nanoparticles[226,227]. The graphene edge in the ideal armchair and/or zigzag geometries can be considered as "closed", i.e. with fully coordinated sp^2 bonds[228]. However, the reactivity of edges in comparison with pristine graphene is much higher (following the reactivity sequence zig-zag>armchair>>pristine), and can be substantially enhanced in presence of defects (such as C dangling bonds, possibly created by the lithography process)[229]. All these factors could make the edges more incline to chemical and/or structural modifications (for example reconstructions[229], N-incorporation induced by N-plasma[212] or even Ga incorporation[225]). At this stage, it is not possible to establish which characteristic of the graphene edge might favor NW nucleation. However, these basic considerations support the idea that the Ga adatoms stability could be enhance by local (structural or chemical) perturbation from an ideal (pristine) bonds configuration.

If the graphene dots radii are further decreased to 50 nm (Fig. 4.18(a)), single vertical NWs are observed in the majority of the dots, while few positions present a 2 to 3 NW occupation (~5%), and many dots (~30%) are empty (pink arrows in panel (b)). Also, the NW lengths are further reduced compared to 200 nm diameter dots (from about 300 nm on 100 nm dots radii to about 250 nm for 50 nm dots radii).

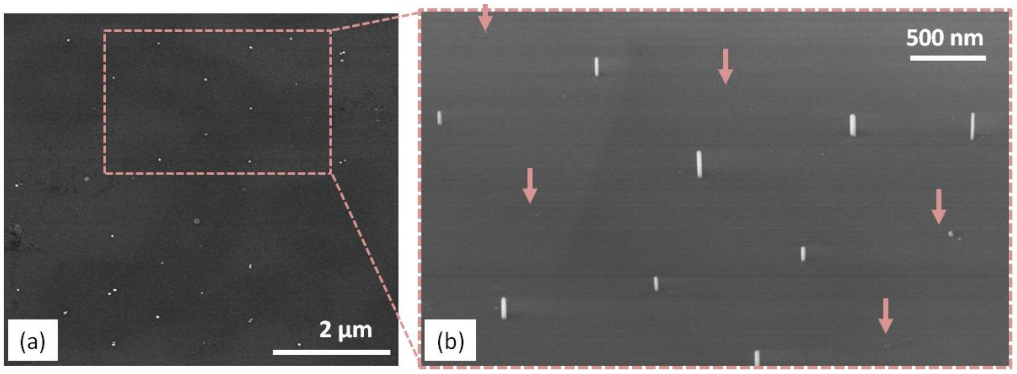

Figure 4.18 Top-view (a) and 45° tilted view SEM images of GaN NWs grown on patterned graphene dots of a 50 nm diameter. The pink arrows indicate empty positions in the pattern.

These results show that SAG of GaN NWs by PA-MBE is possible via transferred graphene patterning. However, the conditions for SAG are still not optimal if one wills to tailor the formation of GaN NWs with a well-controlled positioning and morphology. In fact, single occupation is obtained only for dots of 50 nm radius (2 times larger than a typical NW diameter), and still there are many missing NWs.
These results could saw a doubt on possible damages occurred to the graphene dots during the patterning and/or on the growth processes. Specifically, dots of smaller size could potentially detach from the substrate, or deteriorate due to the N-plasma in such a way that the NW nucleation is not possible anymore. In fact, in this work, we occasionally encountered problems of adhesion of graphene, which ultimately lead to the collapse of the whole pattered structure. However, the decreased NW length for decreased dot size, the high length dispersion observed for all analyzed dots, and the incomplete occupation of the 200 nm diameter dots surface (i.e. decreased NW density), could also suggest a delayed nucleation of the NWs on dots presenting a small lateral dimension.
To further investigate this point and, more generally, the SAG growth on transferred graphene patterned substrates, we tried to increase the GaN deposition time.

4.4.2 "Long" growths

Figure 4.19 depicts top view and side-view SEM images of GaN NWs grown under nominally identical conditions, but for a total GaN deposition time of 4 hours.
Different dot dimensions from 200 nm down to 50 nm radius are shown (inter dot pitch is 250 nm).
For the SEM images (Fig. 4.19(a,d,g,j)), it can be clearly seen that even for a growth of 4 hours, the selectivity is preserved, and only minor parasitic growth of NWs is observed along line-shaped regions. Due to the rather vertical orientation of the NWs grown in these regions, we suppose that these defects form due to a non-perfect RIE removal of the graphene during the patterning process. Specifically, it could occur in positions where graphene forms "wrinkles". More importantly, for all the considered dot radii, 99.9% of the matrix sites are occupied by NWs, and the remaining 0.1% is clearly associated to defects in the pattern (see Fig. 4.19(d)). Specifically, for each dot dimension, multiple NWs are observed (high magnification top-views in Fig.

4.19(b,e,h,k). This observation strongly supports the argument that the reduced NW length and density evidenced for a shorter growth time, do not result from a damage of the graphene dots, but rather from a size-dependent delayed nucleation.

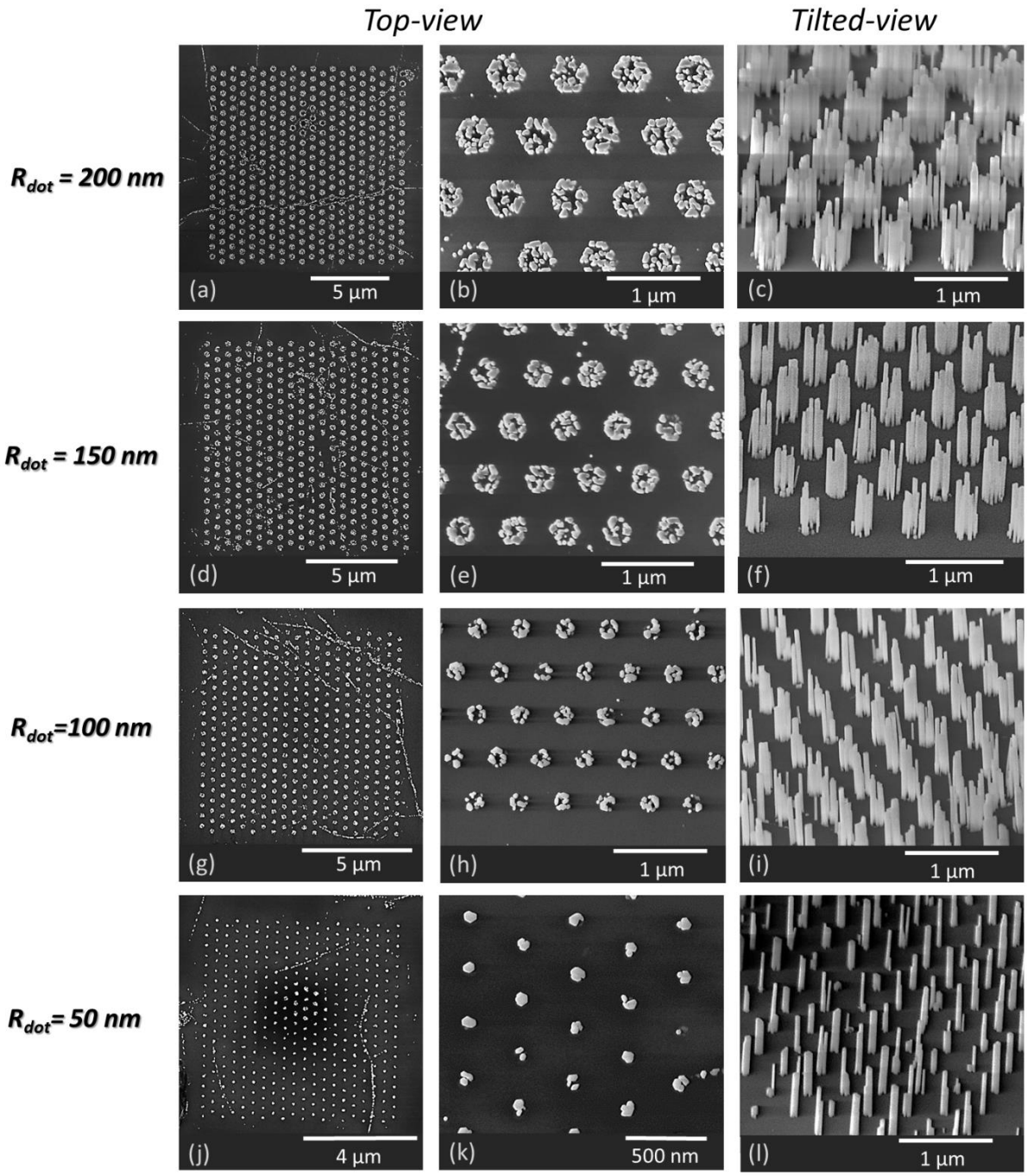

Figure 4.19 Top-view and 45° tilted-view SEM images of GaN NWs grown on patterned MLG for a total deposition time of 4 hours. Rows correspond to the dot radii labeled on the left.

Compatible results in terms of selectivity, were obtained for a total growth time of 6 hours. Representative images of this growth are shown in Figure 4.20. However, in this case, the sample was defective on many areas, with missing or damaged patterns, especially for the lower dots dimeters (Fig. 4.20(d)). Also, a high density of "wrinkle" defects leading to parasitic growth was observed (on the SiO_2 outside from the patterned area of the sample, no growth was observed). Thus, all the further analysis discussed in the chapter, have been performed on the much more successful growth of 4 hours duration.

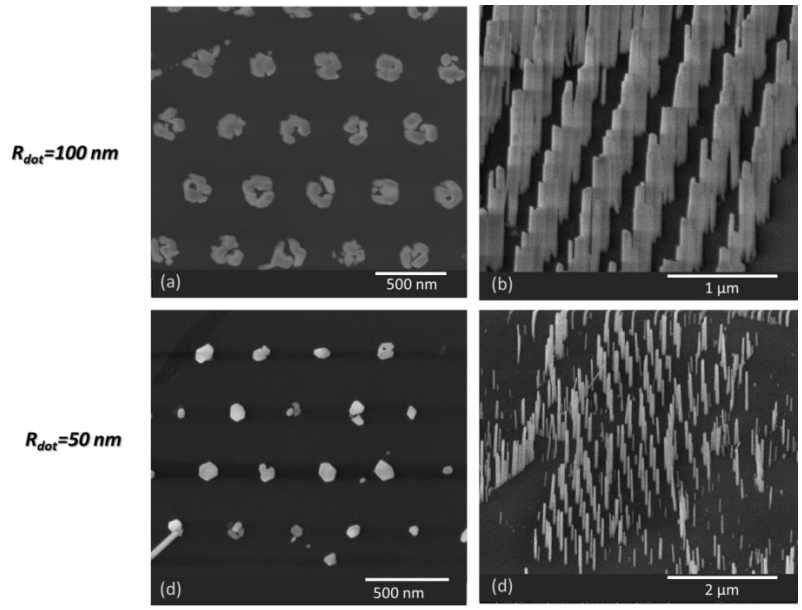

Figure 4.20 Top view (a,c) and 45 tilted view (b,c) SEM images of GaN NWs grown on patterned graphene for a total deposition time of 6 hours.

The fact that all the graphene dots are "filled" after 4 hours of growth, does not guarantee itself that the nucleation stage of the NWs is fully completed. In fact, all dots radii and especially the smaller ones (Fig. 4.19(l)), show significant NW length dispersions. More insight on this aspect can be provided by evaluating the occupation rate of the dots, i.e. the fraction of dot surface occupied by NWs. On top-view images (Fig 4.21(a)), the edges of the NWs (or coalesced NW clusters) were detected with the software IMAGEJ, and the per-dot surface coverage (S_{NW}) was estimated in ~30 single dots per pattern. Then, the surface occupation was estimated as the ratio between S_{NW}

and the nominal surface of the graphene dot (S_{dot})[v]. The results are plotted in Figure 4.21(b) for dot radii between 50 and 200 nm (the standard deviation of the measurements is represented by the error bars). We see that for increasing dot sizes, the occupation rate increases from 0.84 to about 0.94 for dot radii from 50 to 150 nm, and then seems to saturate at about 0.93. Since the occupation rate is in the first approximation proportional to the NWs per-dot density, its non-constant value suggests that the NW nucleation stage might not be fully completed for the smaller dots. This statement correlates well with the increasing standard deviation for decreasing dot sizes: the nucleation events are more and more spread in time, leading to a wider dispersion of NW number from one dot to the other.

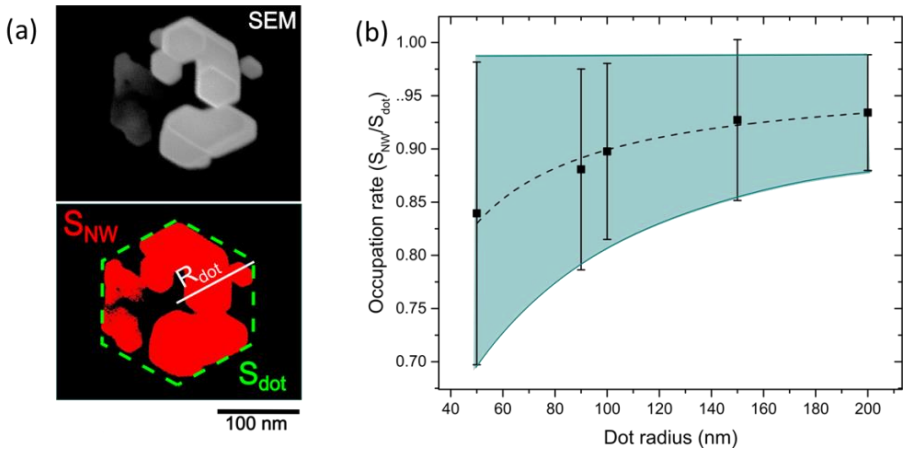

Figure 4.21 (a) SEM picture (top) and S_{NW} estimation by ImageJ (bottom) of a 100 nm radius graphene dot with GaN NWs. (b) Variation of the estimated occupation rate as function of the dot radius. Dashed line is a guide for the eye.

To further investigate this dot-size-dependent phenomenon, we evaluated the NW length statistical distributions by taking into account the incubation time variable. We point out that no appreciable differences of NW length/occupation rate have been observed for the different inter-dot pitches. This means that the NWs do not compete for the Ga adatoms that could, at least in principle, diffuse from the mask to the graphene dots (i.e. this means that at 815 °C the Ga diffusion length on the SiO_2 matrix should be lower than 175 nm, which is half of the lowest inter-dot distance

[v] Note that coalescence of the NWs is present in all dot radii. This implies that surface integration by top-view SEM image must overestimates to a certain extent the graphene dot occupation rate (at the base of the wires). To partially counteract this overestimation, we decreased S_{NW} of a factor of 5%.

considered). Hence, all the analyses have been carried out for the smaller pitch of 250 nm.

4.4.3 Modeling the length distribution in SAG GaN NWs

The average NW lengths were measured on tilted view SEM images. The results are plotted in Figure 4.22 for different dots sizes. We see that the NW lengths increase from about 420±100 nm to 580±100 nm for dots radii from 50 to 100 nm, and then stabilize to 640±110 nm for the higher dots radii. The upper value of ~640 nm fits well with the average NW height measured on big micrometer-size markers (630±100 nm). Note that this value is lower compared to the mean length distribution of GaN NWs grown on large graphene patches under identical growth conditions and deposition time (1.1 um ± 0.1 um). We attribute this phenomenon to the high sensitivity of the growth process to small shifts of the growth conditions (for instance, to a 1-2 degrees higher substrate temperature).

In our growth conditions (N-rich) and owing to the non-inversely tapered shape of the GaN NWs[79], the axial growth rate is limited by the Ga supply reaching the tip, including the direct impingement and the surface diffusion along the sidewalls. The Ga diffusion length should be short at these growth temperatures (40 nm[230]). Thus, we can exclude that the reduced lengths on small dot radii result from a lower (size-dependent) collection of atoms diffusing from the underlying graphene dot to the NW tip. Consistently with the results shown for a growth time of 3 hours, we associate this phenomenon to a delayed nucleation on small dots, resulting in a lower *effective* growth time and subsequent reduced NW length.

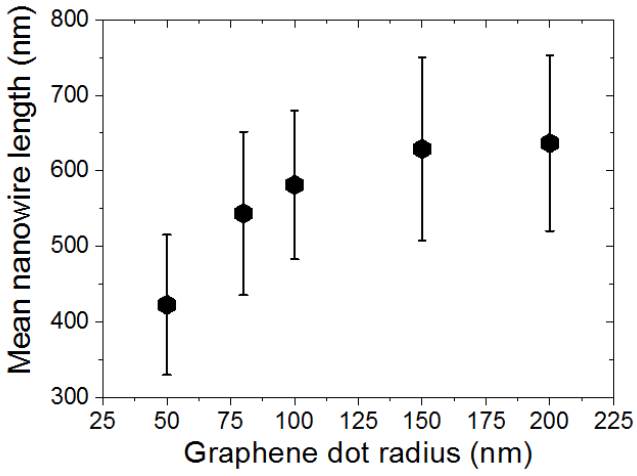

Figure 4.22 Mean NW length (~100 NWs per sample) as function of the graphene dot radius.

The NW growth on graphene dots was modeled in collaboration with V. Dubrovskii from ITMO University. To model the length distribution of self-induced GaN NWs on the graphene dots, we divide the growth process in two stages:

- An incubation stage at the end of which the first NW seeds form;
- An elongation stage, where the NW grows axially with a constant growth rate v.

Note that in this way, we neglect possible shape transitions antecedent to the NW nucleation[75], and the short stage after NW nucleation in which the Ga diffusive flux depends on the NW length[208,231].
Taking these features in consideration, we describe the NW length distribution with a Poissonian functional form, i.e. by considering the nucleation events as uncorrelated. The functional form[232] is the following

$$f(l,t) = \frac{\alpha}{2A} e^{\alpha(l-\tau+\tau_i)+\alpha^2\sigma_0^2/2}\, erfc\left(\frac{\alpha\sigma_0^2 + l - \tau + \tau_i}{\sqrt{2}\sigma_0} \right), \qquad (eq\ \ 4.1)$$

where l is the NW length (in MLs of GaN along the c-axis), t is the time (s), $\tau = v \cdot t$ is the reference NW length (mean of the Green's function[232]) and τ_i represents the incubation time, i.e. the incubation stage in which no NWs nucleate[vi]. The function *erfc* is a regularized complementary error function, defined as $erfc(y) = \left(\frac{2}{\sqrt{\pi}}\right)\int_y^\infty dt\, e^{-t^2}$. Finally, $0 < A < 1$ is a normalization constant, accounting for the fact that not all the nucleation sites may be occupied when the growth is interrupted.
Overall, the shape of the length distributions is controlled by the following two parameters:

- $< l >= \tau - \tau_i - 1/\alpha$, where <l> is the mean NW length and $0 < \alpha < 1$ is the ratio between the axial growth rate and the incubation rate (and thus gives a measure of the NW nucleation delay);
- $\sigma^2 = \sigma_0^2 + 1/\alpha^2$, where σ is the standard deviation of the effective distribution, and σ_0 is the standard deviation that the distribution would have without delayed nucleation.

[vi] τ_i it is the equivalent NW length for a growth rate equal to v in a time equal to the given incubation time.

Figure 4.23 shows the length distributions measured on ~100 NWs per sample for different graphene dot radii (R_{dot}), along with their best fits by eq. 4.1. The length distributions parameters extracted from the fits, summarized in Table 4.1, give a good quantitative correspondence to the shape of the distributions.

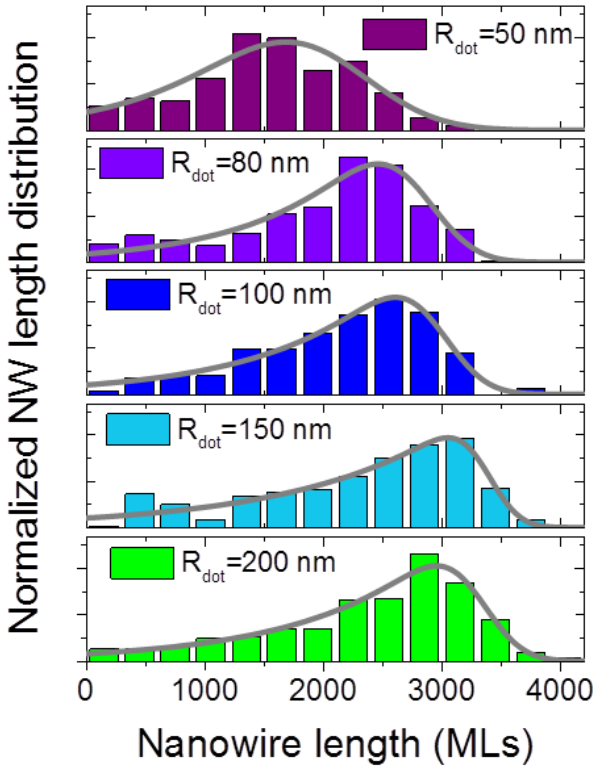

Figure 4.23 Length distribution (in MLs of GaN) measured for graphene dots of different size.

Table 4.1 Parameters of the fitted length distributions as function of the dot radius.

R_{dot} (nm)	$< l >$ (nm)	σ (ML)	$\tau - \tau_i$ (ML)	α	A
50	1565	687	2156±114	0.0013± 0.0001	0.89
80	2013	800	2842±52	0.0011±0.0001	0.97
100	2153	729	2982±27	0.0010±0.0001	0.95
150	2329	898	3380±38	0.008±0.0001	0.96
200	2358	861	3320±36	0.009±0.0001	0.96

It can be readily seen that all distributions feature a very pronounced asymmetry towards shorter lengths, corresponding to NWs that nucleated later. This is quantified by the dimensionless alpha parameter, which is of the order of 10^{-3}: the formation of the very first NW seed takes approximately a 1000 times longer time than the formation of one NW ML during the steady-state elongation.

Most importantly, we estimate that the incubation time increases of a factor of about 1.5 when the dot radius is decreased from 200 to 50 nm. By assuming that the asymptotic value of incubation time for big dot radii is of 1 hour 20 minutes (i.e. as on big patches in selective conditions), we estimate that for a 50 nm dot radius, τ_i is of about 2 hours (shown in Fig. 4.24). Consequently, the nucleation stage is not fully completed for small dot radii (50 nm) even after 4 hours of growth, corresponding to non-zero length distribution for $l = 0$ in Figure 4.23, and to the reduced dots occupation rate observed in the previous section (Fig. 4.21). Also, the fitting parameter v, returns values of about 0.23 ML/s for the different distributions. This value is noticeably smaller than the Ga deposition rate (0.62 ML/s) and should account for the high Ga desorption at these high growth temperatures.

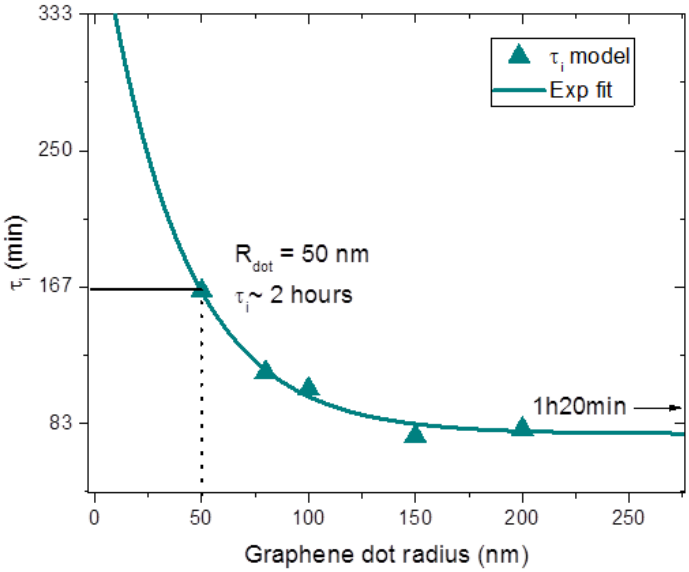

Figure 4.24 Incubation time versus graphene dot radius calculated by considering that in absence of size-related nucleation delay, the incubation stage takes 1 hour and 20 minutes. The data can be fitted by an exponential function.

4.4.4 Possible origin of the size-dependent incubation time

To understand the origin of the dot-size-dependent NW incubation time, we first note that the number of NWs per dot N increases almost linearly with R_{dot} according to Fig. 4.25(a). At first glance, this might be surprising, since the NW number should be proportional to R_{dot}^2(i.e. to the dot surface). However, we recall that the NWs grow preferentially on the dots edges (whose extension scales with R). This is clearly supported by Figures 4.25(b-d) for graphene dots of 100 nm radius, and different growth times.

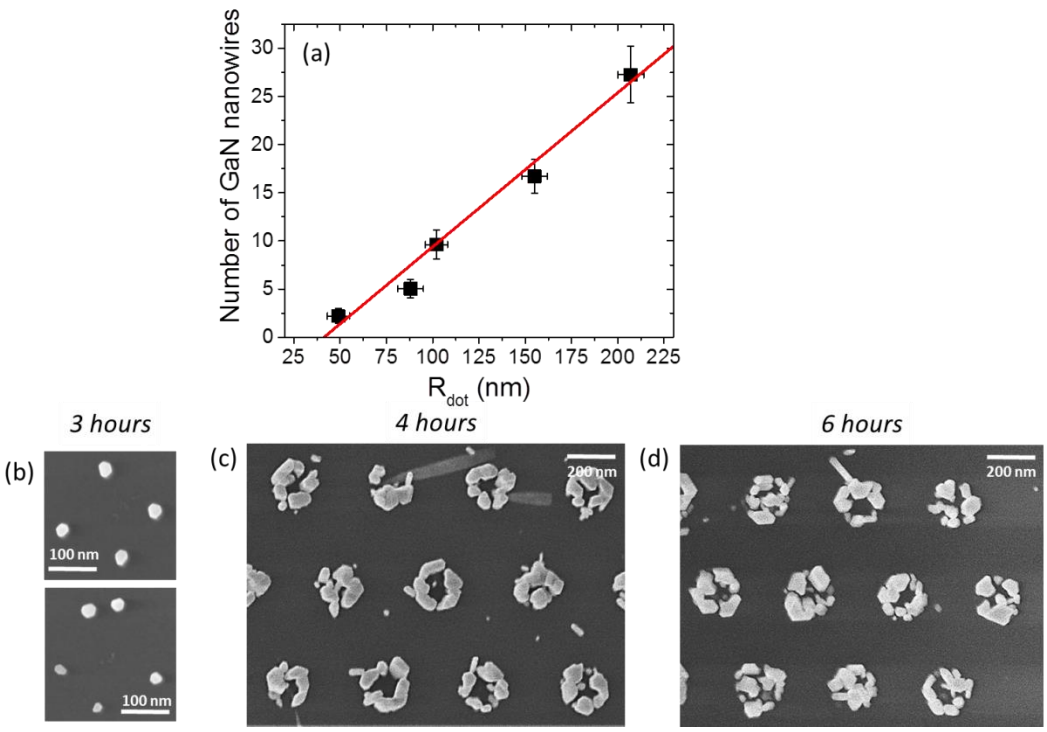

Figure 4.25 (a) Variation of the number N of NWs per graphene dot as function of the dot radius. (a-c) Top-view SEM images of GaN NWs grown on graphene dots of 100 nm diameter for 3, 4 and 6 hours respectively.

Hence, the number of nucleation sites per graphene dot is roughly proportional to R_{dot} regardless of their type (for instance, graphene edges or defects created by the N-plasma). Assuming that Ga atoms diffuse on the graphene and their mean free path before desorption is limited to a certain diffusion length λ_{Ga}, the effective Ga flux per nucleation site equals c_1/R_{dot} for $R_{dot} \ll \lambda_{Ga}$, and $c_2/(\pi\lambda_{Ga}^2)$ for $R_{dot} \gg \lambda_{Ga}$, with positive constants c_1 and c_2. In other words, by considering a simplified picture in which, each dot presents one single nucleation site, the net Ga flux which can potentially diffuse to that site, is limited by the dot radius for $R_{dot} < \lambda_{Ga}$, and is limited by λ_{Ga} for $R_{dot} > \lambda_{Ga}$. These two opposite scenarios are sketched in Figure 4.26.

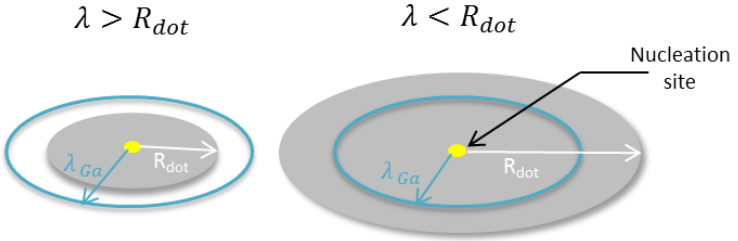

Figure 4.26 Simplified sketch depicting the dot radius limited (left) and diffusion length limited Ga adatom (right) collection around one single GaN NW nucleation site.

The incubation time is inversely proportional to the Ga flux, and hence proportional to R_{dot} for $R_{dot} \ll \lambda_{Ga}$ and independent from R_{dot} for $R_{dot} \gg \lambda_{Ga}$. By assuming that after the first NW ML the axial growth rate is constant, the simplest fitting formula which is reduces to these two asymptotes for small and large graphene dots, can be expressed as

$$< l >=< l >_{max} \left(1 - e^{-\frac{R_{dot}}{\lambda_{Ga}}}\right) \qquad (eq.\,4.2)$$

where $< l >_{max}$ is the maximum NW length at $R_{dot} \gg \lambda_{Ga}$. Figure 4.27 shows that this simple model fits very well the measured mean length of NWs versus the dot radius, for a plausible Ga diffusion length of 45 nm.

Note that in this way, we consider only the direct impingement of Ga atoms on the dot surface, and we neglect a possible contribution of Ga atoms diffusing from the mask to the dots. The main reason is that at this stage, this latter phenomenon is difficult to detect: in quasi-selective conditions, for samples grown in nominally identical conditions, sometimes we observed the presence of a depletion region in vicinity of graphene (where no NWs nucleated, as in Fig. 4.10(e)) and sometimes there was no trace of it (as in Fig. 4.9(c). The extension of this depletion region should be proportional to the Ga diffusion length on SiO_2 ($\lambda_{Ga}^{SiO_2}$). We could thus deduce that $\lambda_{Ga}^{SiO_2}$ decreases rapidly with the temperature, along with the increased Ga desorption from SiO_2. Hence, under selective conditions, $\lambda_{Ga}^{SiO_2}$ might be very low, leading to a current of Ga atoms from the SiO_2 to the dot, which is negligible compared to the one generated by direct impingement of Ga on the dot surface.

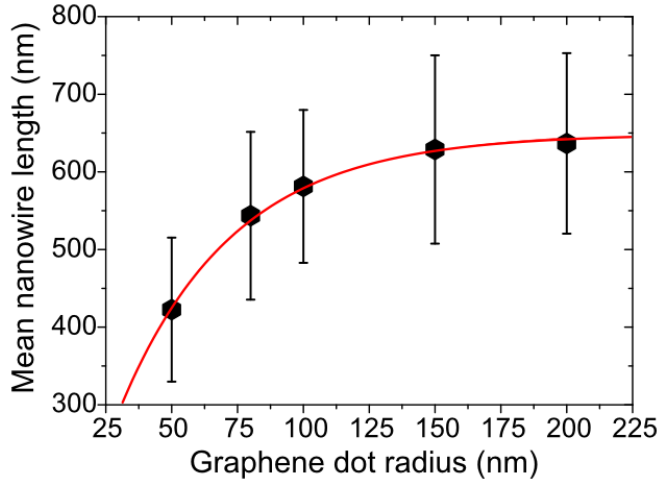

Figure 4.27 NW mean length and its fit (line) as function of the dot radius.

In summary, broad and asymmetric length distributions of GaN NWs on graphene are well fitted by the model. We estimate the characteristic duration of the nucleation step as being ~ 1000 times longer than the time of subsequent ML formation, and it increases when the dot radii are decreased. The incubation stage before the NW nucleation may take more than 2 hours on the smaller dot radii considered. We propose that the increase in NW incubation time is due to a reduced collection length of gallium per nucleation site, when the graphene dots dimensions are comparable or lower than the Ga diffusion length on graphene.

4.4.5 Summary and perspectives of SAG on patterned graphene

We have shown that SAG method of GaN NWs on an amorphous substrate is possible via graphene using PA-MBE, since vertical and in-plane oriented ensembles of NWs can be grown with a very high degree of selectivity on graphene dots ranging from one to few hundreds of nm diameter.

The broad and asymmetric length distributions on graphene dots of different sizes are well fitted by a model which takes into account the dot size-dependent NW incubation time. We derive that the duration of the nucleation step increases as the dot size decreases below 100 nm, leading to a higher spread in time of the nucleation events, which in turn leads to shorter NWs and to a reduced occupation rate of the graphene dots. Specifically, for the smallest dot considered (50 nm radii), we estimate that the nucleation step might take more than 2 hours. Also, for the considered dot radii, we observed that the nucleation takes place preferentially at the borders of the graphene dots, leading to an almost linear dependency of the NW-per-dot number versus dot radius. If this trend is taken into account, the size-dependent mean NW length is well reproduced by taking into account a reduced collection length of Ga adatoms for dots radii smaller than the Ga diffusion length on graphene. Specifically, the experimental length dependency on the dot radius is well fitted by considering a Ga diffusion length equal to 45 nm.

These findings are interesting from a phenomenological point of view, but also intimate that a further decrease of the graphene dot size to ~25 nm, to reach the regime in which one NW per dot is formed, could lead to an even more pronounced nucleation delay. Specifically, in the assumption that growth rate does not depend on the NW length once the NW is formed, we estimate that the incubation time would

exceed 4 hours for dots radii of 25 nm (from the exponential fit of Fig. 4.24). It is worth nothing that, to obtain NWs in all the graphene dots of the pattern, unpractically long total deposition times would be required. In addition, this still would not guarantee a homogeneous NW morphology on different dots, due to the pronounced spread in time of the nucleation events and different effective growth times. Thus, for the further development of this SAG method, it is mandatory to identify a reliable strategy to accelerate the NW nucleation, without affecting the selectivity.

Coming back to the results obtained for growth on graphene patches, we observed that the incubation time is decreased from 1 hour 20 minutes to about 1 hour, when the growth temperature is decreased from 815 to 810 °C. Thus, one possibility could be to perform the growth in two steps: a first nucleation step at lower temperature to complete the NW nucleation phase, and a second elongation step at high temperatures, to preserve the selectivity.

On SiO_2, the incubation time seems to decrease much *faster* than on graphene when the temperature is reduced. Qualitatively, this can be deduced by the evolution of the NW density and length in the different growths considered (Fig. 4.7): at 805 °C, the NWs present comparable lengths and high density on both the surfaces (i.e. comparable nucleation times); at 810 °C the NW density is higher on graphene substrates; finally at 815 °C no growth is observed on SiO_2 while on graphene NWs are still present in high density. In addition, from experiments under nominally identical growth conditions, we observed that selectivity is preserved for 6 hours of deposition. This means that, at 815 °C, the NW incubation time on SiO_2 must be of *at least* 6 hours (lower limit). These results must translate in a higher nucleation barrier (E_N) for growth SiO_2 than on graphene.

The temperature dependence of the incubation time can be described by an Arrhenius law of the form[208]:

$$\tau_i = C_i \exp\left(-\frac{E_N}{k_B T}\right) \qquad (eq.\,4.4)$$

Where C_i is a constant. Based on these considerations, we trace a *qualitative* Arrhenius plot (Fig. 4.28), where the incubation time on SiO_2 and on graphene is similar at 800 °C and increases respectively to 6 hours and 1 hour 20 at 815 °C. It can

be readily seen that, if one wills to accelerate the NW nucleation, the growth temperature is not a suitable parameter to play with, since a quick inversion of selectivity is expected for substrate temperatures low enough to allow an appreciable decrease of τ_i.

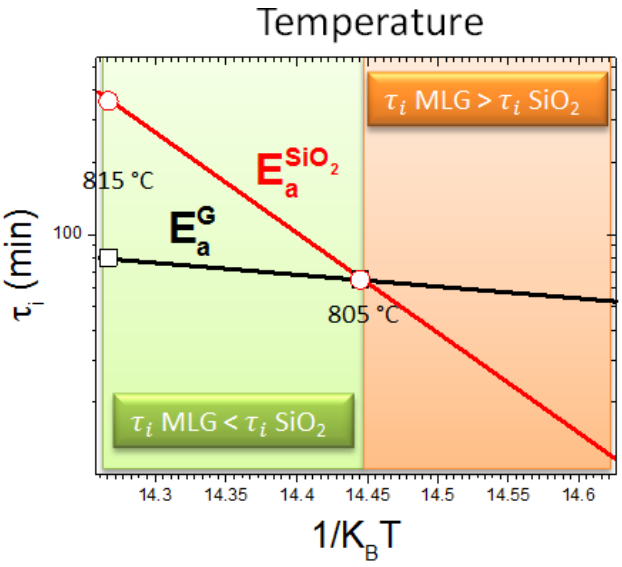

Figure 4.28 Qualitative Arrhenius plot showing the variation of the NW incubation times on SiO_2 and MLG as a function of the growth temperature.

The lower incubation time on graphene for lower substrate temperature suggests that, as observed for other types of substrates, the NW nucleation is limited by the Ga desorption from the graphene surface. Thus, another possible route is to play with the Ga flux to counteract its high desorption from the substrate. This would increase the supersaturation of the surface, decreasing the nucleation barrier on both SiO_2 and graphene.

Some general consideration can be done by considering that on Si(111) the incubation time scales with the Ga flux following this empirical equation[208]:

$$\tau_i = \frac{C}{\phi_{Ga}{}^{3/2}} \qquad eq.4.3$$

where C is a constant. Such a power law was explained by the authors within the framework of the standard island nucleation theory and the 3/2 exponent was related to the critical size of the stable GaN nuclei. Thus, all dependency on the substrate (as well as the appropriate unit conversion factors) should, in principle, be contained in the C constant. By considering the Ga flux used in this work, and the incubation times in selective conditions (lower limit of 6 hours on the SiO_2, and 1 hour 20 on the

graphene surface), we plotted in Fig. 4.29 the incubation time expected from eq. 4.3 for different Ga fluxes.

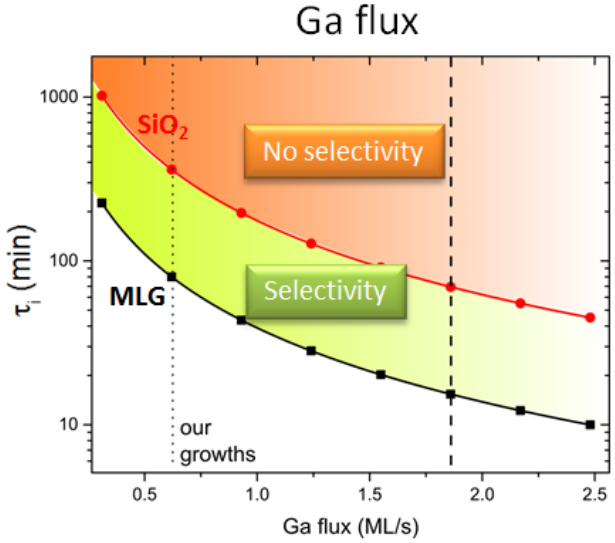

Figure 4.29 Incubation time expected from eq. 4.4, as a function of the Ga flux for the SiO_2 and MLG surfaces.

We see that an increase of Ga flux of a factor of 3 (1.86 ML/s, dashed line in the figure), allows to decrease the NW incubation time to about 15 minutes, while on SiO_2 this still remains reasonably high (70 minutes). In this view, a nucleation step of duration shorter than 70 minutes could allow to nucleate the NWs, possibly even on the smaller graphene dots. Then, in a second step the Ga flux could be decreased to lower values, to pursue the NW elongation while preserving a perfect selectivity.

Of course these considerations are valid if, and only if, the modifications occurring to graphene during the N-plasma exposure are not strictly necessary to allow the NW nucleation. In fact, in this specific case, there might be a "critical" incubation time, below which no growth would be possible, and a N-plasma pre-exposition would be required to create the nucleation sites, prior to start the growth. Also, a different power law for the dependency of the incubation time on the Ga flux could be expected (actually, for both substrates), since its shape could vary depending wither the nucleation is limited by the meeting of two Ga atoms or one Ga atom with a nucleation center[233]. At the present stage, the still limited knowledge on the mechanisms of the NW nucleation on these new substrates, and the lack of appropriate experimental data, doesn't allow to make any speculation on this topic. Further investigations, focused on the study of the GaN nucleation, will be carried out by Camille Barbier in the framework of her PhD thesis.

Conclusions

In conclusion, we demonstrated the successful growth of GaN NWs on big MLG patches, small multi-layered graphene domains and patterned MLG by PA-MBE. The GaN NWs exhibit state-of-the-art optical properties, and, differently from Si(111)/AlN substrates, do not show the optical signature associated to IDBs.
Consistently with previous studies, post-growth characterizations evidenced that MLG is able to withstand the PA-MBE growth process, and in all cases a clear in-plane orientation of the NWs was observed. However, I-V characterizations of the graphene layer after a N-plasma exposure of duration comparable to the NW incubation time, have shown that the MLG conductivity is deteriorated.
On all substrates, a temperature of 815 °C was observed to allow for growing GaN NWs on graphene with a perfect selectivity with respect to SiO_2 within the considered growth rate and V/III ratio. It is worth noting this temperature window was observed to be very small (few degrees). An important consequence of this experimental fact, is that the NWs present very long incubation times (more than one hour on MLG patches). This was found to impact significantly the growth on patterned substrates. Specifically, the statistical analysis of NW length distributions and graphene dot occupation rate for different pattern sizes and growth times, clearly evidenced that if the dot size is reduced below 200 nm diameter, the nucleation of the NWs becomes more and more delayed (up to 2 hours for dot of 100 nm diameter). The main outcome of these results is that growing one single NW in ~50 nm diameter graphene dots might be a very tricky task if the experimental conditions are not adjusted to promote a faster nucleation. We proposed a 2-steps growth involving a nucleation step under a high Ga flux, and a subsequent growth step at a lower Ga flux, as a possible way to shorten the NW incubation time, while allowing to maintain a perfect selectivity compared to the SiO_2 surrounding surface. This strategy could, possibly, also help to preserve at best the graphene electrical properties.

Credits

The graphene transfer has been performed with the valuable help of Nan Guan, who also took great care of the whole graphene patterning process. A. Madouri did the CVD growth and transfer of the graphene domains. µPL analysis was performed by Chiara Sonito at the PDI University of Berlin, and with the help of Lorenzo Mancini. The NW length modeling has been performed by our collaborator Vladimir Dubrovskii. The investigation of the NW SAG on graphene dots is currently continued by C. Barbier in her PhD thesis.

Chapter 5

Perspectives

This brief chapter summarizes some preliminary results obtained on different topics coherent with the objectives of this work, together with some perspectives for their further development. Specifically, it concerns results on: InGaN/GaN NWs growth on transferred graphene 1 cm^2 patches; growth and characterization of of GaN NW p-n junctions and InGaN/GaN NW p-i-n junctions; piezoelectric conversion on InGaN/GaN heterostructured NWs.

5.1 Growth of InGaN/GaN NWs on transferred graphene

All along this work, we have shown that InGaN/GaN NWs can be efficiently and controllably grown on AlN/Si(111) substrates by a self-assembled growth method. However, as evidenced by EDX statistics and PL measurements, the InGaN sections do not exhibit homogeneous properties over the sample, and often show bi-modal distributions of their PL peak energy. We have associated these two experimental facts to: (i) the length and diameter dispersion of the GaN NW pseudo-substrate on which the InGaN sections are grown (ii) the presence of a minority population of NWs presenting IDBs, leading to a further perturbation of the growth process. To avoid these drawbacks, we decided to go for a SAG approach and we have chosen graphene substrates as a way to achieve selective nucleation. This approach would potentially combine a control over the NW positioning and morphology (and hence reduce the overall dispersion of InGaN emission energies from wire to wire) with a very low density (or even absence) of IDBs (absence of their optical signature at 3.45 eV).

To make a first step in this direction, we performed one growth of InGaN/GaN capped NWs on graphene substrates. The conditions were nominally identical to the one used for the capped In-rich disk-like sections analyzed in Section 3.3 (~60 nm thick section grown with a In/Ga flux ratio of 3 and a Ga flux of 0.30 nm/min), except from the GaN base, which was grown for 4 hours under selective conditions. Cross-sectional and SEM images in Figure 5.1(a), show that the growth has been performed successfully on these substrates, but the selectivity is lost: as shown in Figure 5.1(b), the SiO_2 surface is covered by a polycrystalline deposit, which presumably formed during the InGaN and GaN cap growth steps at low substrate temperature. Consistently, EDX analysis (not shown) revealed that In is present on the SiO_2 surface.

These results indicate that for growth on patterned substrates with large (1-2 µm) inter-dot distances, the selective growth of InGaN/GaN heterostructured NWs might not be possible. In fact, for a given GaN NW length and radius, to prevent nucleation of InGaN on the SiO_2 surface surrounding the patterns, the graphene dots pitch should be reduced enough to sufficiently shadow the inter-dot surface[234] from the In and Ga impinging fluxes. For SAG of InGaN/GaN NWs on GaN templates with Ti masks, shadowing effects are

efficient enough for GaN NWs of 500 nm length and pitches of the order of the NW diameter[187,235]. In perspective, by considering these parameters as a rule of thumb, tests of InGaN/GaN NW SAG could be performed on patterned masks presenting comparable dot radii and inter-dot distances.

In Figure 5.1(c), we show the PL spectra acquired with a 375 nm excitation wavelength on this NW array, and in Figure 5.1(d) on one nominally identical InGaN/GaN NW array grown on a standard AlN/Si(111) substrate. On the graphene samples, the InGaN sections present their PL maximum at about 2.33 eV, very near to the one measured on AlN/Si(111) substrate (2.38 eV). The general temperature-dependent PL properties are also very similar: no clear S-shape behavior of the peak position is observed, and the PL optical IQE is about 6%. Notably, the PL broadening is much less pronounced for the InGaN/GaN sample grown on graphene (about 300 meV against 500 meV in the AlN/Si(111) sample). This linewidth reduction could arise from both the higher NW length homogeneity on graphene substrates (Figs 5.1(a,d)), and from the absence of IDBs.

In Section 3.2.3 we speculated that the presence of GaN NWs with IDBs would generate a second population of InGaN NW heterostructures emitting at a higher energy, due to their reduced In incorporation. However, we note that the decreased broadening on graphene substrate, where GaN NWs are free of IDBs, is mainly observed in the low energy part of the PL spectrum. This seems to contradict our hypothesis. It should be pointed out, however, that it is not obvious that the *effective* InGaN growth temperatures were the same on the two substrates. In fact, for the temperature measurements we referred to the pyrometer lecture, and it is not obvious that Si substrates covered by 300 nm presents the same emissivity than the oxide-free Si (i.e. it is not obvious that the same pyrometer lecture corresponds to the same substrate temperature). In this sense, it is possible that the growth temperature was higher for the InGaN heterostructures on graphene. Specifically, referring to the growth of 2D InGaN layers, for compatible N flux and Ga/N conditions, a 5-10 °C higher temperature would be sufficient to decrease the In incorporation of about 10% In, accounting for this discrepancy[122].

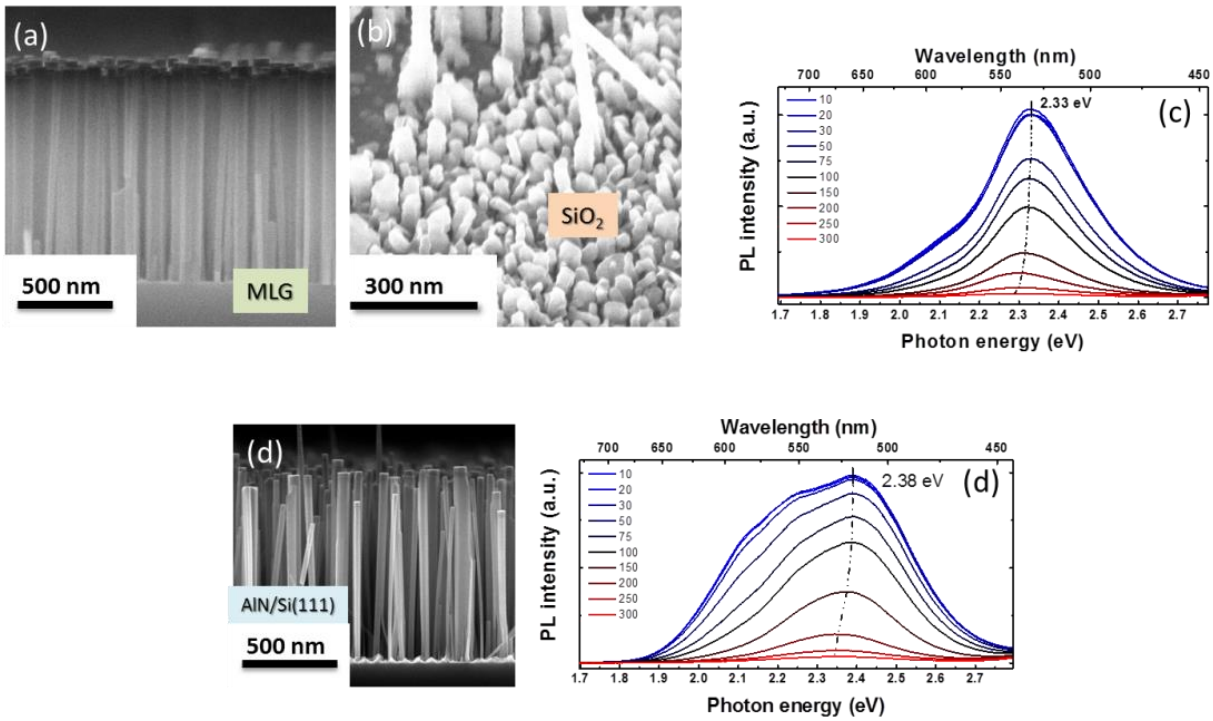

Figure 5.1 Cross-sectional (a, d) and 45°C tilted view (b) SEM images of: capped InGaN/GaN NWs grown on (a,b) MLG transferred on SiO_2/Si(100) and (d) AlN/Si(111) substrate, with their respective PL spectra measured on NW ensembles (c,d).

In this Ph.D. work, we did not investigate the impact of the growth temperature on the InGaN NW heterostructures growth and properties, something that should be done in the future. In fact, the construction of a temperature-dependent growth diagram could allow a wider control over the InGaN section properties (possibly, the growth of disk-like sections in a wider range on alloy compositions), but it could also be used as a guideline to tailor the growth on other substrates (for instance, to identify, if any, the proper "shift" in temperature of the diagram, for InGaN heterostructures growth on graphene/SiO_2 substrates).

5.2 Towards the application: InGaN/GaN NWs for photovoltaic and piezoelectric energy harvesting

This thesis was developed in the framework of the NanoHarvest ERC research project, whose aim is to study a new generation of light-weight solar cells and piezo-generators based on III-N NWs. In this section I will discuss some basic aspects and preliminary results concerning the fabrication of InGaN/GaN NW photovoltaic junctions, and the piezo-conversion in InGaN/GaN NWs.

5.2.1 InGaN/GaN NWs for photovoltaics

Among the renewable sources of energy available on earth, the solar flux represents by far the largest source, with an average incident energy flux which is on the order of 10^4 times larger than the total global power consumption of the humanity. This source of energy can be converted into usable electricity by solar cells, through the well-known photovoltaic effect. As briefly introduced in Section 1.3, this effect involves the production and transportation of electrons and holes across a semiconductor p-n junction, under the effect of light absorption. Before discussing InGaN/GaN NW junctions, let us remind the basics of this effect.

When a p-doped and a n-doped materials are brought in contact, the excess of holes (electrons) in the p-doped (n-doped) portions causes a drift of electrons and holes in the p- and n-doped material, respectively. Following transfer, the diffused electrons come into contact with holes on the p-side and are eliminated by recombination. Likewise for the diffused holes on the n-side. In parallel, the departure of an electron (hole) from the n-side (p-side) leaves a positive (negative) charge behind. The net result is an accumulation of uncompensated charges adjacent to the interface, in a region with no mobile carriers (this is the so-called depletion region). This creates an electric field that provides a force making the further exchange of charge carriers between the n- and p- semiconductor portions unfavorable. When the electric field is sufficient to stop further transfer of holes and electrons, the depletion region has reached its equilibrium dimensions. Hence, when the p-n architecture is connected via an external circuit and exposed to sun light, the e-h

pairs will get separated by the depletion region electric field, generating a flow of charge carriers, i.e. electricity.

In the case for InGaN/GaN solar cells, a homojunction design composed of n- and p-doped InGaN layer is technologically far too challenging due to the difficulties with the efficient p-doping of InGaN. Therefore, a typical structure consists of an intrinsic InGaN absorber section (i.e. a thick InGaN layer or multi QW region with thin GaN barriers), sandwiched between n-GaN and a p-GaN layers. The charges generated in the intrinsic InGaN region drift in accordance to the electric field generated due to the immobile charge carriers at the intrinsic/p-doped and intrinsic/n-doped junctions. This is sketched in Fig. 5.2(b). For InGaN/GaN NW-based solar cells, we consider the same architecture, i.e. a p-i-n junction, whose active region is constituted by an axial intrinsic InGaN heterostructure.

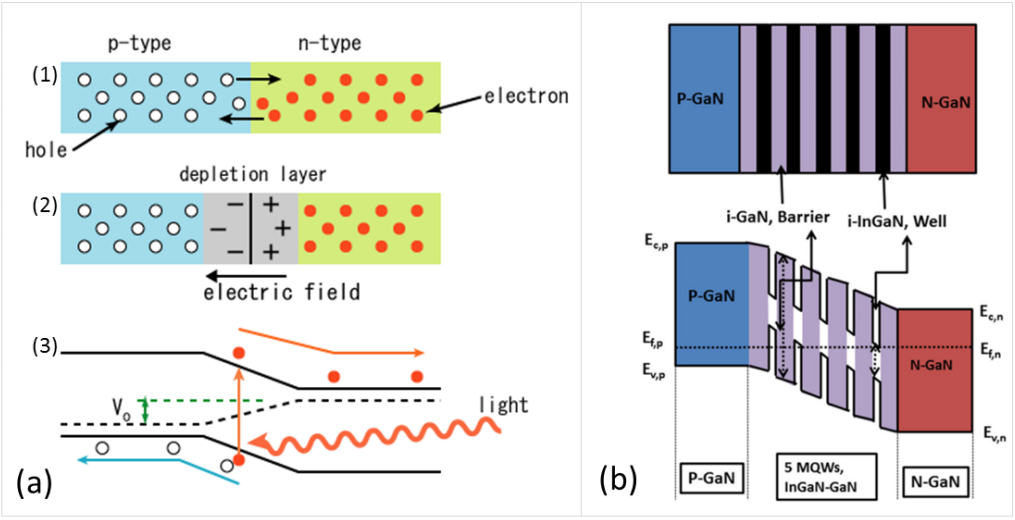

Figure 5.2 (a) Schematization of a p-n junction and photovoltaic effect; (b) Sketch of a photovoltaic p-i-n structure based on 5 InGaN/GaN QWs[236].

From these considerations, it follows that depending on the p-i-n junction design, the junction electric field can enhance or partially screen the built-in polarization field within the InGaN region (which is determined by the material polarity and strain). In section 3.3, we saw that in In-rich disk-like InGaN sections in N-polar NWs, the field leads to an axial e-h separation, where electrons drift towards the InGaN section base, and holes towards its top. Thus, the strong electric field within the In-rich InGaN cores can be advantageous in a photovoltaic device, if the design of the p-i-n InGaN/GaN junction involves a bottom p-doped GaN base, and an upper n-doped GaN cap (as shown in figure

5.3). By contrast, the opposite design could be more indicated if one wants to build an LED structure, where carrier separation has to be minimized.

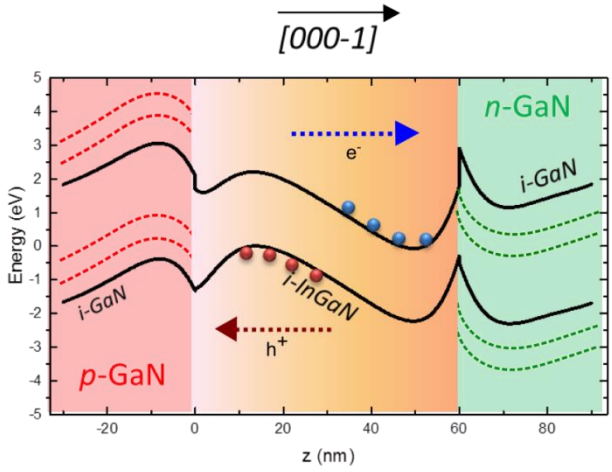

Figure 5.3 Simulated band edge profile along the heterostructure axis of a reference InGaN/GaN NW described in section 3.3. The suggested p-i-n photovoltaic structure, and resulting shift in energy of the p-doped and n-doped GaN segments is also schematized.

Preliminary results on the growth of Mg-doped and Si-doped NWs evidenced that this architecture might be convenient also from the point of view of epitaxial growth, due to a lower radial growth in Si-doped NW segments (n-doping) compared to Mg-doped NWs (p-doping). This effect is qualitatively evidenced by the much higher NW coalescence (and hence final NW diameters) on highly Mg-doped GaN NWs (Fig. 5.4(b)), compared to nominally intrinsic GaN NWs (Fig. 5.4(a)) and highly Si-doped GaN NWs (Fig. 5.4(c)). Note that in these three growths, the growth temperature (800 °C), V/III ratio (1.36), growth time (3 hours) and substrate (AlN/Si(111)) were nominally identical.

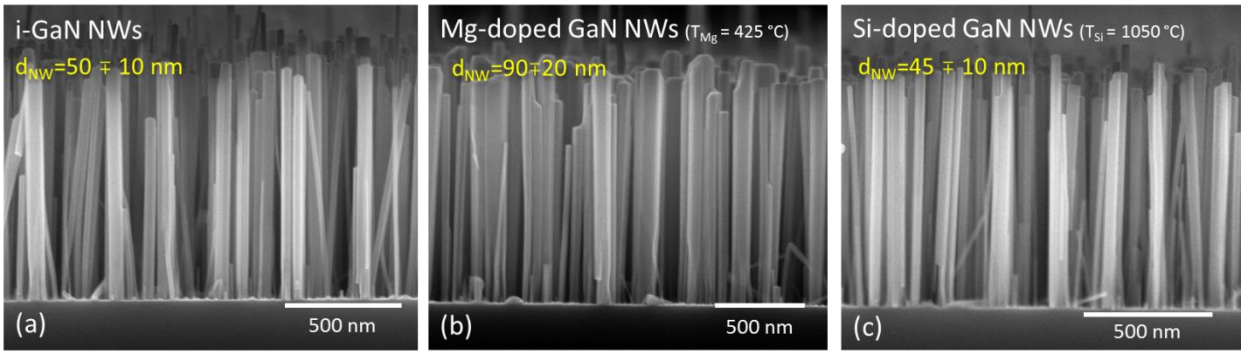

Figure 5.4 Cross-sectional SEM images of GaN NW ensembles grown with different doping: (a) intrinsic, (b) Mg-doped, (c) Si-doped.

These considerations are supported by our Electron-beam induced current characterizations (EBIC) of the two different GaN NW p-n junction structures, described in the following section.

Growth and EBIC characterization of NW p-n and p-i-n junctions

The EBIC microscopy characterization of GaN p-n junctions was performed by the Ph.D. student of our group Omar Saket. In EBIC microscopy electron–hole pairs are locally generated by the electron beam. In structures with a built-in internal field, the electron–hole pairs created close to the field region can be separated and collected producing a measurable current[237–239]. The system used in this study is a Hitachi SU-8000 SEM, where electrical contact to single NWs is achieved using Kleindiek PS4 nano-manipulators equipped with 100 nm radius tungsten tips. I-V measurements were performed by a Keithley 2636 source-meter coupled with a LabView acquisition software, with a measured noise level lower than 0.1 pA in these experimental conditions. EBIC measurements were performed at 2 kV acceleration voltage and 37.7 pA injected current. Injected current is measured by means of a Faraday cup. An external bias ranging from -5 V to +5 V is applied through a Stanford SR560 preamplifier controlled by a Gatan DigiScan system.

Two GaN NW p-n junctions were grown with the same Mg and Si cell temperatures mentioned before (T_{Mg}=425 C, T_{Si}=1050 C), and with an opposite structure: the sample showed in Fig. 5.5(a,c) (p-n junction) consists of a Mg-doped base and a Si-doped cap, while the one showed in Fig. 5.5(b,d) (n-p junction) contains an inverted structure, with a Si-doped (n) base and a Mg-doped (p) cap[i]. The Mg-GaN and Si-GaN segment lengths expected from the axial growth rate (estimated for homogeneously doped GaN NWs grown under nominally identical conditions) and from the corresponding growth time are also depicted. We see that for the n-p structure, the junction (bright contrast in Fig. 5.4(c)) seems markedly displaced towards the NW bottom compared to the expected Si-GaN/Mg-GaN interface. Also, it presents a quite asymmetric shape. This result may suggest that during the growth of the Mg-doped GaN cap, the radial overgrowth of a shell might generate combined axial and core-shell p-n interfaces, leading to a difficulty in defining the position of this mixed axial/radial n-p junction. However, for p-n junctions

[i] Note that to perform EBIC characterization, the n-p GaN NW junctions have been grown on a n-doped Si(111) wafers, while the p-n junction used p-doped Si(111) wafers.

this effect is not observed: in all the analyzed NWs the junction (in dark EBIC contrast) appears at the expected NW height and presents a rather symmetric shape with respect to the NW axis. This homogeneous junction, allows a more reliable estimation of the acceptor (Na) and donor (Nd) concentrations: from the shape of the depletion region and for different applied biases values of Na=7.15 10^{17} cm^{-3} and Nd=1.1 10^{18} cm^{-3} have been extracted.

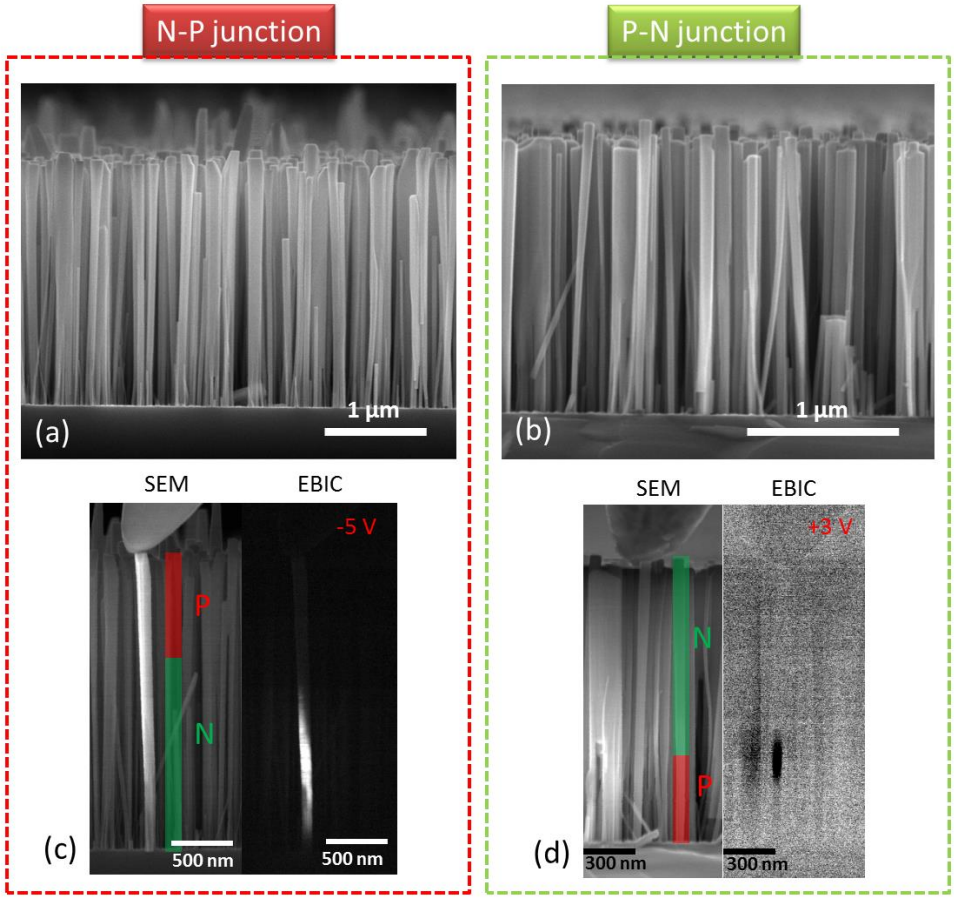

Figure 5.5 Cross-sectional SEM images of n-p (a) and p-n (b) GaN NW junctions, and corresponding EBIC maps (c,d).

In a next step, I synthesized one p-i-n junction where an In-rich 70 nm thick InGaN disk (~ 40% In content) was sandwiched between the two GaN NW doped segments. The growth recipe for the Si-doped segment involved a lower temperature in this case (760 °C), in order to limit at best the InGaN decomposition during the growth of the Si-doped upper GaN segment. As can be seen in the SEM images of Fig. 5.6(a,b) the NWs presented a high degree of coalescence. This phenomenon could stem from both the use of

a lower temperature for the Si-GaN growth (favoring radial growth) and from the slight inverse-tapering of the Mg-doped GaN stems. The NW coalescence could be problematic for the device processing (which should involve a NW encapsulation into a polymer matrix and a subsequent peel-off). In the future, this drawback could be partially counteracted by the use of shorter growth times and/or higher V/III ratios for both the Mg-doped and the Si-doped portions. In particular, this latter modification of the growth receipt should favor the axial growth with respect to the radial growth.

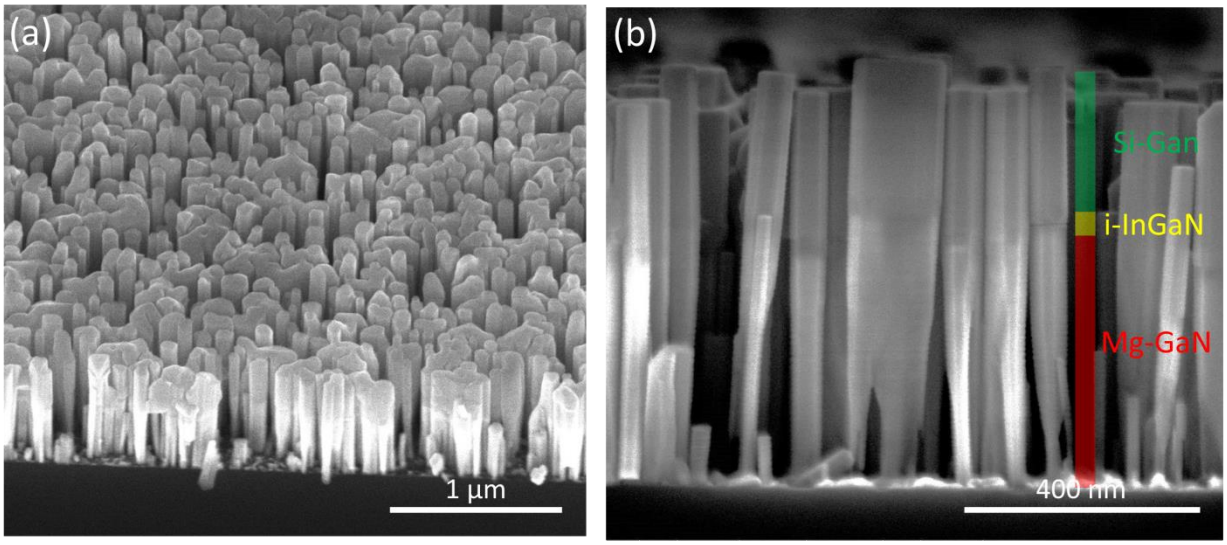

Figure 5.6 45° tilted view (a) and cross-sectional view (b) SEM images of a sample of p-i-n InGaN/GaN NW junctions, grown on p-doped Si(111) substrates on AlN pre-deposition.

EBIC measurements were performed on several NWs of this sample, whose representative results are showed in Figure 5.7. As can be seen in the map of Fig. 5.7(a) and in the extracted profile of Fig. 5.7(b), the EBIC signal is flat and strong in the NW portion where the InGaN section is supposed to be, while it decreases sharply (slowly) in the Si-doped (Mg-doped) GaN NW portions. These results indicate that for the EBIC conditions considered, the e-h pairs created in the InGaN section by e-beam irradiation are able to escape the InGaN insertion to be collected. However, no signal was observed from the junction under zero or positive bias (the conditions at which the solar cell is supposed to operate). This phenomenon could be due to the Schottky contact between the NW and the tungsten tip, which prevents the carrier collection (the Schottky diode is flattened under a negative voltage, allowing to collects the carriers generated in the p-i-n junction). It may also mean that the barriers at the InGaN/GaN interfaces are playing a negative

role. In this case it has been shown that the implementation of graded interfacial InGaN compositional profile could be helpful[240]. We also see that the EBIC signal extends far into the p-doped GaN section. An increase of the p-doping would help to localize the internal field in the InGaN segment. Unfortunately, with the present now-how about the growth of Mg-doped NWs, the implementation of a higher doping might be tricky, since higher Mg cell temperatures lead to a pronounced radial growth (and inverse tapering) of the NWs, further complicating the coalescence issue.

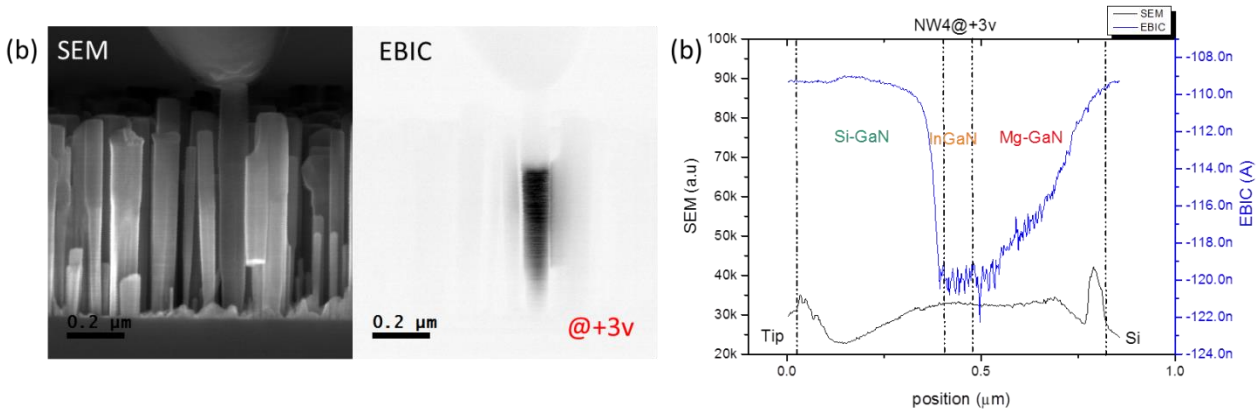

Figure 5.7 SEM and EBIC map (a) and the extracted EBIC signal profile (b) of an InGaN/GaN NW p-i-n junction NW.

These results constitute a starting point for further developments, which may involve a combination of single-NW investigations to gain a fundamental understanding of the energy conversion and transport properties at the nanoscale, with the development of larger-scale NW array devices for PV energy conversion. At the present stage, only a coherent synergy of both material-oriented and device-oriented investigations could provide insights for further developments and improvements of these material systems. Nevertheless, the ensemble of these results open encouraging perspectives towards the synthesis of high quality and, possibly, efficient p-i-n InGaN/GaN NW junctions for new III-N NW-based solar cells.

5.2.2 InGaN/GaN NWs for piezoelectrics

The mechanical vibrations and deformations are a second type of renewable energy sources, which in some cases are more accessible than solar energy, since they are ubiquitous and are not related to the day time. These energies may have various origins,

such as body movements, sound vibrations, hydraulic movements, wind, friction... They can be harvested using piezoelectric materials.

The piezoelectric generators based on ZnO and more recently on nitride NWs have emerged as excellent candidates to fabricate novel ultra-compact and efficient power sources. In this latter case, being the InN material characterized by a higher piezoelectric coefficient in comparison with GaN[24], the integration of thick In-rich InGaN insertions inside the GaN NW volume appears as a promising solution to further improve the conversion efficiency of GaN NWs. We thus investigated the conversion capacity of p-doped GaN-capped 70 nm-thick $In_{0.35}Ga_{0.65}N$/GaN NW heterostructures, and compared it to the one of binary p-doped GaN NWs[ii]. In order to measure accurately the piezoelectric response of individual NWs and because the III-N NWs are characterized by a high flexibility, the NWs have been mechanically consolidated by embedding their bottom portion in an 850 nm thick polydimethylsiloxane (PDMS) layer (sketch in Fig.5.8).

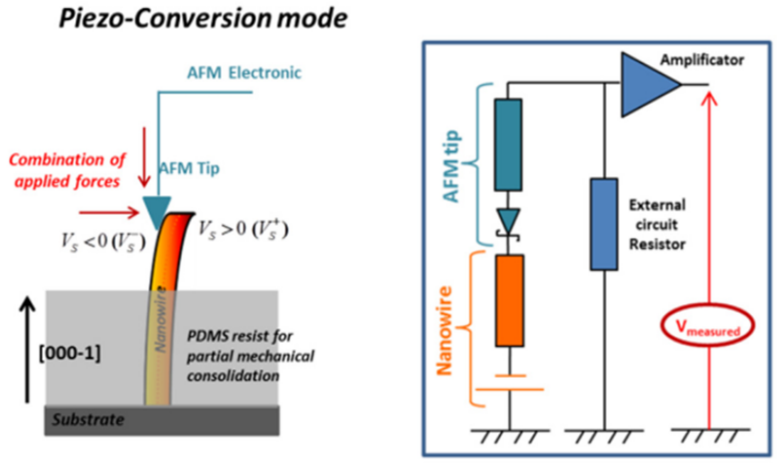

Figure 5.8 Schematic representation of the piezo-generation measurement principle on single NWs, using an atomic force microscope (AFM) system in vertical configuration equipped with a modified Resiscope module.

The piezo-conversion measurements have been performed by Nikoletta Jegenyes, during her post-doc in our research group. The experimental set-up involves an atomic force microscope (Bruker Nano Surface, Palaiseau, France) in the vertical configuration, equipped with a Resiscope module[23] (Fig. 5.8). In this experimental configuration, the AFM tip scans over the surface of the NW array in contact mode and under a controlled

[ii] In both cases, the p-type conductivity is non-intentional and induced by Mg background impurities.

and constant normal force. The AFM tip induces a lateral deflection of the nanostructure, which results in the appearance of an asymmetric strain across the NW: from a tensile strain to the outer face of the NW to a compressive one to the inner face. As a result, a piezoelectric field is created inside the NW evolving respectively from a negative to a positive value as schematized in Figure 5.7 (left image). The electrical response of the NW is monitored by the modified home-made Resiscope, which is connected to the substrate (via an ohmic contact) and to the NW (via a Schottky contanct between the GaN and the conductive PtSi AFM tip). Because the topographic and electric profiles are systematically and simultaneously recorded, it is possible to establish a direct correlation with each voltage output corresponding to one single NW.

Fig. 5.9(b,c) shows the 2D mappings of the output voltage peaks generated by InGaN/GaN and binary GaN NW arrays recorded for a constant normal force (CNF) of 150 nN.

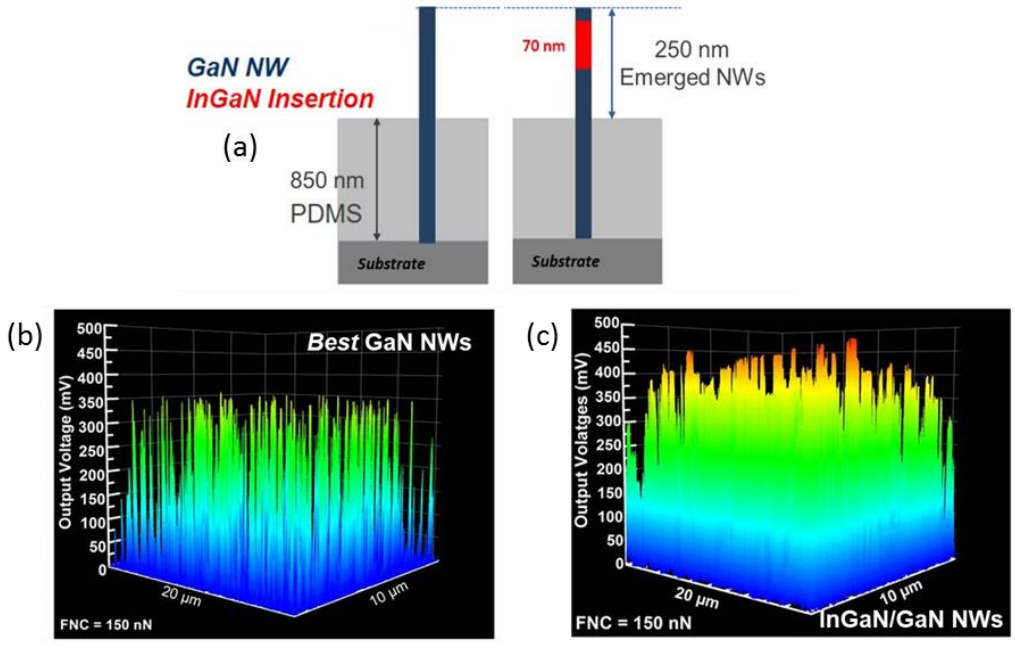

Figure 5.9 (a) Schematization of the consolidated GaN NW and InGaN/GaN NW structures, with their corresponding 2D output voltage mappings (b,c) acquired for an applied normal force of 150 nN.

The maximum output voltage measured on InGaN/GaN NW array reached 470 mV per NW for 150 nN applied force, demonstrating an improvement of approximately 35% over the p-GaN NW piezo-conversion capacity (about 350 mV)[241], as well as an improvement of about 7% in comparison with the highest reported voltage for single n-GaN NWs

(about −442 mV)[23]. This is the first demonstration of piezoelectric conversion from InGaN/GaN heterostructures reported in the literature[242]. These experimental results demonstrate the capability of InGaN insertions to enhance the energy generation and settling the new state-of-the-art for piezoelectric generation from nitride-based NWs. These results offer a promising perspective to develop ultra-compact and high-efficient renewable energy harvesters for powering micro-devices.

Credits

The PL measurements on InGaN/GaN NWs on graphene were performed with the help of the PH.D. stundent H.G. Song, in the framework of the collaborative project “STAR” with the KAIST University of Daejeon (South Corea). The EBIC measurements have been entirely carried out by Omar Saket, a Ph.D. of our group focusing on EBIC characterization. The piezoelectric measurements on InGaN/GaN NWs were entirely carried out by Nikoletta Jegenies in the framework of its post-doc in out group.

Conclusions of the manuscript

This Ph.D. thesis work focused on the growth and characterization of InGaN/GaN heterostructured NWs for photovoltaic and piezoelectric applications. In these contexts, I addressed a number of fundamental questions concerning the material itself and its functional properties *:* (i) the rational and controlled growth of InGaN NW heterostructures; (ii) the theoretical and experimental assessment of their band structure, in accordance with their compositional profile and strain field; and (iii) the identification of viable strategies to achieve the best control over the NW morphology and positioning and, ultimately, the homogeneity of their above-mentioned InGaN heterostructure properties.

The synthesis of InGaN/GaN NW heterostructures has been investigated by different research teams which, however, reported a rather broad panorama of possible morphologies and alloy compositions, with no straightforward relationship to the specific growth conditions. The correlation between morphology, composition and growth conditions is a necessary step to gain understanding of their formation mechanism and to achieve good control over their properties.
In the present work I have built for the first time a comprehensive flux-dependent diagram for the growth of InGaN/GaN NW axial heterostructures by PA-MBE. I have experimentally and theoretically demonstrated that the InGaN deposited on top of GaN NWs may follow distinct growth modes and thus adopt markedly different morphologies depending on the specific V/III conditions at the NW growth front. In summary, I have shown that low In/Ga flux ratios establishing locally N-rich conditions, lead to strain-driven InGaN islanding at the center of the NW top plane. The parallel growth of a Ga-rich non-uniform shell around the narrow InGaN core results in the tapered outer morphology. On the contrary, intermediate In/Ga flux ratios allowing the formation of a stable In adsorbed layer at the NW growth front (locally In-rich conditions), promote the growth of untapered sections. In this case, a disk-like insertion fitting almost the entire NW diameter is surrounded by a thin uniform shell. In agreement with theoretical predictions, the island-to-disk transition is assigned to the surfactant effect of the In adsorbed layer, which inhibits strain-driven islanding by lowering the surface energy of

the InGaN deposit. Finally, high In/Ga flux ratios trigger a pronounced radial overgrowth or morphological deterioration of the InGaN sections (highly metal-rich conditions). The effects of metal fluxes and strain pulling on the In incorporation are discussed. In particular, I have put in an accent on the impact the Ga flux on both the heterostructure growth rate and its composition.
All these results allowed me to identify the best growth conditions to fabricate In-rich (x_{In}~0.40), highly homogeneous InGaN sections presenting abrupt interfaces and a disk-like morphology. Importantly, the fundamental understanding of their growth regime and formation mechanism, allowed me to reproducibly control their growth in terms of both the average growth rate and the In content. Also, these results suggest that, in perspective, the three observed growth regimes may exist also at different growth temperatures (as in the growth of planar InGaN layers), offering the possibility to select the specific heterostructure morphology even for different alloy compositions, which is relevant in view of a full control-by-design of their basic properties.

I have investigated the photoluminescence (PL) of InGaN/GaN NW ensembles and single InGaN/GaN NWs. General features of the InGaN/GaN emission are the following: these structures show a weak (NW ensemble) or absent (single NWs) InGaN PL at room and low temperature under non-resonant optical excitation, and a broad (FWHM of few hundreds of meV) bi-component luminescence under a resonant excitation (NW ensemble). The broad PL emission has been primarily associated to the dispersion of the In content between different NWs, arising from the use of a self-assembled growth approach. In parallel, I tentatively assigned the presence of bi-component PL signals to a decreased In incorporation in NWs presenting inversion domains, a recurrent defect of many (10-30%) GaN NWs grown on AlN/Si(111) substrates.
Generally, temperature-dependent PL measurements have shown that In-rich sections present a lower PL internal quantum efficiency compared to In-poor structures, even though, according to structural characterizations, they do not exhibit extended defects. I tentatively explained this phenomenon by the higher surface-to-volume ratio of the In-rich InGaN sections (with a thin Ga-rich shell), which could increase the non-radiative surface recombination. However, the decreased IQE could also arise from the polar nature of the heterostructures and their anisotropic strain distribution (in principle, more pronounced for In-rich sections). In fact, our structural investigation on thick InGaN NW

heterostructures showed that strain can only marginally be relaxed and the insertions are characterized by: a large relaxation of the In-rich core in-plane strain (above the compositional pulling region), and a compressive out-of-plane strain state all along the section length, due to the presence of the Ga-rich shell. This scenario was also confirmed by our finite elements simulation of the strain field within a coherent disk-like section, presenting a compositional profile and geometrical parameters close to the experimental ones.

Simulations of the InGaN band structure taking into account the simulated strain field, evidenced a highly anisotropic electric field and band edge profile along the heterostructure axis. On the base of power-dependent PL and time-resolved PL on NW ensembles, and cathodoluminescence characterization on single NWs, I propose that this field may lead to a substantial reduction of the InGaN volume allowing an efficient radiative recombination, resulting in an emission process dominated by two transitions in proximity of the InGaN section base and top.

Nevertheless, if these results indicate that In-rich thick disk-like section is unfavorable for LEDs applications, in the last part of the manuscript I have shown that the strong electric field can be advantageous to promote carrier separation in photovoltaic devices. Specifically, the optimal design of the p-i-n InGaN/GaN junction should involve a bottom p-doped GaN base, and an upper n-doped GaN cap. In fact, for this p-n junction orientation the internal field inside the InGaN insertion adds up with the built-in field of the p-n junction. Preliminary results on the growth of Mg-GaN/Si-GaN NW junctions and subsequent Electron-Beam Induced Current (EBIC) characterization evidence that this architecture might be convenient also from the point of view of epitaxial growth, due to the reduced radial growth in Si-doped NW segment (n-doping) compared to the Mg-doped NW part (p-doping). This result opens encouraging perspectives towards the fabrication of high quality InGaN/GaN NW functional junctions for new III-N NW-based solar cells.

All along this work, I have shown that InGaN/GaN NWs can be efficiently and controllably grown on AlN/Si(111) substrates by the self-assembled growth method. However, as evidenced by EDX statistics and PL measurements, the InGaN sections do not exhibit homogeneous properties over the sample, an aspect which primarily arises from the length and diameter dispersion of the GaN NW on which they are grown. To

gather a higher control over the InGaN/GaN NW properties, it is necessary to go for a selective area growth approach (SAG) where the NW positioning and diameter are controlled, resulting in a homogenous and predetermined morphology.

In this context, I have investigated the growth of GaN NWs on a new type of substrate: graphene transferred on a Si/SiO_2 substrate. I have successfully demonstrated the SAG growth on: transferred mono-layer graphene (MLG) 1 cm^2 patches, small multi-layer graphene domains and, for the first time in the literature, on patterned MLG. In all cases, the NWs exhibit a clear in-plane orientation, confirming the establishment of an epitaxial relationship between the graphene honeycomb structure and GaN hexagonal lattice (possibly involving a supercell with 3 unit cells of GaN and 4 of graphene). This observation correlates well with post-growth Raman characterizations, evidencing that the pristine structure of the MLG is able to withstand the PA-MBE growth process.

Concerning the growth conditions for SAG, on all considered substrates, a temperature window of few degrees around 815 °C was observed to allow for growing GaN NWs on graphene with a perfect selectivity within the considered growth rate and V/III ratio. In these conditions, the NWs present very long incubation times (more than one hour on MLG patches). I have shown that this impacts significantly the growth on patterned substrates. Specifically the statistical analysis of NW length distributions and graphene dots occupation rate for different pattern sizes and growth times clearly evidence that if the dot size is reduced below 200 nm diameter, the nucleation of the NWs becomes more and more delayed. In this context, if the NW length distribution is modeled by taking into account the NW incubation time, we estimate that this increases of a factor of ~1.5 when the dot size is reduced from 400 to 100 nm diameter. We propose that the increase in NW incubation time is due to a reduced collection length of gallium per nucleation site, when the graphene dots dimensions are comparable or lower than the Ga diffusion length on graphene (estimated to be around 45 nm based on the modeling of our experimental data).

These results constitute the first demonstration of SAG growth of GaN NWs on transferred patterned graphene. However, the main outcome is that growing one single NW in ~50 nm diameter graphene dots might be longer than what is acceptable for practical applications. To tackle this problematic, I propose a 2-step growth process involving a nucleation step at high Ga fluxes, and a NW elongation step at lower Ga fluxes. This strategy could allow to accelerate the NW incubation time (and thus reduce

the length dispersion), while allowing to maintain a perfect selectivity compared to the SiO_2 surrounding surface. Also, it is possible that a reduced NW incubation time could help to preserve at best the graphene electrical properties, which are otherwise damaged by plasma exposure.
Other experiments are needed to validate this hypothesis. Nevertheless, these results suggest that after an optimization of the growth conditions, SAG of GaN on small MLG patterns could be possible and very promising. This is furthermore supported by the fact that GaN NWs on graphene exhibit state-of-the-art optical properties, and, most of all, they do not show the PL signature associated to IDBs, as verified by PL measurements.

Finally, the piezo-conversion response of GaN NWs embedding single In-rich (x_{In}~0.35) disk-like InGaN sections has been tested. Using an atomic force microscope equipped with a modified Resiscope module, I have shown an important enhancement of the piezoconversion from NWs when integrating in their volume a InGaN section. This improvement is attributed to the higher piezoelectric field in presence of InGaN, since this material has a higher piezoelectric coefficient compared to GaN. Average output voltages up to 330 ± 70 mV and a maximum value of 470 mV per NW have been measured for nanostructures integrating 70 nm-thick InGaN insertion capped with a ~20 nm thick GaN capping layer. This latter value establishes an increase of about 35% of the piezo-conversion capacity in comparison with binary p-doped GaN NWs. Based on the measured output signals, it is estimated that one layer of dense InGaN/GaN-based NWs can generate a maximum output power density of about 3.3 W/cm^2 (this estimation is done assuming that all NWs produce a homogeneous output equal to the best-measured value). These results offer a promising perspective for improving the performances of GaN NW-based piezoelectric sources.

Bibliography

(1) Maruska, H. P.; Tietjen, J. J. *Appl. Phys. Lett.* **1969**, *15* (10), 327–329.

(2) Nakamura, S. *Jap. J. Appl. Phys.* **1991**, *30* (10A), 1705–1707.

(3) Nakamura, S.; Mukai, T.; Senoh, M. *J. Appl. Phys.* **1992**, *71* (11), 5543–5549.

(4) Nakamura, S.; Iwasa, N.; Senoh, M.; Mukai, T. *Jpn. J. Appl. Phys.* **1992**, *31*, 1258–1266.

(5) Nakamura, S.; Mukai, T.; Senoh, M.; Iwasa, N. *Jpn. J. Appl. Phys.* **1991**, *31*, 139–142.

(6) Amano, H.; Kito, M.; Hiramatsu, K.; Akasaki, I. *Jpn. J. Appl. Phys.* **1989**, *28* (Part 2, No. 12), L2112–L2114.

(7) Nakamura, S.; Senoh, M.; Iwasa, N.; Nagahala, S.-I.; Yamada, T.; Mukai, T. *Jpn. J. Appl. Phys.* **1995**, *34*, 1332–1335.

(8) Morkoç, H. *J. Mater. Sci. Mater. Electron.* **2001**, *12* (12), 677–695.

(9) Grandjean, N.; Damilano, B.; Massies, J. *J. Phys. Condens. Matter* **2001**, *13*, 6945–6960.

(10) Wang, S. *Lattice engineering: Technology and applications*; 2012.

(11) Riechert, H.; Averbeck, R.; Graber, A.; Schienle, M.; Strauβ, U.; Tews, H. *MRS Online Proc. Libr.* **1996**, *449*, 149–159.

(12) Heying, B.; Averbeck, R.; Chen, L. F.; Haus, E.; Riechert, H.; Speck, J. S. *J. Appl. Phys.* **2000**, *88* (4), 1855–1860.

(13) Neugebauer, J. *Phys. Status Solidi C* **2003**, *0* (6 SPEC. ISS.), 1651–1667.

(14) Daudin, B.; Feuillet, G.; Mula, G.; Mariette, H.; Rouviere, J. L.; Pelekanos, N.; Fishman, G.; Adelmann, C.; Simon, J. *Phys. Status Solidi* **1999**, *621*, 621–628.

(15) Http://www.ioffe.ru/SVA/NSM/Semicond/InN/basic.html. .

(16) Http://www.ioffe.ru/SVA/NSM/Semicond/GaN/basic.html. .

(17) Jacopin, G.; Rigutti, L.; Largeau, L.; Fortuna, F.; Furtmayr, F.; Julien, F. H.;

Eickhoff, M.; Tchernycheva, M. *J. Appl. Phys.* **2011**, *110*, 64313.

(18) Consonni, V.; Knelangen, M.; Jahn, U.; Trampert, A.; Geelhaar, L.; Riechert, H. *Appl. Phys. Lett.* **2009**, *95*, 241910.

(19) Http://www.ioffe.ru/SVA/NSM/Semicond/AlN/basic.html. .

(20) Holec, D.; Costa, P. M. F. J.; Kappers, M. J.; Humphreys, C. J. *J. Cryst. Growth* **2007**, *303* (1 SPEC. ISS.), 314–317.

(21) Http://www.ioffe.ru/SVA/NSM/Semicond/GaN/mechanic.html. .

(22) Http://www.ioffe.ru/SVA/NSM/Semicond/InN/index.html. .

(23) Gogneau, N.; Chrétien, P.; Galopin, E.; Guilet, S.; Travers, L.; Harmand, J.; Houzé, F. *Phys. Status Solidi RRL* **2014**, *5*, 414–419.

(24) Bernardini, F.; Fiorentini, V. *Phys. Status Solidi Appl. Res.* **2002**, *190* (1), 65–73.

(25) Kuykendall, T.; Ulrich, P.; Aloni, S.; Yang, P. *Nat. Mater.* **2007**, *6* (12), 951–956.

(26) Wu, J. **2009**, *11101*.

(27) Vurgaftman, I.; Meyer, J. R.; Ram-Mohan, L. R. *J. Appl. Phys.* **2001**, *89* (11), 5815.

(28) Butcher, K. S. A.; Tansley, T. L. **2005**, *38*, 1–37.

(29) Urban, A.; Malindretos, J.; Klein-Wiele, J. H.; Simon, P.; Rizzi, A. *New J. Phys.* **2013**, *15*, 1–14.

(30) Glas, F. *Strain in Nanowires and Nanowire Heterostructures*, Semiconduc.; Fontcuberta i Morral, A., Dayeh, S. A., Jagadish, C., Eds.; Burlington Academic Press, 2015; Vol. 93.

(31) Zettler, J. K.; Hauswald, C.; Corfdir, P.; Musolino, M.; Geelhaar, L.; Riechert, H.; Brandt, O.; Fernandez-garrido, S. *Cryst. Growth Des.* **2015**, *15*, 4104–4109.

(32) Chang, Y. L.; Wang, J. L.; Li, F.; Mi, Z. *Appl. Phys. Lett.* **2010**, *96* (1), 13106.

(33) Barletta, P. T.; Berkman, E. A.; Moody, B. F.; El-Masry, N. A.; Emara, A. M.; Reed, M. J.; Bedair, S. M. *Appl. Phys. Lett.* **2007**, *90* (15), 1–4.

(34) Matioli, E.; Neufeld, C.; Iza, M.; Cruz, S. C.; Al-Heji, A. A.; Chen, X.; Farrell, R. M.; Keller, S.; DenBaars, S.; Mishra, U.; Nakamura, S.; Speck, J.; Weisbuch, C.

Appl. Phys. Lett. **2011**, *98* (2), 21102.

(35) Bhuiyan, A. G.; Sugita, K.; Hashimoto, A.; Yamamoto, A. *IEEE J. Photovoltaics* **2012**, *2* (3), 276–293.

(36) Fazio, B.; Artoni, P.; Iat, M. A.; D'Andrea, C.; Lo Faro, M. J.; Del Sorbo, S.; Pirotta, S.; Gucciardi, P. G.; Musumeci, P.; Vasi, C. S.; Saija, R.; Galli, M.; Priolo, F.; Irrera, A. *Light Sci. Appl.* **2016**, *5* (August 2015), 1–7.

(37) Zhu, G.; Yang, R.; Wang, S.; Wang, Z. L. *Nanoletters* **2010**, *10*, 3151–3155.

(38) Zhu, G.; Wang, A. C.; Liu, Y.; Zhou, Y.; Wang, Z. L. *Nano Lett.* **2012**, *12*, 3096–3090.

(39) Jamond, N.; Jamond, N.; Jamond, N. **2017**.

(40) Jamond, N.; Chrétien, P.; Houzé, F.; Lu, L.; Largeau, L.; Maugain, O.; Travers, L.; Harmand, J. C.; Glas, F.; Lefeuvre, E.; Tchernycheva, M.; Gogneau, N. *Nanotechnology* **2016**, *27* (32).

(41) Liu, G.; Zhao, S.; Henderson, R. D. E.; Leonenko, Z.; Abdel-Rahman, E.; Mi, Z.; Ban, D. *Nanoscale* **2015**, *0*, 1–9.

(42) Huang, B. C.; Song, J.; Tsai, C.; Lee, W.; Lien, D.; Gao, Z.; Hao, Y.; Chen, L.; Wang, Z. L. *Adv. Mater.* **2010**, *22*, 4008–4013.

(43) Yang, P.; Yan, R.; Fardy, M. *Nanoletters* **2010**, *10*, 1529–1536.

(44) Zhou, Y. S.; Hinchet, R.; Yang, Y.; Ardila, G.; Songmuang, R.; Zhang, F.; Zhang, Y.; Han, W.; Pradel, K.; Montès, L.; Mouis, M.; Wang, Z. L. *Adv. Mater.* **2013**, *25*, 883–888.

(45) Zhao, M.; Wang, Z.; Mao, S. X. *Nano Lett.* **2004**, *4* (4), 587–590.

(46) Agrawal, R.; Espinosa, H. D. *Nano Lett.* **2011**, *11*, 786–790.

(47) Minary-jolandan, M.; Bernal, R. A.; Kuljanishvili, I.; Parpoil, V.; Espinosa, H. D. *Nanol* **2012**, *12*, 970–976.

(48) Wang, Z.; Pan, X.; He, Y.; Hu, Y.; Gu, H.; Wang, Y. *Adv. Mater. Sci. Eng.* **2015**, *2015*.

(49) Https://www.physik.uni-kl.de/en/hillebrands/research/methods/molecular-beam-epitaxy/. .

(50) Frank, F. C.; van der Merwe, J. H. *Proc. R. Soc. A Math. Phys. Eng. Sci.* **1949**, *198* (1053), 205–216.

(51) Volmer, M.; Weber, A. *Zeitschrift für Phys. Chemie* **1926**, *119* (3–4), 277–301.

(52) Blant, A. V; Hughes, O. H.; Cheng, T. S.; Novikov, S. V; Foxon, C. T. *Plasma Sources Sci. Technol.* **2000**, *9*, 11–17.

(53) Iliopoulos, E.; Adikimenakis, A.; Dimakis, E.; Tsagaraki, K. *J. Cryst. Growth* **2005**, *278*, 426–430.

(54) Kikuchi, T.; Somintac, A. S.; Ariyada, O.; Wada, M.; Ohachi, T. *J. Cryst. Growth* **2006**, *292*, 221–226.

(55) Osaka, J.; Kumar, M. S.; Toyoda, H.; Ishijima, T.; Sugai, H. **2012**, *172114* (2007), 137–140.

(56) Park, T.; Chung, C.; Jung, S.; Jeon, D.; Park, T.; Chung, C.; Jung, S.; Fim, D. J.; Studies, R.; Atomatic, O. N. *J. Phys.* **1988**, *49* (11), 275–280.

(57) Asaoka, H.; Uozumi, Y. *Thin Solid Films* **2015**, *591*, 200–203.

(58) Takayanagi, K.; Tanishiro, Y.; Takahashi, S.; Takahashi, M. *Surf. Sci.* **1985**, *164* (2–3), 367–392.

(59) Koblmüller, G.; Gallinat, C. S.; Bernardis, S.; Speck, J. S.; Chern, G. D.; Readinger, E. D.; Shen, H.; Wraback, M. *Appl. Phys. Lett.* **2006**, *89* (7), 2004–2007.

(60) Dimakis, E.; Iliopoulos, E.; Tsagaraki, K.; Kehagias, T.; Komninou, P.; Georgakilas, a. *J. Appl. Phys.* **2005**, *97* (11).

(61) Cao, Y. G.; Xie, M. H.; Liu, Y.; Ng, Y. F.; Wu, H. S.; Tong, S. Y. *Appl. Phys. Lett.* **2003**, *83* (25), 5157–5159.

(62) Yoshizawa, M.; Kikuchi, A.; Mori, M.; Fujita, N.; Kishino, K. *Jpn. J. Appl. Phys.* **1997**, *36*, 459–462.

(63) Sanchez-Garcia, M. A.; Calleja, E.; Monroy, E.; Sanchez, F. J.; Calle, F.; Muñoz, E.; Beresford, R. *J. Cryst. Growth* **1998**, *183* (1–2), 23–30.

(64) Landré, O.; Bougerol, C.; Renevier, H.; Daudin, B. *Nanotechnology* **2009**, *20* (41), 415602.

(65) Brubaker, M. D.; Levin, I.; Davydov, A. V.; Rourke, D. M.; Sanford, N. a.; Bright,

V. M.; Bertness, K. a. *J. Appl. Phys.* **2011**, *110* (5), 53506.

(66) Songmuang, R.; Landré, O.; Daudin, B. *Appl. Phys. Lett.* **2007**, *91* (25), 91–94.

(67) Reznik, R. R.; Kotlyar, K. P.; Ilkiv, I. V; Soshnikov, I. P.; Kukushkin, S. A.; Osipov, V.; Nikitina, E. V; Cirlin, G. E. *J. Phys. Conf. Ser.* **2016**, *741*, 12027.

(68) Calabrese, G.; Corfdir, P.; Gao, G.; Trampert, A.; Geelhaar, L.; Brandt, O. *Appl. Phys. Lett.* **2016**, *108*, 202101.

(69) Schuster, F.; Winnerl, A.; Weiszer, S.; Hetzl, M.; Garrido, J. A.; Stutzmann, M. *J. Appl. Phys.* **2015**, *117* (4).

(70) Ramsteiner, M.; Gao, G.; Galves, L. A.; Sharma, B.; Corfdir, P.; Calabrese, G.; Schiaber, Z. D. S.; Pfu, C.; Trampert, A.; Lopes, J. M. J.; Brandt, O.; Geelhaar, L. *Nanoletters* **2017**, *17*, 5213–5221.

(71) Tchernycheva, M.; Neplokh, V.; Zhang, H.; Lavenus, P.; Rigutti, L.; Bayle, F.; Julien, F. H.; Babicev, A.; Jacopin, G.; Largeau, L.; Ciechonski, G.; Vescovi, G.; Fryliouk, O. *Nanoscale* **2015**, *0*, 1–2.

(72) Largeau, L.; Dheeraj, D. L.; Tchernycheva, M.; Cirlin, G. E.; Harmand, J. C. *Nanotechnology* **2008**, *19*, 155704.

(73) Largeau, L.; Galopin, E.; Gogneau, N.; Travers, L.; Glas, F. *Cryst. Growth Des.* **2012**, *12*, 2724–2729.

(74) Tchernycheva, M.; Sartel, C.; Cirlin, G.; Travers, L.; Patriarche, G.; Harmand, J.; Dang, L. S.; Renard, J.; Gayral, B.; Nevou, L.; Julien, F. *Nanotechnology* **2007**, *18* (385306).

(75) Consonni, V.; Knelangen, M.; Geelhaar, L.; Trampert, A.; Riechert, H. *Phys. Rev. B - Condens. Matter Mater. Phys.* **2010**, *81* (8), 1–10.

(76) Gacevic, Z.; Gomez Sanchez, D.; Calleja, E. *Nano Lett.* **2015**.

(77) Park, Y.; Jahangir, S.; Park, Y.; Bhattacharya, P.; Heo, J. *Opt. Express* **2015**, *23* (11), A650.

(78) Kumaresan, V.; Largeau, L.; Oehler, F.; Zhang, H.; Mauguin, O.; Glas, F.; Gogneau, N.; Tchernycheva, M.; Harmand, J. C. *Nanotechnology* **2016**, *27* (13), 0.

(79) Fernández-Garrido, S.; Kaganer, V. M.; Sabelfeld, K. K.; Gotschke, T.; Grandal, J.; Calleja, E.; Geelhaar, L.; Brandt, O. *Nano Lett.* **2013**, *13* (7), 3274–3280.

(80) Wei, J.; Neumann, R.; Wang, X.; Li, S.; Fündling, S.; Merzsch, S.; Al-Suleiman, M. A. M.; Sökmen, Ü.; Wehmann, H. H.; Waag, A. *Phys. Status Solidi Curr. Top. Solid State Phys.* **2011**, *8* (7–8), 2157–2159.

(81) Auzelle, T.; Haas, B.; Minj, A.; Bougerol, C.; Rouvière, J.-L.; Cros, A.; Colchero, J.; Daudin, B. *J. Appl. Phys.* **2015**, *117* (24), 245303.

(82) Li, D.; Sumiya, M.; Fuke, S.; Yang, D.; Que, D.; Suzuki, Y.; Fukuda, Y. *J. Appl. Phys.* **2001**, *90* (8).

(83) Nath, D. N.; Gur, E.; Ringel, S. A.; Rajan, S. *J. Vac. Sci. Technol. B* **2011**, *29* (2), 21206.

(84) Koblmüller, G.; Gallinat, C. S.; Speck, J. S.; Koblmüller, G.; Gallinat, C. S.; Speck, J. S. *J. Appl. Phys.* **2009**, *101* (2007), 83516.

(85) Nath, D. N.; Gür, E.; Ringel, S. A.; Rajan, S.; Nath, D. N.; Gür, E.; Ringel, S. A.; Rajan, S. *Appl. Phys. Lett.* **2010**, *97* (71903), 1–4.

(86) Gačević, Ž.; Gómez, V. J.; Rodríguez, P. E. D. S.; Bengoechea, A. *J. Cryst. Growth* **2013**, *364*, 123.

(87) Valdueza-Felip, S.; Bellet-Amalric, E.; Núñez-Cascajero, A.; Wang, Y.; Chauvat, M.-P.; Ruterana, P.; Pouget, S.; Lorenz, K.; Alves, E.; Monroy, E. *Appl. Phys. Lett.* **2014**, *116*, 233504.

(88) Tourbot, G.; Bougerol, C.; Glas, F.; Zagonel, L. F.; Mahfoud, Z.; Meuret, S.; Gilet, P.; Kociak, M.; Gayral, B.; Daudin, B. *Nanotechnology* **2012**, *23* (135703).

(89) Kong, X.; Albert, S.; Bengoechea, A.; Sanchez, M. A.; Calleja, E.; Trampert, A. *Phys. Status Solidi* **2015**, *212* (4), 736–739.

(90) Tourbot, G.; Bougerol, C.; Grenier, A.; Hertog, M. Den. *Nanotechnology* **2011**, *22* (75601).

(91) Gangopadhyay, S.; Schmidt, T.; Einfeldt, S.; Yamaguchi, T.; Hommel, D.; Falta, J. *J. Vac. Sci. Technol. B Microelectron. Nanom. Struct.* **2007**, *25* (3), 791.

(92) Albert, S.; Bengoechea-encabo, A.; Kong, X.; Sa, M. A.; Trampert, A. *Cryst. Growth Des.* **2015**, *15*, 2661–2666.

(93) Guo, W.; Banerjee, A.; Bhattacharya, P.; Ooi, B. S.; Guo, W.; Banerjee, A.; Bhattacharya, P.; Ooi, B. S. *Appl. Phys. Lett.* **2011**, *98*, 193102.

(94) Zhang, X.; Lourenço-Martins, H.; Meuret, S.; Kociak, M.; Haas, B.; Rouvière, J.-L.; Jouneau, P.-H.; Bougerol, C.; Auzelle, T.; Jalabert, D.; Biquard, X.; Gayral, B.; Daudin, B. *Nanotechnology* **2016**, *27* (19), 195704.

(95) Zhang, X.; Lourenço-martins, H.; Meuret, S.; Zhang, X.; Haas, B.; Rouvière, J.; Robin, E. *Nanotechnology* **2016**, *27* (45), 1–8.

(96) Kouno, T.; Sakai, M.; Kishino, K.; Kikuchi, A.; Umehara, N.; Hara, K. *Nat. Publ. Gr.* **2016**, *8* (7), e289-7.

(97) Duff, A. I.; Lymperaki, L.; Neugebauer, J. *Phys. Status Solidi* **2015**, *865* (5), 855–865.

(98) Neugebauer, J.; Zywietz, T. K.; Scheffler, M.; Northrup, J. E.; Chen, H.; Feenstra, R. M. *Phys. Rev. Lett.* **2003**, *90* (5), 56101.

(99) Doppalapudi, D.; Basu, S. N.; Moustakas, T. D. *J. Appl. Phys.* **1998**, *512* (3), 1389–1395.

(100) Woo, S. Y.; Bugnet, M.; Nguyen, H. P. T.; Mi, Z.; Botton, G. A. *1* (c), 1–5.

(101) Kehagias, T. *Phys. E Low-dimensional Syst. Nanostructures* **2010**, *42* (9), 2197–2202.

(102) Lundskog, A.; Palisaitis, J.; Hsu, C. W.; Eriksson, M.; Karlsson, K. F.; Hultman, L.; Persson, P. O. Å; Forsberg, U.; Holtz, P. O.; Janzén, E. *Nanotechnology* **2012**, *23* (30), 305708.

(103) Song, J.; Leung, B.; Zhang, Y.; Han, J. *Nanotechnology* **2014**, *25* (22), 225602.

(104) Tang, F.; Zhu, T.; Oehler, F.; Fu, W. Y.; Griffiths, J. T.; Massabuau, F. C.; Kappers, M. J.; Martin, T. L.; Bagot, P. A. J.; Moody, M. P.; Oliver, R. A. *Appl. Phys. Lett.* **2015**, *106*, 72104.

(105) Kachkanov, V.; Donnell, K. P. O.; Martin, R. W.; Mosselmans, J. F. W.; Pereira, S.; Kachkanov, V.; Donnell, K. P. O.; Martin, R. W. *Appl. Phys. Lett.* **2006**, *89*, 101908.

(106) Kawaguchi, Y.; Shimizu, M.; Hiramatsu, K.; Sawaki, N. *Mater. Res. Soc. Symp. Proceeding* **1997**, *449*, 89–94.

(107) Pereira, S.; Correia, M. R.; Pereira, E.; O'Donnell, K. P.; Trager-Cowan, C.; Sweeney, F.; Alves, E. *Phys. Rev. B* **2001**, *64*, 205311.

(108) Valdueza-Felip, S.; Bellet-Amalric, E.; Núñez-Cascajero, a.; Wang, Y.; Chauvat, M.-P.; Ruterana, P.; Pouget, S.; Lorenz, K.; Alves, E.; Monroy, E. *J. Appl. Phys.* **2014**, *116* (23), 233504.

(109) Hestroffer, K.; Mata, R.; Camacho, D.; Leclere, C.; Tourbot, G.; Niquet, Y. M.; Cros, A.; Bougerol, C.; Renevier, H.; Daudin, B. *Nanotechnology* **2010**, *21* (41).

(110) Leung, M. S. H.; Klockenbrink, R.; Kisielowski, C.; Fujii, H.; Kruger, J.; Sudhir, G. S.; Anders, A.; LilientalWeber, Z.; Rubin, M.; Weber, E. R. *Iii-V Nitrides* **1997**, *449*, 221–226.

(111) Bayram, C.; Razeghi, M. *Appl. Phys. A Mater. Sci. Process.* **2009**, *96* (2), 403–408.

(112) Adelmann, C.; Simon, J.; Pelekanos, N. T.; Samson, Y.; Feuillet, G.; Daudin, B. *Phys. Status Solidi Appl. Res.* **1999**, *176* (1), 639–642.

(113) Gogneau, N.; Jalabert, D.; Monroy, E.; Shibata, T.; Tanaka, M.; Daudin, B. *J. Appl. Phys.* **2003**, *94* (4), 2254–2261.

(114) Adelmann, C.; Gogneau, N.; Sarigiannidou, E.; Rouvière, J.; Daudin, B. *Appl. Phys. Lett.* **2002**, *81* (16), 3064–3066.

(115) Mula, G.; Adelmann, C.; Moehl, S.; Oullier, J.; Daudin, B. *Phys. Rev. B* **2001**, *64*, 1–12.

(116) Xu, K.; Yoshikawa, A. *Appl. Phys. Lett.* **2003**, *83* (2), 251–253.

(117) Nanishi, Y.; Araki, T.; Yamaguchi, T. *Indium Nitride and Related Alloys*; Veal, T. D., McConvilles, C. F., Schaff, W. J., Eds.; CRC Press, 2010.

(118) Monroy, E.; Daudin, B.; Bellet-Amalric, E.; Gogneau, N.; Jalabert, D.; Enjalbert, F.; Brault, J.; Barjon, J.; Dang, L. S. *J. Appl. Phys.* **2003**, *93* (3), 1550.

(119) Choi, S.; Kim, T.; Wolter, S.; Brown, A.; Everitt, H. O.; Losurdo, M.; Bruno, G. *Phys. Rev. B* **2008**, *77*, 115435.

(120) Das, A.; Magalhães, S.; Kotsar, Y.; Kandaswamy, P. K.; Gayral, B.; Lorenz, K.; Alves, E.; Ruterana, P.; Das, A.; Magalhães, S.; Kotsar, Y.; Kandaswamy, P. K.; Gayral, B.; Lorenz, K. *Appl. Phys. Lett.* **2010**, *96*, 181907.

(121) Adelmann, C.; Brault, J.; Mula, G.; Daudin, B.; Lymperakis, L.; Neugebauer, J. *Phys. Rev. B* **2003**, *67* (16), 165419.

(122) Averbeck, R.; Riechert, H. *Phys. Status Solidi* **1999**, *176*, 301–306.

(123) Turski, H.; Siekacz, M.; Wasilewski, Z. R.; Sawicka, M.; Porowski, S.; Skierbiszewski, C. *J. Cryst. Growth* **2013**, *367*, 115–121.

(124) Gomez-Gomez, M.; Garro, N.; Segura-Ruiz, J.; Martinez-Criado, G.; Cantarero, A.; Mengistu, H. T.; Garcia-Cristobal, A.; Murcia-Mascaros, S.; Denker, C.; Malindretos, J.; Rizzi, A. *Nanotechnology* **2014**, *25*, 75705.

(125) Bartolomé, J.; Hanke, M.; Van Treeck, D.; Trampert, A. *Nano Lett.* **2017**, *17* (8), 4654–4660.

(126) Allah, R. F.; Ben, T.; González, D. *Microsc. Microanal.* **2014**, *20*, 1254–1261.

(127) Serban, E. A.; Åke Persson, P. O.; Poenaru, I.; Junaid, M.; Hultman, L.; Birch, J.; Hsiao, C.-L. *Nanotechnology* **2015**, *26* (21), 215602.

(128) Glas, F.; Daudin, B. *Phys. Rev. B* **2012**, *86*, 174112.

(129) Woo, S. Y.; Gauquelin, N.; Nguyen, H. P. T.; Mi, Z.; Botton, G. A. *Nanotechnology* **2015**, *26* (34).

(130) Furtmayr, F.; Teubert, J.; Becker, P.; Conesa-Boj, S.; Morante, J. R.; Chernikov, A.; Schäfer, S.; Chatterjee, S.; Arbiol, J.; Eickhoff, M. *Phys. Rev. B - Condens. Matter Mater. Phys.* **2011**, *84* (20), 1–14.

(131) Gogneau, N.; Fossard, F.; Monroy, E.; Monnoye, S.; Mank, H.; Daudin, B. *Appl. Phys. Lett.* **2004**, *84* (21), 4224–4226.

(132) Niu, X.; Stringfellow, G. B.; Liu, F.; Niu, X.; Stringfellow, G. B.; Liu, F. *Appl. Phys. Lett.* **2011**, *99*, 213102.

(133) Northrup, J.; Neugebauer, J. *Phys. Rev. B* **1996**, *53* (16), R10477–R10480.

(134) Liu, Y.; Cao, Y. G.; Wu, H. S.; Xie, M. H.; Tong, S. Y. *Phys. Rev. B - Condens. Matter Mater. Phys.* **2005**, *71* (15), 0–4.

(135) Gogneau, N.; Monroy, E.; Fossard, F.; Gayral, B.; Monnoye, S.; Mank, H.; Daudin, B. *Phys. Status Solidi C Conf.* **2004**, *1* (10), 2504–2507.

(136) Neugebauer, J. *Phys. Status Solidi* **2001**, *227* (1), 93.

(137) Search, H.; Journals, C.; Contact, A.; Iopscience, M.; Address, I. P. *Semicond. Sci. Technol.* **2012**, *24013* (24013).

(138) Goodman, K. D.; Protasenko, V. V; Verma, J.; Kosel, T. H.; Xing, H. G.; Jena, D.

J. Appl. Phys. **2011**, *109*, 84336.

(139) Auzelle, T.; Haas, B.; Den Hertog, M.; Rouvière, J.-L.; Daudin, B.; Gayral, B. *Appl. Phys. Lett.* **2015**, *107* (5), 51904.

(140) Pfuller, C.; Corfdir, P.; Hauswald, C.; Flissikowski, T.; Kong, X.; Zettler, J. K.; Fernandez-Garrido, S.; Dogan, P.; Grahn, H. T.; Trampert, A.; Geelhaar, L.; Brandt, O. *Phys. Rev. B* **2016**, *94*, 155308.

(141) Pfüller, C.; Corfdir, P.; Hauswald, C.; Flissikowski, T.; Kong, X.; Zettler, J. K.; Fernández-Garrido, S.; Doğan, P.; Grahn, H. T.; Trampert, A.; Geelhaar, L.; Brandt, O. **2016**, No. 111, 1–23.

(142) Lefebvre, P.; Grandal, J.; Risti, J.; Calleja, E. *Appl. Phys. Lett.* **2011**, *98* (2011), 83104.

(143) Demichel, O.; Calvo, V.; Besson, A.; Noé, P.; Salem, B.; Pauc, N.; Oehler, F.; Gentile, P.; Magnea, N. *Nano Lett.* **2010**, *10* (7), 2323–2329.

(144) Mi, Z.; Nguyen, H. P. T.; Djavid, M.; Zhang, S.; Connie, A. T.; Sadaf, S. M.; Wang, Q.; Zhao, S.; Shih, I. *ECT Trans.* **2014**, *61* (5), 9–15.

(145) Nguyen, H. P. T.; Zhang, S.; Connie, A. T.; Kibria, M. G.; Wang, Q.; Shih, I.; Mi, Z. *Nano Lett.* **2013**, *13* (11), 5437–5442.

(146) Bavencove, A.-L.; Tourbot, G.; Garcia, J.; Désières, Y.; Gilet, P.; Levy, F.; André, B.; Gayral, B.; Daudin, B.; Dang, L. S. *Nanotechnology* **2011**, *22* (34), 345705.

(147) Sekiguchi, H.; Kishino, K.; Kikuchi, A. *Appl. Phys. Lett.* **2010**, *96* (23), 96–99.

(148) Zhao, H.; Liu, G.; Zhang, J.; Poplawsky, J. D.; Tansu, N. *Opt. Express* **2011**, *19* (May), 1179–1181.

(149) Kawakami, Y.; Suzuki, S.; Kaneta, A.; Funato, M.; Kikuchi, A.; Kishino, K. *Appl. Phys. Lett.* **2006**, *89* (16), 1–4.

(150) Tsai, W. C.; Chen, Y. T.; Lin, C. H.; Hsu, W. T.; Hsu, Y. S.; Chen, L. C.; Chen, K. H.; Chang, W. H. *Phys. Rev. B - Condens. Matter Mater. Phys.* **2013**, *88* (15), 1–6.

(151) Lahnemann, J.; Brandt, O.; Pf, C.; Flissikowski, T.; Jahn, U.; Luna, E.; Hanke, M.; Knelangen, M.; Trampert, A.; Grahn, H. T. *Phys. Rev. B* **2011**, *84*, 155303.

(152) Cardin, V.; Dion-Bertrand, L. I.; Grégoire, P.; Nguyen, H. P. T.; Sakowicz, M.; Mi, Z.; Silva, C.; Leonelli, R. *Nanotechnology* **2013**, *24* (4), 45702.

(153) Cho, Y.; Gainer, G. H.; Fischer, a J.; Song, J. J.; Keller, S. *Appl. Phys. Lett.* **1998**, *73*, 1370.

(154) Kaufmann, N. A. K. *Ph.D. Diss.* **2013**.

(155) Abell, J.; Moustakas, T. D. *Appl. Phys. Lett.* **2008**, *92* (9), 23–25.

(156) Ebaid, M.; Kang, J. H.; Yoo, Y. S.; Lim, S. H.; Cho, Y. H.; Ryu, S. W. *Sci. Rep.* **2015**, *5* (November), 1–10.

(157) Tung, L. T.; Lin, K. L.; Chang, E. Y.; Huang, W. C.; Hsiao, Y. L.; Chiang, C. H. *J. Phys. Conf. Ser.* **2009**, *187*.

(158) Sun, H.; Ji, Z.; Wang, H.; Xiao, H.; Qu, S.; Xu, X.; Jin, A. **2013**, *93508*.

(159) Armitage, R.; Tsubaki, K. *Nanotechnology* **2010**, *21* (19), 195202.

(160) Nguyen, H. P. T.; Zhang, S.; Cui, K.; Han, X.; Fathololoumi, S.; Couillard, M.; Botton, G. a.; Mi, Z. *Nano Lett.* **2011**, *11* (5), 1919–1924.

(161) Chichibu, S. F.; Abare, A. C.; Minsky, M. S.; Keller, S.; Fleischer, S. B.; Bowers, J. E.; Hu, E.; Mishra, U. K.; Coldren, L. A.; Denbaars, S. P.; Sota, T. *Appl. Phys. Lett.* **1998**, *73* (14), 2006–2008.

(162) Takeuchi, T.; Sota, S.; Katsuragawa, M.; Komori, M.; Takeuchi, H.; Amano, H.; Akasaki, I. *Jpn. J. Appl. Phys.* **1997**, *36*, 382–385.

(163) Wang, Z.; Wang, L.; Xing, Y.; Yang, D.; Yu, J.; Hao, Z.; Sun, C.; Xiong, B.; Han, Y.; Wang, J.; Li, H.; Luo, Y. *ACS Photonics* **2017**, *4* (8), 2078–2084.

(164) Kanta Patra, S.; Wang, T.; Puchtler, T. J.; Zhu, T.; Oliver, R. A.; Taylor, R. A.; Schulz, S. *Phys. Status Solidi* **2017**, *254* (8), 1600675.

(165) Langer, T.; Pietscher, H. G.; Ketzer, F. A.; Jönen, H.; Bremers, H.; Rossow, U.; Menzel, D.; Hangleiter, A. *Phys. Rev. B - Condens. Matter Mater. Phys.* **2014**, *90* (20), 1–9.

(166) Fu, X.; Jacopin, G.; Shahmoammadi, M.; Liu, R.; Benameur, M.; Genière, J.; Feng, J.; Guo, W.; Liao, Z. M.; Deveaud, B.; Yu, D. *ACS Nano* **2014**, *8* (4), 3412–3420.

(167) Lee, W.; Kiba, T.; Murayama, A.; Sartel, C.; Sallet, V.; Kim, I.; Taylor, A.; Jho, Y. D.; Kyhm, K. *Opt. Express* **2014**, *22* (15), 17959–17967.

(168) Badcock, T. J.; Ali, M.; Zhu, T.; Pristovsek, M.; Oliver, R. A.; Shields, A. J. *Appl.*

Phys. Lett. **2016**, *109* (15), 1–6.

(169) Bardoux, R.; Kaneta, A.; Funato, M.; Kawakami, Y.; Kikuchi, A.; Kishino, K. *Phys. Rev. B - Condens. Matter Mater. Phys.* **2009**, *79*, 155307.

(170) Deitz, J. I.; Sarwar, A. T. M. G.; Carnevale, S. D.; Grassman, T. J.; Myers, R. C.; Mccomb, D. W. *Microsc. Microanal.* **2018**, *24*, 93–98.

(171) Kaganer, V. M.; Fernandez-garrido, S.; Dogan, P.; Sabelfeld, K. K.; Brandt, O. *Nano Lett.* **2016**.

(172) Calarco, R.; Meijers, R. J.; Debnath, R. K.; Stoica, T.; Sutter, E.; Lüth, H. *Nano Lett.* **2007**, *7* (8), 2248–2251.

(173) Ristic, J.; Calleja, E.; Fernandez-Garrido, S.; Cerutti, L.; Trampert, A.; Jahn, U.; Ploog, K. *J. Cryst. Growth* **2008**, *310*, 4035–4045.

(174) Grossklaus, K. A.; Banerjee, A.; Jahangir, S.; Bhattacharya, P.; Millunchick, J. M. *J. Cryst. Growth* **2013**, *371*, 142–147.

(175) Park, C.; Chadi, D. *Phys. Rev. B - Condens. Matter Mater. Phys.* **1997**, *55* (19), 12995–13001.

(176) Yi, S. N.; Ahn, H. S.; Yang, M.; Kim, K. H.; Kim, H.; Yi, J. Y.; Chang, J. H.; Kim, H. S.; Lee, S. C.; Kim, S. W. *J. Korean Phys. Soc.* **2004**, *45* (December), S598–S600.

(177) Hahn, W.; Lentali, J.; Polovodov, P.; Young, N.; Nakamura, S.; Speck, J. S.; Weisbuch, C.; Filoch, M.; Wu, Y.-R.; Piccardo, M.; Maroun, F.; Martinelli, L.; Lassailly, Y.; Peretti, J. *https://arxiv.org/abs/1805.09030* **2018**, 1–6.

(178) Shahmohammadi, M.; Ganiere, J.-D.; Zhang, H.; Ciechonski, R.; Vescovi, G.; Kryliouk, O.; Tchernycheva, M.; Jacopin, G. *Nanoletters* **2015**, 1–6.

(179) Lazić, S.; Chernysheva, E.; Gačević, Ž.; Van Der Meulen, H. P.; Calleja, E.; Calleja Pardo, J. M. *AIP Adv.* **2015**, *5* (9), 1–9.

(180) Lazić, S.; Chernysheva, E.; Gačević, Ž.; García-Lepetit, N.; van der Meulen, H. P.; Müller, M.; Bertram, F.; Veit, P.; Christen, J.; Torres-Pardo, A.; González Calbet, J. M.; Calleja, E.; Calleja, J. M. *Proceeding SPIE* **2015**, *9363*, 93630U.

(181) Nakamura, S.; Fasol, G. *The Blue Laser Diode*, Springer.; 1997.

(182) Jacopin, G.; Rigutti, L.; Teubert, J.; Julien, F. H.; Furtmayr, F.; Komninou, P.;

Kehagias, T.; Eickhoff, M.; Tchernycheva, M. *Nanotechnology* **2013**, *24*, 125201.

(183) Marquardt, O.; Hauswald, C.; Wo, M.; Geelhaar, L.; Brandt, O. *Nanoletters* **2013**.

(184) Böcklin, C.; Veprek, R. G.; Steiger, S. *Phys. Rev. B* **2010**, *81* (155306), 1–9.

(185) Kishino, K.; Ishizawa, S. *Nanotechnology* **2015**, *26* (22), 1–13.

(186) Kishino, K.; Hoshino, T.; Ishizawa, S.; Kikuchi, A. *Electron. Lett.* **2008**, *44* (13).

(187) Sekiguchi, H.; Kishino, K.; Kikuchi, A. *Appl. Phys. Express* **2008**, *1*, 124002.

(188) Schumann, T.; Gotschke, T.; Limbach, F.; Stoica, T. *Nanotechnology* **2011**, *22* (95603).

(189) Kruse, J. E.; Lymperakis, L.; Eftychis, S.; Adikimenakis, A.; Doundoulakis, G.; Tsagaraki, K.; Androulidaki, M.; Olziersky, A.; Dimitrakis, P.; Ioannou-Sougleridis, V.; Normand, P.; Koukoula, T.; Kehagias, T.; Komninou, P.; Konstantinidis, G.; Georgakilas, A. *J. Appl. Phys.* **2016**, *119* (22).

(190) Bertness, B. K. A.; Sanders, A. W.; Rourke, D. M.; Harvey, T. E.; Roshko, A.; Schlager, J. B.; Sanford, N. A. *Adv. Mater.* **2010**, *20*, 2911–2915.

(191) Brubaker, M. D.; Du, S. M.; Harvey, T. E.; Blanchard, P. T.; Roshko, A.; Sanders, A. W.; Sanford, N. A.; Bertness, K. A. *Cryst. Growth Des.* **2015**, DOI: 10.1021/acs.cgd.5b00910.

(192) Schuster, F.; Hetzl, M.; Weiszer, S.; Garrido, J. A.; De La Mata, M.; Magen, C.; Arbiol, J.; Stutzmann, M. *Nano Lett.* **2015**, *15* (3), 1773–1779.

(193) Kano, T.; Yoshida, J.; Miyagawa, R.; Mizuno, Y.; Oto, T. *Electron. Lett.* **2015**, *51* (25), 2125–2126.

(194) Bengoechea-encabo, A.; Barbagini, F.; Fernandez-garrido, S.; Grandal, J.; Ristic, J. *J. Cryst. Growth* **2011**, *325* (1).

(195) Sanford, N. A.; Blanchard, P. T.; Brubaker, M.; Bertness, K. A.; Roshko, A.; Schlager, J. B.; Kirchhofer, R.; Diercks, D. R.; Gorman, B. *Phys. Status Solidi* **2014**, *11* (3–4), 608–612.

(196) Kumaresan, V.; Largeau, L.; Madouri, A.; Glas, F.; Zhang, H.; Oehler, F.; Cavanna, A.; Babichev, A.; Travers, L.; Gogneau, N.; Tchernycheva, M.; Harmand, J. C. *Nano Lett.* **2016**, *16* (8), 4895–4902.

(197) Hong, Y. J.; Lee, C. H. *Van der Waals heteroepitaxy of semiconductor nanowires*, 1st ed.; Elsevier Inc., 2015; Vol. 93.

(198) Zhang, G.; Jiang, X. *ACS Appl. Mater. Interfaces* **2013**, *5* (22), 12066−12072.

(199) Park, J. B.; Kim, N. J.; Kim, Y. J.; Lee, S. H.; Yi, G. C. *Curr. Appl. Phys.* **2014**, *14* (11), 1437–1442.

(200) Chung, K.; Yoo, H.; Hyun, J. K.; Oh, H.; Tchoe, Y.; Lee, K.; Baek, H.; Kim, M.; Yi, G. **2016**.

(201) Heilmann, M.; Sarau, G.; Göbelt, M.; Latzel, M.; Sadhujan, S.; Tessarek, C.; Christiansen, S. *Cryst. Growth Des.* **2015**, *15* (5), 2079–2086.

(202) Han, Z.; Kimouche, A.; Kalita, D.; Allain, A.; Arjmandi-Tash, H.; Reserbat-Plantey, A.; Marty, L.; Pairis, S.; Reita, V.; Bendiab, N.; Coraux, J.; Bouchiat, V. *Adv. Funct. Mater.* **2014**, *24* (7), 964–970.

(203) Li, X.; Cai, W.; An, J.; Kim, S.; Nah, J.; Yang, D.; Piner, R.; Velamakanni, A.; Jung, I.; Tutuc, E.; Banerjee, S. K.; Colombo, L.; Ruoff, R. S. *Science (80-.).* **2009**, *324* (5932), 1312–1314.

(204) Yan, Z.; Barron, A. R. *Open-Stax-CNX*. pp 1–4.

(205) Ferrari, A. C.; Katsnelson, M.; Vandersypen, L.; Loiseau, A.; Morandi, V.; Tredicucci, A.; Williams, G. M.; Hong, H. *Nanoscale* **2015**, *7* (11), 4598–4810.

(206) Ferrari, A. C.; Meyer, J. C.; Scardaci, V.; Casiraghi, C.; Lazzeri, M.; Mauri, F.; Piscanec, S.; Jiang, D.; Novoselov, K. S.; Roth, S.; Geim, A. K. *Phys. Rev. Lett.* **2006**, *97*, 187401.

(207) Lekhal, K.; Bae, S.-Y.; Lee, H.-J.; Mitsunari, T.; Tamura, A.; Deki, M.; Honda, Y.; Amano, H. *Jpn. J. Appl. Phys* **2016**, *55*, 05FF03.

(208) Fernández-Garrido, S.; Zettler, J. K.; Geelhaar, L.; Brandt, O. *Nano Lett.* **2015**, *15* (3).

(209) Hu, B.; Ago, H.; Ito, Y.; Kawahara, K.; Tsuji, M.; Magome, E.; Sumitani, K.; Mizuta, N.; Ikeda, K. I.; Mizuno, S. *Carbon N. Y.* **2012**, *50* (1), 57–65.

(210) Juang, Z.; Zhong, Y.; Chen, F.; Li, L.; Keng-Ku, L.; Zhang, W.; Lin, S.-Y.; Juang, Z.-Y.; Zhong, Y.-L.; Chen, F.-R.; Li, L.-J. *Nano Lett.* **2011**, *11*, 3612–3616.

(211) Han, G. H.; Güneş, F.; Bae, J. J.; Kim, E. S.; Chae, S. J.; Shin, H. J.; Choi, J. Y.;

Pribat, D.; Lee, Y. H. *Nano Lett.* **2011**, *11* (10), 4144–4148.

(212) Jung, M. W.; Song, W.; Jung, D. S.; Lee, S. S.; Park, C.-Y.; An, K.-S. *J. Nanosci. Nanotechnol.* **2016**, *16* (3), 2756–2759.

(213) Dusari, S.; Goyal, N.; Debiasio, M.; Kenda, A. *Thin Solid Films* **2015**, *597*, 140–143.

(214) Kranert, C.; Schmidt-Grund, R.; Grundmann, M. *New J. Phys.* **2013**, *15*, 113048.

(215) Dimitrakopulos, G. P.; Sanchez, A. M.; Komninou, P.; Kehagias, T.; Karakostas, T.; Nouet, G.; Ruterana, P. *Phys. Status Solidi Basic Res.* **2005**, *242* (8), 1617–1627.

(216) Zettler, J. K.; Corfdir, P.; Hauswald, C.; Luna, E.; Jahn, U.; Flissikowski, T.; Schmidt, E.; Ronning, C.; Trampert, A.; Geelhaar, L.; Grahn, H. T.; Brandt, O.; Fernández-Garrido, S. *Nano Lett.* **2016**, *16* (2), 973–980.

(217) Monemar, B. *J. Phys. Condens. Matter* **2001**, *13* (32), 7011.

(218) Monemar, B. *Phys. Rev. B* **1974**, *10* (2), 676–681.

(219) Kornitzer, K.; Ebner, T.; Thonke, K.; Sauer, R.; Kirchner, C.; Schwegler, V.; Kamp, M.; Leszczynski, M.; Grzegory, I.; Porowski, S. *Phys. Rev. B* **1999**, *60* (3), 1471–1473.

(220) Brandt, O.; Fernández-Garrido, S.; Zettler, J. K.; Luna, E.; Jahn, U.; Chèze, C.; Kaganer, V. M. *Cryst. Growth Des.* **2014**, *14* (5), 2246–2253.

(221) Kaganer, V. M.; Jenichen, B.; Brandt, O.; Fernández-Garrido, S.; Dogan, P.; Geelhaar, L.; Riechert, H. *Phys. Rev. B* **2012**, *86* (11), 115325.

(222) Jenichen, B.; Brandt, O.; Pfüller, C.; Dogan, P.; Knelangen, M.; Trampert, A. *Nanotechnology* **2011**, *22* (29), 295714.

(223) Robins, L. H.; Bertness, K. A.; Barker, J. M.; Sanford, N. A.; Schlager, J. B. *J. Appl. Phys.* **2007**, *101* (11), 113505.

(224) Corfdir, P.; Zettler, J. K.; Hauswald, C.; Fernández-Garrido, S.; Brandt, O.; Lefebvre, P. *Phys. Rev. B* **2014**, *90* (20), 205301.

(225) Han, Y.; Pei-Cheng, K.; Zhi-Yin, G.; Sheng, L.; Pang, L. *Crystals* **2018**, *8* (58).

(226) Jin, N.; Han, J.; Wang, H.; Zhu, X.; Ge, Q. *Int. J. Hydrogen Energy* **2015**, 1–9.

(227) Goncalves, G.; Marques, P. A. A. P.; Granadeiro, C. M.; Nogueira, H. I. S.; Singh, M. K.; Gr, J. *Chem. Mater.* **2009**, *21*, 4796–4802.

(228) Liu, Z.; Suenaga, K.; Harris, P. J. F.; Iijima, S. *Phys. Rev. Lett.* **2009**, *102* (1), 1–4.

(229) Acik, M.; Chabal, Y. J. *Jpn. J. Appl. Phys.* **2011**, *50*, 70101.

(230) Consonni, V.; Dubrovskii, V. G.; Trampert, A.; Geelhaar, L.; Riechert, H. *Phys. Rev. B - Condens. Matter Mater. Phys.* **2012**, *85* (15), 1–7.

(231) Sabelfeld, K. K.; Kaganer, V. M.; Limbach, F.; Dogan, P.; Brandt, O.; Sabelfeld, K. K.; Kaganer, V. M.; Limbach, F.; Dogan, P.; Brandt, O.; Geelhaar, L. *Appl. Phys. Lett.* **2013**, *103*, 1105.

(232) Dubrovskii, V. G.; Sibirev, N. V.; Berdnikov, Y.; Gomes, U. P.; Ercolani, D.; Zannier, V.; Sorba, L. *Nanotechnology* **2016**, *27* (37), 1–9.

(233) Sobanska, M.; Dubrovskii, V. G.; Tchutchulashvili, G.; Klosek, K.; Zytkiewicz, Z. R. *Cryst. Growth Des.* **2016**, *16*, 7205–7211.

(234) Oehler, F.; Cattoni, A.; Scaccabarozzi, A.; Patriarche, G.; Glas, F.; Harmand, J. *Nano Lett.* **2017**, DOI: 10.1021/acs.nanolett.7b03695.

(235) Albert, S.; Bengoechea-encabo, A.; Lefebvre, P.; Barbagini, F.; Trampert, A. *Appl. Phys. Lett.* **2012**, *100*, 231906.

(236) Cai, X. M.; Zeng, S. W.; Zhang, B. P. *Appl. Phys. Lett.* **2009**, *95* (17), 1–4.

(237) Leamy, H. J. *J. Appl. Phys.* **1982**, *53* (6), R51–R80.

(238) Togonal, A. S.; Foldyna, M.; Chen, W.; Wang, J. X.; Neplokh, V.; Tchernycheva, M.; Nassar, J.; Roca i Cabarrocas, P. *J. Phys. Chem. C* **2015**, *120* (5), 2962–2972.

(239) Yakimov, E. B.; Borisov, S. S.; Zaitsev, S. I. *Semiconductors* **2007**, *41* (4), 411–413.

(240) Golam Sarwar, A. T. M.; Myers, R. C. *Appl. Phys. Lett.* **2012**, *101* (14), 0–5.

(241) Gogneau, N.; Jamond, N.; Chrétien, P.; Houzé, F.; Lefeuvre, E.; Tchernycheva, M. *Semicond. Sci. Technol.* **2016**, *31* (10), 1–14.

(242) Jegenyes, N.; Morassi, M.; Chr, P.; Travers, L.; Lu, L.; Julien, F. H.; Id, M. T.; Gogneau, N. *Nanomaterials* **2018**, *8*, 367.

(243) Cliff, G.; Lorimer, G. W. *J. Microsc.* **1975**, *103* (March), 203–207.

(244) Longo, D. M.; Howe, J. M.; Johnson, W. C. *Ultramicroscopy* **1999**, *80*, 85–97.

Résumé de thèse en français

Les matériaux nitrures (III-N) sont d'excellents semi-conducteurs à large bande interdite, couramment utilisés dans les dispositifs modernes tels que les diodes électroluminescentes (DELs), les lasers, les détecteurs ultraviolets et les transistors à haute mobilité électronique (HEMT). Cependant, la qualité cristalline des couches III-N épitaxiées reste un goulot d'étranglement majeur, qui limite les possibles architectures impliquant l'InN, l'AIN, le GaN et leurs alliages. Cette limitation est principalement due aux désaccords de maille élevés entre ces composés et au manque de substrats cristallins natifs de hautes propriétés. Il en résulte alors une densité élevée de dislocations qui agissent comme centres de recombinaison non radiatifs. Au cours des deux dernières décennies, les hétérostructures III-N à nanofils ont reçu une attention croissante pour leurs applications potentielles en nano-électronique et nano-photonique. La raison principale repose sur la haute qualité cristalline permise par leur géométrie quasi-1D, même s'ils sont épitaxiés sur des substrats hautement désaccordés. De manière notable, ceci provient de leur capacité à fléchir les dislocations vers les facettes latérales, et à accommoder la déformation élastiquement, à travers les déformations de surface. Par ailleurs, leur photoluminescence met généralement l'accent sur l'absence d'états profonds dans la bande interdite, et peut présenter une recombinaison excitonique avec des largeurs de raie comparables l'état du GaN massif. Ce travail de thèse est axé sur la synthèse et la caractérisation de nanofils (NFs) III-N pour les applications photovoltaïques et piézoélectriques.

NFs InGaN/GaN pour les applications photovoltaïques et piézoélectriques : Motivation de la thèse et objectifs.

Dans le cas spécifique des NFs InGaN/GaN, la fabrication et l'efficacité de DELs vertes-jaunes a été démontrée, et, aujourd'hui, ces systèmes sont considérés comme des candidats prometteurs pour la réalisation de cellules solaires et de piézo-générateurs.

Les alliages $In_xGa_{1-x}N$ présentent une combinaison de propriétés intéressantes pour les applications solaires. Ceux-ci se caractérisent par une bande interdite dépendante de la composition qui peut être ajustée de 0,65 eV (InN) à 3,4 eV (GaN), des coefficients d'absorption élevés, des mobilités de porteurs élevées et une grande résistance aux dommages de rayonnement. Cependant, pour les cellules solaires InGaN/GaN à base de puits quantiques (PQs), bien qu'une efficacité quantique externe élevée ait été atteinte

pour des courtes longueurs d'onde (<450 nm), la détérioration de la qualité cristalline des couches épitaxiales due au désaccord de maille croissant avec la teneur d'In (11% entre les deux binaires), entraîne une baisse spectaculaire de l'efficacité pour des énergies de bande interdite plus faibles. Dans cette perspective, l'utilisation des hétérostructures InGaN à NFs comme région active pour la photo-conversion pourrait combiner leur densité de défauts réduite spécifique aux NFs, aux avantages intrinsèques de l'alliage InGaN pour le photovoltaïque dans une gamme plus large de bandes passantes par rapport aux architectures 2D classiques.

Les NFs sont également caractérisés par des propriétés piézoélectriques remarquables (c'est-à-dire la capacité de convertir l'énergie mécanique directement en énergie électrique utilisable). Ils sont ainsi récemment apparus comme d'excellents candidats pour fabriquer une nouvelle génération de dispositifs piézoélectriques ultra-compacts et efficaces. La raison principale réside dans leur grand rapport d'aspect qui leur confère une flexibilité extrêmement élevée, les rendant ainsi plus sensibles aux forces appliquées, et donc entraînant une réponse piézoélectrique plus élevée par rapport aux matériaux 2D et massifs. Bien que ces sources d'énergie puissent générer des densités de puissance de l'ordre du µW-mW/cm^3, leur utilisation en tant que source d'alimentation des micro-dispositifs reste aujourd'hui limitée, notamment en raison de leur faible efficacité de conversion. En effet, pour atteindre des telles puissances, il faut des dispositifs de plusieurs centimètres carrés et/ou l'application de pressions de plusieurs MPa, ce qui ne permet pas dans ces conditions leur utilisation en tant que sources d'énergie intégrées viables. Pour prendre en compte les systèmes de récupération d'énergie à base de NFs, l'amélioration de leur capacité de conversion est un prérequis. Actuellement, les meilleures conversions mécaniques-électriques en termes de tension de sortie ont été démontrées pour les NFs nitrures. Ainsi, des tensions maximales générées d'environ -440 mV et ~ 1 V ont été rapportées respectivement pour des NFs de GaN dopés n et d'InN. Cette dernière valeur reflète les grands coefficients piézoélectriques de l'InN, qui sont les plus élevés parmi tous les matériaux III-N. Dans ce contexte, l'intégration d'hétérostructures axiales InGaN dans des NFs de GaN est une possibilité intéressante pour l'amélioration de leur capacité de piezo-conversion.

Ce travail de thèse a porté sur la croissance épitaxiale d'hétérostructures axiales InGaN/GaN à NFs sur substrats de Si(111) avec une fine couche interfaciale d'AlN, en

utilisant l'épitaxie par jets moléculaires assistée par plasma (EJM-AP), et la caractérisation de leurs propriétés. Si ce bref aperçu met en avant les motivations quant à l'utilisation d'alliages d'InGaN pour des applications précises, il est avant tout crucial de maîtriser sa croissance et ses propriétés fonctionnelles. Dans ce travail de thèse, je me suis focalisée sur ces trois questions fondamentales :

- Le contrôle de la croissance spontanée d'hétérostructures InGaN à NFs, pour contrôler leur morphologie, leur bande interdite et leurs propriétés structurelles ;
- L'évaluation expérimentale de leurs propriétés optiques, en accord avec leur structure de bande interdite, en fonction de leur profil de composition et de leur champ de contrainte. Cette étude est intéressante d'un point de vue fondamental, mais également d'un point de vue applicatif, puisqu'elle est requise dans la conception optimisée de dispositifs photovoltaïques ;
- L'identification de stratégies viables pour obtenir un meilleur contrôle de la morphologie des nanostructures, de leur positionnement et, finalement, de l'homogénéité des propriétés des hétérostructures InGaN mentionnées ci-dessus.

Pour aborder ces problématiques, les trois principaux chapitres de la thèse sont axés sur l'étude de la croissance d'hétérostructures axiales InGaN/GaN, sur leurs caractérisations optiques par cathodoluminescence et photoluminescence, et sur l'étude de la croissance sélective de NFs sur motifs lithographiés de graphène transféré. Un dernier chapitre dédié aux perspectives présente des résultats préliminaires concernant la conversion piézoélectrique des nanostructures hétérostructurées InGaN/GaN, la fabrication d'architectures photovoltaïques intégrant ces mêmes types de NFs dans la zone active, et leurs propriétés optiques quand ils sont synthétisés sur des substrats de graphène.

Croissance d'hétérostructures axiales InGaN/GaN sous forme de nanofils

La fabrication d'hétérostructures InGaN/GaN a jusqu'à présent fait l'objet d'un certain nombre d'études qui offrent un panorama assez large de possibles morphologies et compositions d'alliages. Ainsi les insertions d'InGaN peuvent prendre la forme d'insertions coniques présentant une forme d'îlot avec des concentrations en In relativement faibles ($0{,}15 < x_{In} < 0{,}25$); des morphologies en forme de disque, typiquement riches en In ($0{,}30 < x_{In} < 0{,}60$); et des formes radialement enlargies sous forme de nano-parapluie avec une large gamme de compositions ($0{,}10 < x_{In} < 0{,}60$). Dans tous les cas, une structure cœur-coquille InGaN/GaN formée spontanément a été mise en évidence. Cependant, la

corrélation entre la morphologie, la composition et les conditions de croissance des insertions reste male connue et contribue ainsi au fait que les mécanismes de croissance, ne sont, à ce jour, pas clairement compris.

Dans le présent chapitre, j'ai réalisé une étude systématique de la croissance des hétérostructures axiales InGaN par EJM-AP. Des études détaillées sur leur composition et propriétés structurales ont été effectuées, à la fois sur un ensemble statistique de NFs (par spectroscopie à dispersion d'énergie -EDX- et par diffraction des rayons X -DRX-) et sur NFs uniques (par EDX dans des microscopes électroniques à transmission -TEM- à balayage -MEB- et par analyse de phase géométrique -APG-). Sur la base de toutes ces caractérisations, j'ai construit un diagramme complet de croissance dépendant des flux d'In et Ga. Ce diagramme résume toutes les morphologies rapportées dans la littérature, et surtout fournit des éléments indispensables au contrôler de la croissance et de la composition d'alliage dans une large gamme de teneur d'In (Fig. 1).

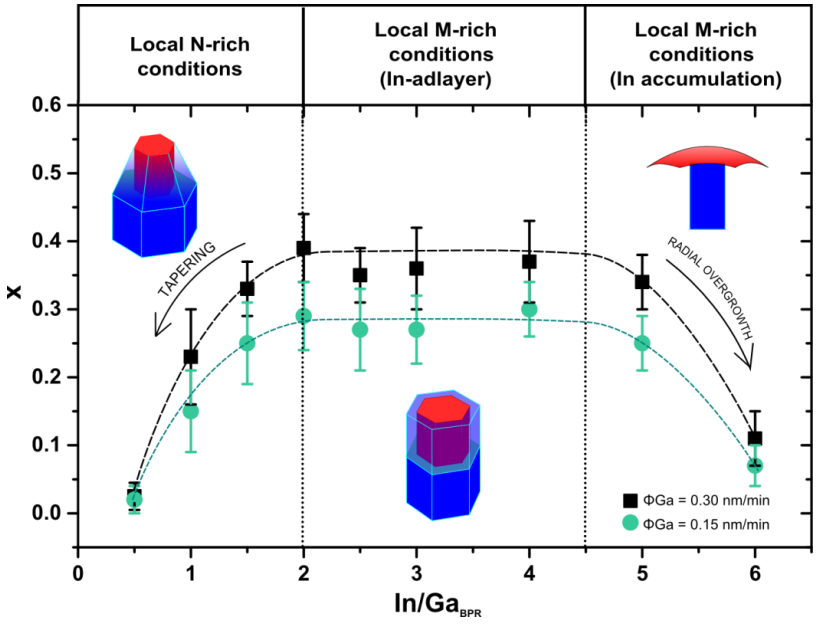

Figure 1 : Diagramme de croissance d'heterostructures InGaN/GaN à NFs presentant l'évolution de leur composition, leur morphologie et leur regime de croissance en fonction du rapport de flux In/Ga.

Des analyses EDX, à l'échelle nanométrique, effectuées dans un montage STEM, ont permis de mettre en évidence que la fraction d'In est plutôt homogène dans les sections InGaN, sauf dans une région localisée à ~ 20 nm au voisinage de l'interface inférieure InGaN/GaN (Fig. 2a). Le bon accord de cette région avec l'épaisseur nécessaire pour une relaxation complète de la déformation dans le plan (montré par des analyses GPA sur la

figure 2b), indique que ce gradient de composition résulte de l'effet dit de *traction du réseau*, c'est-à-dire l'empêchement de l'incorporation d'In due à la contrainte compressive dans le plan, exercée par le NF de GaN sous-jacent.

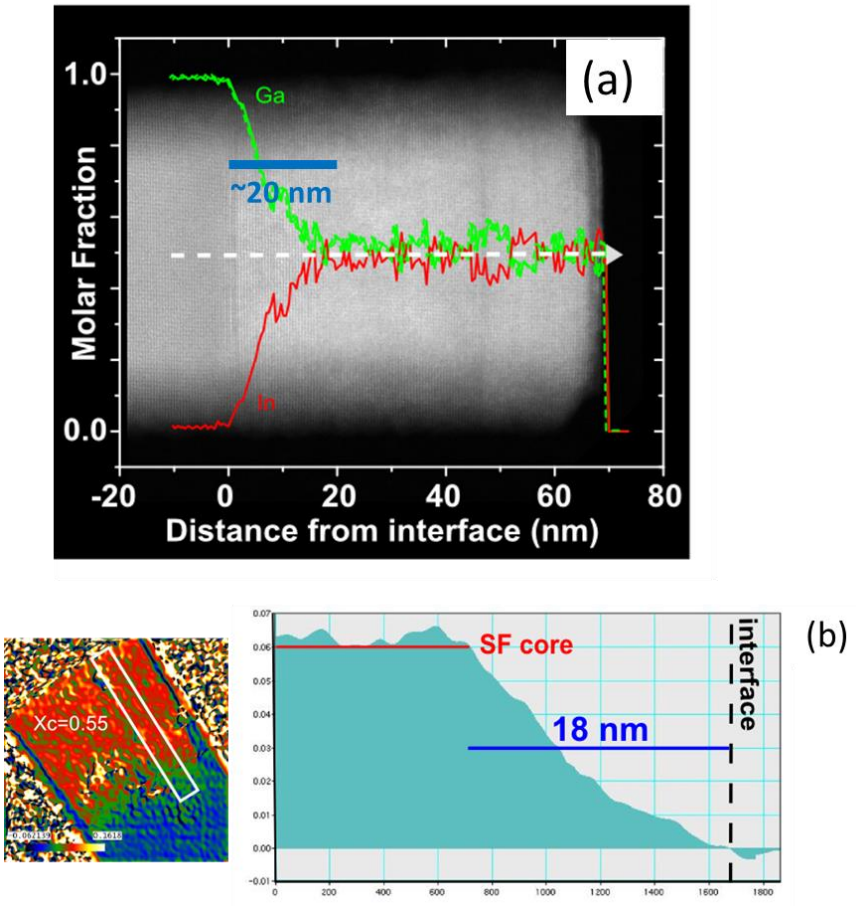

Figure **2** (a) Profils de composition EDX pour l'In et le Ga, réalisés sur l'axe de l'heterostructure InGaN, superposés à l'image STEM, montrant le gradient de composition sur ~20 nm proche de l'interface inferieure. (b) Cartographie du paramètre de maille a (par rapport au GaN relaxé) et son évolution sur l'axe du fil, montrant qu'à partir de 18 nm d'épaisseur, le paramètre de maille coïncide avec celui d'un InGaN relaxé de même composition (SF core).

Ces résultats fournissent des directives utiles pour corréler la croissance des heterostructures InGaN, et leur composition d'alliage dans une large gamme de teneur d'In. Cependant, il est impossible de contrôler leur synthèse sans une bonne compréhension des mécanismes de croissance en jeu. Pour se faire, j'ai analysé la variation de la vitesse de croissance de l'hétérostructure (par STEM) et la stabilité de l'In adsorbé sur les plans (000-1) des NFs (par réflexion par diffraction d'électrons de haute énergie) en

fonction des rapports de flux. A partir des résultats obtenus, et en faisant un parallèle avec les régimes de croissance habituellement observés pour les couches planaires d'InGaN en PA-MBE, j'ai démontré que l'InGaN déposé au sommet du NF de GaN suit des modes de croissance distincts en fonction du rapport V/III local au front de croissance. Plus précisément, j'ai montré que ces conditions sont contrôlées par le rapport des flux In/Ga, avec les trois régimes de croissance identifiés sur la figure 1 résumés comme suit: si les conditions de croissance sont localement riches en N (In/Ga<2), le mode de croissance est 3D, conduisant à une morphologie InGaN conique; si les conditions de croissance sont riches en In, où une couche d'In auto-régulée surfacte le front de croissance (2<In/Ga<4), le mode de croissance est pseudo-2D, conduisant à une morphologie type disque; si les conditions de croissance sont fortement riches en In (In/Ga> 4), la croissance est instable, conduisant à des morphologies « nano-parapluie ».

Caractérisation optique des NW InGaN / GaN

Dans la première partie du chapitre, j'ai étudié les propriétés optiques d'ensembles de NFs et de NFs uniques InGaN/GaN epitaxiés sur AlN/Si(111). Les caractéristiques générales de la photoluminescence (PL) comprennent: une faible émission de lumière sur ensemble de NFs et aucune émission mesurée sur NFs uniques (à température ambiante et cryogenique) sous excitation optique non résonnante et un large signal bi-composant (largeur à mi-hauteur de quelques centaines de meV) sous excitation résonnante (sur ensemble de NFs). La largeur du signal de PL en excitation résonante a été principalement associée à la dispersion en teneur d'In entre les différents NFs qui a été mesurée statistiquement par EDX. En parallèle, la présence de signaux de PL bi-composants peut être attribuée à une incorporation réduite en In dans les NFs présentant des domaines d'inversion (IDB). La présence de ces défauts structuraux est supportée par une signature optique spécifique à 3,45 eV, et par caractérisations STEM.

En général, la mesure PL dépendante de la température a montré que les sections riches en In présentaient une efficacité quantique interne PL inférieure à celle des structures pauvres en In, même si elles ne présentaient pas de défauts structuraux selon nos analyses STEM. Ceci pourrait être expliqué en partie par le haut rapport surface/volume des NFs présentant une coquille mince riche en Ga (structures type disque), qui pourrait augmenter la recombinaison de surface non radiative. Il pourrait également résulter de la nature polaire de l'hétérostructure et de son champ de déformation anisotrope, qui peut

résulter en un grand champ de polarisation dans l'insertion (d'autant plus élevé que la structure est riche en In). En fait, nos études structurales sur les cœurs d'InGaN épais, ont montré que les déformations dues à la contrainte ne peuvent être que partiellement relâchées. En fait, ils montrent: (i) une relaxation importante de la déformation dans le plan (au moins au-dessus de la région de traction compositionnelle); et (ii) un état de contrainte compressive hors plan (~1%) dû à la présence de la coquille riche en Ga. Cette distribution inhomogène de la contrainte a été confirmée par des simulations théoriques du champ de déformation, au sein d'une section d'InGaN cohérente en forme de disque, présentant un profil de composition et des paramètres géométriques issus des données expérimentales (Figure 3).

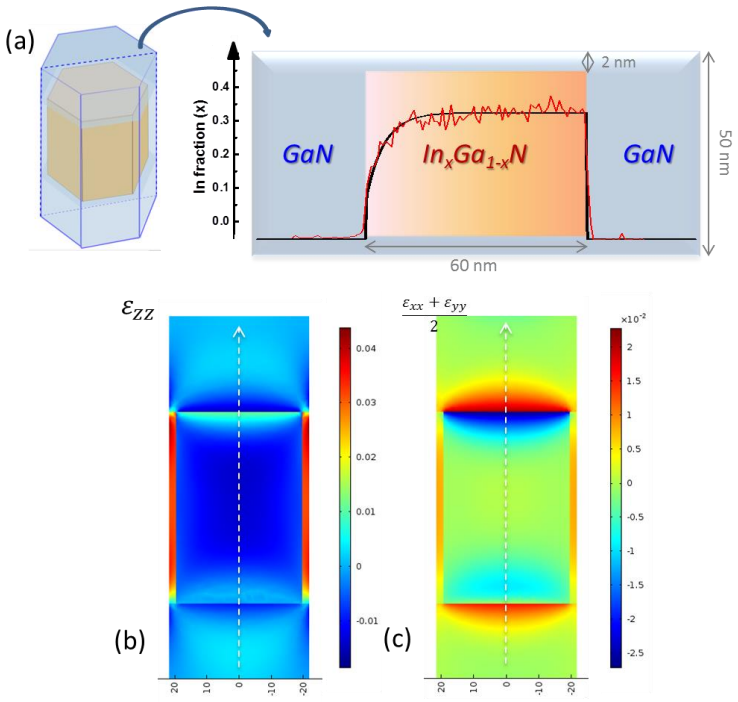

Figure **3** (a) Schemat de la structure InGaN/GaN à NF utilisée pour la simulation de champ de contrainte. Projection latérale du champ de contrainte simulé: contrainte locale hors-plan (b) et dans le plan (c).

La polarisation spontanée et le champs piézoélectrique induit par la contrainte, pourraient conduire à une séparation spatiale entre les électrons et les trous, lorsque ceux-ci ne sont pas confinés par les minima de potentiel locaux, générés par les fluctuations d'In (notamment, à température ambiante).

Pour mieux étudier ce point, dans la deuxième partie du chapitre, j'ai étudié le profil axial du bord de bande et les propriétés optiques résultantes, dans des sections en forme de

disque, riches en In, d'environ 60 nm d'épaisseur. Comme prévu, la distribution particulière des déformations d'une hétérostructure cœur-coquille InGaN/GaN donne un champ électrique et un profil de bord de bande très anisotrope le long de l'hétérostructure, dont la simulation est montrée sur la Figure 4(a). Plus précisément, ce profil simulé indique que les paires électrons-trous générées dans toutes les positions, sauf P1 et P2 (où le champ électrique est trop faible pour dissocier les excitons InGaN), pourraient être séparées très efficacement, et donc générer un très faible émission optique. En effet, l'absence de déplacements spectraux sur les spectres de PL en puissance, les courtes durées de vie radiatives (~ 800 ps à 20 K) mesurées par PL résolue en temps et la présence systématique de deux contributions de cathodoluminescence au fond et au sommet de l'heterostructure (Fig. 4(b)), suggèrent fortement que le processus d'émission est dominé par les deux transitions «verticales», indiquées par des flèches noires (plaines et en tirets) sur la Figure 4(a).

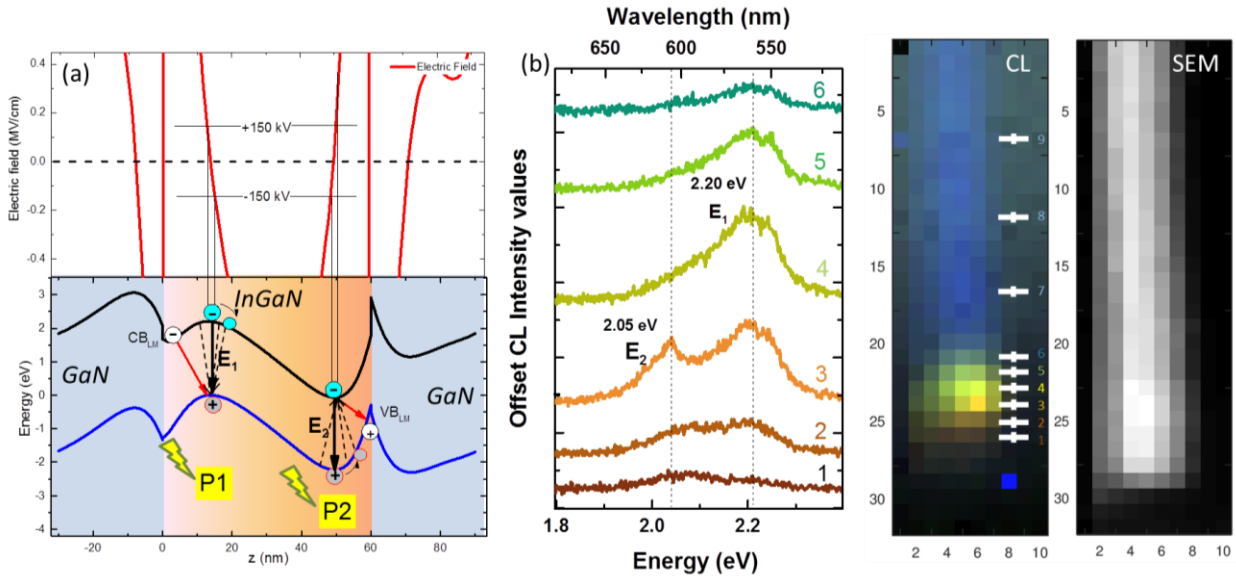

Figure 4 (a) Champ électrique et profils de bande calculés le long de l'axe de la structure InGaN/GaN. (b) Spectres de CL acquis pour différentes positions sur l'axe d'une hétérostructure InGaN/GaN cappée, avec la cartographie CL filtrée en couleur et l'image MEB correspondantes.

Croissance SAG de GaN NWs sur le graphène transféré

Les NFs InGaN/GaN peuvent être epitaxiés de manière efficace sur des substrats AlN/Si(111) par la méthode de croissance auto-assemblée. Cependant, comme ont montré les statistiques EDX de Fig. 1, les sections InGaN ne présentent pas de propriétés

homogènes sur l'échantillon, un aspect qui provient principalement de la dispersion en longueur et en diamètre des NFs de GaN formant le speudo-substrat sur lequel elles sont épitaxiées. Dans le but de mieux contrôler les propriétés des NFs InGaN/GaN, il est nécessaire d'opter pour une approche de croissance sélective (CS) où le positionnement et le diamètre des NFs sont contrôlés, aboutissant à une morphologie homogène et prédéterminée des NFs de GaN.

Très récemment, il a été démontré qu'un haut degré de sélectivité peut être obtenu si la croissance épitaxiale de NFs de GaN est effectuée sur du graphène transféré sur un substrat autre amorphe. Cette nouvelle approche ouvre la possibilité d'utiliser le graphène comme couche épitaxiale pour la croissance sélective des NFs GaN, et en même temps, comme contact électrique de fond, en raison de sa conductivité électrique exceptionnellement haute. Cependant, la croissance de GaN NWs sur le graphène est encore au niveau de la «preuve de concept», et de nombreuses questions restent ouvertes concernant le mécanisme de nucléation, le type de liaison et/ou de relation épitaxiale entre les NFs et le graphène, la capacité du graphène à préserver ses propriétés sous les effets de la croissance (principalement sous l'exposition au plasma N) et le contrôle de la croissance elle-même.

Dans ce chapitre, j'ai étudié la croissance de NFs GaN sur du graphène transféré sur substrat de Si(100) recouvert par 300 nm de SiO_2. Spécifiquement, j'ai démontré la croissance sélective sur des patchs de graphène mono-couche (MCG) de 1 cm^2 (Fig 5(a)), de petits flocons de graphène multi- et mono-couches (Fig 5(b)) et, pour la première fois, sur MCG à motifs lithographiés de 400 jusqu'à 100 nm de diamètre (Fig. 5(c-f)).

Sur tous les substrats analysés, les NFs présentent des propriétés optiques de pointe, et, différemment des substrats Si (111)/AlN, et surtout, ils ne montrent pas la signature PL associée aux IDB.

Concernant les conditions de croissance CS, une fenêtre de quelques degrés centrée autour de 815 °C est requise pour permette la croissance de NFs GaN sur graphène avec une sélectivité parfaite dans les limites du taux de croissance (rapport V/III) considéré. Les NFs présentent des temps d'incubation très longs (plus d'une heure sur les patch mono-couche). Ceci s'est avéré avoir un impact significatif sur la croissance des substrats à motifs où l'analyse statistique révèle une distribution des longueurs NFs et un taux d'occupation des motifs de graphène pour différentes tailles de motifs et temps de

croissance inversement proportionnels à la taille des motifs. Plus leur taille est réduite, plus la nucléation des NFs est retardée. Dans ce contexte, une modélisation appropriée de la distribution de longueur NW prenant en compte le taux d'occupation réel des points, a montré que l'incubation des nanoparticules augmente lorsque le diamètre des motifs est réduit (de 400 à 100 nm). Ainsi, un résultat significatif des études sur substrats patternés, indiquent que la croissance d'un seul NFs dans des motifs de graphène de ~ 50 nm de diamètre pourrait être plus longue que pratique. Dans tous les cas, une nette orientation dans le plan des NFs a été observée, confirmant l'établissement d'une relation épitaxiale entre la structure en nid d'abeille du graphène et les NFs de GaN. Ceci corrèle bien avec les caractérisations post-croissance, montrant que la structure primitive du graphène mono-couche est capable de résister au processus de croissance PA-MBE, car sa signature Raman est presente au-dessous des fils. Cependant, les caractérisations électriques après une exposition au plasma N d'une durée comparable au temps d'incubation des NFs (1 heure), montrent une détérioration de leurs propriétés conductrices.

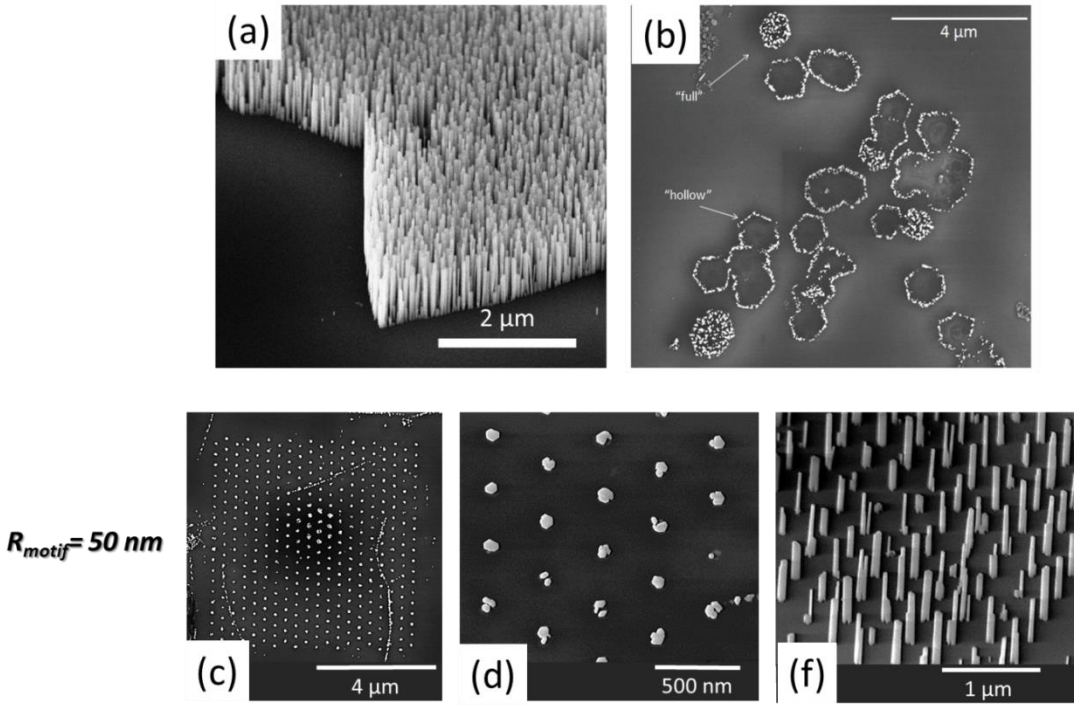

Figure 5 Images MEB en vue de dessus (b-d) et tiltés à 45° (a,f) de NFs GaN épitaxiés sélectivement sur graphène patch (a), flocons de graphène mono-couches et multicouches (b) et patch de graphène mono-couche patterné par lithographie électronique (c-f) avec des motifs de rayon de 50 nm.

Pour adresser ces deux problématiques (temps d'incubation et exposition du graphène au plasma), nous avons proposé un processus de croissance en deux étapes impliquant une étape de nucléation à des flux de Ga élevés, et une étape d'élongation de NFs à des flux de Ga inférieurs. Cette stratégie pourrait permettre d'accélérer le temps d'incubation des nanofils, tout en permettant de maintenir une sélectivité parfaite par rapport à la matrice environnante SiO_2 et, ainsi préserver au mieux les propriétés électroniques du réseau de graphène.

<u>Conclusions et perspectives</u>

Dans ce travail, j'ai systématiquement étudié le mécanisme de croissance des hétérostructures axiales InGaN/GaN à NFs, en effectuant des caractérisations morphologiques, compositionnelles et structurales détaillées. Tous ces résultats m'ont permis d'identifier les meilleures conditions de croissance pour fabriquer des sections InGaN riches en In ($x_{In} \sim 0{,}40$), très homogènes, présentant des interfaces abruptes et une morphologie en disque. Fait important, la compréhension fondamentale de leur régime de croissance et de leur mécanisme de formation m'a permis de contrôler la croissance de façon reproductible.

La combinaison des différentes caractérisations optiques avec des simulations de profils de champ de contrainte et de profils de bande, m'a permis de mettre en évidence un champ de polarisation axiale intense et anisotrope dans le cœur d'InGaN de type disque et, riche en In. Les faibles puissances de luminescence et les faibles IQE mesurés peuvent être expliques par ce champ de interne qui conduit à une réduction substantielle du volume d'InGaN permettant une recombinaison efficace des porteurs.
Ces résultats indiques que ces structures ne peuvent être considérées pour des structures DELs. Cependant, le fort champ électrique dans les noyaux InGaN riches en In peut être avantageux dans les dispositifs photovoltaïques, où les porteurs photo-générés doivent être séparés et extraits pour produire le courant utile. Dans ce cas spécifique, cette séparation de porteurs pourrait être améliorée en considérant une jonction p-i-n InGaN/GaN où la base et le sommet en GaN sont respectivement dopés p et n. En effet, la conception opposée permettrait de masquer partiellement le champ électrique interne et pourrait conduire, en principe, à une collection de porteurs réduite. Des caractérisations préliminaires sur ce type de jonctions par mesures de courent induit par faisceau électronique ont montré que cette architecture pourrait être pratique aussi du point de

vue de la croissance épitaxiale, en raison de la croissance radiale réduite dans le NFs dopé au Si. Ces résultats ouvrent des perspectives très encourageantes pour le développement de nouveaux dispositifs solaires à base de jonctions axiales Mg-GaN/i-InGaN/Si-GaN.

L'étude de la croissance sélective de NFs de GaN sur patches de MCG transférés et de 1 cm^2, petits flocons de graphène mono- et multi-couches et, pour la première fois, sur MCG à motifs lithographiés, ouvres de nouvelles perspectives. Le long temps d'incubation caractérisant ces fils est inversement proportionnel aux dimensions des pseudo-substrats de graphène et conduisent à une détérioration des propriétés électroniques du graphène. Cependant, des simulations montrent qu'un processus de croissance impliquant une étape de nucléation à des flux de Ga élevés et une étape d'allongement des NFs à des flux de Ga plus faibles, pourrait permettre d'accélérer l'incubation, tout en préservant la sélectivité et en conservant au mieux les propriétés électriques du graphène. D'autres expériences sont nécessaires pour tester ces hypothèses. Cepandant, ces résultats montrent que, après une optimisation rationnelle du processus de croissance, l'épitaxie sélective de NFs de GaN sur MCG lithographé est une route possible et très promettent.
Ceci est d'autant plus, intéressant que les NFs de GaN sur graphène présentent des propriétés optiques de pointe, et, différents des substrats Si (111)/AlN, ils se caractérisent par l'absence de signature PL associée aux IDB. Des études préliminaires ont démontré que, conformément à l'influence spéculée des DI sur la composition des hétérostructures InGaN, conduisant à des signaux PL bi-modaux sur les substrats AlN/Si(111), les NFs InGaN/GaN sur MCG sont presque monomodaux et fortement réduits en largeur. Ce point est en faveur de l'utilisation de ces substrats pour la croissance d'hétérostructures III-N fonctionnelles.

Enfin, nous avons testé la réponse piezo-électrique de NFs de GaN intégrant des sections d'InGaN uniques ($x_{In} \sim 0{,}35$). A l'aide d'un microscope à force atomique équipé d'un module Resiscope spécifiquement modifié, nous avons démontré une amélioration importante des propriétés de piézo-conversions des hétérostructures axiales InGaN/GaN. Cette amélioration est attribuée à la création d'un champ piézo-électrique interne plus important en présence d'InGaN, matériau caractérisé par des coefficients piézo-électriques plus grands que pour le GaN. Ainsi des tensions de sortie moyennes atteignant 330 ± 70 mV et une valeur maximale de 470 mV par NF ont été mesurées pour des nanostructures intégrant une insertion d'InGaN de 70 nm d'épaisseur coiffée d'une couche de GaN

d'environ 20 nm d'épaisseur. Cette dernière valeur établit une augmentation d'environ 35% de la capacité de piézo-conversion par rapport aux NFs de GaN binaires. Ces résultats établissent le nouvel état de l'art pour la génération piézoélectrique à partir de NFs à base de GaN et offrent une perspective prometteuse pour étendre les performances des sources piézoélectriques.

ÉCOLE DOCTORALE
Physique et ingénierie : électrons, photons, sciences du vivant (EOBE)

Titre : Croissance de nanofils InGaN pour la récupération des énergies photovoltaïques et piézoélectriques

Mots clés : InGaN, nanofils, MBE, piezoelectrique, photovoltaique

Résumé : Les matériaux III-nitrures sont des semi-conducteurs à bande interdite directe qui présentent plusieurs propriétés intéressantes pour les applications photovoltaïques et piézoélectriques. En même temps, la croissance épitaxiale de ces matériaux sous forme de nanofil (NF) est d'autant plus intéressante, que les NFs nitrures binaires et heterostructurés ont une qualité cristalline supérieure comparée à leurs homologues 2D et massifs. Dans ce contexte, mon travail est axé sur la croissance par Epitaxie par jets moléculaires (EJM) assistée par plasma de NFs InGaN/GaN et sur leur caractérisation. Trois sujets principaux ont été abordés: l'étude de la croissance d'heterostructures InGaN/GaN axiales par EJM, leur caractérisation optique, et l'étude de la croissance sélective de NFs GaN sur graphène transféré. Ces études m'ont permis d'obtenir un control du mode de croissance d'heterostructures InGaN dans une large gamme de teneurs d'In (jusqu'à ~ 40%) et de morphologies; d'étudier leur profil de bande dans la direction axiale, utile pour la conception optimale de la structure p-i-n photovoltaïque ; de démontrer pour la première fois, que l'épitaxie sélective de NFs de GaN sur graphene lithographié est une route possible et très prometteuse pour améliorer leur homogénéité. Enfin, des tests préliminaires ont montré que la capacité de piézo-conversion des NFs GaN peut être améliorée d'environ 35% lors de l'intégration d'une insertion InGaN riche en In dans leur volume.
Tous ces résultats constituent une étape décisive dans le contrôle et la compréhension des propriétés de ces nanostructures, et donnent des perspectives très encourageantes pour leur intégration dans des nano-générateurs à haute efficacité.

Title : Growth of InGaN nanowires for photovoltaic and piezoelectric energy harvesting.

Keywords : InGaN, nanowires, MBE, piezoelectrics, photovoltaics

Abstract : III-nitride materials are direct bandgap semiconductors presenting several interesting properties for photovoltaic and piezoelectric applications. The epitaxial growth of these materials in the form of nanowires (NW) is even more interesting, because binary and heterostructured III-N NWs have a better crystalline quality compared to their 2D and bulk counterparts. In this context, my work focuses on the plasma-assisted molecular beam epitaxy (PA-MBE) growth of InGaN/GaN NWs and their characterization. Three main topics are addressed: the growth of axial InGaN heterostructures by PA-MBE, their optical characterization, and the study of the selective area growth (SAG) of GaN NWs on transferred graphene. These studies allowed me to obtain a good control over the growth mode of InGaN heterostructures in a wide range of In contents (up to ~ 40%) and morphologies; to study their axial band edge profile, useful for the optimal design of the photovoltaic structure; to demonstrate for the first time, that the SAG of GaN NWs on patterned graphene is a possible and very promising strategy to improve their homogeneity. Finally, preliminary tests have shown that the piezoelectric conversion capacity of GaN NWs can be improved by about 35% when integrating an In-rich InGaN insertion into their volume.
All these results constitute a decisive step in the control and understanding of the properties of these nanostructures, and establish very encouraging perspectives for their integration in novel and efficient photovoltaic and piezoelectric nano-generators.

Université Paris-Saclay
Espace Technologique / Immeuble Discovery
Route de l'Orme aux Merisiers RD 128 / 91190 Saint-Aubin, France